

SYNTHESIS AND CHARACTERIZATION OF
ELECTRODEPOSITED NANOCRYSTALLINE
FERROMAGNETIC COBALT-IRON-PLATINUM ALLOY FILMS

TEH SEOH HIAN

FACULTY OF ENGINEERING
UNIVERSITY OF MALAYA
KUALA LUMPUR

FEBRUARY 2013

SYNTHESIS AND CHARACTERIZATION OF
ELECTRODEPOSITED NANOCRYSTALLINE
FERROMAGNETIC COBALT-IRON-PLATINUM ALLOY FILMS

TEH SEOH HIAN

THESIS SUBMITTED IN FULFILLMENT
OF THE REQUIREMENTS FOR THE DEGREE OF DOCTOR OF
PHILOSOPHY

FACULTY OF ENGINEERING
UNIVERSITY OF MALAYA
KUALA LUMPUR

FEBRUARY 2013

UNIVERSITY OF MALAYA

ORIGINAL LITERARY WORK DECLARATION

Name of Candidate: **TEH SEOH HIAN** (I.C No:

Registration/Matric No: **KHA100004**

Name of Degree: **Doctor of philosophy**

Title of Project/Research Report/Dissertation/Thesis ("this Work")

**SYNTHESIS AND CHARACTERIZATION OF ELECTRODEPOSITED
NANOCRYSTALLINE FERROMAGNETIC COBALT-IRON-PLATINUM ALLOY
FILMS**

Field of Study: Nanotechnology and advance materials/Nanomaterials

I do solemnly and sincerely declare that:

- (1) I am the sole author/writer of this Work;
- (2) This Work is original;
- (3) Any use of any work in which copyright exists was done by way of fair dealing and for permitted purposes and any excerpt or extract from, or reference to or reproduction of any copyright work has been disclosed expressly and sufficiently and the title of the Work and its authorship have been acknowledged in this Work;
- (4) I do not have any actual knowledge nor do I reasonably know that the making of this work constitutes an infringement of any copyright work;
- (5) I hereby assign all the copyright to this Work to the University of Malaya ("UM"), who henceforth shall be owner of the copyright in this Work and that any reproduction or use in any form or by any means whatsoever is prohibited without the written consent of UM having been first had and obtained;
- (6) I am fully aware that if in the course of making this Work I have infringed any copyright whether intentionally or otherwise, I may be subject to legal action or any other action as may be determined by UM.

Candidate's Signature

Date

Subscribed and solemnly declared before,

Witness's Signature

Date

Name:

Designation:

ABSTRACT

In this present work, cobalt-iron, cobalt-platinum, iron-platinum and cobalt-iron-platinum systems were synthesized and characterized. Pure Co film was electrodeposited on brass substrates from sulfate plating baths containing sodium saccharin. The compositions of the electrodeposits were found depended on the concentration of Fe in the electrolytic bath. By alloying Co and Fe, binary Co-Fe alloy film was deposited successfully with various composition of Fe in the electrodeposits. Sodium saccharin was added into plating bath as a grain refining agent to improve the quality of the deposits. The crystallite sizes were calculated from the broadening of X-ray diffraction peak and the sizes were in nanoscale. The Co-Fe films with higher Fe content exhibited irregular shaped granules with rougher surfaces. The domain pattern was stripe like for Co and Co₉₄-Fe₆ films. The structure was changed to granular domain structures with increasing Fe content. The best soft magnetic properties with high saturation magnetizations and low coercivities were obtained when body-centered cubic (BCC) and face-centered cubic (FCC) phases of Co-Fe system was present.

Co-Pt nanocrystalline alloy thin films were electrodeposited using a stable single bath system containing ammonium tartrate solution and ammonia solution as a complex forming additive. Ammonium tartrate was added to promote the polarization of Co²⁺ and Pt⁴⁺ and subsequent enhancement of co-deposition of Co-Pt alloy films. The compositions of the electrodeposits were controlled by adjusting the metal ions in the electrolytic bath and by varying the current density. The as-deposited Co-Pt films contained two possible forms of nanocrystals, which were FCC CoPt₃ and face-center tetragonal (FCT) CoPt or amorphous phases. Formation of granules and clusters were observed in all samples. Magnetic Force Microscopy (MFM) characterization of Co₄₃-Pt₅₇ film showed granular domain structure indicating a correlation between magnetic

force and surface topography. The saturation magnetization values of as-synthesized nanostructured Co-Pt thin films increased with increase of the Co content.

Fe-Pt and Co-Fe-Pt nanocrystalline thin films were electrodeposited on brass substrates from tartrate-alkaline plating bath. The effects of the addition of Co on the properties of Fe-Pt film was focused and investigated. Cobalt was preferentially deposited compared to iron during Co-Fe-Pt film electrodeposition. The microstructure of the films was consisted of spherical granules and clusters. XRD analysis of the films showed the formation of disordered FCC Fe-Pt phase and all peaks were shifted slightly to a higher diffraction angles with increasing cobalt content. The average crystallite size was less than 10 nm. Magnetic properties of the films were increased with the increasing of surface roughness, granule size and clusters. The addition of Co was found to enhance the saturation magnetization and coercivity.

ABSTRAK

Dalam kerja ini, sistem yang dikaji termasuk kobalt-besi, kobalt- platinum, besi-platinum and kobalt-besi-platinum. Filem kobalt yang tulen telah didepositkan pada substrat kuningan tembaga dari larutan pemendapan sulfat yang mengandung garam sakarin. Dengan mengaloikan kobalt dan besi, kobalt-besi aloi deposit elektro telah berjaya dihasilkan dalam lingkungan komposisi sehingga 18% atom peratus besi. Garam sakarin telah ditambahkan ke dalam elektrolit untuk berfungsi sebagai ejen penapisan hablur yang meningkatkan mutu deposit. Komposisi deposit-deposit elektrok adalah selaras dengan kepekatan besi dalam larutan elektrolit. Saiz kristal yang dikira daripada sinar-x pembelauan adalah dalam lingkungan ukuran skala nano. Co-Fe filem dengan kandungan besi yang lebih tinggi memaparkan bentuk bijian yang tak sekata dan permukaan yang kasar. Corak domain adalah berbentuk jalur untuk Co dan $\text{Co}_{94}\text{-Fe}_6$ filem. Corak domain telah berubah menjadi bentuk bijian dengan peningkatan kandungan besi. Sifat magnetik lembut yang paling baik, iaitu dengan nilai ketepuan magnetizam yang tinggi dan nilai “coercivity” yang rendah, telah didapati apabila terdapat campuran struktur kubus berpusat badan (BCC) dan struktur kubus berpusat muka (FCC).

Co-Pt nano-struktur aloi filem telah didepositkan dengan menggunakan larutan tunggal yang stabil yang mengandungi ammonia tartrate dan larutan ammonia sebagai bahan tambahan untuk pembentukan kompleks. Ammonia tartrate telah ditambahkan untuk mempromosikan Co^{2+} and Pt^{4+} polarisasi dan seterusnya meningkatkan co-pemendapan antara Co and Pt. Komposisi deposit elektrok boleh dikawal dengan penyerasan nisbah ion logam dalam elektrolit dan dengan menggunakan ketumpatan arus yang berbeza-beza. Co-Pt filem-filem yang baru didepositkan kemungkinan mengandungi dua bentuk nano-kristal, iaitu FCC CoPt_3 dan struktur segi empat berpusat

muka (FCT) CoPt atau berbentuk amorfus. Pembentukan bijian dan kluster telah diperhatikan. Pencirian MFM pada Co₄₃-Pt₅₇ filem menunjukkan struktur domain yang berbentuk bijian dan terdapat korelasi di antara kekuatan magnetik dengan topografi permukaan. Nilai ketepuan magnetizam meningkat dengan peningkatan kandungan kobalt dalam nano-struktur filem.

Fe-Pt and Co-Fe-Pt nano-struktur filem telah didepositkan pada substrat kuningan tembaga daripada larutan pemendapan tartrate beralkali. Kesan tambahan kobalt terhadap Fe-Pt filem telah diberi tumpuan dan dikaji. Kobalt terlebih dahulu didepositkan berbanding dengan besi dalam pemendapan Co-Fe-Pt filem. Filem berstruktur mikro mengandungi bijian berbentuk bulat and kluster. Pencirian XRD menunjukkan pembentukan FCC Fe-Pt dan semua puncak didapati telah dianjakkan kepada sudut pembelauan yang lebih tinggi dengan peningkatan kandungan kobalt. Purata saiz kristal adalah kurang dari 10 nm. Sifat-sifat magnetik meningkat dengan peningkatan kekasaran permukaan, saiz bijian dan kluster. Penambahan kobalt kepada Fe-Pt filem didapati telah meningkatkan nilai ketepuan magnetizam dan “coercivity”.

ACKNOWLEDGEMENTS

First and foremost, I would like to express my utmost gratitude towards my supervisors, Prof. Dr. Iskandar Idris Yaacob and Assoc. Prof. Dr. Mohd. Rafie Johan for their guidance and supports throughout this research. This thesis would never be able to come out without their advice, suggestion and motivation which were the most essential for the completion of this research.

In the past few years, I have been passing through some difficult times and I would like to take this opportunity to acknowledge some of the special people in my life who have helped me tremendously during those times. Millions thanks to Mr. Mohd. Said and Mr. Zaman for providing instrumental and technical support. Not forgetting all of my friends, especially those are in nano-materials group, whom I wish to express my gratitude to for their support throughout my research. I would also like to express special thanks to Dr. Ang Bee Chin, Dr. Chin Yern Chee, Dr. Yusrini Marita and Miss Siti Hajah for their help in my research work. I also want to express my appreciation to the supporting staffs in Mechanical Engineering Department and Postgraduate office. Financial supports from the Sponsored Research Unit (UPDit) of the Institute of Research Management and Consultancy (IPPP), University of Malaya through the grant FS125/2010B is gratefully acknowledged.

Last but not the least; I dedicate my work to my family members for their wonderful support and encouragement in whatever endeavor I choose to undertake. Without them, I would not be able to get it through and complete my studies. I take this opportunity to express a billion thanks to my parents, brothers and sister, my husband Gary Tan and my three lovely sons for everything that they have done for me.

TABLE OF CONTENTS

ABSTRACT	I
ABSTRAK.....	III
ACKNOWLEDGEMENTS.....	V
TABLE OF CONTENTS.....	VI
LIST OF FIGURES	IX
LIST OF TABLES	XVIII
LIST OF SYMBOLS AND ABBREVIATIONS	XX
 CHAPTER 1: INTRODUCTION.....	 1
1.1 Overview	1
1.2 Motivation for the Present Work	2
1.3 Objectives of the Research	5
1.4 Scopes of the Research	7
1.5 Significance of Research	8
1.6 Description of Thesis Organization	9
 CHAPTER 2: LITERATURE REVIEW.....	 10
2.1 Nanostructured or Nanocrystalline Materials	10
2.1.1 Synthesis of Nanocrystalline Materials.....	11
2.1.2 Potential Applications of Nanocrystalline Materials	13
2.2 Solids	14
2.3 Magnetic Materials	15
2.3.1 Ferromagnetic Materials	19
2.4 Magnetism	20
2.4.1 Hysteresis Loop.....	20
2.4.2 Magnetization and Coercivity	22
2.5 Thin Films.....	26
2.6 Electrodeposition	29
2.6.1 Mechanisms of Electrodeposition	32
2.6.2 Electrocrystallization: Nucleation and Growth of Nuclei	33
2.7 Cobalt, Iron and Platinum Elements	37
2.7.1 Cobalt-Iron Nanocrystalline Films.....	39
2.7.2 Cobalt-Platinum Nanocrystalline Films	42
2.7.3 Iron-Platinum and Cobalt-Iron-Platinum Nanocrystalline Films.....	45
 CHAPTER 3: EXPERIMENTAL PROCEDURES.....	 48
3.1 Electrolyte Solution	48
3.1.1 Preparation of Electrolyte Solution	49
3.2 Electrodes	51

3.3	Electrodeposition Apparatus and Experimental Set Up	52
3.3.1	Electrodeposition Procedures	53
3.4	Experimental Details	56
3.4.1	Co-Fe System	56
3.4.2	Co-Pt System.....	57
3.4.3	Fe-Pt and Co-Fe-Pt System.....	59
CHAPTER 4: CHARACTERIZATION TECHNIQUES		61
4.1	Scanning Electron Microscopy (SEM).....	61
4.1.1	Granules Size Measurement (Linear Intercept Method)	63
4.2	Energy Dispersive X-ray Spectroscopy (EDS)	65
4.3	X-Ray Diffraction (XRD).....	69
4.3.1	Crystallite Size Determination (Debye Scherrer Equation)	72
4.4	Atomic Force Microscopy (AFM).....	73
4.5	Magnetic Force Microscopy (MFM)	76
4.6	Infinite Focus Microscopy (IFM)	79
4.7	Alternating Gradient Magnetometer (AGM).....	80
CHAPTER 5: RESULTS AND DISCUSSION.....		83
5.1	Cobalt-Iron Nanocrystalline Films	83
5.1.1	Physical Appearance	83
5.1.2	Chemical Composition.....	84
5.1.3	X-ray Diffraction (XRD) Analysis.....	87
5.1.4	Surface Morphology and Film Thickness	90
5.1.5	Surface Roughness and Magnetic Force	94
5.1.6	Magnetic Properties.....	99
5.1.7	Summary	101
5.2	Cobalt-Platinum Nanocrystalline Films	102
5.2.1	Physical Appearance	102
5.2.2	Chemical Composition.....	102
5.2.3	X-ray Diffraction Analysis.....	107
5.2.4	Surface Morphology and Film Thickness	110
5.2.5	Surface Roughness and Magnetic Force	113
5.2.6	Magnetic Properties.....	121
5.2.7	Summary	123
5.3	Iron-Platinum and Cobalt-Iron-Platinum Films	124
5.3.1	Physical Appearance	124
5.3.2	Chemical Composition.....	124
5.3.3	X-ray Diffraction Analysis.....	132
5.3.4	Surface Morphology and Film Thickness	136
5.3.5	Surface Roughness and Magnetic Force	140
5.3.6	Magnetic Properties.....	144
5.3.7	Summary	146

CHAPTER 6: POTENTIAL APPLICATIONS, CONCLUSIONS AND RECOMMENDATIONS	146
6.1 Potential Applications.....	146
6.2 Conclusions	151
6.3 Recommendations for Future Research.....	153
REFERENCES.....	156
APPENDICES	166
A. Granule size measurement of Co ₄₃ -Pt ₅₇ alloy thin film by linear intercept method by using SEM micrograph	166
B. The SEM micrograph, EDS spectrum, atomic and weight percentage of elements of Co ₄₃ -Pt ₅₇ alloy film.....	167
C. Example of XRD reference peaks: Fe-Pt face-centered cubic (FCC) phase from JCPDS 29-0717.....	168
D. The XRD peak data and experiment parameter of Co ₄₃ -Pt ₅₇ alloy film obtained using X'Pert Graphics & Identify software.....	169
E. Full width at half maximum (FWHM) value of Co ₄₃ -Pt ₅₇ alloy film obtained using Philips Electronics's ProFit TM software.....	170
F. The deconvoluted XRD peak of Co ₄₃ -Pt ₅₇ alloy film obtained using Philips Electronics's ProFit TM software.....	171
G. Crystallite size determination of nanostructured Co ₄₃ -Pt ₅₇ alloy thin film (Debye Scherrer' equation)	172
LIST OF PUBLICATIONS.....	173

LIST OF FIGURES

Figure 1.1:	4
Herzer diagram illustrating the dependence of the coercivity (H_c) with grain size (D) in magnetic alloys (Tang and Sheng, 2003; Cheung, 2001)	4
Figure 1.2:	5
The relationship between permeability (μ_c) (at 1 kHz) and saturation polarization (B_s) for soft magnetic materials (Tang and Sheng, 2003)	5
Figure 2.1:	13
Illustration of building of particles, layers, nanotubes or nanorods from atoms (ions) or molecules (Vollath, 2008)	13
Figure 2.2:	15
Illustration of the difference between (a) single crystal, (b) polycrystalline, and (c) amorphous materials (Suryanarayana and Norton, 1998)	15
Figure 2.3:	18
Illustration of various arrangements of individual magnetic moments that constitute paramagnetic, ferromagnetic, ferrimagnetic and antiferromagnetic materials	18
Figure 2.4:	22
Schematic diagram of M vs. H or hysteresis loop showing magnetic properties and domain structures during different stages of magnetization	22
Figure 2.5:	24
Variation of coercivity with particle size, for particles whose coercivity depends on crystal anisotropy (Cullity and Graham, 2009)	24
Figure 2.6:	25
Schematic diagram of variation of coercivity (H_c) with particle diameter (D)	25

Figure 2.7:	28
Various typical nanostructured films	28
Figure 2.8:	32
Schematic diagram of electrodeposition process	32
Figure 2.9:	36
Schematic diagram of kink site, step edge and adatom (Internet Reference, b)	36
Figure 2.10:	41
Equilibrium phase diagram of the iron-cobalt system (Martin, 1999)	41
Figure 2.11:	44
Equilibrium phase diagram for the cobalt-platinum system (Nalwa, 2002)	44
Figure 2.12:	46
Equilibrium phase diagram of Fe–Pt binary alloy system (Wang et al., 2004)	46
Figure 3.1:	49
Co ²⁺ and Fe ²⁺ ion sources were added to electrolyte solution for electrodeposition process	49
Figure 3.2:	53
Arrangement of electrodeposition apparatus	53
Figure 3.3:	54
Experimental setup of electroplating cell	54
Figure 3.4:	55
Preparation route of magnetic nanostructured thin films by electrodeposition process	55
Figure 4.1:	62
Schematic diagram of a scanning electron beam incident on a solid sample, showing some of the signals generated that can be used to characterize the microstructure (Brandon and Kaplan, 2008)	62

Figure 4.2:	64
Granule size is defined in several discrete ways which are not related to one another, for example (a) the mean caliper diameter and (b) average intercept length along a random line	64
Figure 4.3:	66
The ionization process of an atom. An inner (K) shell electron is ejected by a high-energy electron. When the hole in the K shell is filled by an electron from the L shell, characteristic ($K\alpha$) X-ray emission occurs. The beam electron loses energy but continues on through the specimen (William et al., 2009)	66
Figure 4.4:	67
The schematic diagram of a complete range of possible electron transitions that give rise to K, L, and M characteristic X-rays (William et al., 2009)	67
Figure 4.5:	68
Image of energy dispersive X-ray spectroscopy (EDS: Model EDAX) attached on a scanning electron microscope	68
Figure 4.6:	69
Philips X'pert MPD system was used for phase analysis and crystallite size calculation	69
Figure 4.7:	70
The incident X-rays and reflected X-rays make an angle of symmetric θ to the normal of crystal plane	70
Figure 4.8:	71
Full width half maximum (FWHM) of an X-ray diffraction peak	71
Figure 4.9:	73
XRD diffraction patterns of standard calibration material (LaB_6)	73

Figure 4.10:	75
Image of Quesant atomic force microscopy (AFM)	75
Figure 4.11:	75
Image of Q Scope magnetic force microscopy (MFM)	75
Figure 4.12:	76
Illustration of the AFM beam deflection system, using a laser and photo-detector to measure the beam position	76
Figure 4.13:	78
A special cantilever with a magnetized tip is placed in a magnetic field for magnetization before the MFM measurement	78
Figure 4.14:	78
Magnetic imaging is generated by lift mode. Cantilever traces surface topography on first trace and retrace (1&2). Cantilever ascends to “lift scan height” (3). Lifted cantilever profiles topography while responding to magnetic influences on second trace and retrace to acquire magnetic force data (4 & 5)	78
Figure 4.15:	79
Illustration of the infinite focus microscopy (IFM) beam deflection system, using a laser and photo=detector to measure the beam position	79
Figure 4.16:	80
Image of infinite focus microscopy (IFM)	80
Figure 4.17:	81
Image of alternating gradient magnetometer (AGM: Model 2900 MicroMag, Princeton Measurements Corporation)	81
Figure 4.18:	82
Image of transducer probe	82

Figure 5.1:	84
Physical appearance of as-deposited nanocrystalline films: (a) Co ₁₀₀ , (b) Co ₉₄ -Fe ₆ , (c) Co ₈₉ -Fe ₁₁ , (d) Co ₈₆ -Fe ₁₄ , (e) Co ₈₂ -Fe ₁₈ , (f) Co-Fe film deposited without saccharin and (g) Co ₄₀ -Fe ₆₀ film deposited with saccharin.....	84
Figure 5.2:	85
Effect of FeSO ₄ concentration in electrolyte solutions on Fe content in the deposits	85
Figure 5.3:	86
Energy dispersive X-ray spectroscopy (EDS) spectra of (a) Co ₁₀₀ and (b) Co ₈₂ -Fe ₁₈ films	86
Figure 5.4:	89
X-ray diffraction (XRD) patterns of as-synthesized nanostructured Co-Fe thin films at various compositions: (a) Co ₁₀₀ , (b) Co ₉₄ -Fe ₆ , (c) Co ₈₉ -Fe ₁₁ , (d) Co ₈₆ -Fe ₁₄ and (e) Co ₈₂ -Fe ₁₈	89
Figure 5.5:	90
The face centered cubic (FCC), body centered cubic (BCC) and hexagonal closed packed (HCP) Bravais lattices.....	90
Figure 5.6:	92
Scanning electron microscopy (SEM) images of as-synthesized nanocrystalline films: (a) Co ₁₀₀ and (b) Co ₉₄ -Fe ₆ (at 20000x magnification); (c) Co ₈₉ -Fe ₁₁ , (d) Co ₈₆ -Fe ₁₄ and (e) Co ₈₂ -Fe ₁₈ (at 2000x magnification).....	92
Figure 5.7:	93
Cross-sectional scanning electron microscopy (SEM) images of (a) Co ₁₀₀ , (b) Co ₉₄ -Fe ₆ , (c) Co ₈₉ -Fe ₁₁ , (d) Co ₈₆ -Fe ₁₄ and (e) Co ₈₂ -Fe ₁₈ alloy films	93

Figure 5.8:	96
2-D atomic force microscopy (AFM) images (i) and 3-D topographic images (ii) of as-synthesized films: (a) Co ₁₀₀ , (b) Co ₉₄ -Fe ₆ , (c) Co ₈₉ -Fe ₁₁ , (d) Co ₈₆ -Fe ₁₄ and (e) Co ₈₂ -Fe ₁₈	96
Figure 5.9:	98
2-D magnetic force microscopy (MFM) images (i) and 3-D topographic images (ii) of as-synthesized films: (a) Co ₁₀₀ , (b) Co ₉₄ -Fe ₆ , (c) Co ₈₉ -Fe ₁₁ , (d) Co ₈₆ -Fe ₁₄ and (e) Co ₈₂ -Fe ₁₈	98
Figure 5.10:	99
Separation of magnetic domains in ferromagnetic materials by <i>Bloch</i> walls	99
Figure 5.11:	100
Typical parallel hysteresis curves at room temperature of as-synthesized nanocrystalline thin films: (a) Co ₁₀₀ , (b) Co ₉₄ -Fe ₆ , (c) Co ₈₉ -Fe ₁₁ , (d) Co ₈₆ -Fe ₁₄ and (e) Co ₈₂ -Fe ₁₈	100
Figure 5.12:	102
Physical appearance of as-synthesized nanocrystalline thin films: (a) Co ₉₇ -Pt ₃ , (b) Co ₉₅ -Pt ₅ , (c) Co ₈₆ -Pt ₁₄ , (d) Co ₅₆ -Pt ₄₄ and (e) Co ₄₃ -Pt ₅₇	102
Figure 5.13:	104
Energy dispersive X-ray spectroscopy (EDS) spectra of as-synthesized nanocrystalline (a) Co ₉₇ -Pt ₃ and (b) Co ₄₃ -Pt ₅₇ films	104
Figure 5.14:	105
Effect of CoCl ₂ concentration in electrolyte solutions on Co content in deposits	105
Figure 5.15:	106
Elemental mapping of as-synthesized Co ₈₆ -Pt ₁₄ nanocrystalline thin film	106
Figure 5.16:	108
X-ray diffraction (XRD) patterns of as-synthesized nanostructured Co-Pt alloy films: (a) Co ₉₇ -Pt ₃ , (b) Co ₉₅ -Pt ₅ , (c) Co ₈₆ -Pt ₁₄ (d) Co ₅₆ -Pt ₄₄ and (e) Co ₄₃ -Pt ₅₇	108

Figure 5.17:	109
The face centered cubic (FCC) and face centered tetragonal (FCT) Bravais lattices ...	109
Figure 5.18:	111
Scanning electron microscopy (SEM) images of as-synthesized nanocrystalline thin films: (a) Co ₉₇ -Pt ₃ , (b) Co ₉₅ -Pt ₅ , (c) Co ₈₆ -Pt ₁₄ , (d) Co ₅₆ -Pt ₄₄ and (e) Co ₄₃ -Pt ₅₇ at 1000x magnification.....	111
Figure 5.19:	112
Cross-sectional scanning electron microscopy (SEM) images of as-synthesized nanocrystalline thin films: (a) Co ₉₇ -Pt ₃ , (b) Co ₉₅ -Pt ₅ , (c) Co ₈₆ -Pt ₁₄ , (d) Co ₅₆ -Pt ₄₄ and (e) Co ₄₃ -Pt ₅₇	112
Figure 5.20:	116
2-D atomic force microscopy (AFM) image (i) and 3-D AFM topographical image (ii) of as-synthesized films: (a) Co ₉₇ -Pt ₃ (surface area 80 μm x 80 μm), (b) Co ₈₆ -Pt ₁₄ (surface area 40 μm x 40 μm), (c) Co ₅₆ -Pt ₄₄ (surface area 80 μm x 80 μm) and (d) Co ₄₃ -Pt ₅₇ (surface area 80 μm x 80 μm).	116
Figure 5.21:	116
3-D atomic force microscopy (AFM) topographic images of as-synthesized Co ₈₆ -Pt ₁₄ film at surface area of 80 μm x 80 μm. The data is unusable as the granules shape was found be distorted and evidence of tearing of surface feature	116
Figure 5.22:	117
2-D MFM, (b) 3-D MFM, (c) 2-D IFM and (d) 3-D IFM images of as-synthesized nanostructured Co ₄₃ -Pt ₅₇ thin films. (Note: IFM magnification at 100x)	117
Figure 5.23:	119
3-D IFM images (in pseudo color) of as-synthesized nanocrystalline thin films: (a) Co ₉₇ -Pt ₃ , (b) Co ₉₅ -Pt ₅ , (c) Co ₈₆ -Pt ₁₄ , (d) Co ₅₆ -Pt ₄₄ and (e) Co ₄₃ -Pt ₅₇	119

Figure 5.24:	121
Histogram analysis of surface roughness obtained from (a) AFM, (b) MFM and (c) IFM for as-synthesized nanostructured Co ₄₃ -Pt ₅₇ thin films	121
Figure 5.25:	122
Typical parallel hysteresis curves at room temperature of as-synthesized nanocrystalline thin films: (a) Co ₉₇ -Pt ₃ , (b) Co ₉₅ -Pt ₅ , (c) Co ₈₆ -Pt ₁₄ , (d) Co ₅₆ -Pt ₄₄ and (e) Co ₄₃ -Pt ₅₇	122
Figure 5.26:	124
Physical appearance of as-synthesized nanocrystalline thin films: (a) Fe ₅₄ -Pt ₄₆ , (b) Co ₁₅ -Fe ₁₈ -Pt ₆₇ , (c) Co ₁₇ -Fe ₁₁ -Pt ₇₂ , (d) Fe ₇₀ -Pt ₃₀ , (e) Co ₅₃ -Fe ₈ -Pt ₃₉ , (f) Co ₆₉ -Fe ₅ -Pt ₂₆ and (g) Pt ₁₀₀	124
Figure 5.27:	126
Energy dispersive X-ray spectroscopy (EDS) spectra of (a) Fe ₇₀ -Pt ₃₀ , (b) Co ₅₃ -Fe ₈ -Pt ₃₉ and (c) Co ₆₉ -Fe ₅ -Pt ₂₆ films	126
Figure 5.28:	127
Structure of complexing agent: tartrate	127
Figure 5.28:	129
Elemental mapping of as-synthesized Fe ₇₀ -Pt ₃₀ nanocrystalline thin film	129
Figure 5.29:	130
Elemental mapping of as-synthesized Co ₅₃ -Fe ₈ -Pt ₃₉ nanocrystalline thin film	130
Figure 5.30:	131
Elemental mapping of as-synthesized Co ₆₉ -Fe ₅ -Pt ₂₆ nanocrystalline thin film.....	131
Figure 5.31:	133
X-ray diffraction (XRD) patterns of as-synthesized nanocrystalline thin films: (a) Fe ₅₄ -Pt ₄₆ , (b) Co ₁₅ -Fe ₁₈ -Pt ₆₇ and (c) Co ₁₇ -Fe ₁₁ -Pt ₇₂	133

Figure 5.32:	134
X-ray diffraction (XRD) patterns of as-synthesized nanocrystalline thin films: (d) Fe ₇₀ -Pt ₃₀ , (e) Co ₅₃ -Fe ₈ -Pt ₃₉ and (f) Co ₆₉ -Fe ₅ -Pt ₂₆	134
Figure 5.33:	135
Schematic illustration of the unit cell of disordered FCC Fe-Pt or FCC Co-Fe-Pt. The darker lattice points are to the front of the unit cells.....	135
Figure 5.34:	137
Scanning electron microscopy (SEM) of as-prepared nanostructured alloy thin films: (a) Fe ₅₄ -Pt ₄₆ , (b) Co ₁₅ -Fe ₁₈ -Pt ₆₇ , (c) Co ₁₇ -Fe ₁₁ -Pt ₇₂ , (d) Fe ₇₀ -Pt ₃₀ , (e) Co ₅₃ -Fe ₈ -Pt ₃₉ , (f) Co ₆₉ -Fe ₅ -Pt ₂₆ and (g) Pt ₁₀₀	137
Figure 5.35:	140
Cross sectional scanning electron microscopy (SEM) of as-prepared alloy thin films: (a) Fe ₅₄ -Pt ₄₆ , (b) Co ₁₅ -Fe ₁₈ -Pt ₆₇ , (c) Co ₁₇ -Fe ₁₁ -Pt ₇₂ , (d) Fe ₇₀ -Pt ₃₀ , (e) Co ₅₃ -Fe ₈ -Pt ₃₉ and (f) Co ₆₉ -Fe ₅ -Pt ₂₆	140
Figure 5.36:	142
2-D atomic force microscopy (AFM) images (i) and 3-D images (ii) of as-prepared thin films: (a) Fe ₇₀ -Pt ₃₀ , (b) Co ₅₃ -Fe ₈ -Pt ₃₉ and (c) Co ₆₉ -Fe ₅ -Pt ₂₆	142
Figure 5.37:	143
2-D Magnetic force microscopy (MFM) images (i) and 3-D images (ii) of as-prepared thin films: (a) Fe ₇₀ -Pt ₃₀ , (b) Co ₅₃ -Fe ₈ -Pt ₃₉ and (c) Co ₆₉ -Fe ₅ -Pt ₂₆	143
Figure 5.38:	145
Typical parallel hysteresis curves at room temperature of as-synthesised nanocrystalline thin films: (a) Fe ₅₄ -Pt ₄₆ , (b) Co ₁₅ -Fe ₁₈ -Pt ₆₇ , (c) Co ₁₇ -Fe ₁₁ -Pt ₇₂ , (d) Fe ₇₀ -Pt ₃₀ , (e) Co ₅₃ -Fe ₈ -Pt ₃₉ and (f) Co ₆₉ -Fe ₅ -Pt ₂₆	145

LIST OF TABLES

Table 2.1: Classification of magnetic materials (Judy and Myung, 2001).....	17
Table 2.2: Experimental anisotropy constants for different chemically ordered alloys thin films (Nalwa, 2002).....	28
Table 2.3: General properties of Cobalt, Iron and Platinum.....	38
Table 2.4: Equilibrium crystal structures of iron-cobalt alloys.....	42
Table 3.1: The molarities of electrolyte solutions and electrodeposition operating conditions for Co-Fe films synthesis.....	57
Table 3.2: The molarities of electrolyte solutions and electrodeposition operating conditions for Co-Pt films synthesis.....	58
Table 3.3: The electrolyte compositions and electrodeposition conditions for the synthesis of Fe-Pt and Co-Fe-Pt films.....	60
Table 5.1: The atomic percentage of Co and Fe in the deposited film determined by EDS.....	87
Table 5.2: Crystallite structure, phases and sizes of as-synthesized Co-Fe nanocrystalline alloy films.....	88
Table 5.3: Structural and magnetic results of as-synthesized Co-Fe thin films.....	91
Table 5.4: The atomic percentage of Co in the as-deposited films at current density of 2000Am^{-2} and 3000Am^{-2}	103
Table 5.5: Crystallite structure and sizes of as-synthesized Co-Pt nanocrystalline alloy films.....	109
Table 5.6: Structural and magnetic results of as-synthesized Co-Fe thin films. (ND=Non-detectable).....	113

Table 5.7:	
Molar ratio of electrolyte solutions and atomic percentages of Co, Fe and Pt determined by EDS.....	128
Table 5.8:	
Crystallite structure, phases and sizes of as-synthesized Fe-Pt and Co-Fe-Pt nanostructured alloy thin films.....	135
Table 5.9:	
Film thickness, granule size, saturation magnetization and coercivity values of Fe-Pt and Co-Fe-Pt thin films.....	138
Table 5.10:	
Surface roughness, average height, maximum height and magnetic force of Fe-Pt and Co-Fe-Pt thin films.....	141
Table 6.1:	
Potential applications of various thin films system synthesized from this research and summarized from literatures.....	149

LIST OF SYMBOLS AND ABBREVIATIONS

Symbol or Abbreviations	Meaning
a	Lattice parameter (nm)
B_s	Saturation polarization
d	Inter atomic spacing
D	Crystallite/ grain size (nm)
D_c	Caliper diameter
D_L	Mean linear intercept
e-	Electron
E	Applied potential
E_{eq}	Equilibrium potential
F	Faraday's constant (coulombs)
H	Applied field
H_c	Coercivity/ coercive field
K_I	Anisotropy constant
K_u	Magnetocrystalline anisotropy
I	Applied current (A)
MW	Molecular weight
m	Mass reacted
M	Molarities (mol/l)/ internal cation molarity (mol/l)
M	Magnetization
M_s	Saturation magnetization
M_r	Remanance/ remanent magnetization
$Mass_{act}$	Actual weight
$Mass_{theo}$	Theoretical weight

n	The number of electrons in the reaction
N_L	The number of intercepts per unit length of a test line
Q_j	Number of coulombs required
Q_{total}	Total number of coulombs
Ra	Average surface roughness
RMS	Root mean square roughness
s	Stoichiometric coefficient
t	Charging time
AFM	Atomic force microscopy
AGM	Alternating gradient magnetometer
BCC	Body centered cubic
DC	Direct current
EDS	Energy dispersive x-ray
FCC	Face centered cubic
FCT	Face centered tetragonal
FWHM	Full width half maximum
HCP	Hexagonal closed-packed
IFM	Infinite focus microscopy
MFM	Magnetic force microscopy
SEM	Scanning electron microscopy
SHE	Standard hydrogen electrode
XRD	X-ray diffraction
λ	X-ray wavelength
θ	Bragg angle/ diffraction angle (radian)
η	Over potential/ current efficiency

χ	Susceptibility
μ	Permeability
μ_c	Permeability at 1 kHz
μ_0	Magnetic permeability of free space, $4\pi \times 10^{-7} \text{ Hm}^{-1}$
μ_r	Relative permeability
δ_w	Domain <i>Bloch</i> wall thickness

CHAPTER 1: INTRODUCTION

1.1 Overview

Nano-, a prefix denoting a factor of 10^{-9} has its origin in the Greek words *nanos*, meaning dwarf (Geoffrey and Andre, 2006). Nanoscience is a field on studies of the properties of matter that has at least one dimension in the order of a billionth of a meter, called a nanometer (Owens and Poole, 2008). In general, nanosciences study nano-objects, i.e. nanometric-sized objects and their transformation into nanomaterials (Corriu and Trong Anh, 2009).

Nanotechnology literally means any technology in nanoscale that has applications in the real world (Bhushan, 2010). The science and engineering for creating materials, functional structures and devices in the order of nanometer scale is termed as nanotechnology (Nalwa, 2000). The fundamental concepts of modern nanotechnology originate from ideas of Professor Richard Feynman. He suggested that in the near future engineers would be able to take atoms and place them exactly where they wanted to, without infringing the laws of nature (Feynman, 1992). This is based upon a conceptual understanding of the manipulation of materials in the atomic length scale. Today, Professor Feynman's lecture, which was entitled "There is Plenty of Room at the Bottom", is considered a milestone of the current technological and scientific era. The main difference between nanotechnology and conventional technologies is that the 'bottom-up' approach is preferred in nanotechnology, whereas conventional technologies usually use the "top-down" approach (Vollath, 2008).

In this thesis, the term crystallites and grains will be used interchangeably. Nanostructured materials are material with a structure having the characteristic length in the order of a few (typically 1-100) nanometers (Tang and Sheng, 2003). The fundamental physical, chemical, and biological properties of materials are surprisingly altered as their constituent grains are decreased to nanometer scale owing to their size,

shape, surface chemistry and topology (Nalwa, 2002). Nanocrystalline materials have received much attention because of their unique physical, chemical and mechanical properties and have been a subject of intensive research activities both in the scientific and industrial communities. The industrial applications of nanomaterials continue to grow in number, with hundreds of products are available now worldwide. The ever faster progress in nanotechnology is aimed at obtaining smaller and smaller feature sizes of the functional and structural components with high degree of control which allows higher integration densities, higher speed in addition with lower energy consumption and lower costs.

The nanotechnological applications included nanosized particulates for scratch protection on eye glasses, for UV light absorption in lotions form sun protection by adjusting the viscosity, wear minimization in the rubber of car tires, etc (Wilde, 2009). Most recently, novel gold nanoparticles, a highly sensitive assay has been developed and applied to monitor the progression and treatment of Alzheimer's disease in model mice (Internet Reference, a). With most of the future applications that are in the background of today's basic research, not only the functional units need to be nanosized, but also the material that used for interfacing the micro- or even the macro-world might be nanosized systems such as substrates, supports or leads will have to be structured at nanoscale.

1.2 Motivation for the Present Work

The initiation of the research project was motivated by the ever increasing interest in the rapid development of nanosciences and nanotechnologies. Nanotechnology has gradually emerged from a micro technology journey towards producing ever smaller scale devices. Due to interdisciplinary nature of nanotechnology, researchers from various disciplines have been involved creating growth of

nanotechnology as a promising field of study. This demand is quantified by the famous Moore's law which predicts that the performance of electronic components increase by one order of magnitude in every two years. The microprocessors are therefore miniaturized towards nano dimensions for increasing processing speed.

In the early work on nanocrystalline materials, it was believed that the grain possesses a single domain when the grain size is below a critical size as described by the classical model of rotational hysteresis presented by Stoner-Wolfarth (Martin, 1999). Recent developments in the understanding of the mechanism of magnetic coercivity has led to the realization that the coercivity (H_c) decreases rapidly with decreasing grain size for very small grain sizes ($D < \sim 100$ nm) as shown in Figure 1.1 (Tang and Sheng, 2003; Cheng, 2001). This curve shows that coercivity has an inverse relationship with the grains size especially when the grain size is in the range between 1 nm to 50 nm (Cheng, 2001). The D^6 dependence of coercivity exists when the grain sizes are below 50 nm which was explained by the random anisotropy model. This phenomenon is accounted from the averaging of anisotropy due to the exchange interaction or grain coupling when the grain size is below the ferromagnetic exchange length (Martin, 1999).

With the discovery of tremendous reduction in coercivity at very small grain, considerable research efforts were initiated in last few decades to develop nanocrystalline ferromagnetic materials for application as soft magnet. Furthermore, materials with very small crystallite or grain size exhibit enhanced properties such as increased electrical resistivity and mechanical hardness. These research efforts in nano-processing led to a new class of exceptional soft magnetic materials.

As a result, high saturation magnetization, high permeability with zero magnetostriction magnetic alloys have been developed for the use in toroidal cores, choke coils and pulse transformers (Martin, 1999). The relationship between saturation polarization (B_s) and permeability μ_c (at 1 kHz) for these soft magnetic materials are

shown in Figure 1.2. In this research, we discussed the nanoprocessing as well as the significant technological advancement and applications of these soft magnetic materials. Nanoprocessed soft magnetic alloys with high saturation magnetization, electrical resistivity, wear resistance and low coercivity represent excellent venues for future applications such as high performance transformers, motors, amplifiers and field sensors.

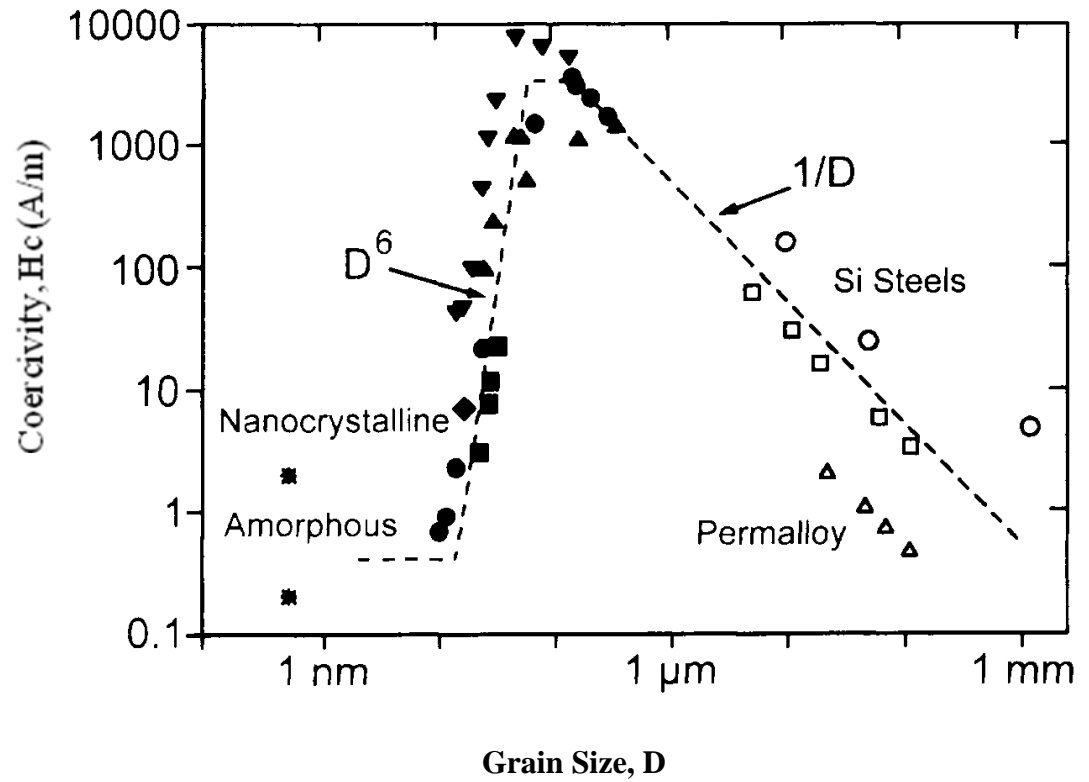


Figure 1.1:
Herzer diagram illustrating the dependence of the coercivity (H_c) with grain size (D) in magnetic alloys (Tang and Sheng, 2003; Cheung, 2001)

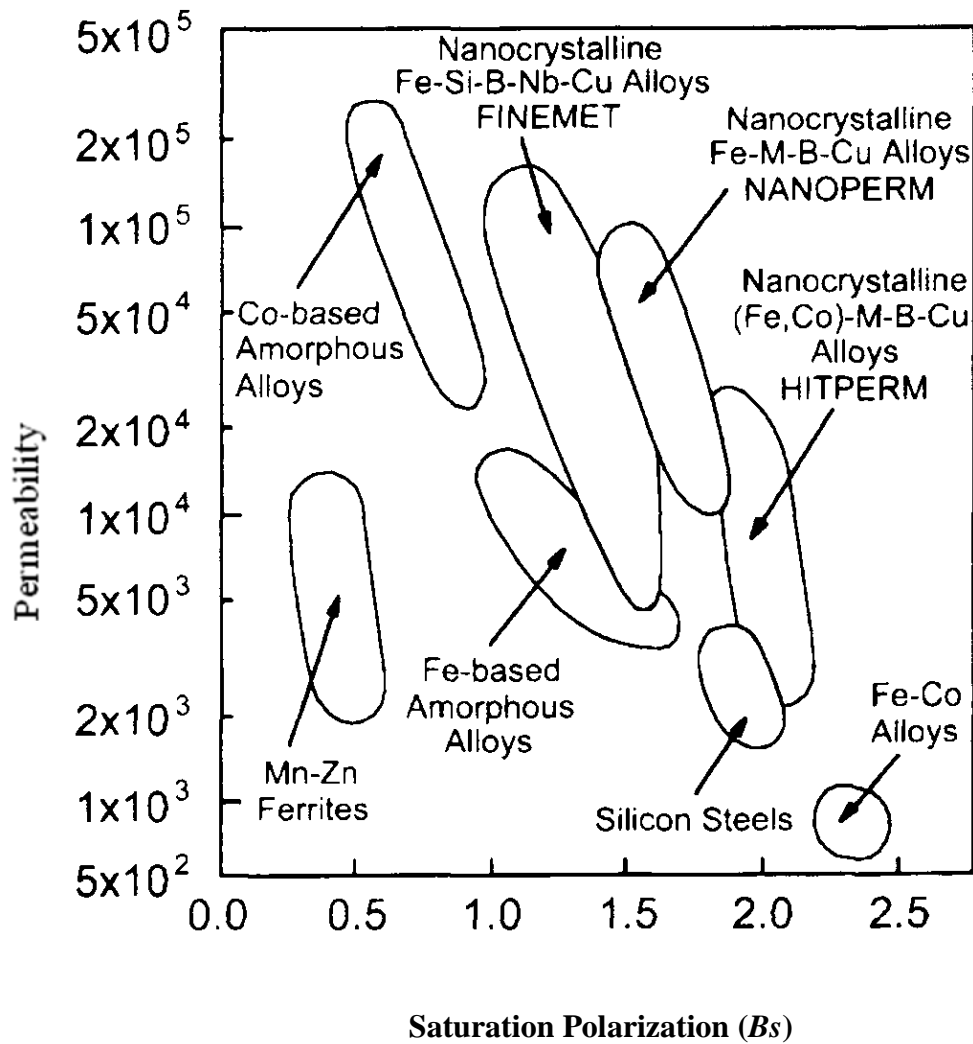


Figure 1.2:
The relationship between permeability (μ_c) (at 1 kHz) and saturation polarization (B_s) for soft magnetic materials (Tang and Sheng, 2003)

1.3 Objectives of the Research

The primary objective of this research is to develop a novel synthesis method for producing soft magnetic materials that are nanocrystalline or having nanostructured microstructure. This research is aimed to fill the existing research gap by covering a useful overview of related nanostructured magnetic materials in addition with their preparation methods, processing and fabrication into thin film. In other words, the research work is focused on the synthesis, characterization and development of

nanostructured soft magnetic films in terms of their composition, crystallographic structure, surface morphology and magnetic properties. Although an electrodeposition process has been proven to be a feasible and effective means for synthesizing various functional nanostructured materials, however, there is lacking of information because of the great difficulty in preparing stable and effective deposition electrolytes. Efforts to develop a stable and effective electrodeposition process are essential for industry aspiration.

A wide variety of microstructural and nanoscale characterization methods were carried out in this research to determine the chemical, structural and magnetic properties of nanostructured magnetic films. The magnetic properties of alloy films are strongly dependent on their compositions, crystal structures, grain sizes and interfacial structures. By understanding these variables the factors that affect the magnetic properties can be elucidated. Therefore, the effect of the composition of plating solution on the composition of film, surface morphologies, crystallographic structures and magnetic properties were also investigated. Target materials include cobalt-iron alloys, cobalt-platinum alloys, iron-platinum alloys and cobalt-iron-platinum alloys.

In this context, the objectives of this research study can be stated as:

- to synthesize Co-Fe, Co-Pt, Fe-Pt and Co-Fe-Pt nanocrystalline thin films by electrodeposition technique
- to characterize and correlate physical, structural and magnetic properties of the Co-Fe, Co-Pt, Fe-Pt and Co-Fe-Pt thin films
- to investigate the processing factors in order to optimize the physical and magnetic properties of Co-Fe, Co-Pt, Fe-Pt and Co-Fe-Pt thin films
- to determine the effects of complex forming additive and grain refining agent in alloy thin film formation

1.4 Scopes of the Research

This research work was divided into two stages for each type of alloy films. In the first stage, the plating solutions were selected, deposition parameters were optimized and plating bath concentration was determined. Although there were a lot of attempts for determining an optimum plating bath condition, only those plating baths with excellent physical properties are discussed in this work. For the recent stage, the as-deposited magnetic thin films with good quality (physical appearance and chemical composition) are selected for further characterizations such as X-ray diffraction (XRD) analysis, scanning electron microscopy (SEM), energy dispersive X-ray spectroscopy (EDS), atomic force microscopy (AFM), magnetic force microscopy (MFM), infinite focus microscopy (IFM), and alternating gradient magnetometer (AGM). As coercivity and saturation magnetization are strongly dependent on the grain size and the morphology of materials, the correlation between magnetization behavior with nanostructure and morphology of alloy films was also investigated in this research.

Firstly, the research was started with the fabrication of Co-Pt nanocrystalline alloy thin films which were electrodeposited on brass substrates using a novel stable single bath system containing ammonium tartrate and ammonia solution as complex forming additive. Subsequently, attempt was taken to synthesize Fe-Pt and Co-Fe-Pt nanocrystalline thin films by electrodeposition technique with the addition of tartrate-alkaline additives into the plating bath. To the author's best knowledge, there is no publication on Co-Fe-Pt thin films prepared by electrochemical deposition method as the preparation of stable and effective electrolyte is very difficult. The effects of various concentrations of cobalt on the composition, crystallographic structure, microstructure and magnetic properties of the Fe-Pt alloy films were studied. Finally, a novel approach for the fabrication of soft magnetic Co-Fe films is demonstrated via electrodeposition

process from a sulfate salt-based solution containing sodium saccharin which acted as a grain refining agent to improve the quality of deposits.

1.5 Significance of Research

Thin films of ferromagnetic metal alloys produced by electrodeposition have attracted a considerable attention to the researchers due to their excellent magnetic properties. Numerous physical and chemical methods have been employed to produce metal alloys such as sputtering, metal evaporation, grinding, metal salt reduction in liquid phase, etc. Electrodeposition is an alternative technique which is quite simple. However, preparation of stable and effective single plating baths for Co-Pt, Fe-Pt and Co-Fe-Pt alloy deposition is very difficult due to the big difference in standard equilibrium potentials of Co, Fe and Pt. The work presented in this thesis could be potentially useful in the field of nanostructured ferromagnetic thin film processing.

This research also provides a significant insight and development with new information for the fabrication of nanostructured thin films with the addition of complex forming additive and grain refining agent. Nanocrystalline alloy thin films with various compositions were successfully electrodeposited on brass substrates. The fabrication of nanostructured magnetic thin films was controlled by selectively changing the plating bath compositions and deposition parameters. Electrodeposition method is a very simple and economically attractive technique. However, a very good knowledge of the deposition parameters is required to produce reproducible magnetic thin films. The present synthesis procedure provides a unique, effective and inexpensive electrochemical method for the preparation of ferromagnetic thin films from single aqueous solution. Definitely, the information can be shared among the researcher around the world. The data and results from this research work were published in international journals as well as highly visible conferences.

1.6 Description of Thesis Organization

This thesis consists of six chapters. Chapter 1 gives a brief introduction about the field of study, motivation, objectives, scope and significance of this research. Chapter 2 reviews the literature on nanotechnology, nanostructured or nanocrystalline materials, magnetic materials, thin films, electrodeposition methods and Co-Fe-Pt alloys. Chapter 3 describes the experimental procedure for the fabrication of nanocrystalline magnetic alloy films. Since this research is emphasized on nanomaterial characterization methods, Chapter 4 describes general features of the instrumentation and data interpretation. The results of Co-Pt, Fe-Pt and Co-Fe-Pt as well as Co-Fe alloy films that were obtained from these characterization methods are analyzed and discussed in Chapter 5. Several interesting conclusions, potential applications and recommendations for future work are summed up and presented in Chapter 6.

CHAPTER 2: LITERATURE REVIEW

2.1 Nanostructured or Nanocrystalline Materials

What are nanomaterials? There are two definitions. The first and the broadest definition states that nanomaterials are materials where the sizes of the individual building block are less than 100 nm, at least in one dimension (Rao et al., 2002; Vollath, 2008). The second definition is much more restrictive and states that nanomaterials have properties which depend inherently on the small grain size and as nanomaterials are usually quite expensive, such a restrictive definition makes more sense (Vollath, 2008).

The prefix “nano”, the word used in nanotechnology means a billionth (1×10^{-9}). Nanostructured materials or nanomaterials are those materials having structural units in nanometer scale at least in one direction. These types of materials have received a considerable amount of attention worldwide over the past decade (Ejtekhari, 2008). Materials with this kind of a nanometer-sized structure are often called “nanostructured materials”, or –synonymously nanophase materials, nanocrystalline materials or supramolecular solids (Tang and Sheng, 2003). Many of the physical and structural properties are different in nanomaterials from those observed at the micrometric scale. Since material properties become different in the nanoscale, much effort is currently being dedicated to the synthesis, structural control and properties improvement of the nanomaterials.

Herbert Gleiter is deemed to be the initiator and pioneer of research related to nanocrystalline materials who found ways to produce materials with this new atomic structure (Cheung, 2001). Professor Gleiter’s work in the fields of particle hardening of alloys as well as atomic structure and properties of grain and phase boundaries in crystalline substances belongs to the classical foundation that has entered in the studies of textbooks. Nanostructured or nanocrystalline material is basically polycrystalline materials having a bulk shape consisting of a dense array of crystallites in the size range

well below to 100 nm (Widle, 2009). In short, single phase polycrystalline materials are made up of many small crystals or grains (Brandon and Kaplan, 2008). Owing to decreasing dimensions, the fraction of surface atoms located at grain boundaries or interfaces increases in the nanocrystalline materials. From a simple geometrical estimation considering the grains as spheres or cubes, it can be shown that 50%, 30% and about 3% volume fraction is exposed in the 5 nm, 10 nm and 100 nm grains, respectively (Widle, 2009).

2.1.1 Synthesis of Nanocrystalline Materials

Nanostructured materials and nanocomposites can be produced by a variety of different methods. Besides the fabrication of clusters, thin films and coatings from the gas or liquid phase, chemical methods such as sol-gel processes and electrodeposition are common methods of processing nanostructures. Many techniques have been used to synthesize magnetic thin films including gas condensation, ball milling, chemical processing, metal-organo complex routes, solution reduction, co-precipitation, sol-gel, sputtering, rapid solidification, devitrification of amorphous alloy and electrodeposition (Martin, 1999). Synthesis of nanomaterials might be very simple or quite complex depending on the routes. The methods that are applied for the synthesis of nanostructured materials can be categorized into two groups: “top down synthesis routes” and “bottom up synthesis” (Tang and Sheng, 2003).

- ***Top-down synthesis routes.*** This approach involves the assembly of nanostructured materials from pre-fabricated or pre-existing structural elements such as pre-fabricated nanometer sized crystals, supramolecular units, etc. These elements or building blocks are assembled into a bulk solid having microstructure in nanometer scale. Chemistry is sometime not really involved in this approach.

- ***The bottom-up synthesis.*** This approach starts from individual atoms or molecules and assembles them into a bulk piece of materials. The nanomaterials are chemically assembled from elementary chemical component by employing chemical routes (Corriu and Trong Anh, 2009). Nanotechnologies are usually connected to bottom-up processes and are characterized by the use of atoms or molecules as building blocks. Bottom-up processes result in particles, nanotubes, nanorods, thin films or layered structures. The electrodeposition method used in this research can be considered as an example of bottom-up synthesis.

The top down approach relies mostly on physics and the bottom up approach which is related with chemistry (Corriu and Trong Anh, 2009). The top down approach corresponds to the miniaturization processes in electronics and chemistry is not really involved in this approach. In contrast, the bottom-up approach, which aims to prepare materials with well-defined properties (optical, magnetic, mechanical, chemical, etc.) from the nanometric-sized materials, corresponds to the perfect knowledge on chemistry. Figure 2.1 demonstrates the building of particles, layers, nanotubes or nanorods from atoms (ions) or molecules. In this approach, knowledge on chemistry is required for the synthesis, assembling and organizing the nanomaterials. Nano-objects are predicted to be the building blocks of the materials in the future. They are chemical products (molecules, metal complex, cluster, etc) (Corriu and Trong Anh, 2009). Nano-objects are synthesized by special procedure considering a specific property. Subsequently, the nano-object must have chemical functions permitting its transformation into a nanomaterial, that is to say a material having the desired properties and special shape for a specific application.

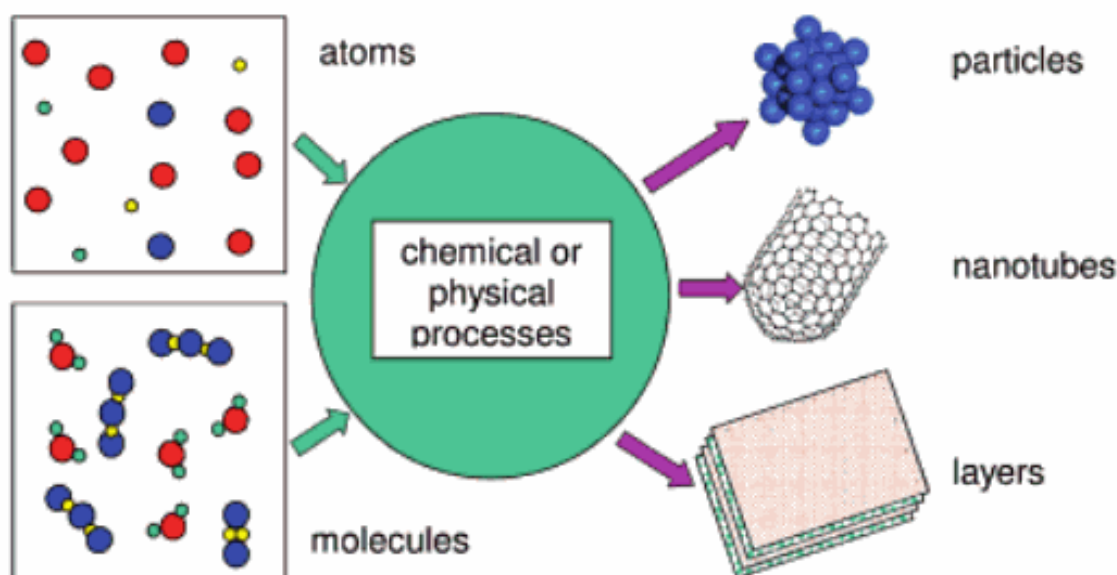


Figure 2.1:
Illustration of building of particles, layers, nanotubes or nanorods from atoms (ions) or molecules (Vollath, 2008)

2.1.2 Potential Applications of Nanocrystalline Materials

In nanotechnology, in terms of diameter, a nanocrystal usually is a microscopic particle sized in between 1 to 100 nm (Li et al., 2011). Nanostructured materials or nanocrystalline materials are widely used in many applications where people do not expect to see nanotechnology. Most people probably know that the huge storage capacity of a computer hard disk is achieved due to the development of nanosized magnetic particles. However, few people will realize that making an omelet on an aluminum frying pan is benefited from an anodic alumina coating having a thickness of less than 100 nm possessing well-aligned cylindrical pores of diameter less than 20 nm (Ejtekhari, 2008). These coating are produced by an electrochemical process, the anodization of alumina, and are widely used to provide protection and give specific colors to aluminum surface.

Nanostructured materials lead to major advances in electrochemical energy storage areas such as lithium-ion batteries. In addition, nanomaterials also promise to revolutionize the field of supercapacitors and thus opening the doors for many applications such as hybrid electric vehicles (HEV), portable electronic devices etc (Ejtekhari, 2008). Beside these, nanoelectronics have started an emerging, enabling and multidisciplinary field with a wide range of potential applications such as quantum devices, molecular electronics, nanodevices, carbon nanotube interconnects, nanowires, etc (Iniewski, 2011). Yet, there are vast areas of research on nanoscale systems that just have begun to surface with prominent examples such as an atomic-scale electrical switch, inorganic/organic composite structures for bio-mimicked structural applications, nano-biological transporter systems for targeted drug delivery or the bio-functionalization of surfaces for advancing new nano-lithography techniques (Wilde, 2009).

2.2 Solids

The magnetic alloy films synthesized in this research are nanosolids. In general, solids can be classified into three general categories: (1) single crystalline, (2) polycrystalline and (3) amorphous (Suryanarayana and Norton, 1998). Simple schematics representing these three categories are shown in Figure 2.2. A crystal is said to possess long-range order because it is composed of atoms arranged in a regular ordered pattern in three dimensions. A polycrystalline material consists of many small single-crystal regions (called grains) separated by grain boundaries (Brandon and Kaplan, 2008). The grains on either side of grain boundary are mis-oriented with respect to each other. The grains in a polycrystalline material can have different shapes and sizes. The boundary between the grains depends on the mis-orientation of the two grains and the rotation axis about which the mis-orientation has occurred. In amorphous

material, the atoms are not arranged in a regular periodic manner. Amorphous is a Greek word meaning “without definite form.” (Suryanarayana and Norton, 1998). Amorphous materials possess only short-range order.

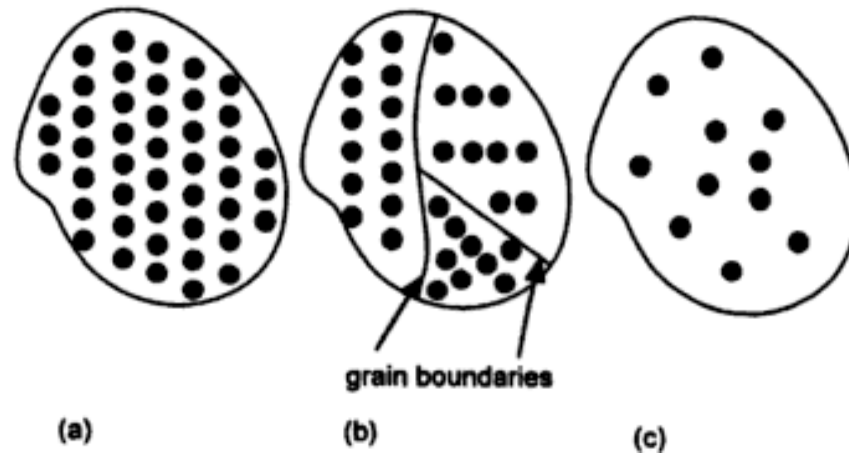


Figure 2.2:
Illustration of the difference between (a) single crystal, (b) polycrystalline, and (c) amorphous materials (Suryanarayana and Norton, 1998)

2.3 Magnetic Materials

Magnetic materials are one of the most vital and fastest growing areas of research in the field of nanotechnology. Magnetic materials can be tailored into nanoparticles, nanowires, self-assemblies, nanoclusters, nanogranules, multilayers and ultrathin films by a number of chemical, physical and mechanical nanofabrication techniques (Nalwa, 2000) including sputtering, metal evaporation, grinding and liquid phase metal salt reduction (Wang et al., 2004). Magnetic materials are all around us and understanding their properties underlies the engineering efforts applied for their developments. The range of the applications of magnetic materials involves audio, video, telecommunications, automotive sensors, electric motors, medical equipment, energy supply, transportation, computer technology as well as the design of stealth airplanes (Lacheisserie and Schlenker, 2003). In addition, the magnetic nanostructures

have commercial applications in magnetic hard disks for information storage in computers, magnetic sensors, data storage, bio-sensors, spin valves, magnetic tunnel junctions, high speed nonvolatile magnetic random access memories (MRAMs), magnetic imaging, magnetic recording heads, magnetoelectronics, magneto-optics and other spintronic devices, nanomagnets, magnetic fluids, magnetic toner, microwave electronics devices, etc (Aktas et al., 2003; Nalwa, 2002).

From a technological point of view, the magnetic nanostructures impart much larger storage density due to a phenomenal increase of bits stored in a unit area that makes them quite attractive for a wide range of applications. Among all the five types of magnetic materials mentioned as below, ferromagnetic and ferrimagnetic materials have been studied widely and used in magnetic applications. Recently, with the extensive research and the promising application of GMR spin valves, antiferromagnetic materials also attracted much attention.

Magnetic materials have been widely used in many areas of modern technologies. When crystals are formed from atoms having a net magnetic moment, a number of different situations can occur. This also relates the magnetic moments of the individual atoms and their alignment with respect to each other. Figure 2.3 illustrates some of the possible arrangements that can occur in two dimensions. According to different spin configurations, magnetic materials can be divided into five types:

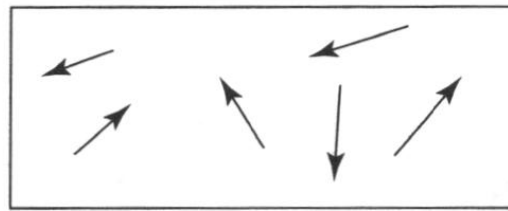
1. ***Paramagnetic materials.*** In this kind of materials, the spins point in random directions, resulting in little apparent net moment
2. ***Ferromagnetic materials.*** The spins are spontaneously arranged parallel to each other, resulting in a net moment.
3. ***Antiferromagnetic materials.*** Half of spins are antiparallely aligned to the other half, resulting in no apparent net moment.

4. ***Ferrimagnetic materials***. One set of spins are antiparallely aligned to the rest, however, the number of spins in these two sets are not equal, resulting in a net moment.
5. ***Diamagnetic materials***. Spin moments are cancelled out and external field increases the classical velocity of the orbital electron resulting in a small and negative net moment.

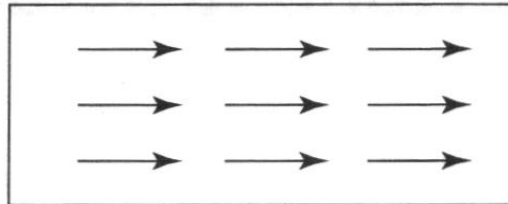
Magnetic materials can also be classified according to their magnetic susceptibility $\chi = M / H$ and relative permeability $\mu_r = \mu / \mu_0$. Table 2.1 shows the typical ranges of relative permeability μ_r (as in χ / μ_0) for each category of magnetic material and examples of each are identified. The relation between the magnetizing field H and the magnetic field B can also be expressed as the magnetic permeability: $\mu = B / H$ or the *relative permeability* $\mu_r = \mu / \mu_0$, where μ_0 is the magnetic permeability of free space and equal to $4\pi \times 10^{-7} \text{ Hm}^{-1}$ (Blitz, 1991). The unit of M is the same as B in this case.

Table 2.1:
Classification of magnetic materials (Judy and Myung, 2001)

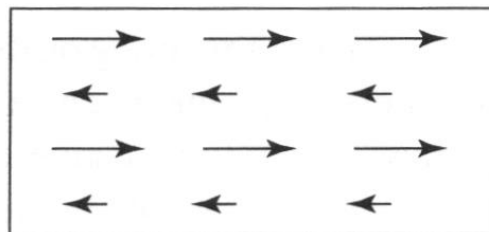
Category	χ / μ_0	Examples
Ferromagnetic	10^7 to 10^2	Ni, Fe, Co, NiFe, NdFeB
Ferrimagnetic	10^4 to 10^1	Fe_3O_4 , ferrites, garnets
Antiferromagnetic	small	MnO, NiO, FeCO_3
Paramagnetic	10^{-3} to 10^{-6}	Al, Cr, Mn, Pt, Ta, Ti, W
Diamagnetic	-10^{-6} to -10^{-3}	Ag, Au, C, H, Cu, Si, Zn
Superconducting	-1	$\text{YbBa}_2\text{Cu}_3\text{O}_x$



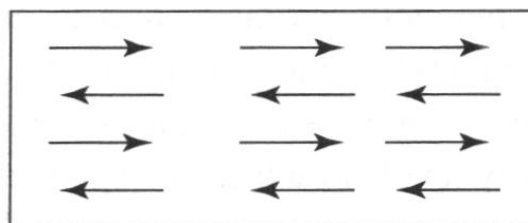
(a) Paramagnetic



(b) Ferromagnetic



(c) Ferrimagnetic



(d) Antiferromagnetic

Figure 2.3:
Illustration of various arrangements of individual magnetic moments that constitute paramagnetic, ferromagnetic, ferrimagnetic and antiferromagnetic materials

2.3.1 Ferromagnetic Materials

There are five ferromagnetic elements in the periodic table, nickel (Ni), cobalt (Co), iron (Fe), gadolinium (Gd) and dysprosium (Dy). The magnetic properties in nanostructures are governed by a number of factors such as composition, shape, size, surface morphology, topology, anisotropy, array spacing, symmetry, thickness of the layer, molecular interactions, alignment, etc (Nalwa, 2002). Approaches to improve the intrinsic and extrinsic properties of soft ferromagnetic materials involve the tailoring of chemistry and optimizing the microstructure. Significant effect of microstructural control has been found to alter the magnetic hardness (the coercivity, H_c) which is inversely proportional to the grain size (D) where this grain sizes is in the range of ~ 0.1 - $1 \mu\text{m}$ and D exceeds the domain (*Bloch*) wall thickness (δ_w) (Tang and Sheng, 2003). Here grain boundaries act as impediments to domain wall motion and thus fine-grained materials are usually magnetically harder than large grain materials. H_c decreases rapidly with decreasing grain size. This can be understood by the fact that the domain wall whose thickness (δ_w) exceeds the grain size (D), fluctuations in magnetic anisotropy at the grain boundaries become irrelevant to domain wall pinning. This important concept of random anisotropy suggested that nanocrystalline and amorphous alloys have significant potential as soft magnetic materials. The nanocrystalline grains should be exchange coupled which is a requirement for soft magnetic properties.

Ferromagnetic materials are the most useful class of magnetic materials. They have the distinct ability to acquire and maintain larger magnetic fields upon the application of relatively small magnetic fields. Ferromagnetic substances are usually anisotropic. Ferromagnetic materials are partitioned into microscopic domains within which the spins are all spontaneously aligned in a given direction, even in the absence of an external field (Lorrain et al., 1988). In the unmagnetized state, the spins of the various domains are randomly oriented and the net macroscopic field is zero. Soft

magnetic materials possess a high permeability and a narrow hysteresis loop. These materials are used in electromagnets, transformers, motors, etc (Lorrain et al., 1988). Hard materials are characterized by broad hysteresis loops. They are used mainly for permanent magnets.

2.4 Magnetism

In this research, the magnetic properties of Co-Fe, Co-Pt, Fe-Pt and Co-Fe-Pt were studied using hysteresis loops. The saturation magnetization (M_s) and coercivity (H_c) are important parameters to consider in the investigation of the effects of composition, complex forming additive and grain refining agent on the magnetic properties of alloy thin films. Therefore, a brief introduction about the hysteresis loops, saturation magnetization and coercivity is discussed below.

2.4.1 Hysteresis Loop

Hysteresis comes from the Latin verb “hyster”, meaning “to lag” (Martin, 1999). The hysteresis loop gives the relation between magnetization (M) and the applied field (H). The magnetization/demagnetization curve for a given ferromagnetic material provides a great deal of information during magnetic characterization. Coercivity (H_c) is defined as the applied field that is required to reduce the component of saturation magnetization (M_s) in the direction of H_c to zero (Wee, 1997). Figure 2.4 shows a schematic plot of the magnetization curve of a ferromagnetic material. It is the representation of total magnetization and demagnetization of a sample in terms of applied DC field (H). In the MKS (millimeter-kilogram-second) system the unit of both H and M are amperes per meter; in the CGS (centimeter-gram-second) system the unit of M is emu/g (electromagnetic units per gram), and the unit of H is oersteds (Oe) (Owens and Poole, 2008).

At point zero, the materials is in the virgin or demagnetized state and incurs an applied field (H) until the materials achieves magnetic saturation (M_s) at point (a). When H is decreased from the saturation point, M does not decrease to the same value as it had earlier; rather it possesses some of the magnetization. This is called hysteresis and is associated with a loss of energy (Hammond, 1978). This phenomenon occurs due to the alignment of domains which do not return to their original orientations when the field is lowered. From point (a) the field is reduced to zero and still the magnetization remains in the material. This is called remanence magnetization and denoted by the symbol of M_r . In order to remove the remanence magnetization (M_r), the field has to be applied in the opposite direction to the initial applied field. Therefore, from point M_r , a negative field is applied to the sample until the induced magnetization is reduced to zero at point (b). The amount of field required to reach zero magnetization in a particular sample is defined as coercive point. The sample is negatively magnetized up to point (c) which corresponds to magnetic saturation in the opposite direction. Lastly, the field is applied in the positive direction to bring the sample back to positive magnetic saturation crossing the applied field axis at point (d) and joining the initial saturation at point (a). The area enclosed from point (a) counterclockwise to point (a) is the hysteresis loop. Although hysteresis loops are always in the same general shape, they might take many forms. They can be as narrow as shown in the Figure 2.4, or broader, or even rectangular in vertical and horizontal sides.

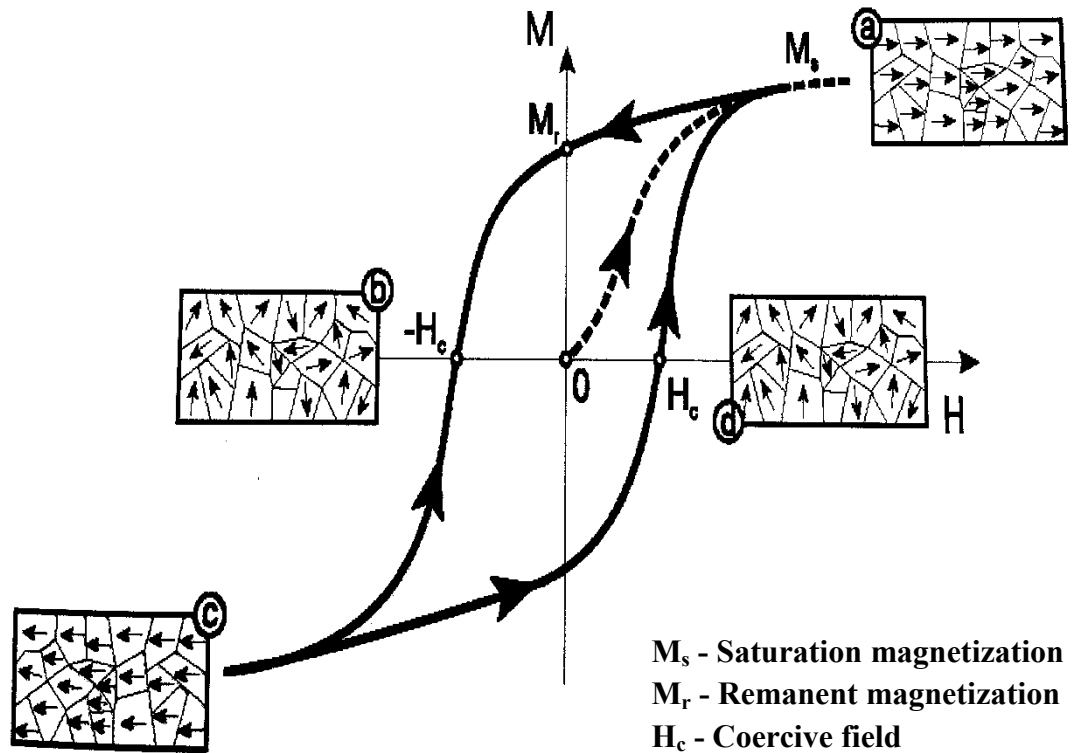


Figure 2.4:
 Schematic diagram of M vs. H or hysteresis loop showing magnetic properties and domain structures during different stages of magnetization

2.4.2 Magnetization and Coercivity

The saturation magnetizations for technologically important metals like nickel, cobalt and iron are 0.6 Tesla ($T = \text{Wb} \cdot \text{m}^{-2}$, and $\text{Wb} = \text{Weber}$), 1.6 Tesla and 2.2 Tesla, respectively (Cheung, 2001). Saturation magnetization (M_s) is the state of a material when the value of the magnetization remains same and cannot be further increased by increasing the applied external field (H) (Lacheisserie et al., 2003). For most ferromagnetic materials, a specimen will remain magnetized to some extent after the removal of an external magnetic field; this effect is known as remanence (M_r) (Vollath, 2008).

In the studies of nanostructured magnetic films, the single property that is the point of most interest is the coercivity. It should be noted that the width of the hysteresis loop is twice of the coercivity value and as such, the coercivity determines the magnetic properties of a material to a great deal. Vibrating sample or alternating gradient magnetometer are the typical equipment used to acquire the data of hysteresis loop. When the coercivity of a ferromagnet material is large, the materials is said to be a hard or permanent magnet. Permanent magnets find applications in electric motors, magnetic recording media (e.g. hard drives, floppy disks, or magnetic tapes) and magnetic separation. A ferromagnet material with a low coercive field is said to be soft and may be used in microwave devices, magnetic shielding, transformers or recording heads.

The coercivity of nanostructured thin films has a striking dependence on their size. Significant recent development in the understanding of magnetic coercivity mechanisms has led to the realization that for very small grains having diameter less than 100 nm, H_c decreases rapidly with decreasing grain size (Tang and Sheng, 2003). Figure 2.5 shows the variation of coercivity with particle size for particles whose coercivity depends on crystal anisotropy. As the crystallite size is reduced, it is typically found that the coercivity is increased, goes through a maximum and then tends toward zero. This is clearly shown for the three different materials in Figure 2.5 (left side). For the other three materials located at the right side in Figure 2.5, the maximum in coercivity is not reached yet (Cullity and Graham, 2009). The size of the smallest particles is less than 10 angstrom, while the largest are 0.1 mm in diameter.

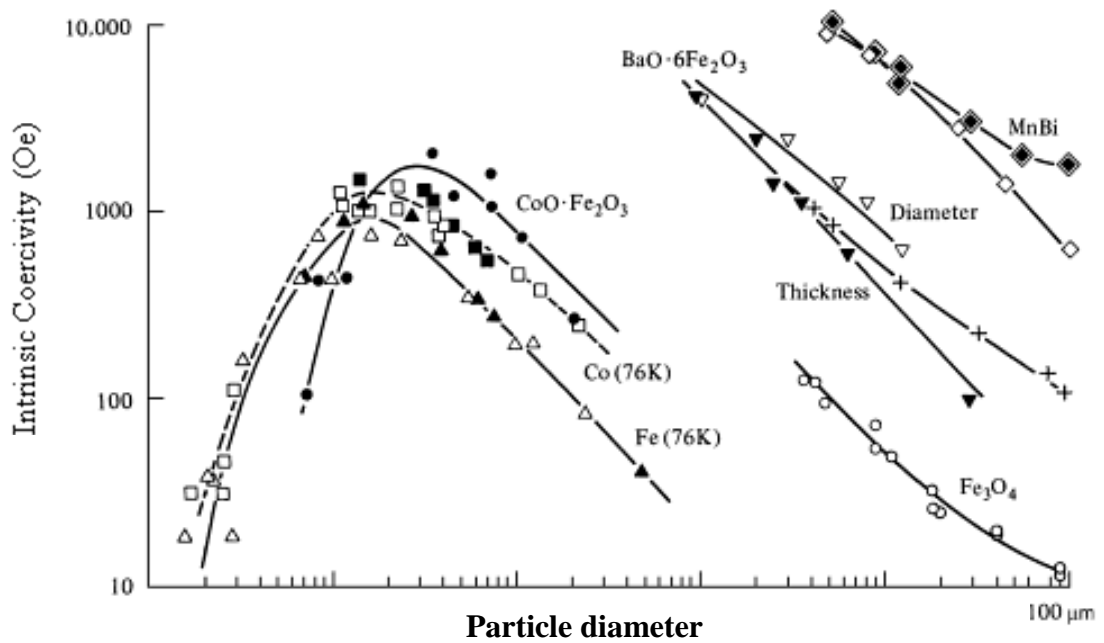


Figure 2.5:
Variation of coercivity with particle size, for particles whose coercivity depends on crystal anisotropy (Cullity and Graham, 2009)

Figure 2.6 shows schematically the variation in the coercivity in terms of size of the particles, D . The following regions can be distinguished:

1. *Multidomain*. Magnetization is changed by domain wall motion. For some materials, the size dependence of the coercivity is experimentally found to be as follows

$$H_c = a + \frac{b}{D} \quad (2.1)$$

where a and b are constants (Teh, 2003). This equation shows a reciprocal relation of coercivity with crystallite size. As particle diameter decreases, the coercivity increases. This relation has no theoretical foundation.

2. *Single-domain*. Below a critical diameter D_s , the particles become single domains and in this size range the coercivity reaches the maximum. Particles with the size of D_s or smaller change their magnetization by spin rotation, but more than one mechanism of rotation can be involved.
3. As the particle size decreases below D_s the coercivity decreases, because the thermal effects are strong enough to demagnetize a previously saturated assembly and the coercivity become zero. The relation is given by equation 2.2 (Teh, 2003) where g and h are constants. This phenomenon is known as superparamagnetism.

$$H_c = g - \frac{h}{D^{3/2}} \quad (2.2)$$

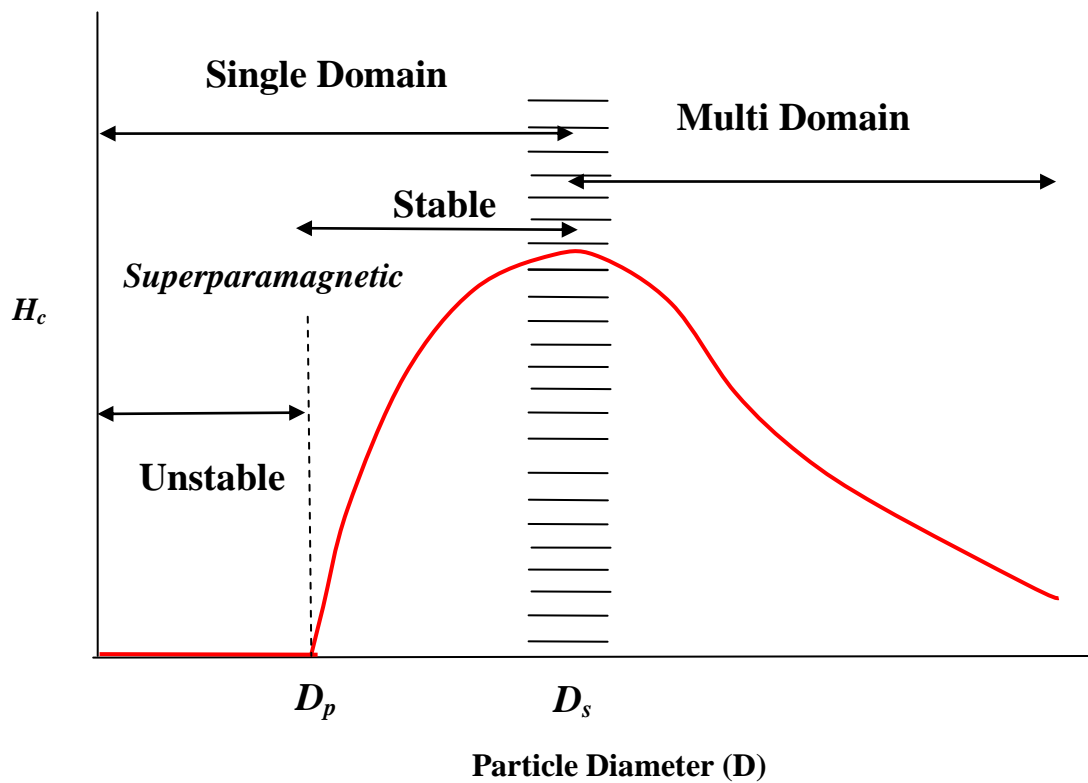


Figure 2.6:
Schematic diagram of variation of coercivity (H_c) with particle diameter (D)

2.5 Thin Films

The innovative and cost effective processing of films provides a useful source of reference for both academician and industrial researchers. Thin film is considered as one of the new processing methods which are emerging for the fabrication of different engineering materials for wide range of applications. It will thus stimulate the scientific and technological interest and lead to the eventual exploitation and implementation of these techniques in materials processing. It is envisaged that these materials processing methods have the potential to produce new advanced materials with novel nanostructures and functions to meet the demand for the industrial and social requirement of this century.

Nanostructured films can be defined as any matter in the form of film that has structural features in the range of nanoscale (Lee, 2008). These structural features can be nanoporous, nanoparticles, a flat surface having thickness that is in the nanometer range or surface roughness ranged in the nanometer scale (Lee, 2008). It is fair to mention that electrodeposits are often non-homogeneous, both in the macroscale and in the nanoscale (Hodes, 2001). The nucleation and growth of the deposits produce thin or thick film with either dense or porous microstructure. The nucleation and growth kinetics are influenced by the deposition temperature and concentration of reactive species, which in turn influence the microstructure and thus the properties of the coatings (Choy, 2002). The nucleation of polycrystalline coatings normally occurs at different sites on the substrate surface, leading to the growth of islands which subsequently coalesce to form a polycrystalline layer (Choy, 2002).

Figure 2.7 shows the schematic representation of the three typical nanostructured films that are commonly found in the field of nanotechnology. Nanoporous film has nanometer-scale porous structures either inside or on its surface (Lee, 2008). The nanolayered type includes monolayer, bilayer and multilayered films.

The nanopatterned film has patterned structural features within the nanometer scale on its surface. In this study, the as-deposited nanostructured alloy films are categorized as nanoporous film.

Magnetocrystalline anisotropy is the magnetic energy of a system in the direction of magnetization within the sample (Lacheisserie and Schlenker, 2005). Magnetocrystalline anisotropy determines the capability of a magnetic material to be a good hard magnet, a good soft magnet or neither. The magnetocrystalline anisotropy value directly affects the coercivity, that is, the magnetic films with higher anisotropy constant will possess higher coercivity (Lai et al., 2004). A compilation of the experimental anisotropy constants for different alloy thin films is shown in Table 2.2. Thin films can be created on the surfaces of metals in a variety of ways, including techniques such as vacuum or gaseous deposition, electrodeposition, spraying, gaseous reaction, ion implantation and surface segregation (Holloway and Vaidyanathan, 2010). The electrodeposition technique has major advantages over other methods for the production of thin films because of having the possibility of performing deposition at normal pressure and temperature. In addition, it is a relatively easy and inexpensive technique with many parameters (current, potential, temperature, bath composition and additives) that can be adjusted in order to obtain better quality of deposits. Typical applications of thin films on metals include catalysis, electrode processes and various aspects of microelectronics such as electrical contacts, diffusion barriers, adhesives, dielectrics and magneto-optics (Holloway and Vaidyanathan, 2010).

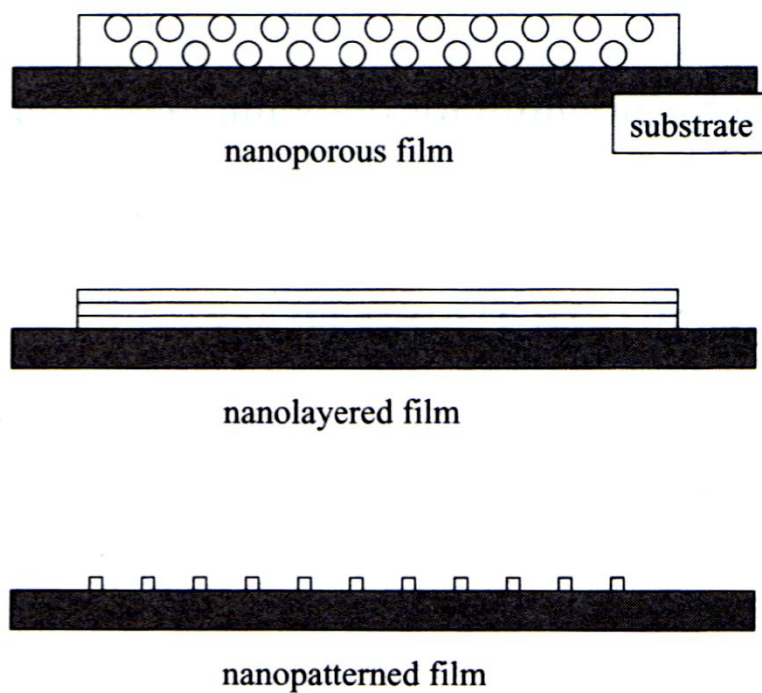


Figure 2.7:
Various typical nanostructured films

Table 2.2:
Experimental anisotropy constants for different chemically ordered alloys thin films
(Nalwa, 2002)

System	Sample Form	K_I (J/m ³)
FePt (001)	Thin film	$K_u = 1 \times 10^7$
FePt (001)	Ordered thin film	$K_u \geq 8 \times 10^5$
FePt	Bulk	$K_I = 1.9 \times 10^6$
FePt (110)	Partially ordered thin film	$K_u = 1.5 \times 10^6$
FePt (110)	Ordered thin film	$K_u \sim 1 \times 10^7$
CoPt (001)	Bulk (ordered)	$K_u = 1.2 \times 10^6$
CoPt (111)	Bulk (disordered)	$K_I = -6 \times 10^4$
CoPt (001)	Ordered thin film	$K_u = 1.9 \times 10^6$
Co ₃ Pt	Hcp like	$K = 1.5 \times 10^6$
CoPt ₃	Disordered fcc	$K_u = 1 \times 10^6$

2.6 Electrodeposition

Electrodeposition is a most widely technique for producing thin film of different substrate of various engineering applications. When a conducting surface is immersed in a solution containing metal ions and this surface is electrically connected to a power supply which passes current through the surface to the solution, metal will be deposited on the surface. This is called electrodeposition, or –synonymously- electrochemical deposition (ECD) or electroplating. In principle, the choice of substrate and coating metals may encompass a large number of single metals and alloys.

Electrodeposition is a technique that is conceptually well-suited for the preparation of nanostructures. It is usually a low temperature technique which discourages the crystal growth and eventually the electrodeposited materials tend to have a very small grain size (Hodes, 2001). Another important property of electrodeposition is the ability to control the amount of metal deposition to a very precise extent by using Faraday's law, which relates the amount of material deposited to the amount of charge passed (Hodes, 2001). Faraday's law as shown in equation 2.3, which can be used to calculate the thickness of the deposited metal in electrodeposition process (Jack, 1993),

$$It\eta = nF \left[\frac{m}{sMW} \right] \quad (2.3)$$

where I is the applied current, t is the charging time, η is the current efficiency, n is the number of electrons transferred, m is the mass reacted, s is the stoichiometric coefficient and MW is the molecular weight.

According to Faraday's law, the production of one gram equivalent of a product at the electrode in electrochemical cell requires 96500 coulombs. This constant is

termed as Faraday's constant, F . With two or more reactions occurring simultaneously at the cathode, the total charge passed corresponds to the sum of the individual charge from each reaction. The current efficiency of a simultaneous reaction is defined as the ratio of the number of coulombs required for that reaction, Q_j , and the total number of coulombs passed, Q_{total} . It is also defined as the ratio of actual weight of metal deposited at the cathode, $Mass_{act}$, and the theoretical weight of metal according to Faraday's law, $Mass_{theo}$:

$$\eta = \frac{Q_j}{Q_{total}} = \frac{Mass_{act}}{Mass_{theo}} \times 100\% \quad (2.4)$$

Figure 2.8 shows the schematic diagram of electrodeposition process. An electroplating bath consists of a conducting salt and the metal ions that are to be electroplated on the substrate as well as a buffer and additives. It also has an electronically conducting substrate which is called cathode. There is also an anode which is also electronically conducting and might be soluble or insoluble. A direct current electrical power source is usually used to regulate as a transformer or rectifier. There are four fundamental processes involved in the electrodeposition reaction as shown below:



- The metal-solution interface as the locus of the deposition process,
- Kinetics and mechanism of the deposition process,
- Nucleation and growth processes of the metal (M), and
- Structure and properties of the deposits.

The objective of an electrodeposition process is to prepare a deposit which adheres well to the substrate and has the required mechanical, chemical and physical properties. Moreover, it is very important that the deposits' properties meet their specification in all occasions, such as predictable and reproducible results. It is also important that the plating bath is stable for a long period of time because of the importance of reproducibility of the deposit. It is also necessary that the quality of deposit is maintained over a range of operating conditions, since some variations in concentrations and current density are bound to occur, particularly when different objects are to be plated. The electrodeposition method involves a large number of processing steps including mixing, chemical reactions, filtration, purification, drying and are therefore both tedious and liable to contamination. It also has poor chemical utilization and there are environmental concerns over the waste recycling of the chemical precursors and the disposal of by-products, especially during large-scale production (Choy, 2002).

The quality of an electroplated finish is dependent upon a wide range of process variables, including electrolyte composition and purity, addition of agent level, pH, temperature, current density, electrode-anode-cell geometry and flow conditions. Therefore, the quality control procedures must consider the track record of both the electrolyte and the deposit. One of the most important parameters is the acceptable or optimum current density range. In this range, the electroplated layer must show satisfactory properties such as brightness, freedom from rough deposits, uniform texture, etc.

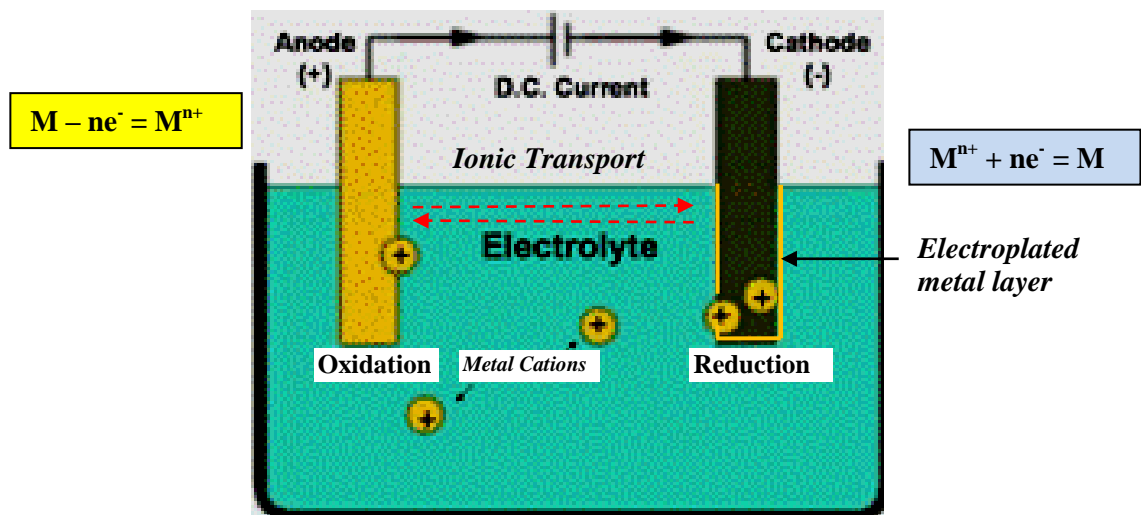


Figure 2.8:
Schematic diagram of electrodeposition process

2.6.1 Mechanisms of Electrodeposition

Electroplating is the process of electrolytically depositing a metal layer onto a substrate surface. For a successful electroplating process, the correct pretreatment of the cathode is crucial in addition with the careful selection of the anode material. The plating bath, current density and other electrolysis conditions are essential for good deposition. The object to be plated is made as cathode in an electrolyte bath containing the metal ion M^{n+} . During electrodeposition, the metallic species go through a multi-stage process before depositing onto the substrate. In general, the electrodeposition process can be divided into the following steps:

- a driving force is introduced into the electroplating system (plating cell), usually it is in the form of an imposed potential leading to a current flow;
- mass transfer: diffusion of metallic species from bulk solution to the vicinity of the cathode (negative terminal) surface;

- reduction of the metallic species from positive to the electronically neutral state;
- adsorption of the species onto the cathode;
- deposition can be continued either by nucleating new grains or contributing to the growth of existing grains (Cheung, 2001).

In order to deposit metal ions on the substrate, an external potential E , must be supplied to shift the system of electrochemical cell from equilibrium. Potential is the driving force that causes charged particles to move. The difference between the applied potential and the equilibrium potential, $E - E_{eq}$, is called the overpotential (η) (Parthasaradhy, 1989). An electrolyte containing more than one species of metal ions is possible to deposit under certain conditions in the form of alloys. The values of standard potential serves as an approximate guide for determining whether two metals can be co-deposited from one salt solution. In general, metals, which have similar values of standard reduction potentials, are more readily co-deposited. Apparently, the electrodeposition process is made up of a number of individual stages and within each stage a rather complicated process takes place. Although numerous publications are available to describe the processes that take place at the cathode's surface, reports pertaining to the theoretical aspects of electrodeposition of nanocrystals are limited.

2.6.2 Electrocrystallization: Nucleation and Growth of Nuclei

In electrodeposition processes, the theoretical understanding of crystallite formation is not well understood. This is because of intrinsic complexity of solution chemistry. It is well known that numerous operating parameters affect the deposition process which is not mutually independent. Since all metals exhibit a potential (reference to the standard hydrogen reaction), it is therefore; the applied potential to the

electrolyte must be more negative to ensure the electrodeposition process. This is defined as the overpotential. The higher the overpotential, the higher the driving force for the metallic species in solution to be reduced and to form deposition. Once the cations reach the cathode surface, they are ready to be reduced.

After receiving the required charge from the cathode, the metal will become an atom with no electronic charge. However, even at this stage, the atom is simply adsorbed onto the cathode surface, becoming an adatom. The adatom will travel a short distance before depositing onto the substrate or on the already deposited layers. This distance is limited by the diffusion of the adsorbed atom on the surface.

Nucleation is the first step in the deposition process. Nucleation is always an improbable event and is achieved at an electrode surface by the application of a large overpotential or driving force. The density of nucleation is dependent on the condition of plating bath and is extremely sensitive to the electrode potential and current density. The nuclei, once formed, grow quite rapidly at comparatively low overpotential. In a constant current situation the potential will decrease substantially once nucleation has started. The growth of the crystals occurs by incorporation of the individual metal atoms into the crystal lattice. The newly incorporated metal atom is likely to be stable when it enters the lattice at a site where it interacts with several other atoms which are already in the lattice.

It is at this point of the deposition process where either nucleation of a new grain or the growth of an existing grain occurs. During electrodeposition, operating parameters can be adjusted to optimize certain deposit qualities of interest. In this study, the primary focus is the crystallite size and chemical composition. A conceptually simple approach to produce small-grained deposits was dependent on the condition of the system whether it is activation controlled or diffusion controlled. In an activation controlled system, the current density is low compared to the concentration of metallic

species at the cathode surface. In other words, deposition is dependent on the “arrival” of electrons at the cathode. As a results, a longer time is required for cations to move to the cathode. In addition, each deposited crystal is surrounded by a large number of metallic ions to be deposited, hence producing a deposit with a coarse grain size.

In contrast, for diffusion controlled systems, the rate-determining step in the deposition process is the diffusion of cations to the cathode surface. This mode is typical at high current densities. The deposition of the metallic ions is controlled by the rate of arrival of these species from the bulk to the cathode. In addition, the deposited crystals do not have an abundance of adjacent metallic ions to “permit” their growth. As a result, ions reaching the cathode surface will get deposited without much surface diffusion as in the activation controlled case, therefore producing a finer-grained deposit. The main factor that would promote nucleation and retard grain growth is the surface diffusion experienced by an adatom before depositing onto the cathode.

Figure 2.9 shows schematic diagram of kink site, step edge and adatom. Of the sites which are possible in a perfect crystal lattice, incorporation will be most favorable at a kink site where the atom can interact with three neighbors. Some incorporation will also take place at edge sites with two neighbors. The adatoms with one neighbor are likely to diffuse to more favorable sites or to re-dissolve, although a very small number will expand into new nuclei. The structure of the growing layer will be determined largely by the relative rates of electron transfer to form an adatom and diffusion of the adatom across the surface into a position in the lattice. At low current density, the surface diffusion is fast compared with electron transfer and the adatom is likely to end up in a favored position in the lattice. At higher current densities, surface diffusion is no longer fast compared with electron transfer and further nuclei must form; the layer will be less ordered. Moreover, the presence of suitable bath additives may radically modify the growth process.

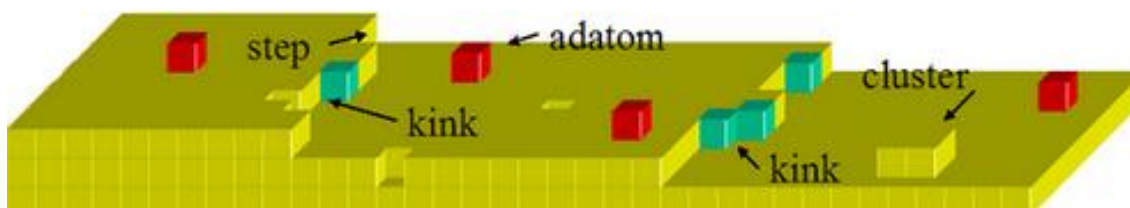


Figure 2.9:
Schematic diagram of kink site, step edge and adatom (Internet Reference, b)

Extra precaution must be taken to ensure that the bath should be designed with diffusion controlled deposition mechanism. In general, the electrocrystallization has received a great deal of attention over recent years and some of the fundamental theories have emerged which seem to be sufficient for practical purposes. However, during examining the nanocrystalline materials produced from electrodeposition techniques, many empirical mechanisms are estimated. In order to further understand, a thorough electrochemical study should be carried out having a wide variety of plating solutions with different variables. However, this is beyond the scope of this present research.



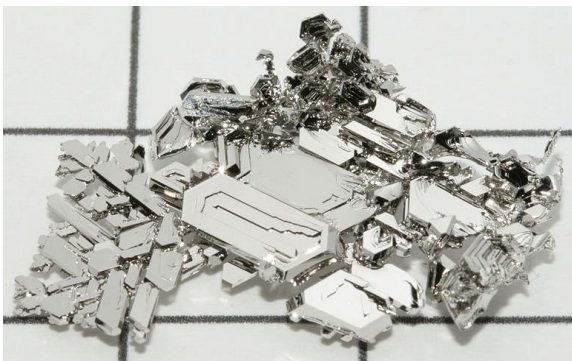
2.7 Cobalt, Iron and Platinum Elements

Cobalt is found in chemically combined form in nature. The Curie temperature of cobalt is 1115 °C and the magnetic moment is in between of 1.6 to 1.7 Bohr magnetons per atom. Cobalt has a relative permeability two thirds that of iron. Cobalt-based alloys are also corrosion and wear-resistant. Metallic cobalt can be found in two crystallographic structures: hexagonal close-packed (HCP) and face centered cubic (FCC). The ideal transition temperature between the HCP to FCC structures is 450 °C.

Iron and iron alloys are the most common source of ferromagnetic materials for everyday use. This metal is the fourth most abundant element in the earth by weight which makes the crust of the earth. The pure iron is a lustrous silvery soft metal, chemically very reactive and corrodes rapidly especially in moist air or at elevated temperatures.

Platinum is a heavy, malleable, ductile, precious, gray-white transition metal. Platinum is resistant to corrosion and occurs in some nickel and copper ores along with some native deposits. Generally, platinum is used in jewelry, laboratory equipment, electrical contacts, dentistry and automobile emissions controlling devices (Parthasaradhy, 1989). Table 2.3 shows the general properties of cobalt, iron and platinum.

Table 2.3:
General properties of Cobalt, Iron and Platinum

Element	General properties
<p><u>Cobalt (Co)</u></p> <p>(Internet Reference, c)</p> 	<p>Name, symbol, number : Cobalt, Co, 27</p> <p>Element category: Transition metals</p> <p>Group, period, block: 9, 4, d</p> <p>Standard atomic weight: 58.933 g.mol⁻¹</p> <p>Electron configuration: [Ar] 3d⁷ 4s²</p> <p>Electron per shell : 2, 8, 15, 2</p> <p>Appearance: Hard lustrous gray metal</p>
<p><u>Iron (Fe)</u></p> <p>(Internet Reference, d)</p> 	<p>Name, symbol, number : Iron, Fe, 26</p> <p>Element category: Transition metals</p> <p>Group, period, block: 8, 4, d</p> <p>Standard atomic weight: 55.845 g.mol⁻¹</p> <p>Electron configuration: [Ar] 3d⁶ 4s²</p> <p>Electron per shell : 2, 8, 14, 2</p> <p>Appearance: Lustrous metallic with a grayish tinge</p>
<p><u>Platinum (Pt)</u></p> <p>(Internet Reference, e)</p> 	<p>Name, symbol, number : Platinum, Pt, 78</p> <p>Element category: Transition metals</p> <p>Group, period, block: 10, 6, d</p> <p>Standard atomic weight: 195.084 g.mol⁻¹</p> <p>Electron configuration: [Xe] 4f¹⁴ 5d⁹ 4s¹</p> <p>Electron per shell : 2, 8, 18, 32, 17, 1</p> <p>Appearance: grayish white</p>

2.7.1 Cobalt-Iron Nanocrystalline Films

Cobalt alloys have been electrodeposited on various substrates for about 100 years (Cheung, 2001). Co-Fe alloys are soft magnetic materials which are particularly useful in magnetic storage applications because they possess high saturation magnetizations and low coercivities (Zhou et al., 2008). The composing magnetic crystals of the alloy system must be in nanoscale in order to produce higher density capacity in storage media. However, these nanosized magnetic particles might produce thermal fluctuation in the device. This is due to the superparamagnetic effect, which means that the size of magnetic crystals is below a critical value which eventually results in the disappearance of memory information (Teh and Yaccob, 2011a). Co-Fe alloys are also used in magnetic amplifiers, switching devices, relay armatures, magnetic transducers and some high quality telephone receivers (Martin, 1999). The high permeability and high flux density makes this alloy film a prime candidate for the components to be miniaturized.

Co-electrodeposition of cobalt and iron from a single electrolyte is a cost effective and reproducible mean of fabricating Co-Fe alloy films. Generally, sulfate baths are most commonly used for the electrodeposition of binary Co-Fe films, although other baths such as chloride and Watts type solutions are also utilized. Conventional Co-Fe electrolytes have stability issues. However, these can be alleviated by the addition of ammonium citrate as a complexing agent. Zhang and Ivey (2007) electrodeposited Co-Fe thin film on silicon wafers coated with Ti/Au blanket metallizations by using boric acid, sodium dodecyl sulfate, ammonium citrate, $\text{CoSO}_4 \cdot 7\text{H}_2\text{O}$ and $\text{FeSO}_4 \cdot 7\text{H}_2\text{O}$. Similarly, Zhou et al. (2008) electrodeposited Co-Fe thin film by using same plating bath which results in co-deposition of soft magnetic Co-Fe alloy films. Yokoshima et al. (2004) applied a mixture of boric acid, sodium dodecyl sulfate, NH_4Cl , $\text{CoSO}_4 \cdot 7\text{H}_2\text{O}$ and $\text{FeSO}_4 \cdot 7\text{H}_2\text{O}$ as electrolyte system to deposit Co-Fe film on Cu foil and glass plate.

On the other hand, Lallemand et al. (2002) used H_3BO_3 , NaCl , CoSO_4 , FeSO_4 and organic additives to deposit Co-Fe thin film.

In addition, the low pH level (typically 2.0 to 3.0) can be employed to improve the stability of conventional Co-Fe alloy plating baths (Zhang and Ivey, 2007). Acids such as H_2SO_4 or HCl acts as a stabilizer to prevent metal precipitation as precipitation occurs with time which is a critical issue for commercial production. Furthermore, employment of low pH in conventional baths leads to significant hydrogen evolution at the cathode surface which results in the formation of voids in the as-deposited films and the efficiency of current density is lowered. Voids can degenerate the film uniformity and magnetic properties (Zhang and Ivey, 2007). Saccharin is known to be used as a strong leveling agent for surface and a grain refiner by decreasing the internal stresses of the deposit (El-Sherik and Erb, 1995). The use of additives such as saccharin in the plating bath often results in carbon and sulphur as impurities in the film that are often found to be segregated at the grain boundaries and strongly affect the grain boundary diffusion (Wilde, 2009).

Figure 2.10 illustrates thermal equilibrium phase diagram of Fe-Co binary alloy system (Martin, 1999). Table 2.4 presents the crystal structure and phases of iron-cobalt at various Fe content. Co-Fe alloys can exist in three distinct phases at room temperature: the ϵ (hexagonal closed packed, HCP), γ (face centered cubic, FCC) and α (body centered cubic, BCC). The ϵ (HCP) phase is present in pure Co and at low concentration of Fe at room temperature. At 3 to 5 at. % of Fe in Co, a mixture of ϵ (HCP) and γ (FCC) phases is observed. Upon addition of more than about 5 at. % Fe, the alloy transforms into γ (FCC) phase and at approximately 25 at. % of Fe, the alloy transforms to α (BCC), which is the characteristic crystal phase of iron. In between these single phase area a mixture of γ (FCC) and α (BCC) phases co-exists.

Even though there are many studies on Co-Fe alloy thin film, there is a lack of systematic studies relating the magnetic properties of electrodeposits with the deposit compositions and phases. In fact, several attempts have been made to synthesize Co-Fe film but were not successful at the early stage. Adhesion strength for some of the Co-Fe films was poor and therefore detaching from the substrates was common. Some of the Co-Fe films were changed from grey to yellowish color after exposing to ambient environment. This was because the as-deposited Co-Fe film was found to be easily oxidized due to the presence of Fe in the electrodeposited film. In this study, a systematic and novel approach is demonstrated for the fabrication of soft magnetic Co-Fe films via electrodeposition from a sulfate salt-based solution containing sodium saccharin. The effect of the composition of the initial bath solution is also investigated in terms of the composition of the films, surface morphology, crystallographic structures and magnetic properties.

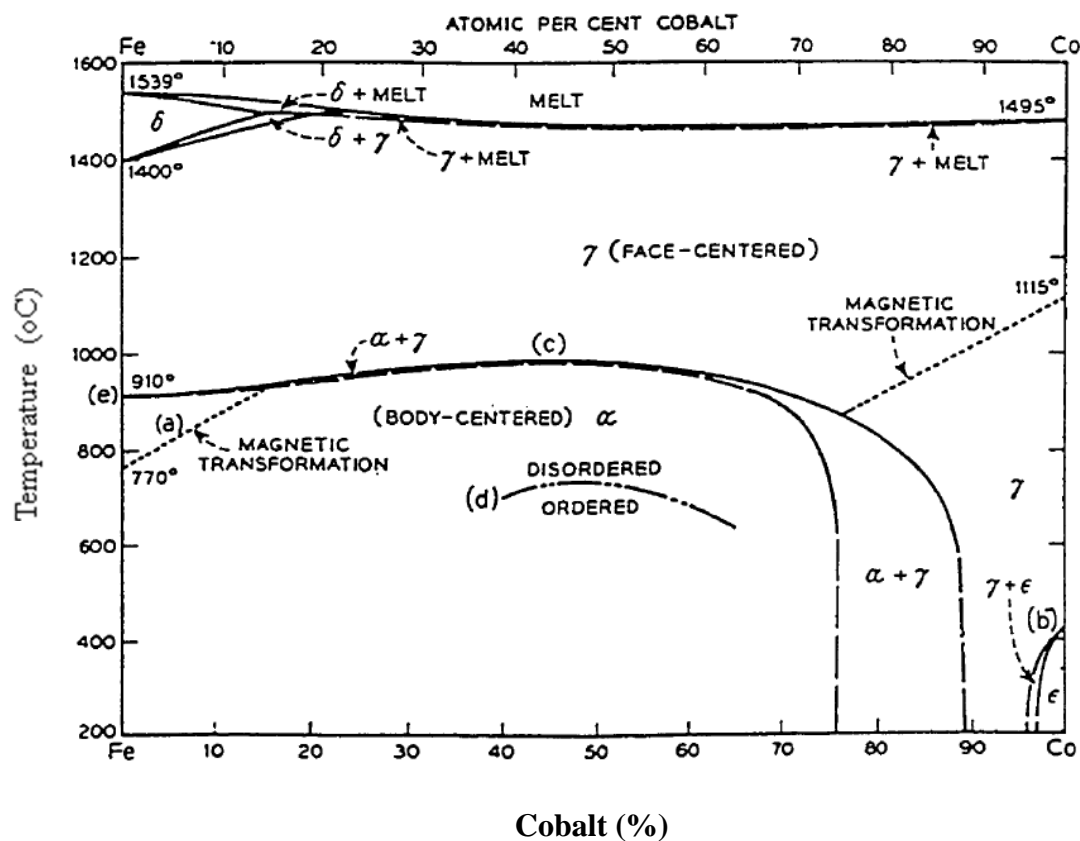


Figure 2.10:
Equilibrium phase diagram of the iron-cobalt system (Martin, 1999)

Table 2.4:
Equilibrium crystal structures of iron-cobalt alloys

Iron content (at. %)	Iron content (wt. %)	Crystal structure	Phase
0-3	0-3	HCP	ϵ
3-5	3-5	HCP+FCC	$\epsilon + \gamma$
5-12	5-11	FCC	γ
12-25	11-24	BCC+FCC	$\gamma + \alpha$
25-100	24-100	BCC	α

2.7.2 Cobalt-Platinum Nanocrystalline Films

Thin films of ferromagnetic Co–Pt alloys produced by electrodeposition have attracted considerable attention due to their excellent magnetic properties (Samardzija, 2009). Cobalt and its alloys are common magnetic materials which are used in various fields such as micro-electromechanical system (MEMS) devices, magnetic recording head, reading heads and data storage media (Wei et al., 2008). All of these devices stand to benefit from the enhanced physical, chemical and magnetic properties when the constituent grains or crystallites of a material are decreased to nanometer scale (Wilde, 2009). Areal density enhancement performed by reducing the grain size is a major challenge in magnetic recording because of thermal fluctuations of superparamagnetic grains when their sizes are below a critical value (Abes, 2006). The coercivity also plays an important role in the recording process, since it governs the domain size, shape and read-stability. Any fluctuation in coercivity may cause an inhomogeneity in domain shape, which in turn contributes to recording noise (Suzuki, 1992). Therefore, it is important to understand the origin of the coercivity in order to further improve recording performance.

Electrodeposition technique is widely used for the preparation of cobalt alloy films because of its cost effectiveness, easy maintenance and good quality of deposits (Wei et al., 2008). Electrodeposition is a high efficiency material conversion method with high deposition rates compared with typical vapor deposition techniques. In electrodeposition, the growth mechanism, morphology and microstructural properties of the films depend on electrodeposition conditions such as electrolyte pH, deposition potential and electrolyte composition (Kockar et al., 2010). The electronic industry relies exclusively on vacuum deposition techniques for recording media. Industrial tools based on electrolytic deposition would decrease the fixed assets by one order of magnitude, still producing magnetic films comparable to those obtained by vacuum deposition (Franz et al., 2007). The through-mask electroplating technology has been developed for the production of miniaturized write/read heads for magnetic recording systems and has been extended to MEMs processing enabling the fabrication of micro-inductor, transformers and sensors (Pattanaik et al., 2006). However, preparation of stable and effective single plating baths for Co-Pt alloys deposition is very difficult due to the big difference in standard equilibrium potentials of Co and Pt.

Co-Pt alloys were electrodeposited onto Si/SiO₂/TiN/Cu (111) substrates from a chloride-based electrolyte, containing CoCl₂, (NH₄)₂ PtCl₄, NH₄Cl, C₆H₈O₇, Na₂HPO₄ and NaH₂PO₂ (Franz et al., 2007). Co-Pt alloy thin films were galvanostatically electrodeposited on Ru buffer layer substrate from an aqueous electrolyte consisting of an amino-citrate based solution which contained ammonium citrate, glycine and sodium hypophosphite (Jeong et al., 2008). Preparation of the Co-Pt films on ITO glass substrate was carried out from a reaction solution containing Pt(NH₃)₂(NO₂)₂, Co(NH₂SO₃)₂ and (NH₄)₂C₆H₆O₇ at the temperature of 333K (Fujita et al., 2007).

Historically, the phase diagram of Co-Pt has been thoroughly explored over the entire compositional range at high temperatures, but there is a lack of investigation at low temperatures particularly in the Co-rich region. It was reported that films with about 20 at% Pt exhibit high magnetic anisotropies due to the presence of the hexagonal close-packed (HCP) microstructure (Zana et al., 2005). In addition, the equilibrium line between the CoPt FCC and the CoPt₃ HCP phases could be crossed at the room temperature in Co rich films.

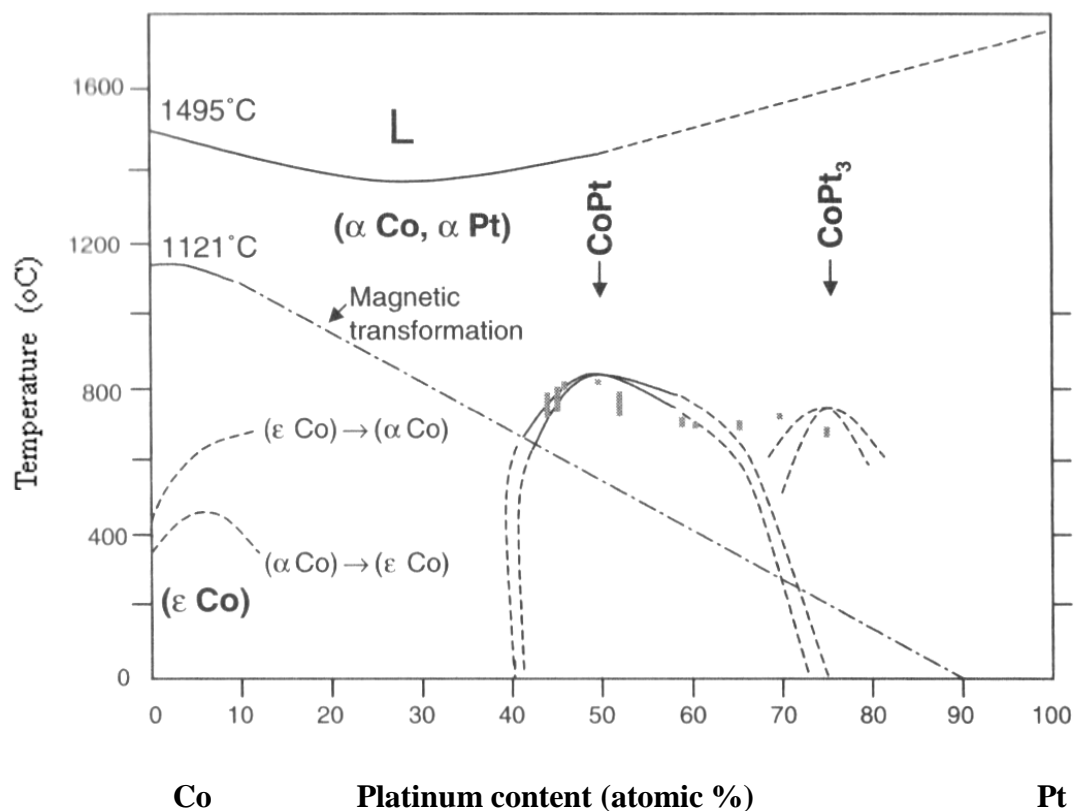


Figure 2.11:
Equilibrium phase diagram for the cobalt-platinum system (Nalwa, 2002)

The magnetic properties of Co-Pt alloys and Co/Pt multilayers are strongly dependent on their compositions, crystal structures, grain sizes and interfacial effects. By understanding these variables the factors affecting the magnetic properties of this system could be elucidated. In this study, a novel approach is demonstrated for the

development of electrolytic deposition techniques suitable for producing soft magnetic Co-Pt nanostructured thin films. The effect of the composition of plating solution on the composition of the alloy films, surface morphologies, crystallographic structures and magnetic properties are also investigated.

2.7.3 Iron-Platinum and Cobalt-Iron-Platinum Nanocrystalline Films

One motivation for the synthesis of ultra-high density magnetic recording media is to meet the demands of rapid development in the area of information technology. The density of magnetic recording media is expected to reach Terabit/in² within a few years and this can be achieved through the advancement in fabrication technology of nanostructured thin film (Wei et al., 2007). The unit size of composing magnetic crystal must be in nanoscale, approximately in the range of 10 nm or smaller in order to produce higher density capacity storage media (Seki et al., 2004). However, areal density enhancement is a major technical challenge in magnetic recording because of the loss of magnetization of superparamagnetic grains due to thermal fluctuations. This phenomenon is prominent when the grain size is below a critical value and eventually results in the disappearance of memory information (Wang et al., 2004; Abes et al., 2006).

Co-Pt and Fe-Pt alloys have attracted large interest to researchers and industries due to their versatile magnetic properties that fit a wide range of potential applications such as magneto-optical recording, perpendicular magnetic recording and most recently hard magnetic components in microelectro-mechanical systems (MEMS) (Zana et al., 2005; Zuzek Kozman et al., 2007). Fe-Pt and Co-Pt alloys have excellent intrinsic magnetic characteristic such as adequate thermal stability, good chemical stability, corrosion resistance and excellent wear resistance and strong perpendicular anisotropy (Ding et al., 2005; Ge et al., 2007). Fe-Pt and Co-Pt possess large mangtocrystalline anisotropy

values of 2.8×10^6 and 7×10^6 J/m³ respectively, resulting from the anisotropic crystal structure and larger spin orbital interactions (Lai et al., 2004). The integration of soft magnetic materials by microfabrication processes was successfully achieved in the 1970s, when the through-mask electroplating technology was developed for the production of miniaturized wire/read heads for magnetic recording systems (Pattanaik, 2007).

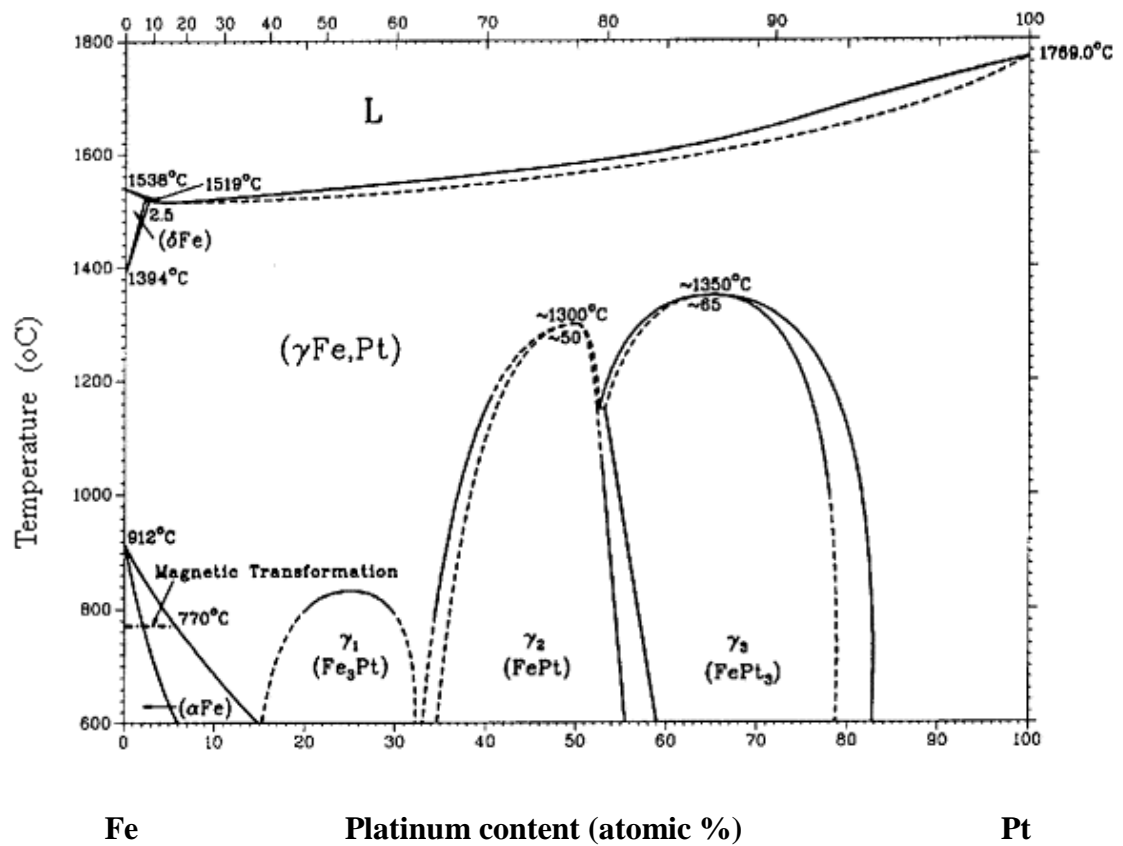


Figure 2.12:
Equilibrium phase diagram of Fe–Pt binary alloy system (Wang et al., 2004)

For thin films of Fe-Pt and Co-Pt alloys, the crystal structure of the film deposited at room temperature is typically a face-centered cubic (FCC) with disordered phase (a space group of Fm 3m), and these materials exhibit soft magnetic behavior (Lai et al., 2007). Figure 2.12 illustrates the equilibrium phase diagram of Fe–Pt binary alloy system (Wang et al. 2004). In the Fe-Pt alloy system, there are three major types of ordered Fe-Pt alloys, namely, Fe₃Pt, FePt, and FePt₃ (Capek, 2006) which formed at

~800 °C, ~1300 ° and ~650 °C, respectively. The phase diagram is determined only above 600°C and phase boundaries are unknown at lower temperatures. These uncertainties results in some ambiguity in understanding of kinetics of the inter-diffusion process at low temperatures (Nalwa, 2002).

In general, the magnetization process, and therefore the coercivity and saturation magnetization, should depend strongly on the characteristic size and the morphology of the materials. However, little work has been done to correlate the magnetization behavior with the actual nanostructural information of ultrathin films. To our knowledge, there is no publication on Co-Fe-Pt thin films prepared by electrochemical deposition method because of the lack of stability and difficulty in the preparation of a suitable electrolyte. Lai et al. (2004 and 2007) investigated the effect of Co addition on the crystallographic ordering temperature and magnetic properties of sputter-deposited films of Fe-Pt. Lai et al. (2004) reported the improvement of saturation magnetization but the coercivity was reduced as the Co content was increased. Besides, thin films of $(\text{Fe}_x\text{Co}_{100-x})_3\text{Pt}$ were fabricated by e-beam evaporation onto Al_2O_3 (001) substrate at temperature of 400°C and large perpendicular magnetic anisotropy of $\sim 10^7$ erg/cc was reported (Nahid et al, 2004; Nahid et al, 2005). In this study, the effect of cobalt addition towards the chemical composition, crystallographic structures, surface morphology and magnetic properties of the as-synthesized alloy films are also investigated.

CHAPTER 3: EXPERIMENTAL PROCEDURES

This chapter describes the detail techniques applied for the synthesis of nanocrystalline magnetic films as well as explain the general terms and terminology of this study. Specific experimental parameters such as bath composition, pH, temperature, anode and cathode materials would be described in this chapter for the synthesis of various materials.

3.1 Electrolyte Solution

Electrolyte is defined as an ionic conductor. It is a chemical substance or mixture, usually in liquid state containing ions that moves in an electric field. In this research, the nanostructured magnetic thin films were electrodeposited on brass substrate by electrochemical deposition technique. In the synthesis process, Pt complex ion was obtained from chloroplatinic acid hexahydrate ($\text{H}_2\text{PtCl}_6 \cdot 6\text{H}_2\text{O}$) [99.9% purity] which was purchased from Strem Chemicals (Newburyport, MA, USA). The $\text{H}_2\text{PtCl}_6 \cdot 6\text{H}_2\text{O}$ was sealed tightly and stored in cold refrigerator due to its moisture sensitivity. Iron (II) sulfate heptahydrate ($\text{FeSO}_4 \cdot 7\text{H}_2\text{O}$) [$\geq 99\%$ purity] (Figure 3.1) as Fe^{2+} source was bought from Sigma Aldrich (St. Louis, Missouri, USA). Cobalt (II) sulfate heptahydrate ($\text{CoSO}_4 \cdot 7\text{H}_2\text{O}$) [$\geq 99\%$ purity] (Figure 3.1) and Cobalt (II) chloride hexahydrate ($\text{CoCl}_2 \cdot 6\text{H}_2\text{O}$) [$\geq 98\%$ purity] was bought from Sigma Chemical to provide Co^{2+} ion. In addition, complex forming additives such as ammonium tartrate ($(\text{NH}_4)_2\text{C}_4\text{H}_4\text{O}_6$) [99.9% purity], sodium chloride (NaCl) and boric acid (H_3BO_3) [99+% purity] were obtained from Fluka Analytical and ammonia solution ($\text{NH}_3 \cdot \text{H}_2\text{O}$) was obtained from Univar (Seven Hills, NSW, Australia). Sodium saccharin ($\text{C}_6\text{H}_4\text{CONHSO}_2$) which served as a grain refining agent and with 98% purity was obtained from Sigma. All the chemicals were reagent grade. Distilled water was used throughout this experiment.



Figure 3.1:
 Co^{2+} and Fe^{2+} ion sources were added to electrolyte solution for electrodeposition process

3.1.1 Preparation of Electrolyte Solution

The nanocrystalline alloy films with various compositions were prepared by adjusting the molar ratio of electrolyte solution. The details of molar ratio and sample preparation techniques are explained in sub-chapter 3.4. The dilution and preparation of electrolyte solution is shown below:

(a) To prepare 0.005M concentration of $\text{CoSO}_4 \cdot 7\text{H}_2\text{O}$ in 100ml electrolyte solution:

$$\begin{aligned} \Rightarrow \text{Weight of } \text{CoSO}_4 \cdot 7\text{H}_2\text{O} &= 0.005\text{M} \times 0.1\text{L} \times 281\text{g/mole} \\ &= 0.141 \text{ g} \end{aligned}$$

0.141g of $\text{CoSO}_4 \cdot 7\text{H}_2\text{O}$ powder is required to be dissolved in 100ml of distilled water for preparation of 0.005M CoSO_4 solution.

(b) To prepare 0.020M concentration of $\text{FeSO}_4 \cdot 7\text{H}_2\text{O}$ in 100ml electrolyte solution:

$$\begin{aligned}\Rightarrow \text{Weight of } \text{FeSO}_4 \cdot 7\text{H}_2\text{O} &= 0.020\text{M} \times 0.1\text{L} \times 278\text{g/mole} \\ &= 0.556 \text{ g}\end{aligned}$$

0.556g of $\text{FeSO}_4 \cdot 7\text{H}_2\text{O}$ powder is required to be dissolved in 100ml of distilled water for preparation of 0.020M FeSO_4 solution.

(c) To prepare 0.025M concentration of $\text{H}_2\text{PtCl}_6 \cdot 6\text{H}_2\text{O}$ in 100ml electrolyte solution:

$$\begin{aligned}\Rightarrow \text{Weight of } \text{H}_2\text{PtCl}_6 \cdot 6\text{H}_2\text{O} &= 0.025\text{M} \times 0.1\text{L} \times 518\text{g/mole} \\ &= 1.295 \text{ g}\end{aligned}$$

1.295g of $\text{H}_2\text{PtCl}_6 \cdot 6\text{H}_2\text{O}$ powder is required to be dissolved in 100ml of distilled water for preparation of 0.025M H_2PtCl_6 solution.

(d) To prepare 0.02M concentration of $(\text{NH}_4)_2\text{C}_4\text{H}_4\text{O}_6$ in 100ml electrolyte solution:

$$\begin{aligned}\Rightarrow \text{Weight of } (\text{NH}_4)_2\text{C}_4\text{H}_4\text{O}_6 &= 0.02\text{M} \times 0.1\text{L} \times 184\text{g/mole} \\ &= 0.368 \text{ g}\end{aligned}$$

0.368g of $(\text{NH}_4)_2\text{C}_4\text{H}_4\text{O}_6$ powder is required to be dissolved in 100ml of distilled water for preparation of 0.02M $(\text{NH}_4)_2\text{C}_4\text{H}_4\text{O}_6$ solution.

(e) To dilute concentrated NH_4OH [28% (w/w) and specific gravity 0.9] to 100ml 0.75M electrolyte solution:

$$\begin{aligned}\Rightarrow \text{Morality of concentrated } \text{NH}_4\text{OH} &= [900\text{g/L} \times 0.28] \div (17 \text{ g/mole}) \\ &= 14.8\text{M}\end{aligned}$$

$$\Rightarrow \text{Volume of concentrated NH}_4\text{OH} = [0.1\text{L} \times 0.75\text{M}] \div 14.8\text{M}$$

$$\cong 5\text{ml}$$

5ml concentrated NH_4OH solution is required to be diluted with distilled water for the preparation of 100ml 0.75M ammonia solution.

(f) To prepare 0.012M concentration of saccharin ($\text{C}_7\text{H}_5\text{NO}_3\text{S}$) 100ml electrolyte solution:

$$\Rightarrow \text{Weight of saccharin (C}_7\text{H}_5\text{NO}_3\text{S)} = 0.012\text{M} \times 0.1\text{L} \times 205\text{g/mole}$$

$$= 0.246\text{ g}$$

0.246g of saccharin ($\text{C}_7\text{H}_5\text{NO}_3\text{S}$) powder is required to be dissolved in 100ml of distilled water for preparation of 0.012M saccharin solution.

(g) To prepare 0.005M concentration of $\text{CoCl}_2 \cdot 6\text{H}_2\text{O}$ in 100ml electrolyte solution:

$$\Rightarrow \text{Weight of CoCl}_2 \cdot 6\text{H}_2\text{O} = 0.005\text{M} \times 0.1\text{L} \times 238\text{g/mole}$$

$$= 0.119\text{ g}$$

0.119g of $\text{CoCl}_2 \cdot 6\text{H}_2\text{O}$ powder is required to be dissolved in 100ml of distilled water for preparation of 0.005M CoCl_2 solution.

3.2 Electrodes

Electrode is an electronic conductor that is used to establish electrical contact within an electrolyte (ionic conductor). An immersed electrode on which oxidation occurred and electrons are produced is called anode. An immersed electrode on which reduction is occurred and electrons are consumed is defined as cathode. Metal substrates are polycrystalline materials which are built from a multiplicity of small crystals. Platinum film coated on titanium mesh as insoluble anode is common to be used to

deposit precious metal or its alloys. It was used repeatedly throughout the experiment to complete the circuit without dissolving in the electrolyte solution. The hull cell panel brass substrate (67% Copper-33% Zinc alloy) with mirror polished surface was used as cathode. The size of the hull cell panel brass is 100mm x 70mm x 0.5mm. The brass substrate was then cut into dimension of 20mm x 20mm x 0.5mm for electrodeposition of magnetic films.

3.3 Electrodeposition Apparatus and Experimental Set Up

Generally, electrodeposition process refers to transfer of current between an electronic conductor and an ionic conductor through chemical reactions by exchanging free electrons. In this research, electrodeposition process was carried out using a direct current power supply (Model: GWINSTEK GPS-3303). Figure 3.2 shows the experimental set up of electrodeposition process. Distilled water was obtained from Aquation distiller for the preparation of electrolyte solutions and final washing of the glassware. Microbalance (SCAITEC) was used to measure the weight of samples throughout the experiment. Fisher stirring hot plate was used to heat up and stir the electrolyte solution while Teflon-coated magnetic stirring bar was used to stir and therefore prevent precipitation of the electrolyte solution. The temperature of the electrolyte solution was controlled and measured by a thermometer. The pH of the electrolyte solution was measured using a Cyberscan 250G pH meter. The plating cell was a 100ml beaker.

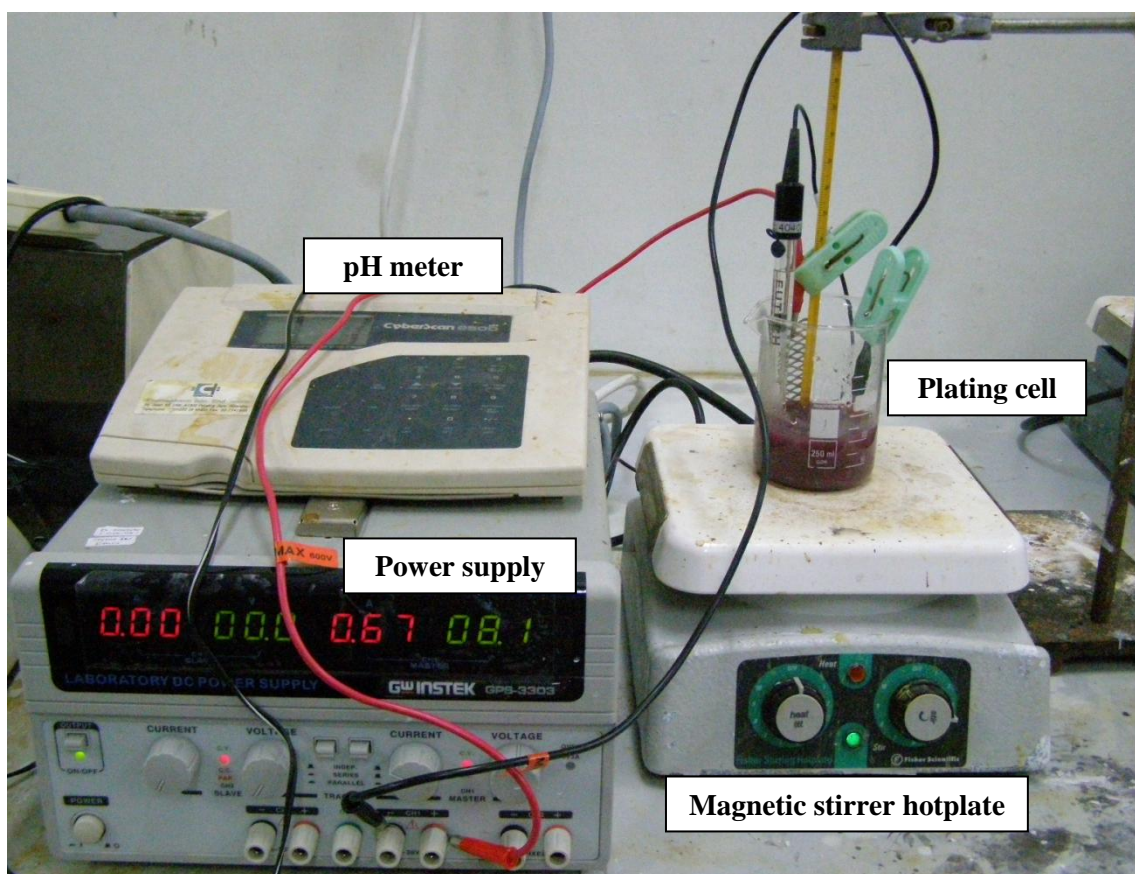


Figure 3.2:
Arrangement of electrodeposition apparatus

3.3.1 Electrodeposition Procedures

The hull cell panel brass substrate was cut into the dimension of approximately 2cm x 2cm. The protective sticker on the mirror polished surface was removed. Prior to the electrodeposition process, the brass substrates were dipped into a 10% H_2SO_4 solution to remove surface contamination. The bottom of the brass substrate was coated with a tape and 2cm x 1.5cm was exposed at the top surface for electrodeposition process. Magnetic stirrer was used to stir the electrolyte solution during the experiment. The nanocrystalline alloy film was deposited on the brass substrate by immersing it into the cell with a fixed current density. After a fixed period of electrodeposition time, the specimen was quickly removed from the cell and the power supply was turned off

immediately. Finally, the as-deposited film on brass substrate was rinsed with distilled water and dried. Figure 3.3 shows the electroplating cell set up. A flow diagram of the overall procedure is shown in Figure 3.4 to represent the preparation routes.

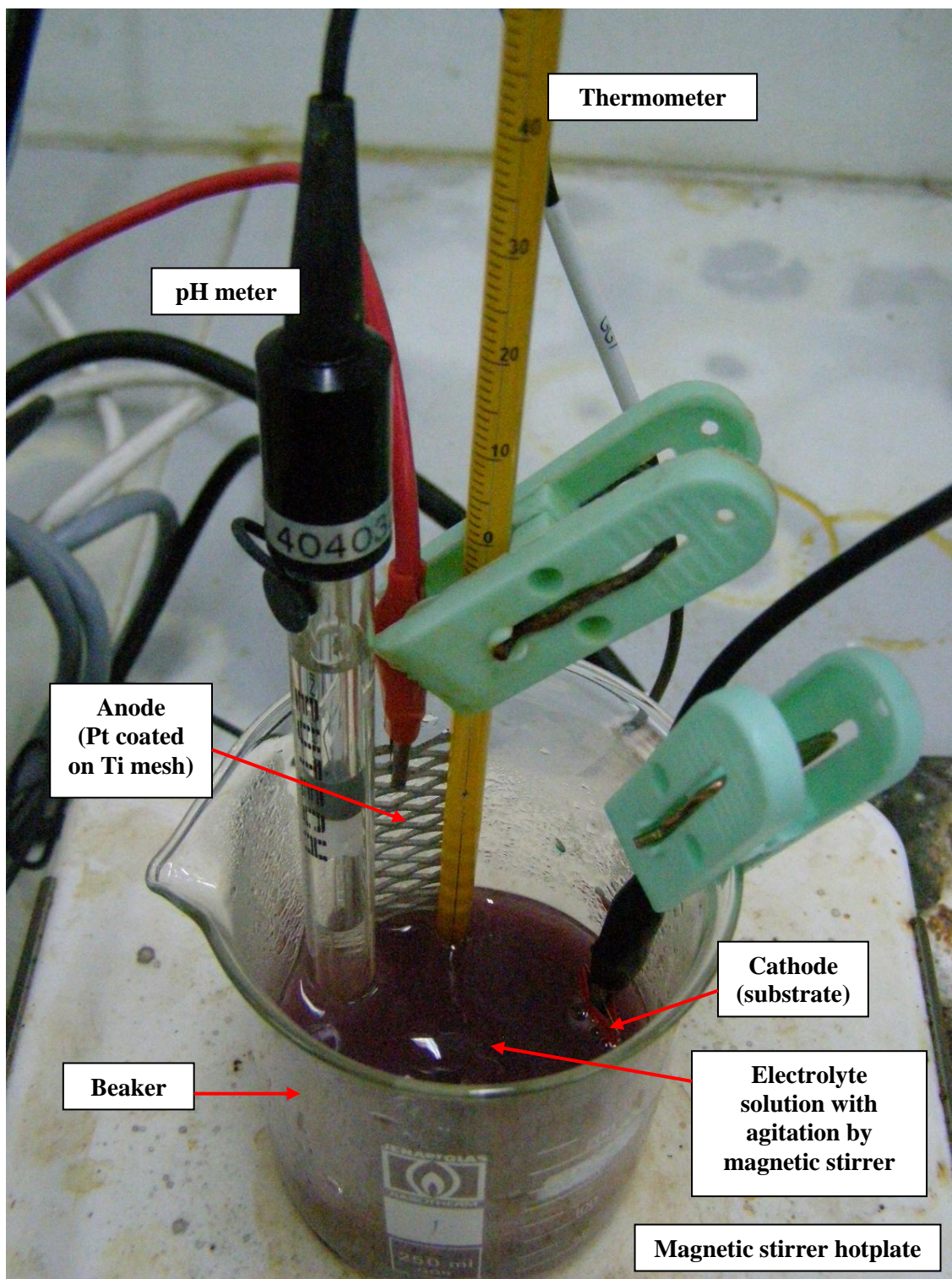


Figure 3.3:
Experimental setup of electroplating cell

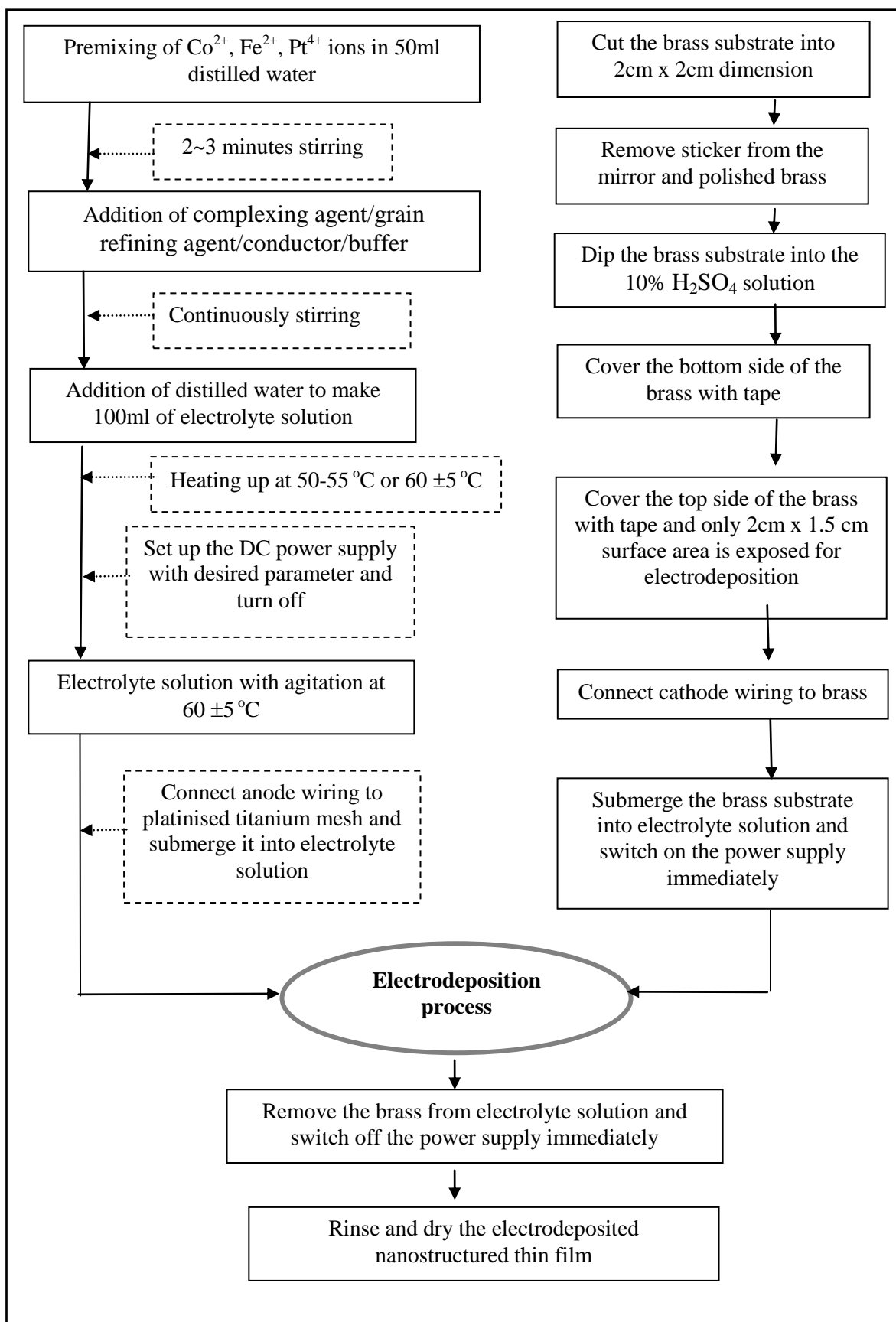


Figure 3.4:
Preparation route of magnetic nanostructured thin films by electrodeposition process

3.4 Experimental Details

3.4.1 Co-Fe System

The five electrolyte solutions used in this synthesis process were mixtures of x M $\text{FeSO}_4 \cdot 7\text{H}_2\text{O}$ (with $x = 0, 0.036\text{M}, 0.072\text{M}, 0.108\text{M}$ and 0.144M), 0.53M $\text{CoSO}_4 \cdot 6\text{H}_2\text{O}$, 0.6M NaCl and 0.32M H_3BO_3 . 0.012M saccharin ($\text{C}_6\text{H}_4\text{CONHSO}_2$) as a grain refining agent was added to the solution to improve the leveling and brightness of the deposits (Manhabosco and Muller, 2008). In addition, another two samples (plating bath 6 and 7) were prepared with and without the addition of saccharin. This step was performed to study the effect of addition of this grain refining agent. NaCl was used as a supporting electrolyte. A $1\text{ cm} \times 4\text{ cm}$ titanium mesh coated with platinum was used as an insoluble anode. Table 5.2 shows the composition of electrolyte solution and the plating conditions that were used in this study. The brass substrates were dipped into a $10\text{ vol } \%$ H_2SO_4 solution for few seconds for the removal of contamination before used. Firstly, the bath solution was prepared by dissolving boric acid. Distilled water was heated close to boiling point and boric acid was added and stirred until it was completely dissolved. NaCl , $\text{CoSO}_4 \cdot 6\text{H}_2\text{O}$ and $\text{FeSO}_4 \cdot 7\text{H}_2\text{O}$ were then added sequentially. The temperature of the electrolyte was controlled in between 50°C to 55°C . The pH values of plating baths were monitored and adjusted in between 3 to 3.5 by using sulfuric acid. The plating bath was constantly stirred using a magnetic stirrer to ensure proper mixing of the electrolyte solution. Electrodeposition was carried out using direct current (DC) at current density of 1000 Am^{-2} . The films were deposited by immersing the substrates into the electrolyte solutions. After 30 minutes, the specimen was quickly removed from the cell, rinsed with distilled water and dried.

Table 3.1:
The molarities of electrolyte solutions and electrodeposition operating conditions for Co-Fe films synthesis

Plating Bath	Concentration (M)			Temperature (°C)	pH
	CoSO ₄	FeSO ₄	C ₆ H ₄ CONHSO ₂		
1	0.53	0	0.012	50 - 55	3.0 – 3.5
2	0.53	0.036	0.012	50 - 55	3.0 – 3.5
3	0.53	0.072	0.012	50 - 55	3.0 – 3.5
4	0.53	0.108	0.012	50 - 55	3.0 – 3.5
5	0.53	0.144	0.012	50 - 55	3.0 – 3.5
6	0.35	0.35	0	40 - 45	2.8 – 3.3
7	0.35	0.35	0.012	40 - 45	2.8 – 3.3
Electrodes & Parameter			Description		
Anode			Platinised titanium mesh		
Cathode			Hull cell panel brass substrate		
Current density			1000Am ⁻²		
Plating duration			30 minutes		
Agitation			Yes		

3.4.2 Co-Pt System

The electrolyte solutions used in this synthesis process were mixtures of (0.05- x) M H₂PtCl₆.6H₂O, x M CoCl₂.6H₂O and complex forming additives containing 2 x M (NH₄)₂C₄H₄O₆ and NH₃.H₂O, where x = 0.005, 0.015, 0.025, 0.035 and 0.045, respectively. Table 3.2 summarizes the plating bath compositions and plating process conditions for Co-Pt film deposition. Platinum film coated on titanium mesh was used as insoluble anode. Deposition was performed on brass substrates. The substrates were

dipped into a 10% H_2SO_4 solution for several seconds to remove surface contamination prior to deposition procedure. The plating cell was a beaker containing 100 ml electrolyte solution. The film was deposited by immersing the brass substrate into the cell. Direct current was applied using a power supply. The effects of two different current densities were investigated (2000Am^{-2} and 3000Am^{-2}). The temperature of the electrolyte was controlled at $60\pm 5^\circ\text{C}$ while the pH was maintained in the range of 7-9.5 by the addition of diluted ammonia solution. The plating bath was constantly stirred using a magnetic stirrer. After 30 minutes, the specimen was quickly removed from the electrolyte solution, rinsed with distilled water and dried.

Table 3.2:
The molarities of electrolyte solutions and electrodeposition operating conditions for Co-Pt film synthesis

Plating Bath	Concentration (M)		
	CoCl_2 [M]	H_2PtCl_6 [M]	$(\text{NH}_4)_2\text{C}_4\text{H}_4\text{O}_6$ [M]
1	0.045	0.005	0.09
2	0.035	0.015	0.07
3	0.025	0.025	0.05
4	0.015	0.035	0.03
5	0.005	0.045	0.01
Electrodes & Parameter		Description	
Anode		Platinised titanium mesh	
Cathode		Hull cell panel brass substrate	
Current density		2000 and 3000Am^{-2}	
pH		7 – 9.5	
Plating duration		30 minutes	
Agitation		Yes	

3.4.3 Fe-Pt and Co-Fe-Pt System

The electrolyte solutions used in this synthesis process were mixtures of chloroplatinic acid hexahydrate, iron sulfate heptahydrate, cobalt chloride hexahydrate and complex forming additives containing ammonium tartrate and ammonia solution. The electrolyte compositions and electrodeposition conditions are summarized in Table 3.3. Platinum film coated on titanium mesh was used as an insoluble anode. The brass substrates were dipped into 10 vol% H_2SO_4 solution for several seconds to remove surface contamination. The films were deposited by immersing the substrates into the cell with direct current density of 1000 Am^{-2} . The temperature of the electrolyte was controlled at $60 \pm 5^\circ\text{C}$ while the pH was maintained in the range of 7-9.5 by addition of ammonia solution or sulfuric acid. The plating bath was constantly stirred by using a magnetic stirrer to ensure proper mixing of the electrolyte solution. After 30 minutes, the specimen was quickly removed from the cell, rinsed in distilled water and dried.

The concentration of electrolyte solution was fixed at 0.05M. Electrolyte solutions of 1, 2 and 3 were prepared with 0.025 M H_2PtCl_6 and 0.02M $(\text{NH}_4)_2\text{C}_4\text{H}_4\text{O}_6$, while 0.03M H_2PtCl_6 and 0.03M $(\text{NH}_4)_2\text{C}_4\text{H}_4\text{O}_6$ were used for electrolyte solutions of 4, 5 and 6. Cobalt concentration was varied at 0, 0.005M and 0.01M. In addition, plating bath 7 was prepared without the addition of complex forming additive. NaCl was added into the bath as electrolytic conductor to increase its conductivity and pH was controlled at about 4 with the addition of diluted HCl solution.

Table 3.3:
The electrolyte compositions and electrodeposition conditions for the synthesis of Fe-Pt
and Co-Fe-Pt films

Bath	Concentration [M]				Current Density (Am^{-2})	pH
	CoCl_2	FeSO_4	H_2PtCl_6	$(\text{NH}_4)_2\text{C}_4\text{H}_4\text{O}_6$		
1	0	0.025	0.025	0.020	1000	7 – 9
2	0.005	0.020	0.025	0.020	1000	7 – 9
3	0.010	0.015	0.025	0.020	1000	7 – 9
4	0	0.020	0.030	0.030	1000	7 – 9
5	0.005	0.015	0.030	0.030	1000	7 – 9
6	0.010	0.010	0.030	0.030	1000	7 – 9
7	0	0.001	0.100	0	200	3.5 - 4.5
Electrodes & Parameter			Descriptions			
Anode			Platinised titanium mesh			
Cathode			Hull cell panel brass substrate			
Bath temperature			$60 \pm 5^\circ\text{C}$			
Plating duration			30 minutes			
Agitation			Yes			

CHAPTER 4: CHARACTERIZATION TECHNIQUES

In the last decade several major changes has taken place in the arena of armory tools that are routinely used by materials scientists and engineers for nanostructural characterization. The “nanoworld” deals with physical instruments such as scanning tunneling microscope, atomic force microscopes, transmission electron microscope, scanning electron microscope, etc. These characterizations are important, as it is already known that physical properties vary at different scales in the materials. To develop the advanced materials for supporting new technologies in the future, it is essential to have a detailed knowledge of the structures of those materials. In the fabrication of nanocrystalline thin film materials, the quantitative information about the structure and composition in nanometer scale is indispensable to understand their properties. Virtually all known analytical techniques have been applied to the study of coatings and thin films on metals. The techniques applied in this research were sensitive to the topography, composition, structure of the surfaces of metals, crystal structure, and magnetic behavior. In this chapter, a brief introduction and principle of the various characterization techniques used in this research will be reviewed.

4.1 Scanning Electron Microscopy (SEM)

Scanning electron microscope (SEM) is a widely used materials characterization technique for its large depth of focus, excellent contrast, high-resolution and three dimensional-like images of solid samples. In the present study, the surface morphology and granules size of the films was examined using a Philip XL40 SEM. Figure 4.1 summarizes the various signals produced as a result of electron-specimen interaction in SEM.

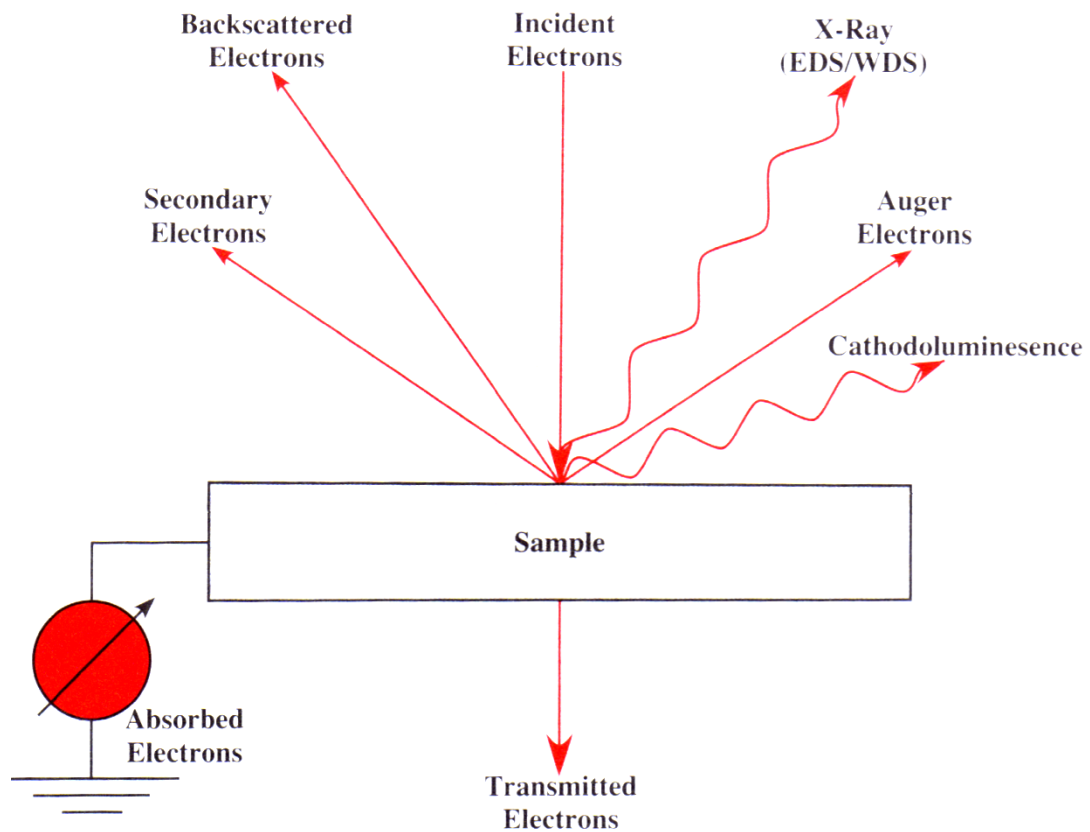


Figure 4.1:

Schematic diagram of a scanning electron beam incident on a solid sample, showing some of the signals generated that can be used to characterize the microstructure (Brandon and Kaplan, 2008)

In general, the term ‘secondary electrons’ is used to describe any electrons that escape from the specimen with kinetic energies below about 50eV (Kelsall et al., 2005). Some primary electrons undergo large deflections and leave the surface with little change in their kinetic energy; these are termed backscattered electrons (Kelsall et al., 2005). In SEM, the signals of greatest interest are the secondary and backscattered electrons. An incident electron beam is raster-scanned across the sample's surface, and the resulting electrons emitted from the sample are collected to form an image of the surface. Imaging is typically obtained by using secondary electrons for the best resolution of fine surface topographical features. Alternatively, imaging with

backscattered electrons gives contrast based on atomic number to resolve microscopic compositional variations as well as topographical information. Generally, metals are not coated prior to imaging in SEM because the samples are conductive and provide their own pathway to ground. In this study, the conductive magnetic alloy films on brass was placed onto a double-sided carbon tape, and subsequently attached on the surface of an aluminum specimen stub. Film thickness was obtained by cross sectioning the thin films on brass substrate. The specimen was vertically mounted in resin and polished by using appropriate metallographic techniques before putting onto a double-sided carbon tape on aluminum stub for SEM analysis.

4.1.1 Granules Size Measurement (Linear Intercept Method)

In this research a granule refers to a conglomeration of many crystallites or grains. Most engineering and structural materials are polycrystalline, that is, they consist of a three-dimensional assembly of individual grains each of which is a single crystal and whose crystal lattice orientation in space differs from its neighbors (Brandon and Kaplan, 2008). The size and shape of these individual granules are varied to a great and wide extent. If the polycrystalline aggregate are separated out into individual granules, the granules size can be defined as the average separation of two parallel tangent planes that touch the surfaces of any randomly orientated granule and this definition is termed the caliper diameter D_c , as it is shown in Figure 4.2 (a). It is rather difficult to measure granules size using this method.

In the present work, granules size of nanostructured film was determined by the average intercept length along a random line obtained from the SEM images. A set of lines were laid down in random directions on SEM micrograph and the number of intercepts with the grain boundaries was counted (Figure 4.2 (b)). The number of intercepts per unit length (N_L) of a test line provides the measurement of granules size

(D_L) by the following equation $D_L = N_L^{-1}$. The method is called the *mean linear intercept* and is commonly accepted method for the determination of granules size (Brandon, 2008). In this study, the test lines were drawn parallel or perpendicular to specific directions. A total 10 set of test lines were drawn for counting the number of intercepts to enhance the accuracy of granules size measurement. An example of granules size measurement of $\text{Co}_{43}\text{-Pt}_{57}$ alloy film is shown in Appendix A.

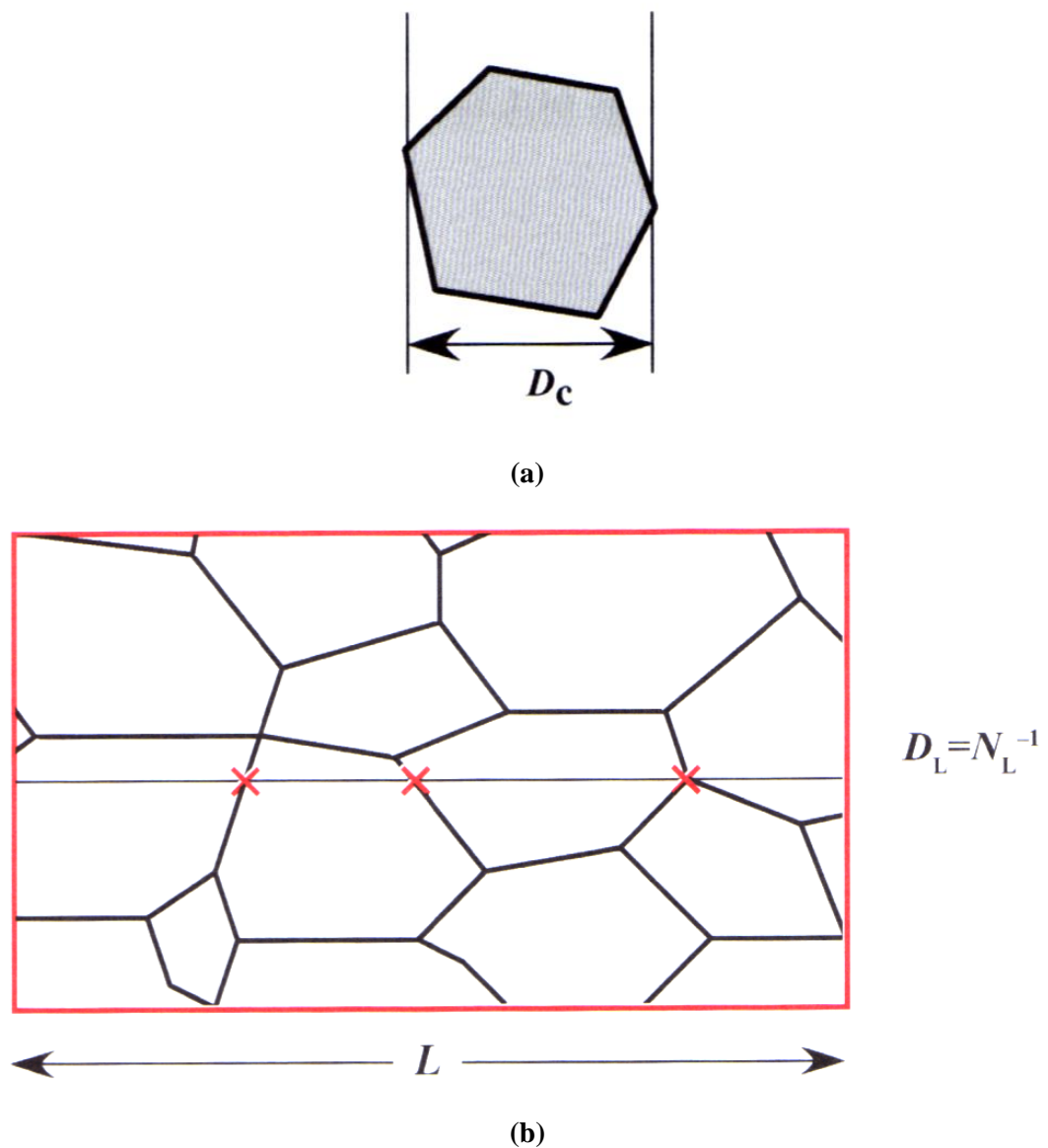


Figure 4.2:
Granule size is defined in several discrete ways which are not related to one another, for example (a) the mean caliper diameter and (b) average intercept length along a random line

4.2 Energy Dispersive X-ray Spectroscopy (EDS)

Energy dispersive X-ray spectroscopy (EDS or EDX) is an analytical technique used for the elemental analysis or chemical characterization of a sample. The EDS system is commonly attached with scanning electron microscope (SEM), transmission electron microscope (TEM) or electron probe microanalyzer (EPMA). Furthermore, EDS extends the usefulness of SEM in terms of elemental analysis that can be performed within regions as small as of a few nanometers in diameter. When the high energy radiation beams such as electrons, ions, X rays, neutrons, gamma rays strikes the specimen, the beam penetrates through the outer conduction/valence bands and interact with the inner-shell electrons. As a results, the inner shell electron escapes from the attractive field of the nucleus leaving a hole in the inner shell. This excited state of atom is described as “ionized”. The ionized atom can return to its lowest energy level (ground state) by filling the hole with an electron from an outer shell. The transition is accompanied by the emission of X-Rays. The energy of this emission is equal to the difference of the energy between the two shells involved. This energy difference is unique for an atom which allows atomic identification in the materials of interest.

The process of X-ray emission is shown schematically in Figure 4.3. In fact, it is much more complex than the schematic figure because there are many different α , β and γ X-rays (such as α_1 , α_2 , β_1 , β_2 , β_3 , γ_1 , γ_2 , γ_3 , etc.) depending on which subshell of the outer shell the electron falls from to fill the hole. A complete range of possible electron transitions that give rise to K, L, and M characteristic X-rays is shown in Figure 4.4. The EDS detector converts the energy of each individual X-ray into a voltage signal. The signal processing electronics count the number of pulses of each different amplitude, resulting in a histogram of X-ray energy versus intensity. The X-ray energies allow atom identification and the relative peak intensities can be related to relative atomic concentrations by comparison to standards, or by theoretical calculations

(Holloway and Vaidyanathan, 2010). An example of EDS spectrum, atomic and weight percentage of $\text{Co}_{43}\text{-Pt}_{57}$ alloy film is shown in Appendix B.

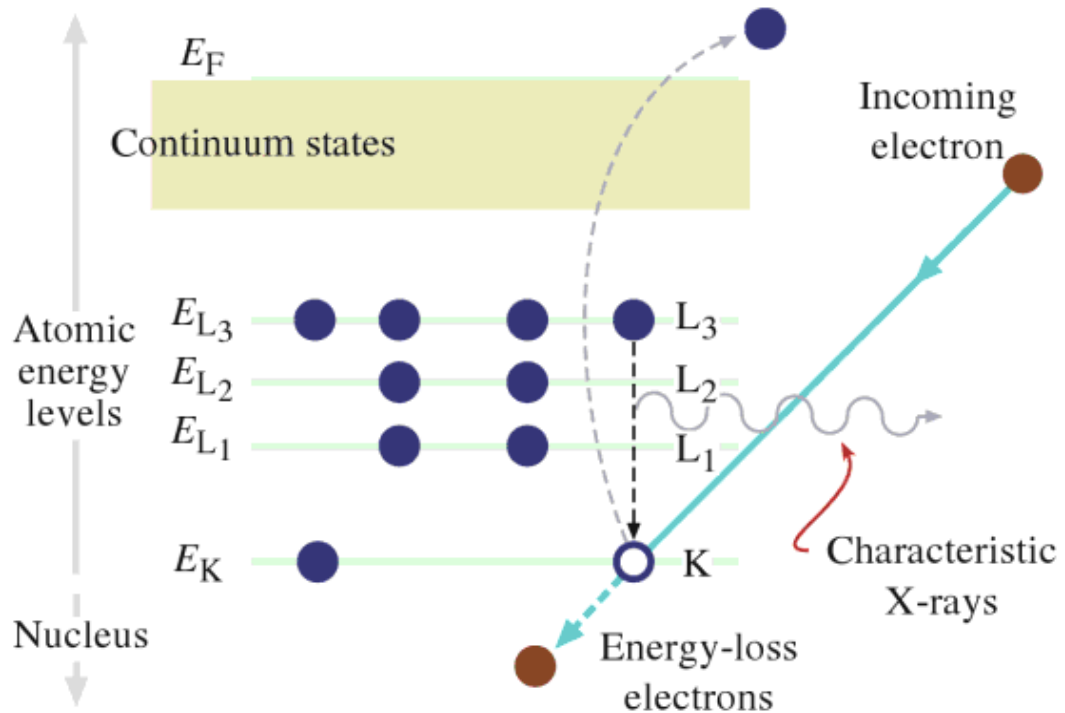


Figure 4.3:

The ionization process of an atom. An inner (K) shell electron is ejected by a high-energy electron. When the hole in the K shell is filled by an electron from the L shell, characteristic ($K\alpha$) X-ray emission occurs. The beam electron loses energy but continues on through the specimen (William et al., 2009)

Elemental mapping is an effective way to analyze the distribution of the constituent elements in two dimensions (Shindo and Oikawa, 2002). Elemental mappings can be performed at the regions of interest, where the EDX spectrum is utilized for detection of a particular element. Elemental Mapping is represented by photographic images depicting the distribution of the elements of interest. The image consists of dots which represent the relative concentration of each element. Areas with greater number of dots indicate higher concentrations of the element. Ideally, the surface of the specimens for EDX analysis needs to be perfectly flat and smooth. The topography of the sample can produce artifacts in EDX data due to non-uniform absorption and blockage of X-rays (Thomas and Stephen, 2010).

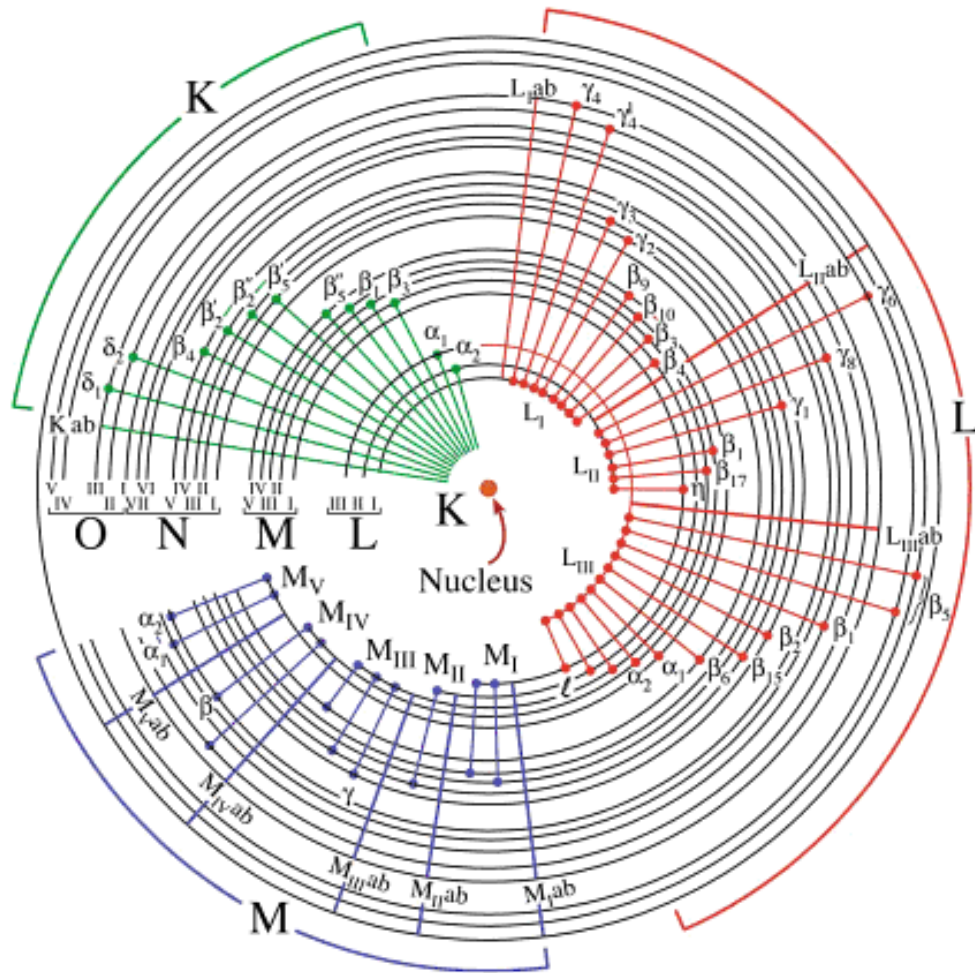


Figure 4.4:
The schematic diagram of a complete range of possible electron transitions that give rise to K, L, and M characteristic X-rays (William et al., 2009)



Figure 4.5:
Image of energy dispersive X-ray spectroscopy (EDS: Model EDAX) attached on a scanning electron microscope

4.3 X-Ray Diffraction (XRD)

X-ray Diffraction (XRD) is a very important nondestructive characterization technique for the identification of crystal structures, phases, lattice constant, geometry, preferred crystal orientations, average crystallite size, strain, crystal defects, etc. In this research, crystallographic phases and average crystallite sizes were investigated by using Philips X'pert MPD PW3040 X-ray diffractometer (XRD) with Cu-K α ($\lambda=1.5418\text{\AA}$) radiation (Figure 4.6).



Figure 4.6:
Philips X'pert MPD system was used for phase analysis and crystallite size calculation

When a monochromatic X-ray beam hits a sample, it generates scattered X-rays with the same wavelength as the incident beam in addition with some absorption and other losses. The peak intensities are determined by the atomic pattern within the lattice planes. There are many theories and equations about the relationship between the diffraction pattern and the material structure. Bragg law is a simple way to describe the diffraction of X-rays within a crystal. The incident X-rays hit the crystal planes with an incident angle θ (Figure 4.7.). The diffraction peak is observed only when the Bragg's condition is satisfied:

$$n\lambda = 2d \sin \theta \quad (4.1)$$

where λ is the wavelength of incident X-rays; d is the distance between adjacent crystal planes (d-spacing), θ is the incident angle of the X-ray and n is an integer number, called the order of reflection. (Bob, 2009; Abbaschian et al., 2001; Heimendahl, 1980; Goldstein et al., 1981).

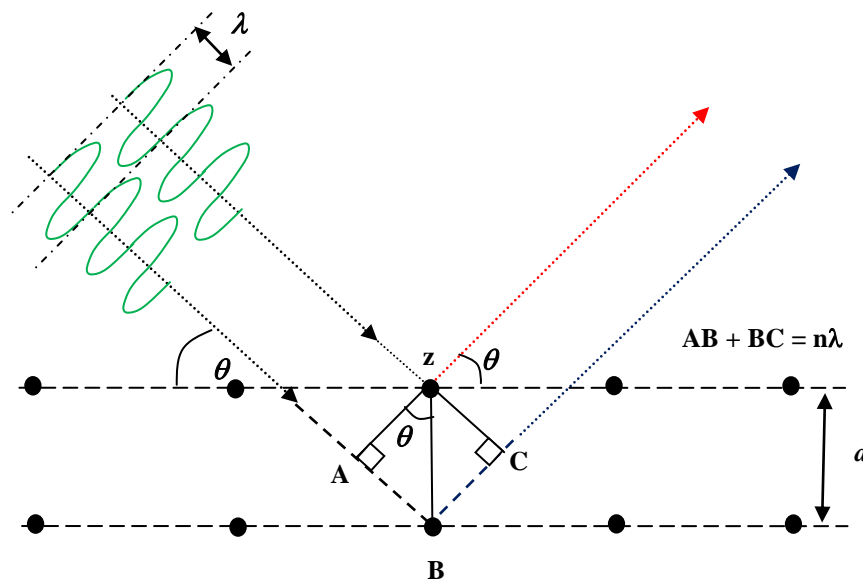


Figure 4.7:
The incident X-rays and reflected X-rays make an angle of symmetric θ to the normal of crystal plane

A typical diffraction peak is represented by the curved line in Figure 4.8. The highest point on the curve gives the maximum intensity of the peak, I_{max} . The width of a peak is typically measured by its full width at half maximum (FWHM). The total diffracted energy for a certain peak can be measured by the area under the curve, which is referred as integrated intensity. In this work, the diffraction pattern was obtained by scanning the magnetic alloy film samples at 2θ angle starting from 30° to 100° at an increment rate of $0.020^\circ/\text{second}$. Phase identification was conducted by using the Joint Committee on Powder Diffraction Standard (JCPDS) database. Furthermore, the lattice parameters can be calculated based on the Miller indices of each set of crystal planes.

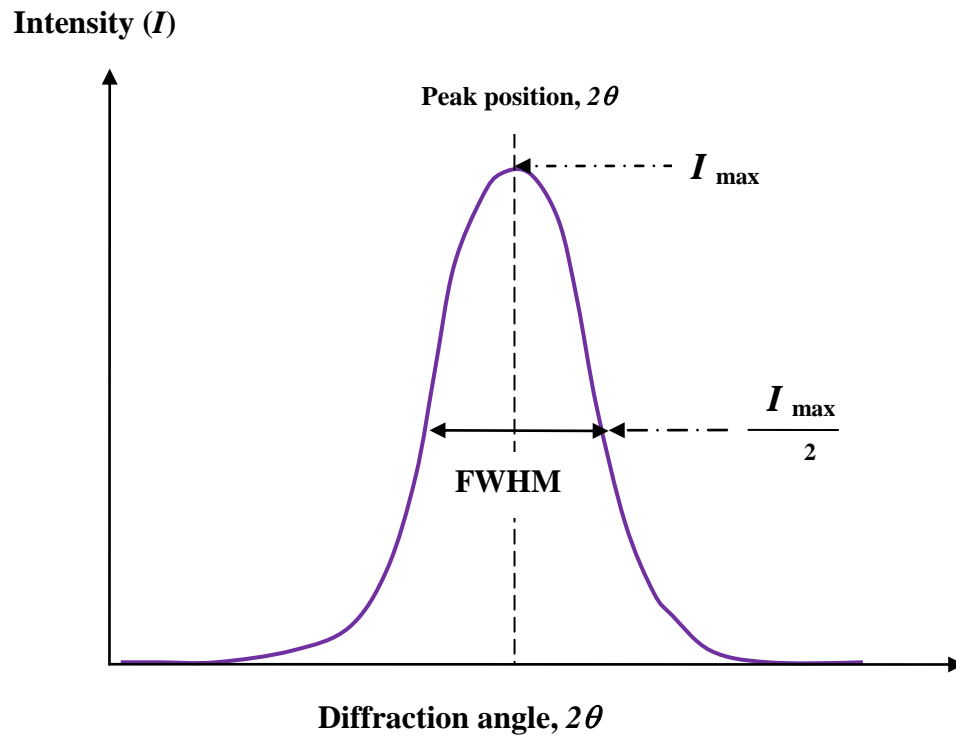


Figure 4.8:
Full width half maximum (FWHM) of an X-ray diffraction peak

4.3.1 Crystallite Size Determination (Debye Scherrer Equation)

How large are the crystallites? The crystallite size (D) can be estimated from XRD patterns by substituting the value of full-width at half maximum (FWHM) of the broadened peaks to Debye Scherrer equation given as:

$$D = \frac{0.9\lambda}{FWHM \cos\theta} \quad (4.2)$$

Where λ = wavelength of the X-ray and θ = angles of diffraction

Full width at half maximum (FWHM) is the width of the intense characteristic peak at the half of the intensity as shown in Figure 4.8. The broadening effect is quantified as FWHM in the unit of radian from the XRD peaks. FWHM can be obtained by using Philips Electronics's ProFitTM software. This software can deconvolute the diffraction pattern into its constituent Bragg reflections by fitting the analytical profile to as-measured intensity data. In addition, it can also identify various profile parameters which define the position, intensity, breadth and shape of each reflection. As a standard calibration material, Lanthanum hexaboride (LaB₆) was used for determining the broadening of XRD peaks caused by the equipment as shown in Figure 4.9. The obtained FWHM value was 0.1492 at about 43°. An example for determining the crystallites size of Co₄₃-Pt₅₇ alloy film is shown in Appendix C. The FWHM value and deconvoluted XRD peak of Co₄₃-Pt₅₇ alloy film obtained from Philips Electronics's ProFitTM software are shown in appendix D and E, respectively.

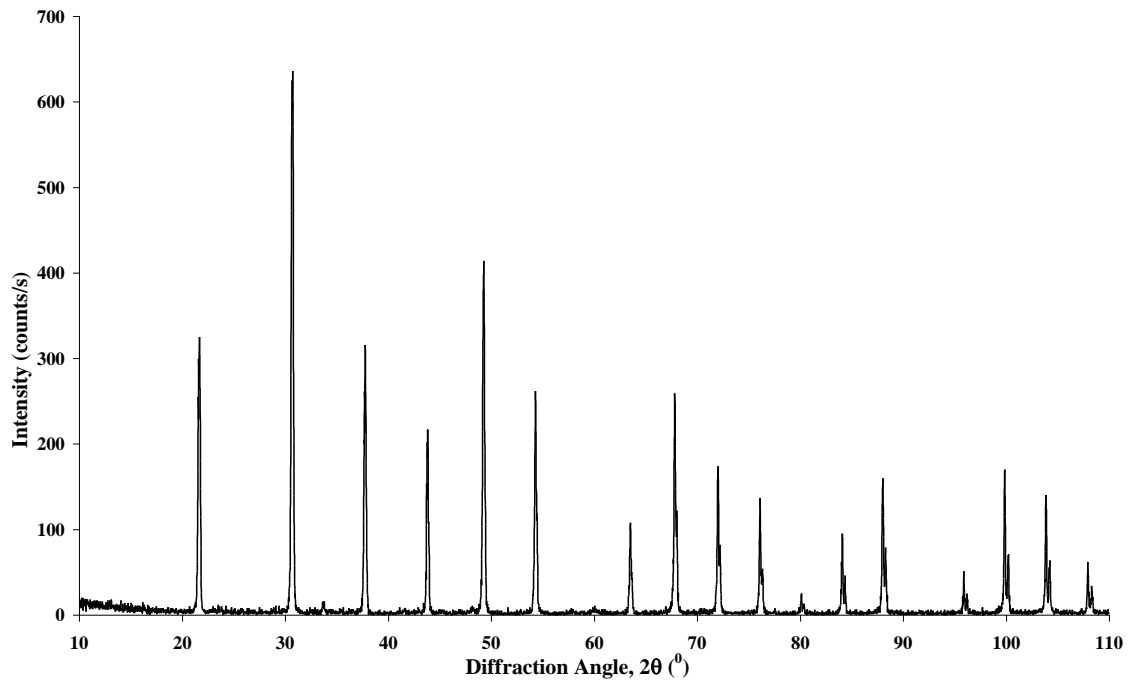


Figure 4.9:
XRD diffraction patterns of standard calibration material (LaB₆)

4.4 Atomic Force Microscopy (AFM)

A significant portion of the experimental data reported in subsequent chapters which were acquired from atomic force microscopy (AFM) and magnetic force microscopy (MFM) and it is thus essential to describe these important instruments. AFM was invented by G. Binnig, C. Quate and C.H. Gerber in 1986 (Bhushan et al, 2004). It provides 3-D topographical information (such as shape, roughness value of the surface) when the tip is in contact with the sample. Many different tip materials have been used for AFM including diamond, tungsten, tungsten carbide, etc. But silicon nitride is often preferred, since this material possesses good chemical and physical resistance to tip damage (Brandon and Kaplan, 2008). The AFM can operate in a close contact mode in which the core-core repulsive forces with the surface predominates or in a greater separation “noncontact” mode in which the relevant force is the gradient of

the Van der Waals potential (Owen and Poole, 2008). The average height and surface roughness of some nanostructured alloy films were studied by Quesant AFM in contact mode as shown in Figure 4.10. The table-top instrument was mounted on a rigid base having high damping capacity in order to avoid extraneous mechanical vibration. In addition, AFM and MFM (Q Scope, Ambios Technology) as shown in Figure 4.11 were used to measure both topography and magnetic properties simultaneously for some film samples.

The probe of AFM is mounted on a piezoelectric x, y and z scanner which scans over a surface and reveal three dimensional images down to atomic level. Image with details of the order of a few nanometers are achievable. This principle permits registration of both the normal deflection of the cantilever with sub angstrom resolution and its twisting angle, so that normal and lateral forces can be measured simultaneously. In contact mode, the instrument lightly touches a tip at the end of a leaf spring or "cantilever" to the sample. As a raster-scan drags the tip over the sample, photo-detector measures the vertical deflection of the cantilever, indicating the local sample height. AFM is considered a non-destructive means of scanning since the force used to probe the sample is very small. It also has the advantage of little to no preparation time to prepare the sample. In this research, the thin film sample on brass substrate was directly placed under the AFM sample holder. However, the specimen must be flat and even to prevent damage of the cantilever. Figure 4.12 illustrates the AFM beam deflection system.



Figure 4.10:
Image of Quesant atomic force microscopy (AFM)

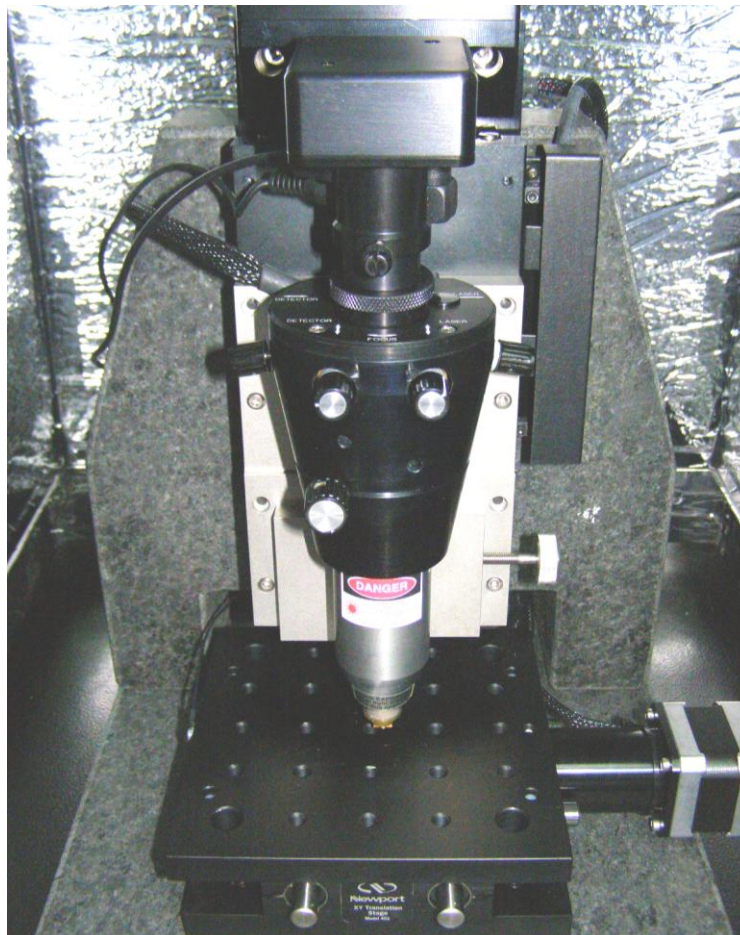


Figure 4.11:
Image of Q Scope magnetic force microscopy (MFM)

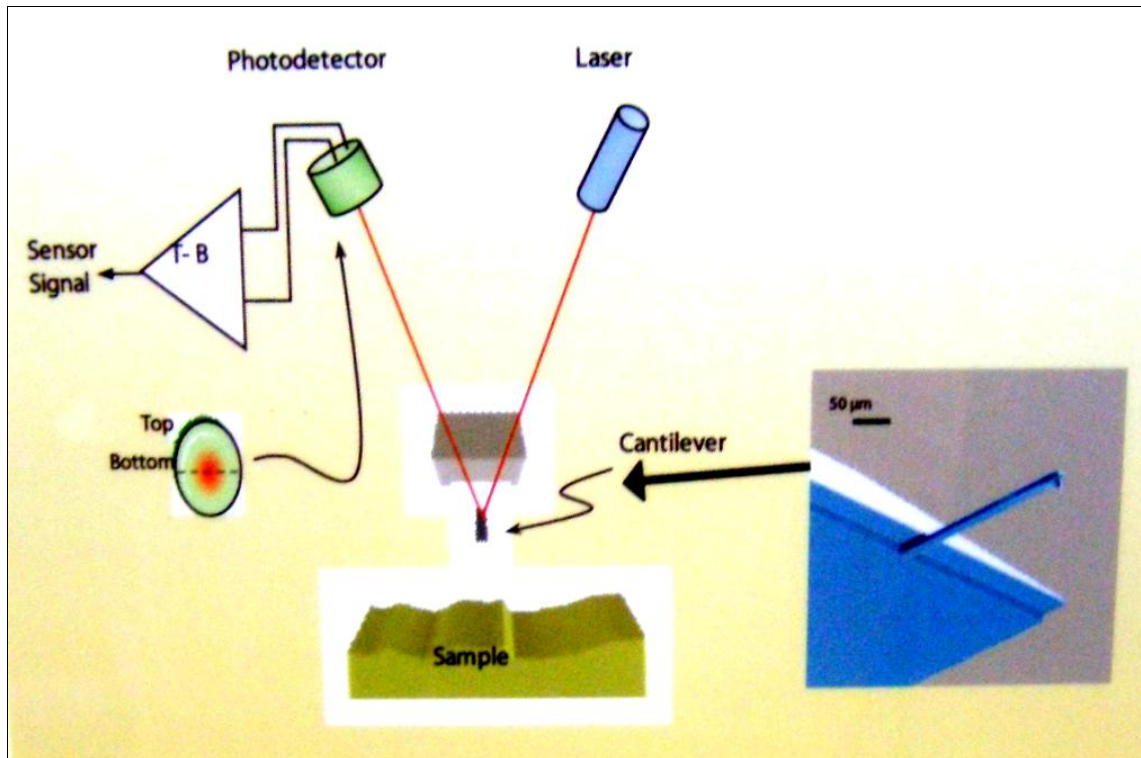


Figure 4.12:
Illustration of the AFM beam deflection system, using a laser and photo-detector to measure the beam position

4.5 Magnetic Force Microscopy (MFM)

Magnetic force microscopy (MFM) is used to image naturally occurring and deliberately written domain structures in magnetic materials. MFM requires a special cantilever with a magnetized tip. When the cantilever is vibrated to its resonance frequency, it is rastered out of contact with the sample surface in order to detect the fields near the surface through the changes in cantilever vibration amplitude or phase. In general, the bright color represents higher signal of magnetic properties in the sample. Magnetic domains within a grain are separated by Bloch walls (Vollath, 2008). Typical MFM applications include imaging the magnetic bit profiles of data stored in magnetic media and imaging the fields near Bloch wall boundaries and other domain boundaries in magnetic solids. The scanning method of MFM is called "lift height" method. When the tip scans the surface of a sample at close distances (<100 nm), the magnetic forces as

well as atomic and electrostatic forces are scanned. Therefore, the atomic force of the sample can be obtained simultaneously with magnetic force measurement.

In this study, the surface roughness and magnetic force of some of the films were determined by AFM and MFM (Q Scope, Ambios Technology). The operating mechanism of MFM is different from the topographic modes of Q-scope operation, where bright and dark features in an image are simply interpreted as the high and low features of the surface. Interpreting MFM images requires an understanding of the physical interactions between the magnetic probe and the magnetic field near the surface and the mechanism by which the image contrast is generated. No special surface preparation or coating is required for MFM imaging. A magnetic cantilever was magnetized with a magnetic field (Figure 4.13) and then it was installed into the probe holder. The small magnets behind the probe holder pull the metal against the holder to keep it in place. The magnetic field from these magnets is weak enough to allow MFM imaging of high coercivity materials (> 100 Oe). Firstly, the topographic profile of each scan line was measured. That is, the tip was brought into a close proximity of the sample to take AFM measurements. The magnetized tip was then lifted further away from the sample. On the second pass, the magnetic signal was extracted (Figure 4.14).



Figure 4.13:
A special cantilever with a magnetized tip is placed in a magnetic field for magnetization before the MFM measurement

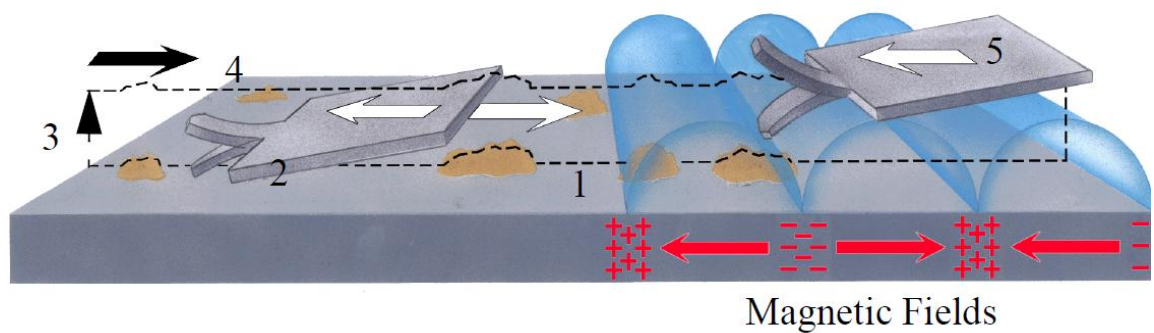


Figure 4.14:
Magnetic imaging is generated by lift mode. Cantilever traces surface topography on first trace and retrace (1&2). Cantilever ascends to “lift scan height” (3). Lifted cantilever profiles topography while responding to magnetic influences on second trace and retrace to acquire magnetic force data (4 & 5)

4.6 Infinite Focus Microscopy (IFM)

The infinite focus microscope (IFM) is a useful tool for profiling the area, volume, 2-D image analysis and automation via scripting. The technique of infinite focus is based on focus-variation. Its operating principle combines the small depth of focus of an optical system with vertical scanning. Figure 4.15 illustrates the IFM beam deflection system. In the research, the specimens were placed onto the motorized stage and it was illuminated by modulated white light. The coaxial white light was provided by a light source delivered through a beam splitter to a series of selectable objectives contained in a six-place nosepiece. The light from the specimen was projected through the beam splitter onto a digital color sensor.

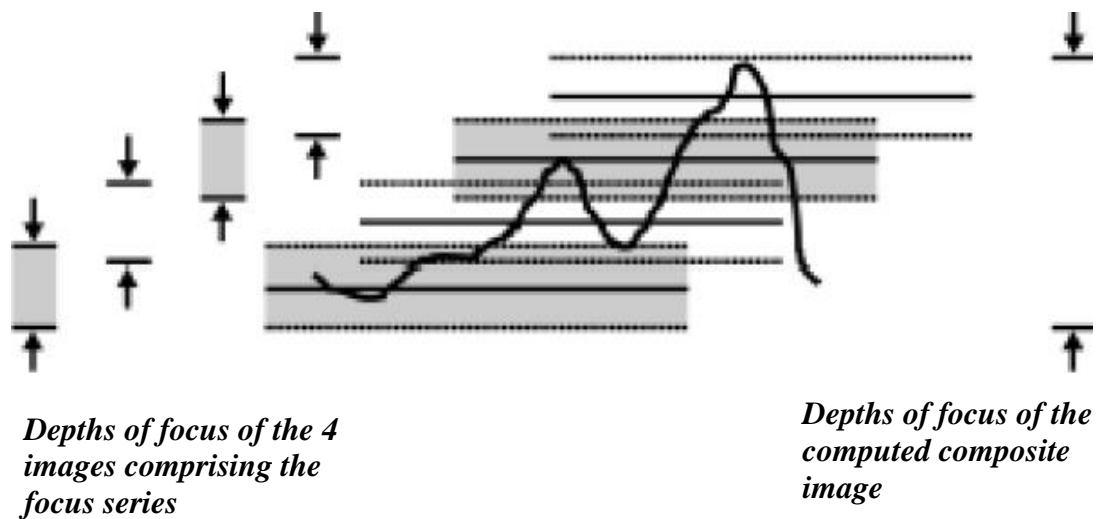


Figure 4.15:
Illustration of the infinite focus microscopy (IFM) beam deflection system, using a laser and photo=detector to measure the beam position

In IFM both vertical and lateral resolution can be realized by a simple change in the objectives. The resulting image is similar to conventional light microscopy in a way that it shows limited depth of focus. As the distance between the object and objective is varied, images are being captured continuously. Each position is differently imaged

depending on the 3-D structure of the specimen. The harmonized interaction between modulated illumination, vertical scanning and sensor capturing is crucial for this process. Figure 4.16 shows the IFM equipment used in this research.

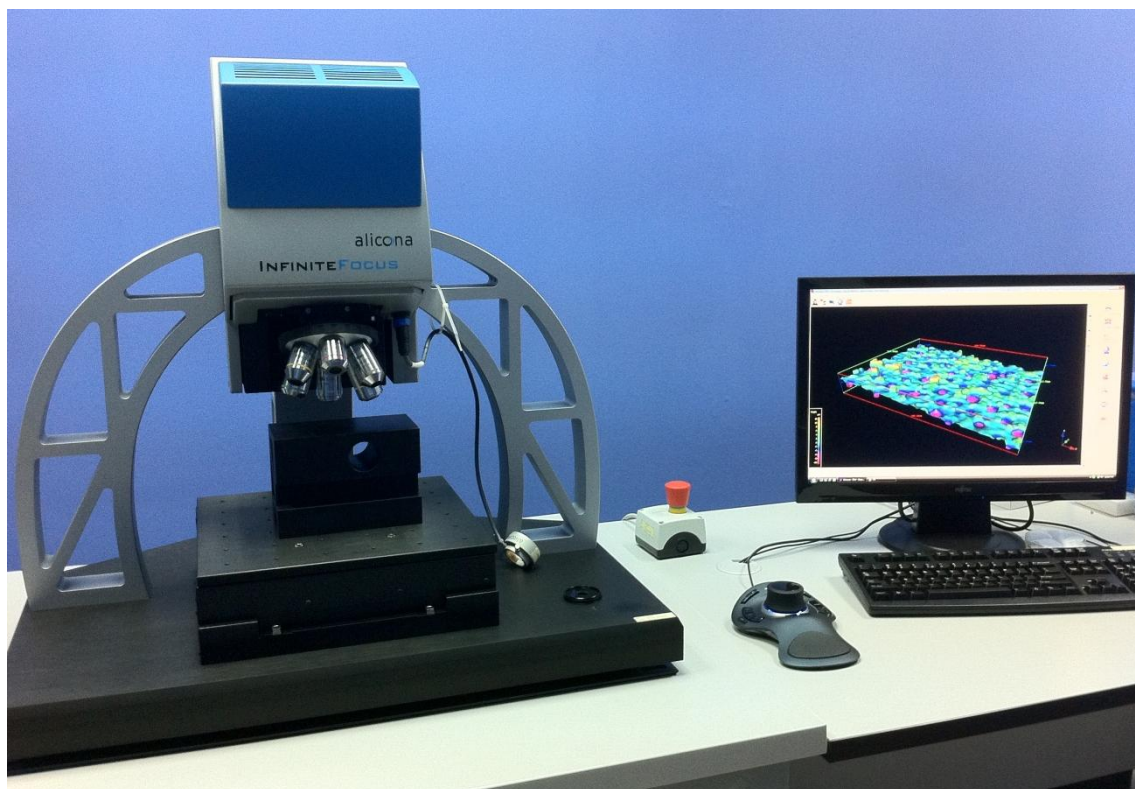


Figure 4.16:
Image of infinite focus microscopy (IFM)

4.7 Alternating Gradient Magnetometer (AGM)

The magnetic properties of the films were measured at room temperature by an alternating gradient magnetometer (AGM: MicroMag™ Model 2900, Princeton Measurements Corporation) as shown in Figure 4.17. It is a powerful system for measuring the magnetic properties of a wide range of materials. It has extremely high sensitivity (10 nemu rms - corresponding to less than 50 pg of iron) and high speed of measurement (100 ms per point), combined with compact design with easy operating system which makes it well-suited for nanoscale research. The MicroMag™ system accommodates all types of samples (up to the dimension of 5 mm x 5 mm x 2 mm: 200 mg mass): solids, ultra thin films, powders, liquids and even slurries.

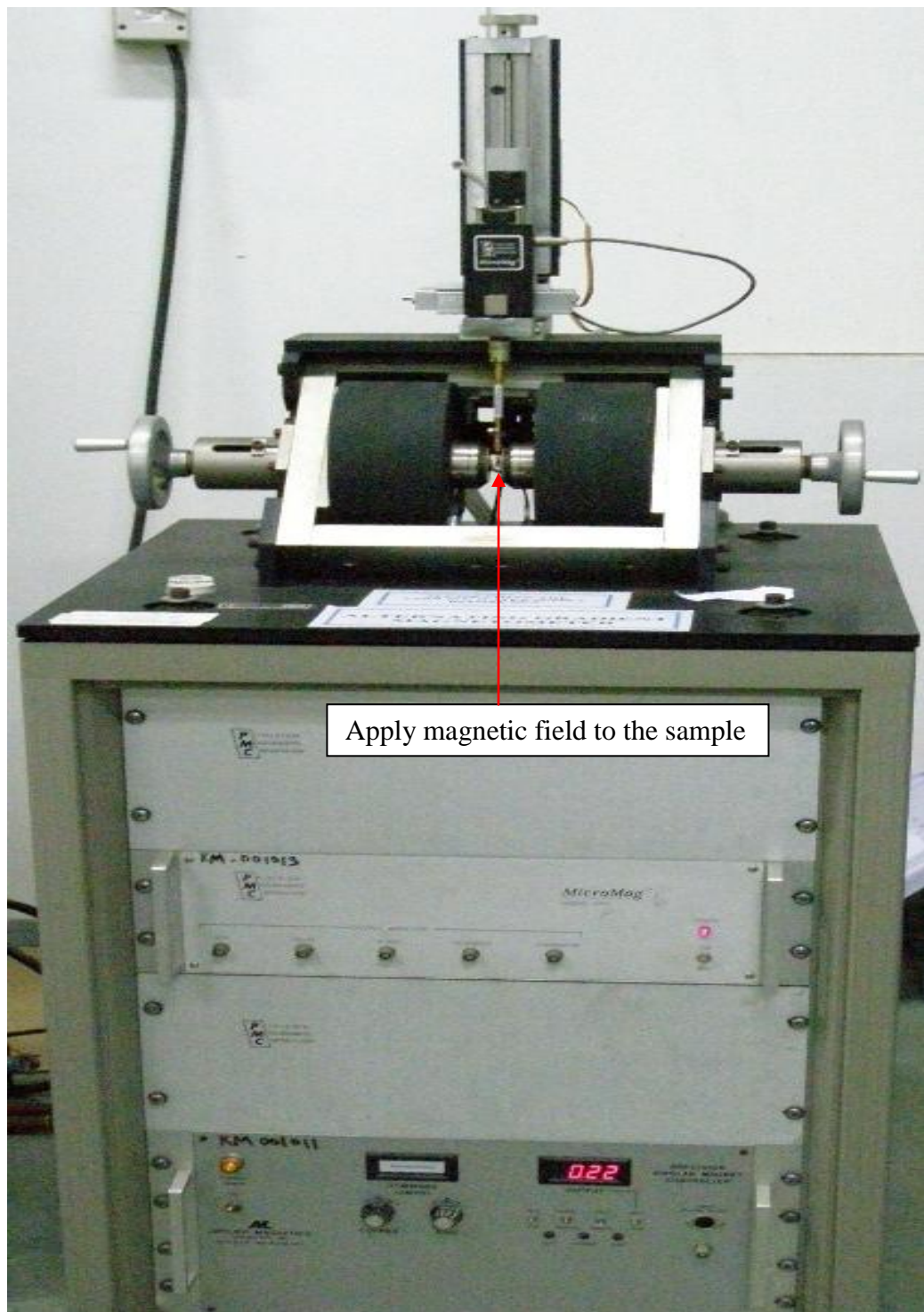


Figure 4.17:
Image of alternating gradient magnetometer (AGM: Model 2900 MicroMag, Princeton Measurements Corporation)

AGM utilizes an alternating gradient field to exert a force on a sample that results a deflection in the sample within the field. This deflection is measured by a pizeoelectric sensing element mounted on the probe arm and signals are carried to a computer connected to the magnetometer. Magnetic properties such as coercivity, saturation magnetization and remanence can be obtained by AGM. Figure 4.18 shows the transducer probe inside the AGM where a typical sample was placed on the tip of the probe. The film sample of less than 200 mg was scraped off carefully from brass substrate and sealed with transparent tape having the size of the tip of the probe which was approximately 2mm x 2mm in dimension. It was then mounted to the transducer probe using silicone grease. Prior to the actual measurement, calibration was carried out by using a pure nickel standard calibration material with known magnetic saturation value. Applied field of +10 kOe to -10kOe was subjected to the samples. Typically, the AGM system is suitable for the applications in magnetic recording media, MRAM, spin-valves, GMR heads, amorphous metals, rare earth compounds, high temperature superconductors, weak ferro-fluids, biological specimens, toner material, magneto-optic devices, paleomagnetic samples and very weak diamagnetic and paramagnetic materials.

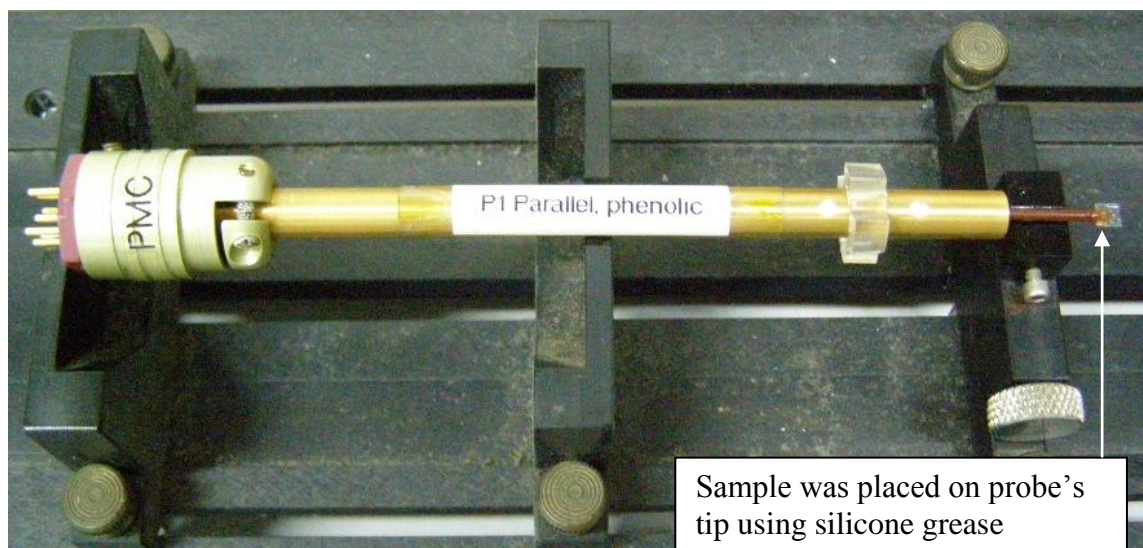


Figure 4.18:
Image of transducer probe

CHAPTER 5: RESULTS AND DISCUSSION

5.1 Cobalt-Iron Nanocrystalline Films

5.1.1 Physical Appearance

Physical observation of the electrodeposited films showed dependence on the composition of the electrolytic bath. The Co film was dark grey in color. In comparison, Co₉₄-Fe₆ and Co₈₉-Fe₁₁ films were grey. On the other hand, films deposited with higher concentration of Fe were light grey in color. This might be because of the original color of Co is grey whereas Fe is genuinely grey tinge and lighter in color as shown in Table 2.3. This physical observation of the as-deposited films is shown in Figure 5.1. The difference in color might be an indication of different phases of Co-Fe system.

In addition, Co-Fe film deposited without saccharin (Figure. 5.1 (f)) was cracked and detached from substrate, whereby Co₄₀-Fe₆₀ film deposited with the addition of saccharin (Figure 5.1 (g)) showed smoother and better adhesion with the brass substrate. This result revealed the importance of grain refining agent during the deposition of fine quality films. However, the Co₄₀-Fe₆₀ film was easily oxidized when exposed to environment due to high Fe content in the as-deposited films. This was evident with the change of color from grey to yellowish. Therefore, these two films were not used for further characterization.

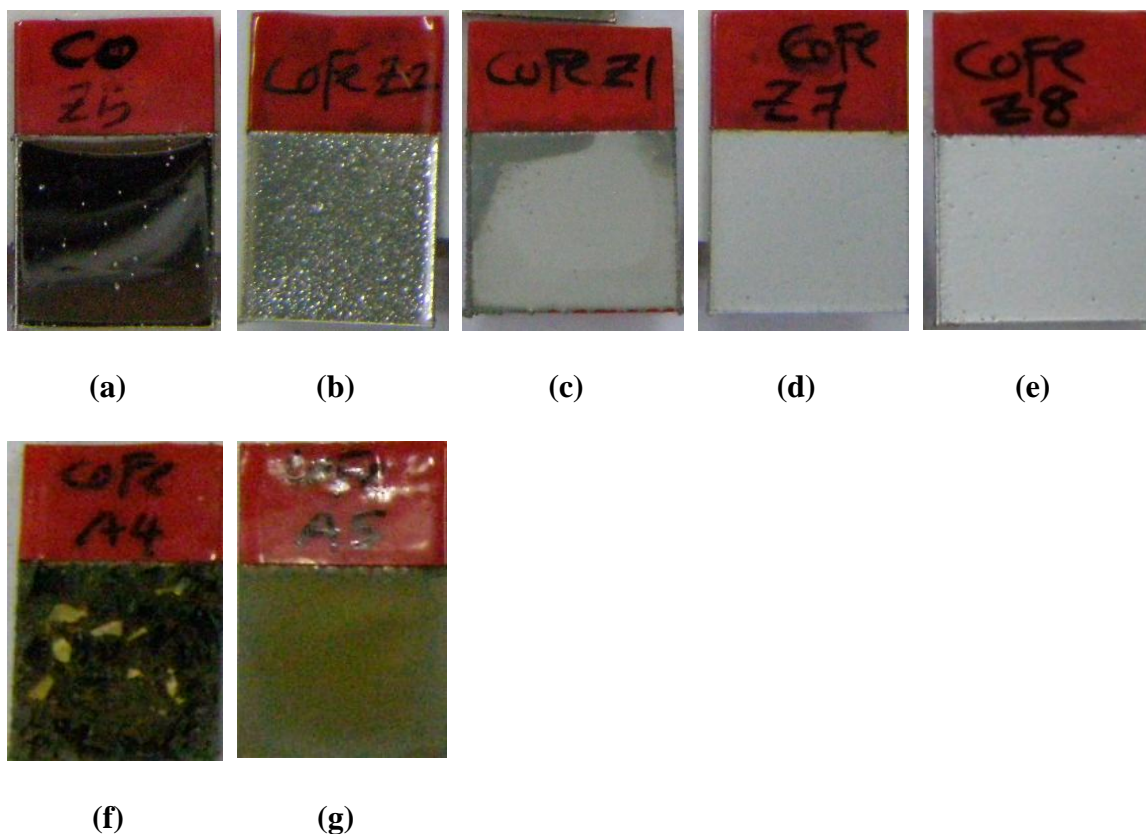


Figure 5.1:

Physical appearance of as-deposited nanocrystalline films: (a) Co_{100} , (b) $\text{Co}_{94}\text{-Fe}_6$, (c) $\text{Co}_{89}\text{-Fe}_{11}$, (d) $\text{Co}_{86}\text{-Fe}_{14}$, (e) $\text{Co}_{82}\text{-Fe}_{18}$, (f) Co-Fe film deposited without saccharin and (g) $\text{Co}_{40}\text{-Fe}_{60}$ film deposited with saccharin

5.1.2 Chemical Composition

At low concentrations of iron sulfate in the plating bath, the energy dispersive X-ray spectroscopy (EDS) analysis showed an upward linear relation of iron content in the deposited films with the iron sulfate concentrations in the plating bath. However, deviation from this linear trend was observed at higher concentration of iron ions in the plating bath as shown in Figure 5.2. The standard equilibrium potentials of the Co and Fe are -0.277V and -0.440V , respectively with respect to standard hydrogen electrode (Skoog et al., 1996). This indicates that Co is more noble than Fe and is expected to be preferentially deposited on the substrate. Therefore, from thermodynamic considerations, it is expected that Co would be deposited first followed by Fe (Correia et al., 2006).

The EDS spectrum of Co_{100} and $\text{Co}_{82}\text{-Fe}_{18}$ films are shown in Figure 5.3. The EDS spectrum of Co_{100} film (Figure 5.3 (a)) showed the existence of Co peak only whereas Co and Fe peaks were observed in the EDS spectrum of $\text{Co}_{82}\text{-Fe}_{18}$ film (Figure 5.3 (b)). The as-synthesized films were labeled according to the atomic percentage of Co and Fe in the film. The deposits obtained from $\text{FeSO}_4 \cdot 7\text{H}_2\text{O}$ solutions with concentration higher than 0.144M were easily oxidized and the results of these deposits are not included in this thesis. Fe^{2+} ions are quite unstable and easily oxidized to Fe^{3+} , causing precipitation of $\text{Fe}(\text{OH})_3$ complexes (Shigeru et al., 2005). This causes a decrease in saturation magnetization (M_s) and coercivity (H_c) of the electrodeposited thin film (Kovacs et al., 2007). Three data points were taken for EDS analysis for each sample. The average atomic percentages of Co and Fe determined by EDS were then compiled and shown in Table 5.1.

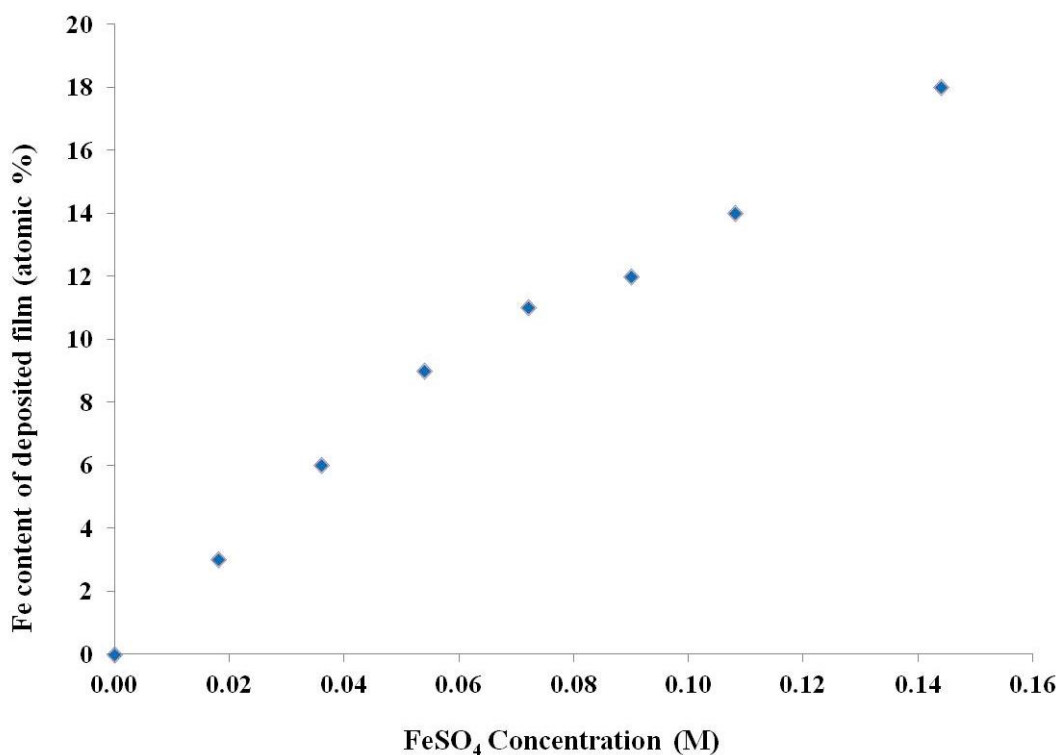


Figure 5.2:
Effect of FeSO_4 concentration in electrolyte solutions on Fe content in the deposits

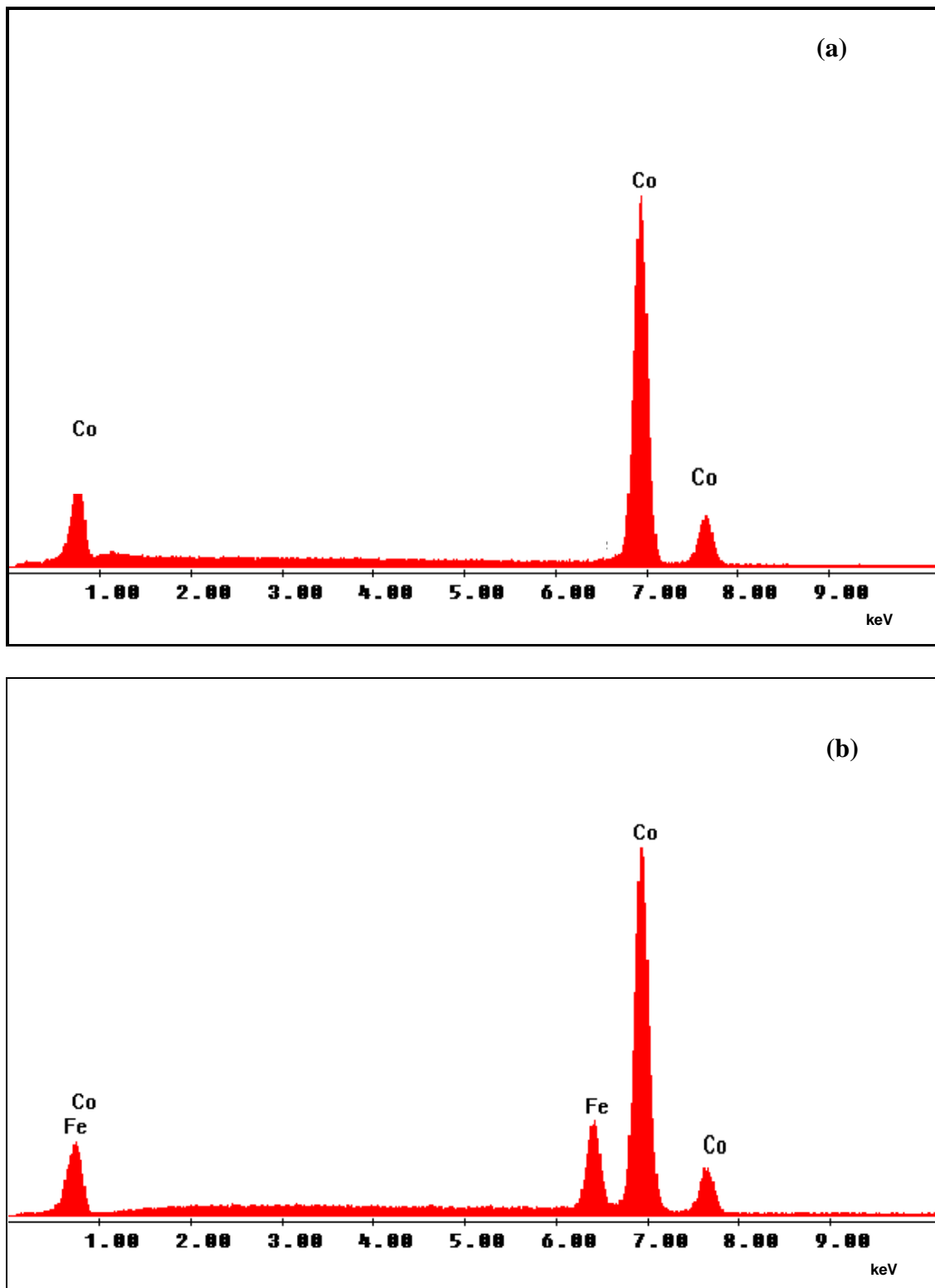


Figure 5.3:
Energy dispersive X-ray spectroscopy (EDS) spectra of (a) Co_{100} and (b) $\text{Co}_{82}\text{-Fe}_{18}$ films

Table 5.1:
The atomic percentage of Co and Fe in the deposited film determined by EDS

Plating Bath	Concentration (M)			Composition			Thin film sample
	CoSO ₄	FeSO ₄	C ₆ H ₄ CONHSO ₂	Co at. %	Fe at. %	Fe wt. %	
1	0.53	0	0.012	100	0	0	Co ₁₀₀
2	0.53	0.036	0.012	94	6	6	Co ₉₄ -Fe ₆
3	0.53	0.072	0.012	89	11	11	Co ₈₉ -Fe ₁₁
4	0.53	0.108	0.012	86	14	13	Co ₈₆ -Fe ₁₄
5	0.53	0.144	0.012	82	18	17	Co ₈₂ -Fe ₁₈
6	0.35	0.35	0				
7	0.35	0.35	0.012	40	60	58	Co ₄₀ -Fe ₆₀

5.1.3 X-ray Diffraction (XRD) Analysis

Figure 5.4 shows the XRD patterns of the as-synthesized Co-Fe thin films. The XRD spectrum of Co₈₉-Fe₁₁, Co₈₆-Fe₁₄ and Co₈₂-Fe₁₈ showed mixture of body-centered cubic (BCC) (JCPDS 50-0795) and face-centered cubic (FCC) phase. The reflections from the characteristic (111), (200), (220), (311) crystal planes of FCC structure were observed at 2θ of 44° , 52° , 76° and 93° , respectively (Alper et al., 2010). In addition, the (110), (200), (211) peaks of BCC phase were observed at 2θ of 45° , 65° , 84° . However, hexagonal close packed (HCP) phase was also observed for Co₈₉-Fe₁₁ film with the appearance of (002), (101) and (112) peaks approximately at 2θ of 44° , 47° and 93° (Manhabosco and Muller, 2008). The XRD spectrum of Co₁₀₀ film is similar to HCP Co phase, whereas Co₉₄-Fe₆ showed mixture of HCP Co and FCC Co-Fe phases. Figure 5.5 presents FCC, BCC and HCP Bravais lattices which were found in Co-Fe

nanostructured alloy films. The crystallographic structure and phase of the deposits was changed according to the composition of the alloy films which correspond to the Co-Fe phase diagram produced by Ellis and Grenier as shown in Figure 2.10 (Martin, 1999). The crystal structure and phase obtained from XRD patterns are similar to equilibrium crystal structure as illustrated in Table 2.4.

The full width at half maximum (FWHM) of the peak at 2θ of about 45° was used to calculate crystallite size of the alloy films (Table 5.2) by using Debye Scherrer's equation. The Co_{100} and $\text{Co}_{94}\text{-Fe}_6$ films show broader FWHM, indicating that the crystallite sizes were smaller. The crystallite sizes of Co_{100} and $\text{Co}_{94}\text{-Fe}_6$ were approximately 11 nm and 10 nm, respectively. These samples are expected to be in the single domain region as discussed in Figure 2.6. In addition, the crystallite sizes of $\text{Co}_{89}\text{-Fe}_{11}$, $\text{Co}_{86}\text{-Fe}_{14}$ and $\text{Co}_{82}\text{-Fe}_{18}$ films were larger, in the range of 85 nm to 99 nm. The crystallite sizes for all the as-deposited films were larger than superparamagnetic limit of Co-Fe.

Table 5.2:
Crystallite structure, phases and sizes of as-synthesized Co-Fe nanocrystalline alloy films

Sample	Crystal Structure	Phase	(hkl)	2θ ($^\circ$)	FWHM ($^\circ$) $\Delta 2\theta$	Crystallite size (nm)
Co_{100}	HCP	ε	(002)	44.65	0.900	11
$\text{Co}_{94}\text{-Fe}_6$	HCP+FCC	$\varepsilon + \gamma$	(002)	44.20	1.000	10
$\text{Co}_{89}\text{-Fe}_{11}$	HCP+FCC+BCC	$\varepsilon + \gamma + \alpha$	(110)	45.30	0.236	99
$\text{Co}_{86}\text{-Fe}_{14}$	BCC+FCC	$\gamma + \alpha$	(110)	45.30	0.236	99
$\text{Co}_{82}\text{-Fe}_{18}$	BCC+FCC	$\gamma + \alpha$	(110)	45.20	0.250	85

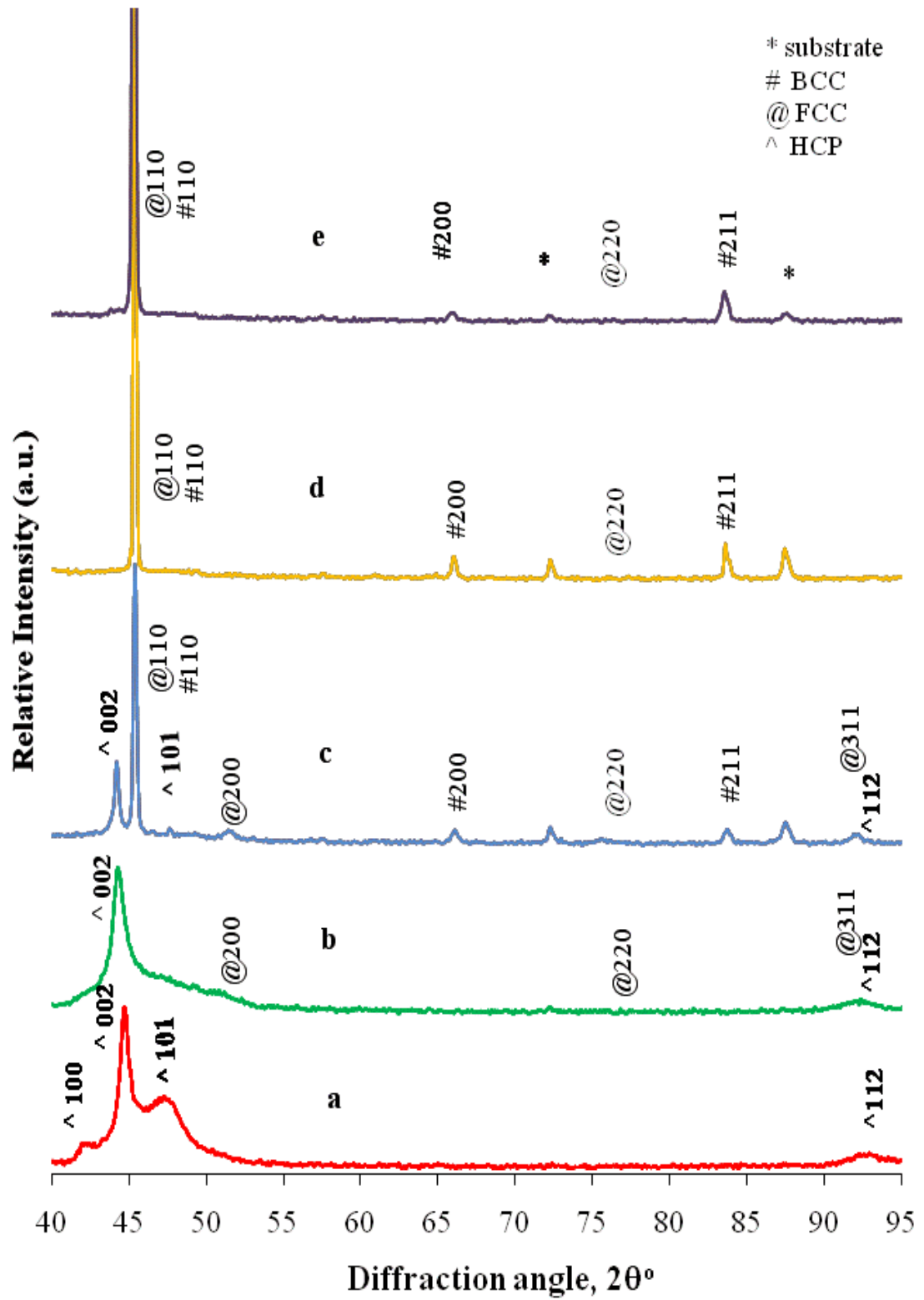


Figure 5.4:
X-ray diffraction (XRD) patterns of as-synthesized nanostructured Co-Fe thin films at various compositions: (a) Co_{100} , (b) $\text{Co}_{94}\text{-Fe}_6$, (c) $\text{Co}_{89}\text{-Fe}_{11}$, (d) $\text{Co}_{86}\text{-Fe}_{14}$ and (e) $\text{Co}_{82}\text{-Fe}_{18}$

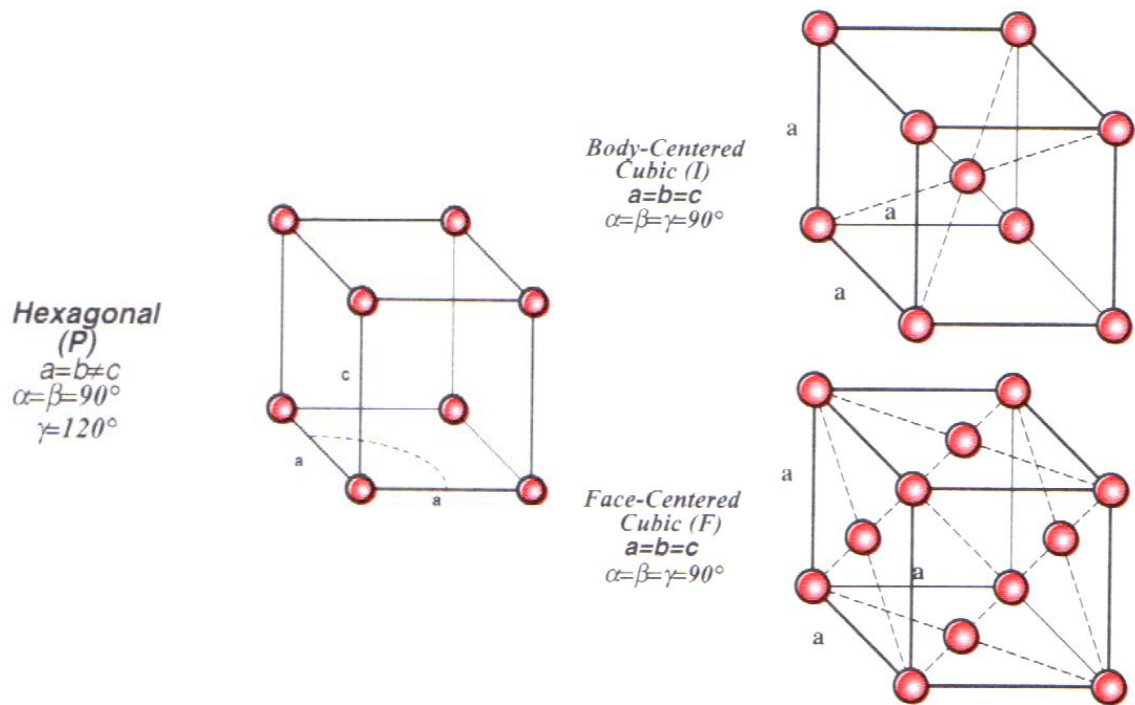


Figure 5.5:
The face centered cubic (FCC), body centered cubic (BCC) and hexagonal closed packed (HCP) Bravais lattices.

5.1.4 Surface Morphology and Film Thickness

Figure 5.6 shows the scanning electron microscopy (SEM) images of the as-deposited Co-Fe films at various compositions. Co₁₀₀ film showed the formation of smooth ripple surface deposits whereas Co₉₄-Fe₆ film revealed the random distribution of fresh nuclei and growth over the brass surface causing incomplete granule formation. The Co₈₉-Fe₁₁, Co₈₆-Fe₁₄ and Co₈₂-Fe₁₈ thin films exhibited irregular shaped granules in the form of clusters. These granules were made up of a number of crystallites because the crystallite sizes estimated from XRD were much smaller than the size of granules as shown in Table 5.3 (Teh, 2009). Crystallites or grains in a polycrystalline material are

generally found to be distributed in many different orientations (Suryanarayana and Norton, 1998).

Figure 5.7 shows cross-sectional SEM images of Co-Fe films. The films are relatively thick and the growth of grains were not visible clearly. The thicknesses of the films were determined from the cross-sectional view by using SEM measurements as shown in Table 5.3. The Co₁₀₀ and Co₈₂-Fe₁₈ films were detached from the substrates after cross-section. This is due to mechanical stress caused by bending of substrate during resin encapsulation, grinding and polishing process at cross sectioning.

Table 5.3:
Structural and magnetic results of as-synthesized Co-Fe thin films

Thin Film	Film thickness [μm]	Granules Size [μm]	Roughness (RMS), [nm]	Magnetic Force [a.u.]	M_s [emu/g]	H_c [Oe]
Co ₁₀₀	51.5	ND	21.4	25.3	182.3	13.9
Co ₉₄ -Fe ₆	53.4	ND	22.9	40.6	292.3	15.5
Co ₈₉ -Fe ₁₁	62.7	1.5	570.8	189.4	1617	48.2
Co ₈₆ -Fe ₁₄	54.7	5.9	897.0	256.2	1592	46.6
Co ₈₂ -Fe ₁₈	45.7	6.6	534.1	125.9	1649	51.5

Note: ND (Non-detectable). The granules size of the samples Co₁₀₀ and Co₉₄-Fe₆ were not measured because the formation of granules are not obvious.

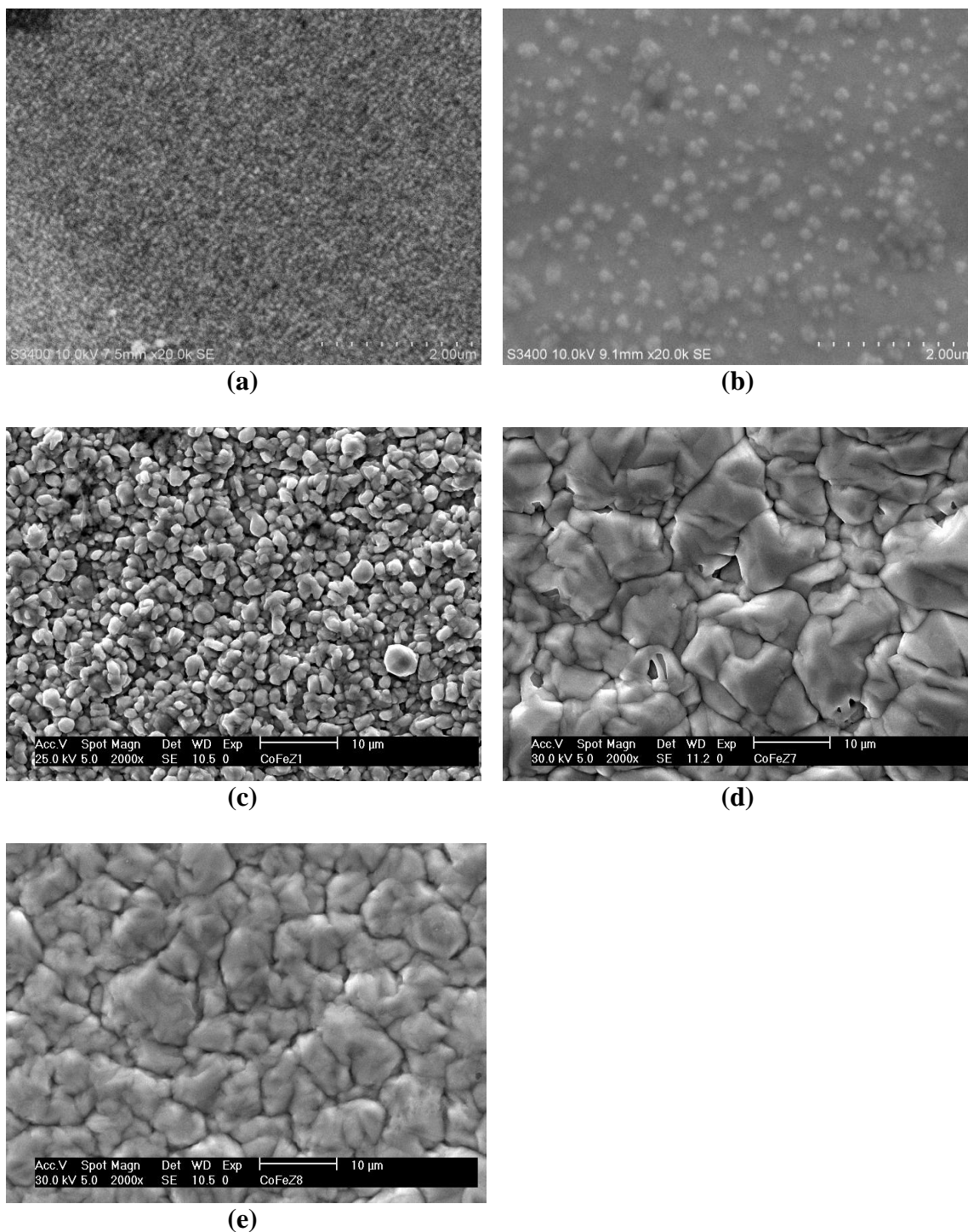


Figure 5.6:
Scanning electron microscopy (SEM) images of as-synthesized nanocrystalline films: (a) Co_{100} and (b) $\text{Co}_{94}\text{-Fe}_6$ (at 20000x magnification); (c) $\text{Co}_{89}\text{-Fe}_{11}$, (d) $\text{Co}_{86}\text{-Fe}_{14}$ and (e) $\text{Co}_{82}\text{-Fe}_{18}$ (at 2000x magnification)

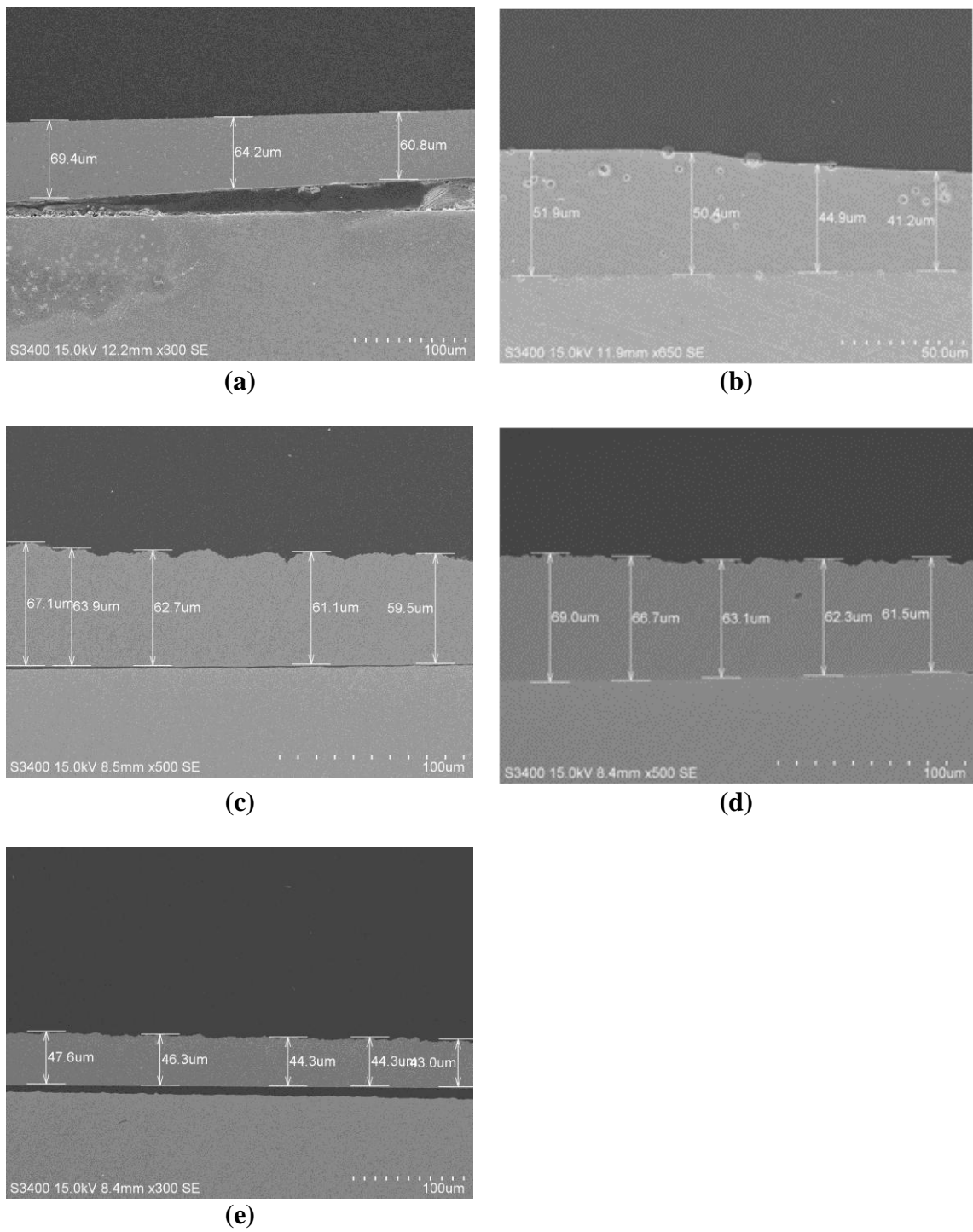
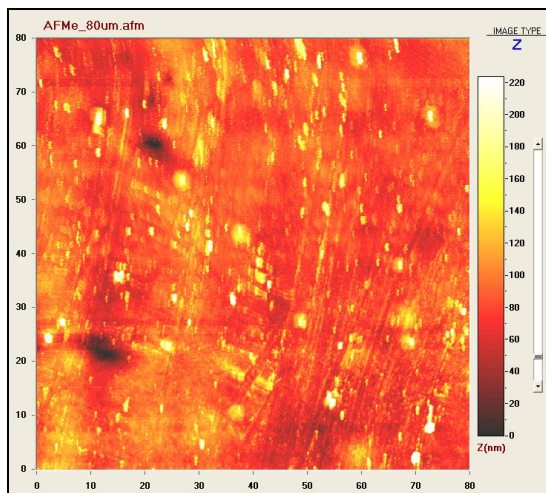


Figure 5.7:
Cross-sectional scanning electron microscopy (SEM) images of (a) Co_{100} , (b) $\text{Co}_{94}\text{-Fe}_6$,
(c) $\text{Co}_{89}\text{-Fe}_{11}$, (d) $\text{Co}_{86}\text{-Fe}_{14}$ and (e) $\text{Co}_{82}\text{-Fe}_{18}$ alloy films

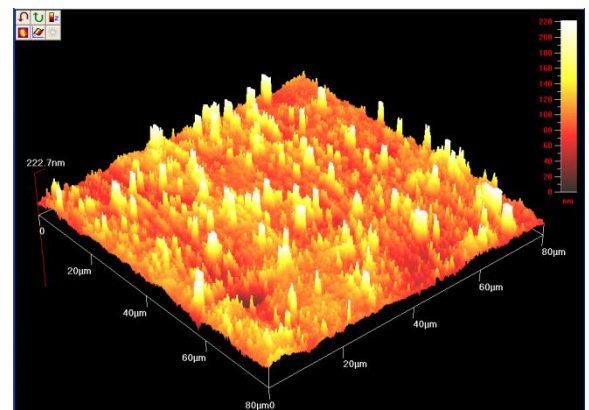
5.1.5 Surface Roughness and Magnetic Force

Figures 5.8 and 5.9 represent the atomic force microscopy (AFM) images and magnetic force microscopy (MFM) domain structure of as-deposited Co-Fe films at various compositions. Co₈₉-Fe₁₁, Co₈₆-Fe₁₄ and Co₈₂-Fe₁₈ showed rougher surfaces with granular morphologies. The Co₁₀₀ and Co₉₄-Fe₆ films showed smoother surface. Similar results were observed during SEM inspections. In general, magnetic domains within a grain are separated by Bloch walls (Vollath, 2008) as shown in Figure 5.10. It is important to note that the existence of magnetic domains and Bloch walls helps to change the direction of magnetization. For most of the ferromagnetic materials, the specimen remains magnetized to some extent after the removal of an external magnetic field. The bright color represents higher signal of magnetic properties in the sample (Teh and Yaccob, 2011b).

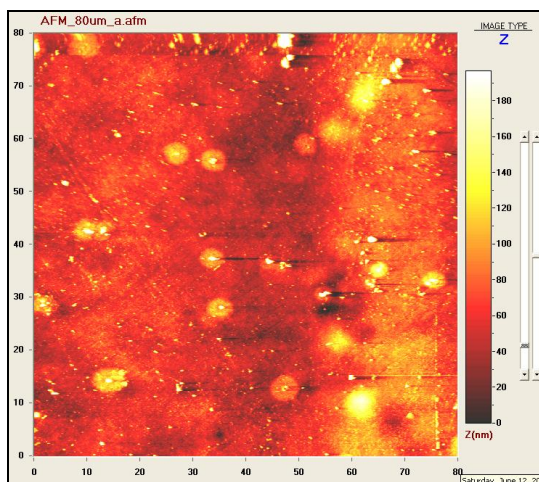
It was observed that there is a correlation between the magnetic force and surface topography for Co₈₉-Fe₁₁, Co₈₆-Fe₁₄ and Co₈₂-Fe₁₈ films. The magnetic force was increased with increasing surface roughness, granule size and clusters of the films. Co₁₀₀ and Co₉₄-Fe₆ films showed magnetic force microscopy (MFM) stripe structure which indicates lower magnetic force. These results are in agreement with the saturation magnetization (M_s) and coercivity (H_c) values as shown in Table 5.3. This regular striped domain structure has been attributed to the averaging of crystal anisotropy energy according to the random anisotropy model and presence of internal stress (Martin, 1999). These domains are possibly in the order of nanoscale, indicating existence of one domain per grain as predicted by single domain theory (Martin, 1999).



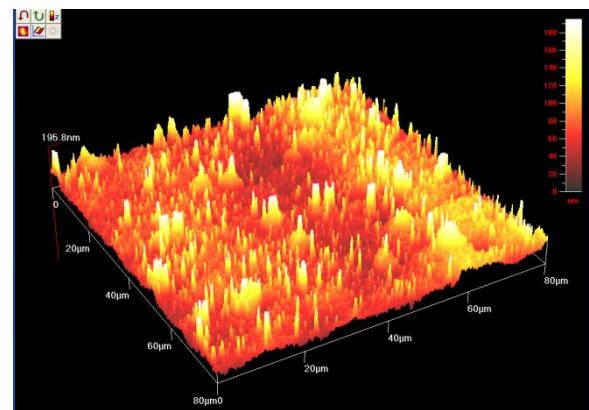
(a)i



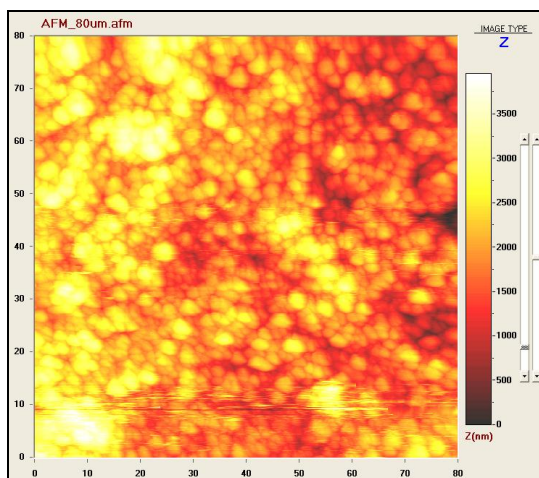
(a)ii



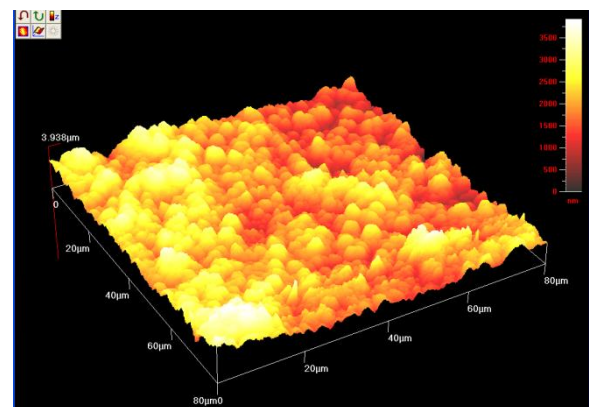
(b)i



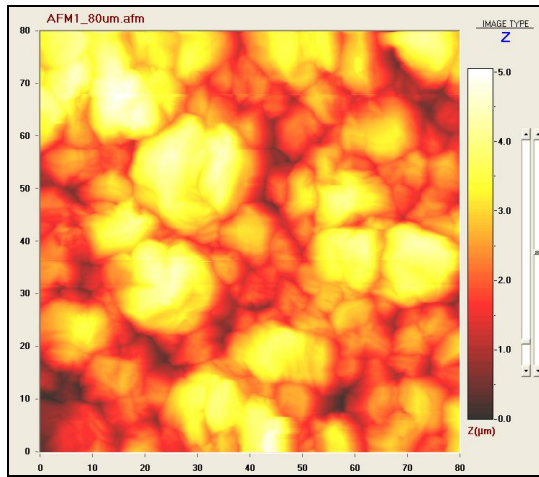
(b)ii



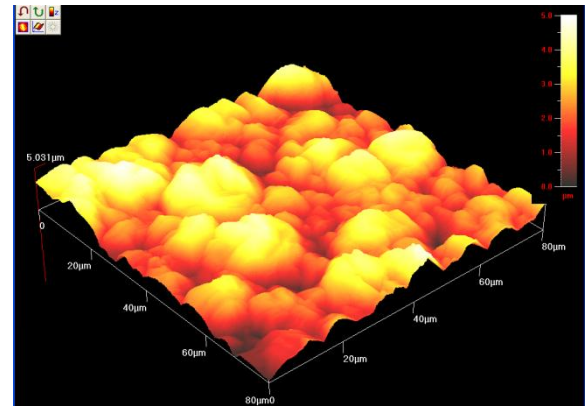
(c)i



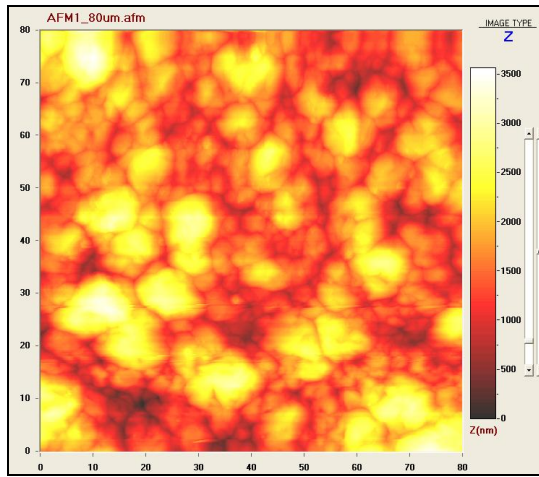
(c)ii



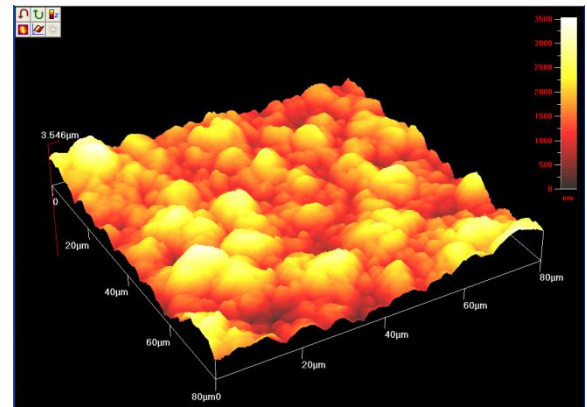
(d)i



(d)ii

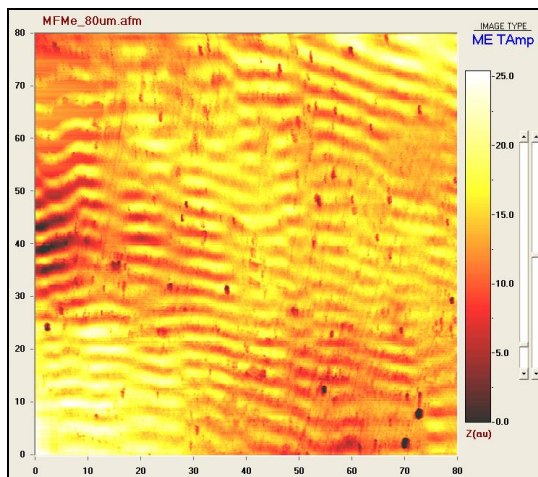


(e)i

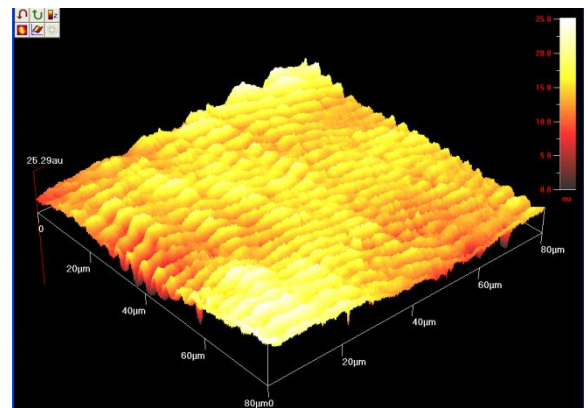


(e)ii

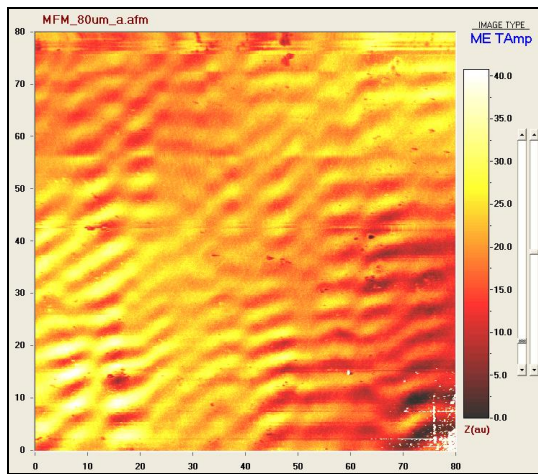
Figure 5.8:
2-D atomic force microscopy (AFM) images (i) and 3-D topographic images (ii) of as-synthesized films: (a) Co_{100} , (b) $\text{Co}_{94}\text{-Fe}_6$, (c) $\text{Co}_{89}\text{-Fe}_{11}$, (d) $\text{Co}_{86}\text{-Fe}_{14}$ and (e) $\text{Co}_{82}\text{-Fe}_{18}$



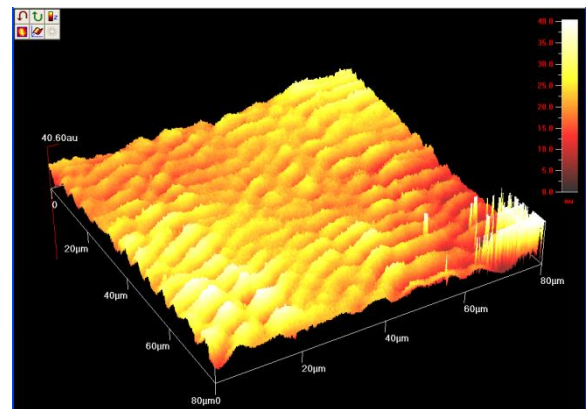
(a)i



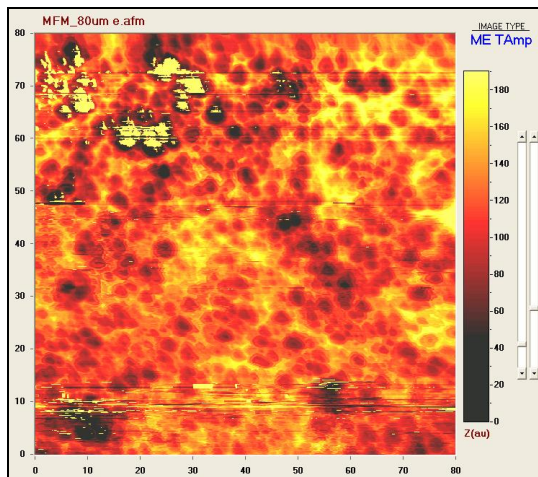
(a)ii



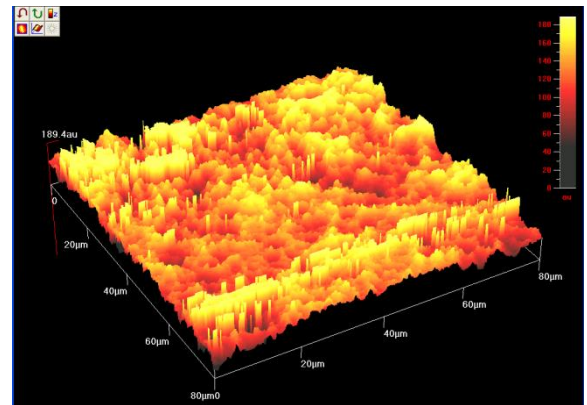
(b)i



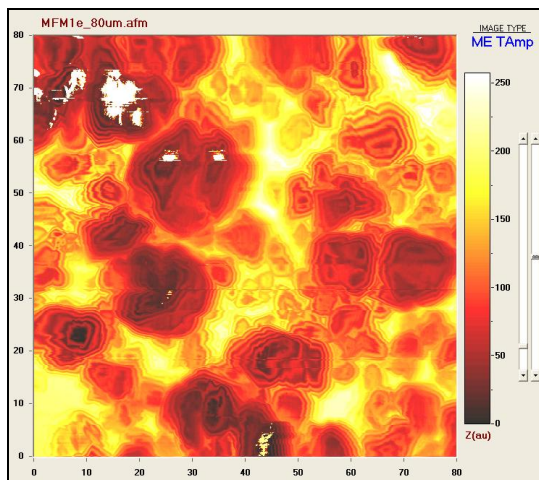
(b)ii



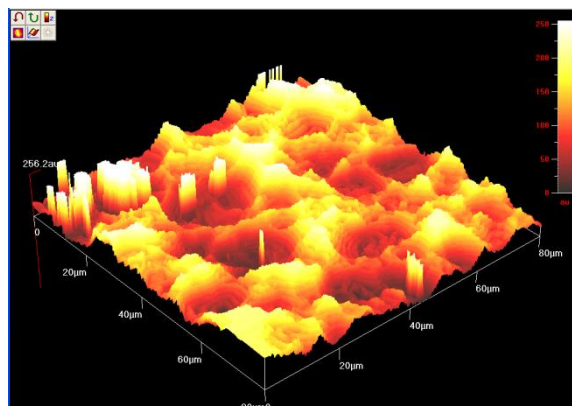
(c)i



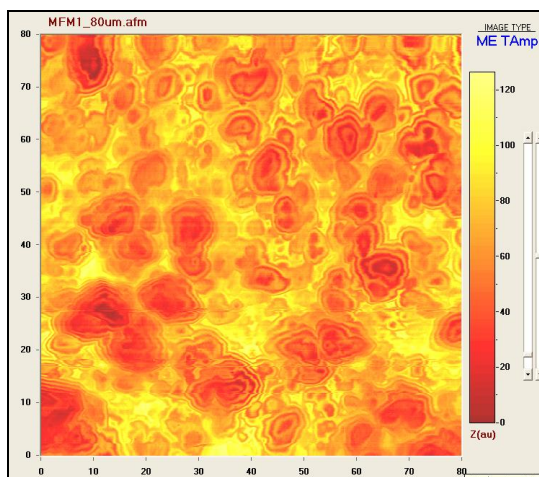
(c)ii



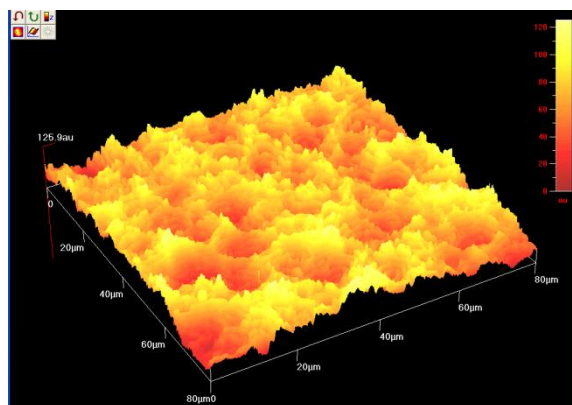
(d)i



(d)ii



(e)i



(e)ii

Figure 5.9:
2-D magnetic force microscopy (MFM) images (i) and 3-D topographic images (ii) of as-synthesized films: (a) Co_{100} , (b) $\text{Co}_{94}\text{-Fe}_6$, (c) $\text{Co}_{89}\text{-Fe}_{11}$, (d) $\text{Co}_{86}\text{-Fe}_{14}$ and (e) $\text{Co}_{82}\text{-Fe}_{18}$

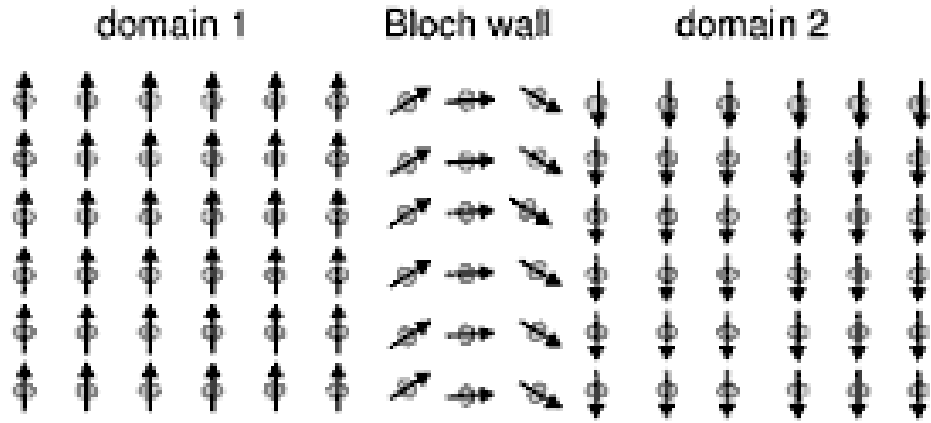


Figure 5.10:
Separation of magnetic domains in ferromagnetic materials by *Bloch* walls

5.1.6 Magnetic Properties

Figure 5.11 shows typical hysteresis curves of as-synthesized Co-Fe thin films. It was observed that the increase of saturation magnetization (M_s) of these films was correlated with the crystal structure or phases of the films. The saturation magnetization (M_s) and coercivity (H_c) value of as-synthesized Co₈₉-Fe₁₁, Co₈₆-Fe₁₄ and Co₈₂-Fe₁₈ films were increased dramatically compared with Co₁₀₀ and Co₉₄-Fe₆ films. This was shown by wider hysteresis loops as well as higher M_s value. The reason of higher M_s value is possibly due to the co-existence of both BCC and FCC Co-Fe phases (Liu et al., 2000) and the presence of irregular granules in the Co-Fe alloy films. Alper et. al. (2010) reported that M_s values are affected by the change of the FCC to BCC ratio caused by the variation of the Co content. In addition, larger granule sizes usually result in increase of H_c value (Yokoshima et al., 2004). Co₁₀₀ film shows the lowest H_c value of 13.9 Oe.

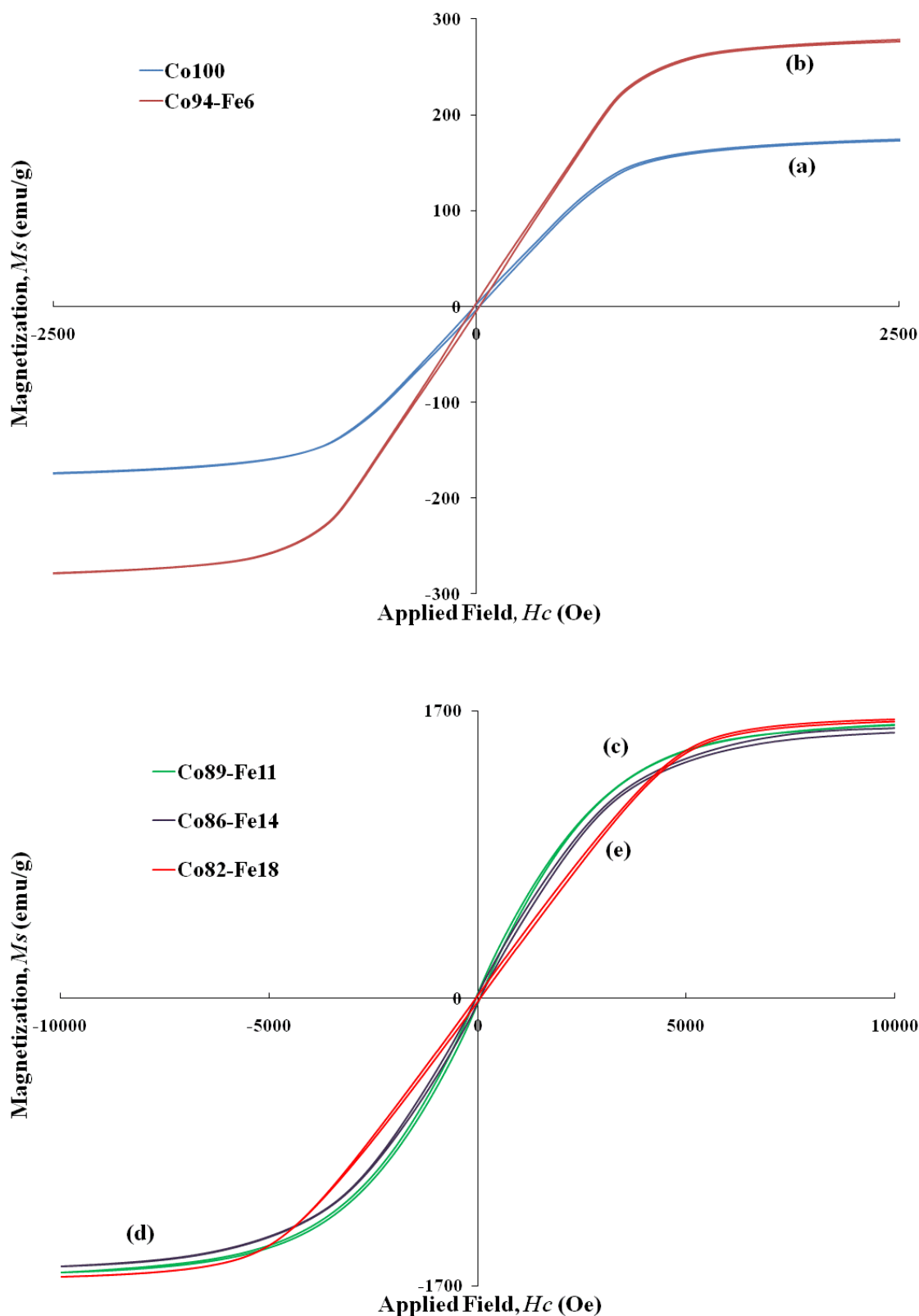


Figure 5.11:

Typical parallel hysteresis curves at room temperature of as-synthesized nanocrystalline thin films: (a) Co_{100} , (b) $\text{Co}_{94}\text{-Fe}_6$, (c) $\text{Co}_{89}\text{-Fe}_{11}$, (d) $\text{Co}_{86}\text{-Fe}_{14}$ and (e) $\text{Co}_{82}\text{-Fe}_{18}$. *Note: Hysteresis curves of sample (a) and (b) are shown from -2500Oe to + 2500Oe to emphasis the differences of H_c and M_s values of the samples.*

5.1.7 Summary

Co-Fe thin films with various compositions successfully prepared by electrodeposition technique using sulfate based electrolytes containing sodium saccharin. Crystallite sizes were calculated from the peak broadening of XRD pattern and thus were in nanometer dimensions. The Co-Fe nanocrystalline thin films showed the best soft magnetic properties when a mixture of BCC and FCC crystal phases were present. In addition, it was found that the magnetization values were higher when the crystallite and granule sizes were larger.

5.2 Cobalt-Platinum Nanocrystalline Films

5.2.1 Physical Appearance

Figure 5.12 shows the physical appearance of as-synthesized nanocrystalline Co-Pt binary alloy films. It is observed that the physical appearance of the electrodeposits depends on the composition of the electrolytic bath. The films deposited with lower concentration of Co ions were dark grey in color.

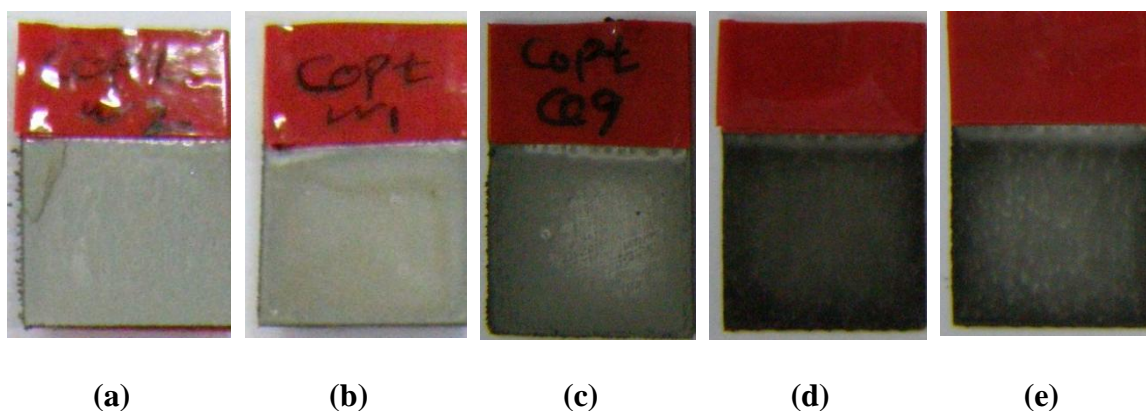
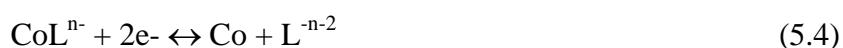


Figure 5.12:
Physical appearance of as-synthesized nanocrystalline thin films: (a) Co₉₇-Pt₃, (b) Co₉₅-Pt₅, (c) Co₈₆-Pt₁₄, (d) Co₅₆-Pt₄₄ and (e) Co₄₃-Pt₅₇

5.2.2 Chemical Composition

Figure 5.13 shows the energy dispersive X-ray spectroscopy (EDS) spectra of Co₉₇-Pt₃ and Co₄₃-Pt₅₇ films. It is clearly seen that EDS spectra of Co₄₃-Pt₅₇ film showed more Pt peaks compared with the Co₉₇-Pt₃ film, indicating higher Pt content in Co₄₃-Pt₅₇ films. The atomic percentages of Co and Pt electrodeposited with current densities of 2000Am⁻² and 3000Am⁻² are shown in the Table 5.5. The as-synthesized films which were electrodeposited at 3000Am⁻² were labeled according to their Co and Pt atomic percentage and were then subjected for further characterizations. Co-Pt films with alloy composition ranging from 43 to 97 at. % of Co were successfully prepared by adjusting

the metal ions ratio in the plating bath. In general, deposition of Co was increased with increasing concentration of CoCl_2 and ammonium tartrate in the electrolyte solution. The $\text{Co}_{95}\text{-Pt}_5$ and $\text{Co}_{97}\text{-Pt}_3$ films showed high concentration of Co which indicates high deposition rate of Co. This was resulted from saturated amount of Co ions and Co complex tartrates in the electrolyte solutions. Platinum, on the other hand, was electrodeposited from complex PtCl_6^{2-} ions in two consecutive steps (5.1) and (5.2). The deposition of Co is shown in equations (5.3) and (5.4).



where L represents the complex tartrates.

Table 5.4:
The atomic percentage of Co in the as-deposited films at current density of 2000Am^{-2} and 3000Am^{-2}

Plating Bath	Concentration (M)			Composition		Thin film
	CoCl_2 [M]	H_2PtCl_6 [M]	$(\text{NH}_4)_2\text{C}_4\text{H}_4\text{O}_6$ [M]	Co [at.%] at 2000Am^{-2}	Co [at.%] at 3000Am^{-2}	
1	0.045	0.005	0.09	96.43	97.36	$\text{Co}_{97}\text{-Pt}_3$
2	0.035	0.015	0.07	94.36	94.70	$\text{Co}_{95}\text{-Pt}_5$
3	0.025	0.025	0.05	84.70	86.23	$\text{Co}_{86}\text{-Pt}_{14}$
4	0.015	0.035	0.03	48.39	56.35	$\text{Co}_{56}\text{-Pt}_{44}$
5	0.005	0.045	0.01	34.29	42.56	$\text{Co}_{43}\text{-Pt}_{57}$

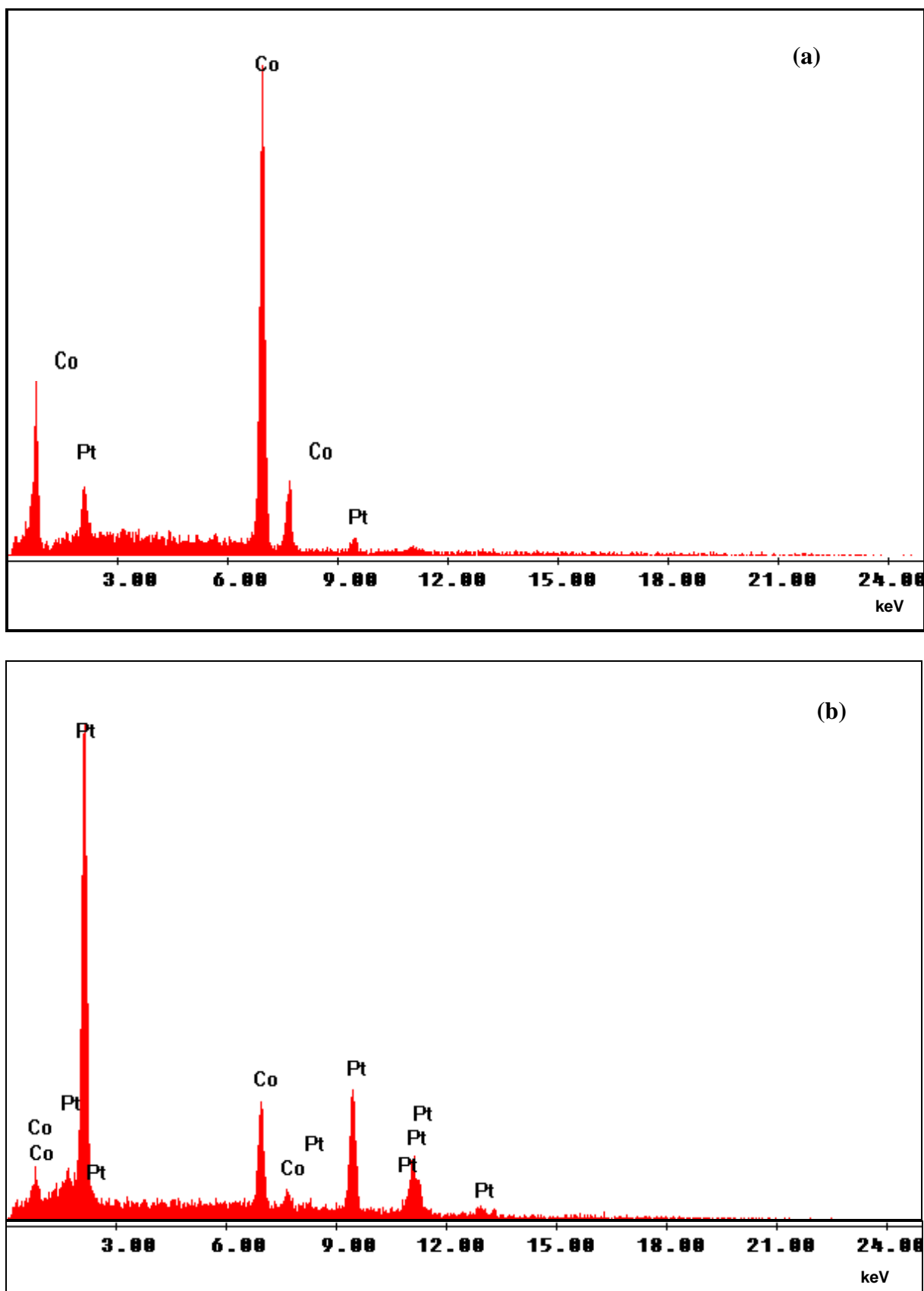


Figure 5.13:
Energy dispersive X-ray spectroscopy (EDS) spectra of as-synthesized nanocrystalline
(a) $\text{Co}_{97}\text{-Pt}_3$ and (b) $\text{Co}_{43}\text{-Pt}_{57}$ films

The standard reduction potentials for reactions (5.1) and (5.2) are +0.68V and +0.73V relative to standard hydrogen electrode (Skoog et al., 1996). The standard equilibrium potential of cobalt is -0.277V (Skoog et al., 1996). This indicates that platinum is more noble than cobalt and therefore Pt is expected to be deposited preferentially. However, anomalous co-deposition mechanism was observed in present study whereby an electrochemically less noble Co metal deposited preferentially. This is due to addition of ammonium tartrate and ammonia in the plating bath, which promoted the polarization of Co^{2+} and Pt^{4+} (Ge et al., 2007). As a result, the difference between equilibrium electrode potentials of Co and Pt became closer which led to Co and Pt co-deposition. The tartrate complex ions could be attached with Co^{2+} by coordination. The carboxyl group adjacent to hydroxyl groups in tartrate complex ions made them easier to coordinate with the metal ions due to the electron donating effect (Wei et al., 2008). Therefore, cobalt can be obtained by electroreduction of either “pure” Co^{2+} or complexed ions as shown in reactions (5.3) and (5.4).

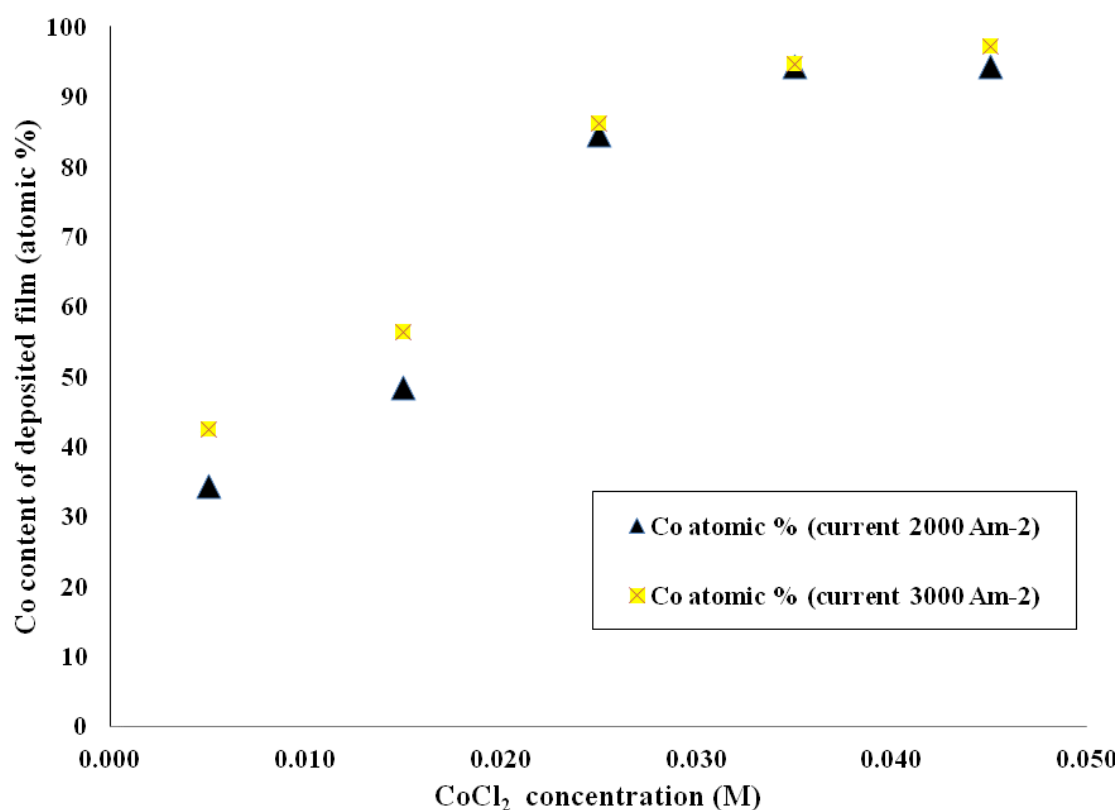


Figure 5.14:
Effect of CoCl_2 concentration in electrolyte solutions on Co content in deposits

In addition, Co content in the as-synthesized films was increased with increasing current density as shown in Figure 5.14. Pt^{4+} ion requires four electrons for Pt deposition. Simultaneously, Co^{2+} ion only requires two electrons to produce Co deposit. Therefore Co deposition rate is faster compared to Pt when more electrons were flowing at higher current density. In addition, elemental mapping of $\text{Co}_{86}\text{-Pt}_{14}$ film scanned by EDS showed that the distribution of Co and Pt elements are homogenous (Figure 5.15).

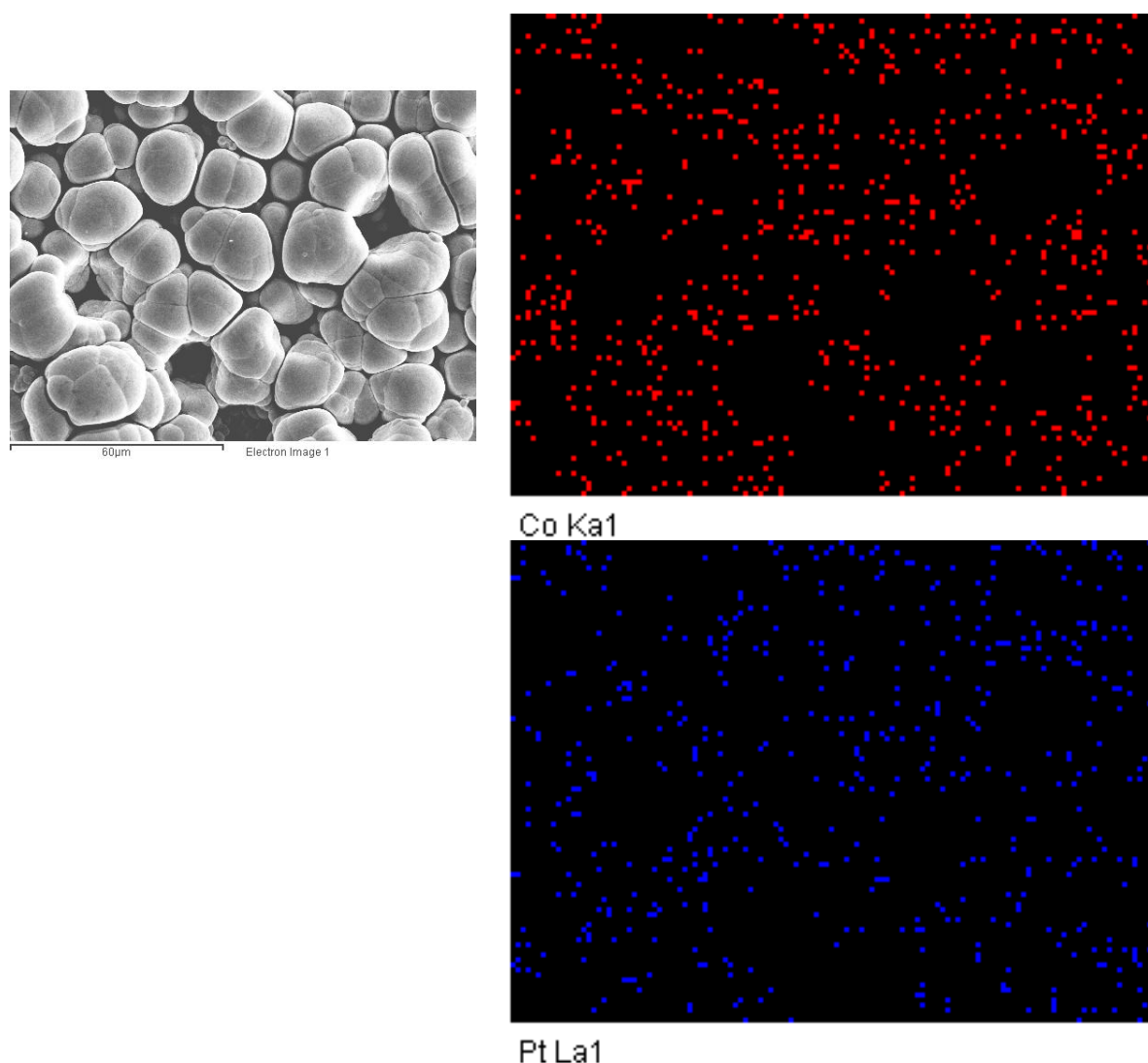


Figure 5.15:
Elemental mapping of as-synthesized $\text{Co}_{86}\text{-Pt}_{14}$ nanocrystalline thin film

5.2.3 X-ray Diffraction Analysis

Figure 5.16 shows the X-ray diffraction (XRD) patterns of the as-synthesized Co-Pt thin films. The CoPt₃ face-centered cubic (FCC) phase (JCPDS 29-0499) was observed for Co₉₇-Pt₃, Co₉₅-Pt₅ and Co₈₆-Pt₁₄ films with the existence of (111), (200), (300) and (222) peaks at 2θ of 40.5°, 47.1°, 73.6° and 87.6°. The XRD spectra of Co₅₆-Pt₄₄ and Co₄₃-Pt₅₇ films showed the formation of CoPt face-centered tetragonal (FCT) phase (JCPDS 29-0498). The peaks from the characteristic (101), (110), (200), (211) crystal planes of Co-Pt FCT structure were observed approximately at 2θ of 41.7°, 47.9°, 70.1° and 85.0° respectively. In fact, it was very difficult to distinguish between CoPt FCT and CoPt₃ FCC phases because of their similarity in XRD patterns. The present results suggest that there were two possible forms of Co-Pt nanocrystals, FCC CoPt₃ and FCT CoPt for the Co-Pt films. Figure 5.17 shows the face centered cubic (FCC) and face centered tetragonal (FCT) Bravais lattices. According to Jeong et al. (2008), the difference between CoPt FCT and CoPt₃ FCC crystal structure could be identified by using XRD θ - 2θ patterns with Co-K α radiation at different χ angles. However, this measurement could not be performed on our equipment since it did not have that capability.

The full width at half maximum (FWHM) of the (101) peak was used to calculate crystallite size using Debye Scherrer's equation. For Co₉₇-Pt₃, Co₉₅-Pt₅ and Co₈₆-Pt₁₄ films, the (300) peak was used to determine the FWHM because of overlapping (111) and (200) peaks. The crystallite sizes of Co₄₃-Pt₅₇, Co₅₆-Pt₄₄, Co₈₆-Pt₁₄, Co₉₅-Pt₅ and Co₉₇-Pt₃ films were 6.3 nm, 4.2 nm, 7.4 nm, 7.8 nm and 6.9 nm, respectively, which were larger than superparamagnetic limit (~3 nm) of Co-Pt. The crystallographic structure and phase of the deposits varied according to the composition of the alloy films which correspond to Co-Pt phase diagram (Nalwa, 2002).

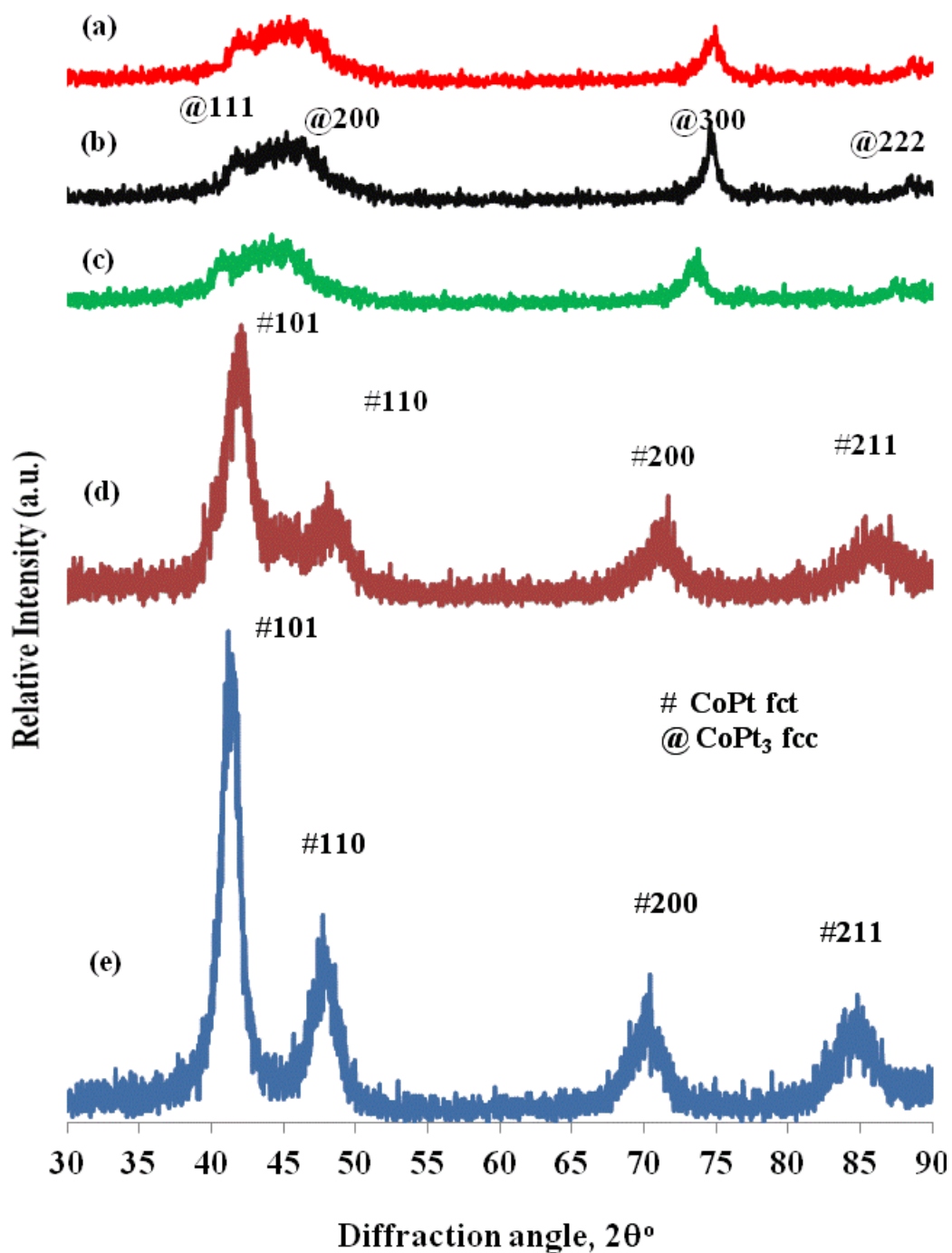


Figure 5.16:
X-ray diffraction (XRD) patterns of as-synthesized nanostructured Co-Pt alloy films: (a) Co₉₇-Pt₃, (b) Co₉₅-Pt₅, (c) Co₈₆-Pt₁₄ (d) Co₅₆-Pt₄₄ and (e) Co₄₃-Pt₅₇

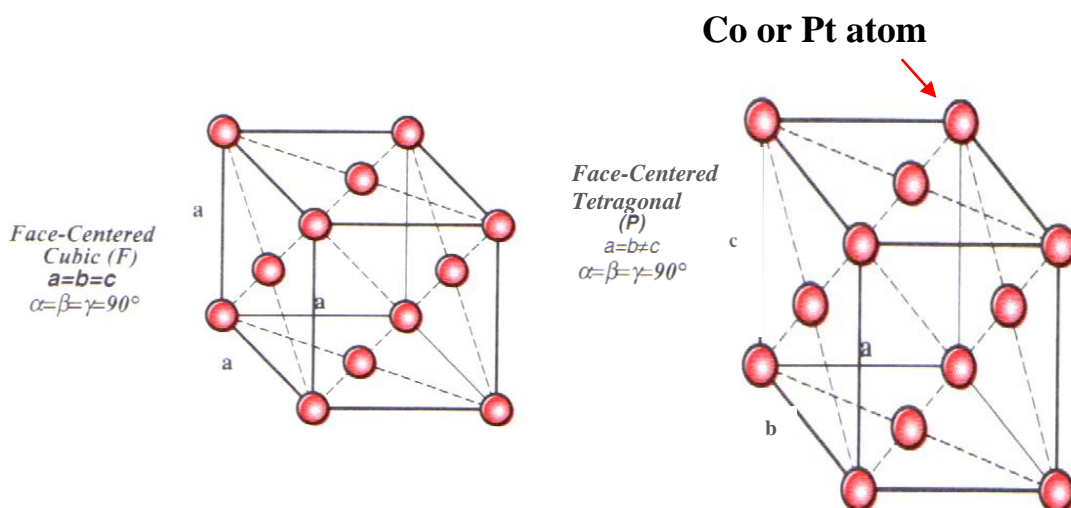


Figure 5.17:
The face centered cubic (FCC) and face centered tetragonal (FCT) Bravais lattices

Table 5.5:
Crystallite structure and sizes of as-synthesized Co-Pt nanocrystalline alloy films

Sample	Crystal Structure	(hkl)	2θ ($^\circ$)	FWHM ($^\circ$) $\Delta 2\theta$	Crystallite size (nm)
Co ₉₇ -Pt ₃	CoPt ₃ fcc	(300)	73.93	1.427	6.9
Co ₉₅ -Pt ₅	CoPt ₃ fcc	(300)	73.68	1.455	7.8
Co ₈₆ -Pt ₁₄	CoPt ₃ fcc	(300)	73.47	1.486	7.4
Co ₅₆ -Pt ₄₄	CoPt fct	(101)	41.80	2.187	4.2
Co ₄₃ -Pt ₅₇	CoPt fct	(101)	41.26	1.488	6.3

5.2.4 Surface Morphology and Film Thickness

Figure 5.18 (a)-(e) shows the scanning electron microscopy (SEM) images of as-deposited Co-Pt films for various alloy compositions. The Co₉₇-Pt₃ (Figure 5.18 (a)) and Co₉₅-Pt₅ (Figure 5.18 (b)) thin films exhibited irregular granule shapes in the form of clusters. The largest granules size of about 10 μm was observed in Co₈₆-Pt₁₄ film (Figure 5.18 (c)). Co₅₆-Pt₄₄ (Figure 5.18 (d)) and Co₄₃-Pt₅₇ (Figure 5.18 (e)) films showed smaller granular morphology and formation of cluster. The crystallite sizes (Table 5.6) estimated from XRD were much smaller than the size of granules (Table 5.7), indicating that the granules are polycrystalline (Teh, 2011). Polycrystalline materials are crystalline with random grain size, shape, and orientational packing (Kazmerski, 1980).

Figure 5.19 shows the cross-sectional SEM images of Co-Pt films. Regardless of the compositions, the growth of the Co-Pt films were observed as tree-shaped with the presence of void. This may be due to the presence of non-conducting phases such as slag particles on the substrate which were not plated and pores were formed as the deposit were bridged over them (Durney, 1996). In addition, low hydrogen overvoltage might produce hydrogen bubbles which may be occluded by the growing deposit or create channels through the deposits as the bubble evolved from the surface (Durney, 1996). The granules were connected to adjacent granules to form a wavy surface demonstrating the grain growth was favored compared to nucleation. The film thicknesses were determined from SEM image (shown in Table 5.7). The granule sizes were increased with increasing film thickness. However, the granules were smaller than the thicknesses of the films.

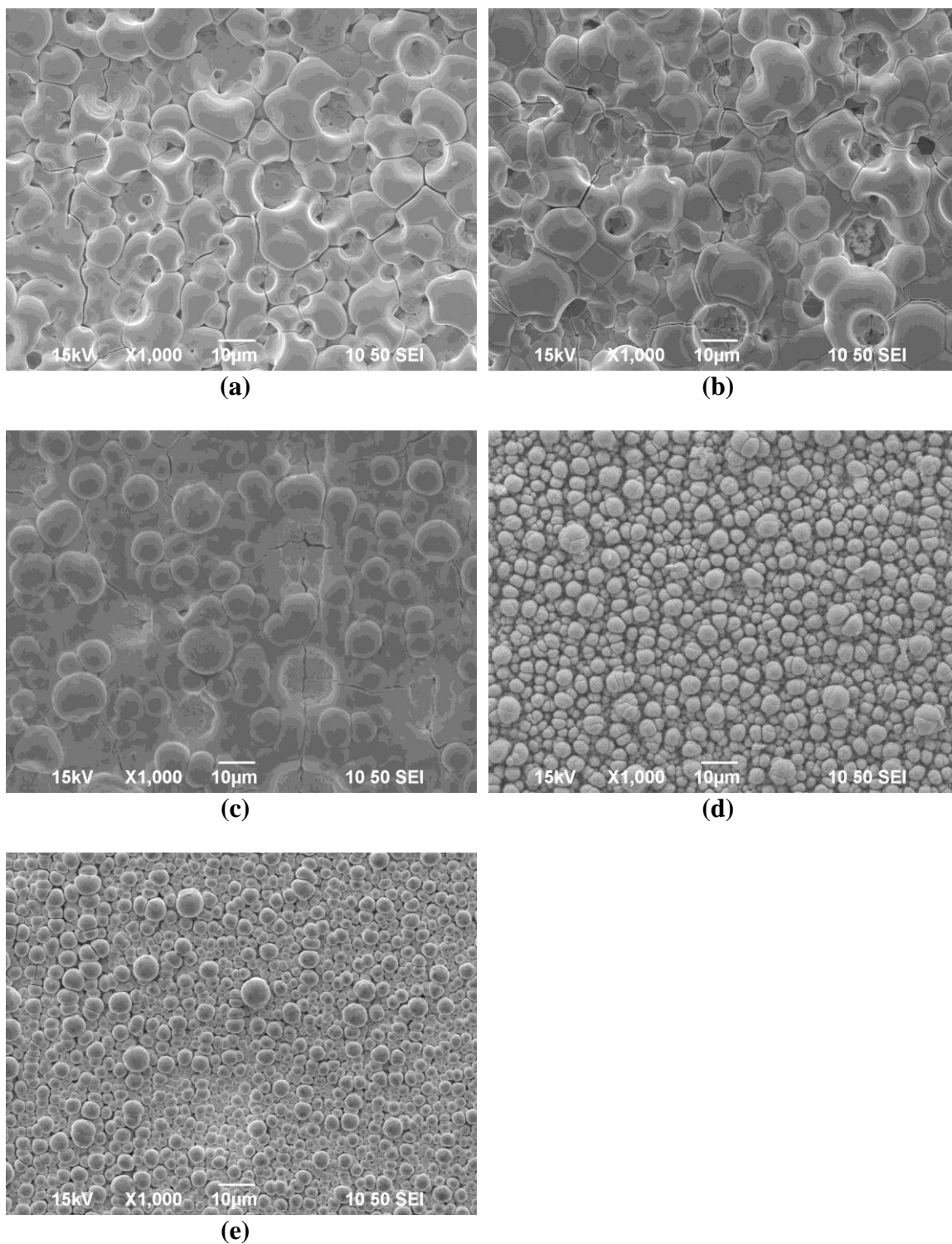


Figure 5.18:
Scanning electron microscopy (SEM) images of as-synthesized nanocrystalline thin films: (a) Co₉₇-Pt₃, (b) Co₉₅-Pt₅, (c) Co₈₆-Pt₁₄, (d) Co₅₆-Pt₄₄ and (e) Co₄₃-Pt₅₇ at 1000x magnification

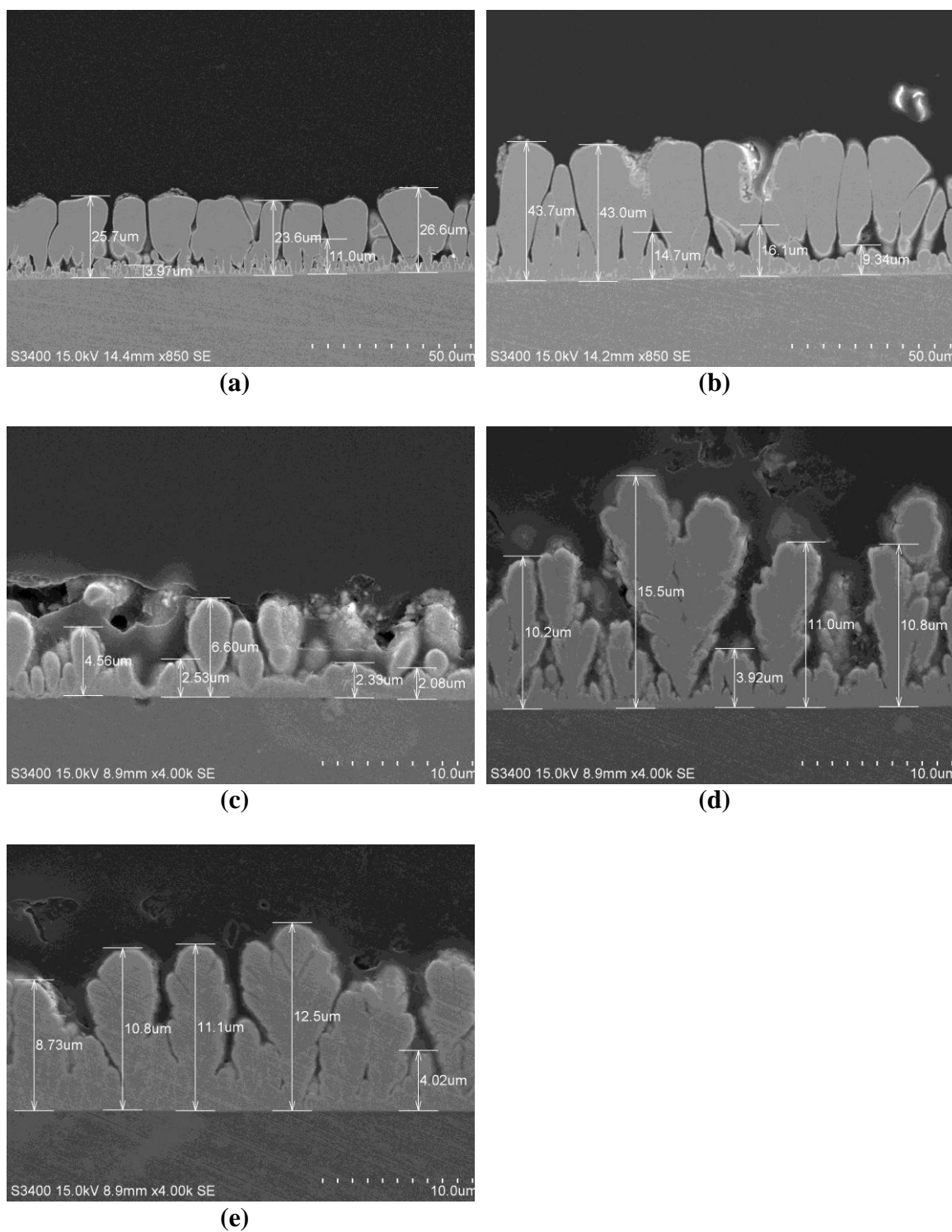


Figure 5.19:

Cross-sectional scanning electron microscopy (SEM) images of as-synthesized nanocrystalline thin films: (a) $\text{Co}_{97}\text{-Pt}_3$, (b) $\text{Co}_{95}\text{-Pt}_5$, (c) $\text{Co}_{86}\text{-Pt}_{14}$, (d) $\text{Co}_{56}\text{-Pt}_{44}$ and (e) $\text{Co}_{43}\text{-Pt}_{57}$

Table 5.6:
Structural and magnetic results of as-synthesized Co-Fe thin films. (ND=Non-detectable)

Thin Film	Film thickness [μm]	Granules Size [μm]	AFM Roughness (RMS) [μm]	IFM Roughness (RMS) [μm]	M_s [emu/g]	H_c [Oe]
Co ₉₇ -Pt ₃	23.4	8.3	0.77	2.10	432.1	64.6
Co ₉₅ -Pt ₅	41.7	10.1	ND	2.71	397.0	122.8
Co ₈₆ -Pt ₁₄	23.7	8.4	1.03	2.62	359.7	118.1
Co ₅₆ -Pt ₄₄	13.5	3.0	0.85	1.01	249.1	172.6
Co ₄₃ -Pt ₅₇	10.6	2.1	0.80	0.88	93.09	126.3

5.2.5 Surface Roughness and Magnetic Force

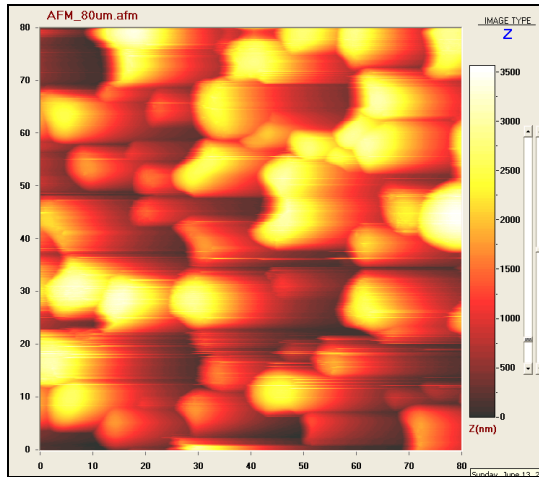
The atomic force microscopy (AFM) and magnetic force microscopy (MFM) (Q Scope) were performed simultaneously. The AFM is force sensitive microscope which generates a direct consequence of the observation of sizable interaction forces between a near field probe and a sample surface (Bhushan et al, 2004). Figure 5.20 shows 2-D AFM images (i) and 3-D images (ii) of Co₉₇-Pt₃, Co₈₆-Pt₁₄, Co₅₆-Pt₄₄ and Co₄₃-Pt₅₇. The AFM is a useful tool which allows investigation and manipulation of surfaces down to atomic scale (Bhushan et al., 2004). The AFM image of Co₈₆-Pt₃₄ film was scanned at smaller surface area of 40 μm x 40 μm because the cantilever was unable to detect the topography of rough surface and large granules at larger surface area. The AFM image of Co₈₆-Pt₃₄ film which was scanned at surface area of 80 μm x 80 μm was unusable as the granules shape was found to be distorted and showed tearing of surface feature (Figure 5.21). It was also worth to note that AFM was not performed on Co₉₅-Pt₅ due to extremely large granule size. All the Co-Pt films (except Co₉₅-Pt₅) showed granular topology. In general, the surface was rougher when the Co content in the deposit was

higher. The cantilever of AFM is capable to detect maximum 8 μm roughness in Z dimension. The surface roughness of the samples captured by AFM are shown in Table 5.7. The maximum surface roughness was found to be about 1 μm which is possibly the upper bound limit of AFM sensitivity. Moreover, it was found that surface roughness was still about 1 μm for larger granular samples, such as $\text{Co}_{86}\text{-Pt}_{14}$ film.

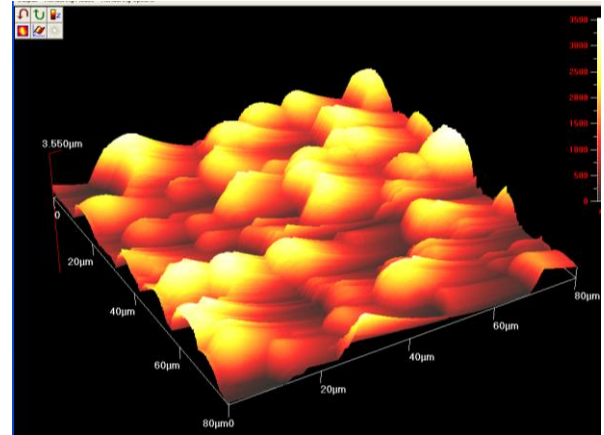
Figure 5.22 (a) shows MFM domain structure in 2-D while Figure 5.22 (b) shows MFM in 3-D of as-deposited $\text{Co}_{43}\text{-Pt}_{57}$ film. The 2-D MFM image shows granular surface morphology. The bright color region represents higher signal of magnetic properties in the sample (Teh, 2011 (b)). The magnetic force was found to be correlated with the granular surface topography. This is due to the increased magnetic force at grain boundary or *bloch* wall. MFM domain structure could only be obtained for $\text{Co}_{43}\text{-Pt}_{57}$ film as this sample has the smallest granule size of 2.1 μm . The MFM images obtained from other film samples revealed that the magnetic cantilever was unable to capture the accurate magnetic force values.

Infinite focus microscopy (IFM) is a fully digital light microscope that allows capturing 2-D and 3-D images of virtually infinite-depth-of-focus for rough surface sample. Since AFM could not be performed accurately for rougher film sample, IFM was utilized to measure the surface roughness of Co-Pt films. Figure 5.22 (c) and (d) shows 2-D and 3-D images obtained from IFM. The surface roughness of $\text{Co}_{43}\text{-Pt}_{57}$ film obtained from AFM was 0.80 μm . The surface roughness measured by IFM showed an almost similar value of 0.88 μm . It was found that the surface roughness obtained from IFM is higher compared to AFM. This is due to the limitation of AFM which can only measure surface roughness up to about 1 μm . Moreover, the cantilever of AFM can be easily damaged if the sample is too rough and hard. Figure 5.23 shows 3-D images which were obtained from IFM in pseudo color for Co-Pt samples. All the samples demonstrated granular structure, which is similar with the SEM and AFM results. The

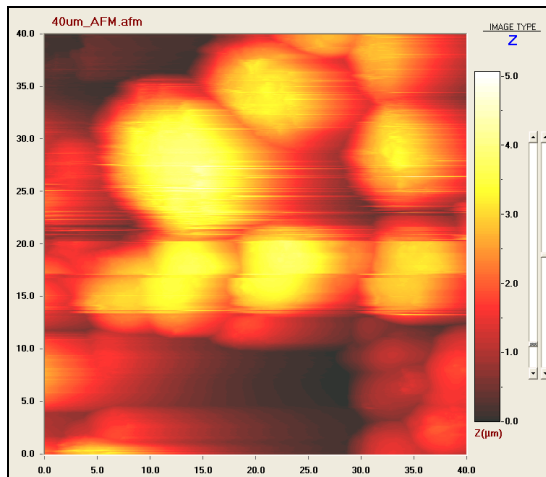
surface roughness was found in agreement with granule sizes, which meant the larger the granules the rougher the sample. Figure 5.24 presents comparison of histogram analysis for the surface roughness of $\text{Co}_{43}\text{-Pt}_{57}$ film obtained from AFM, MFM and IFM, respectively.



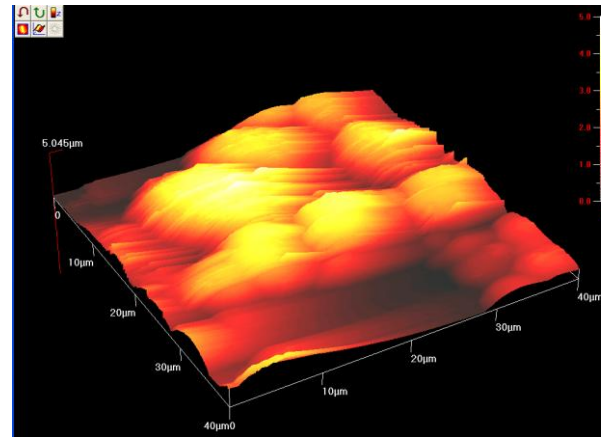
(a) i



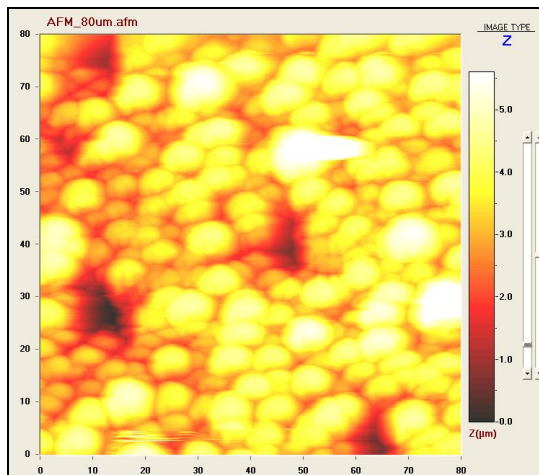
(a) ii



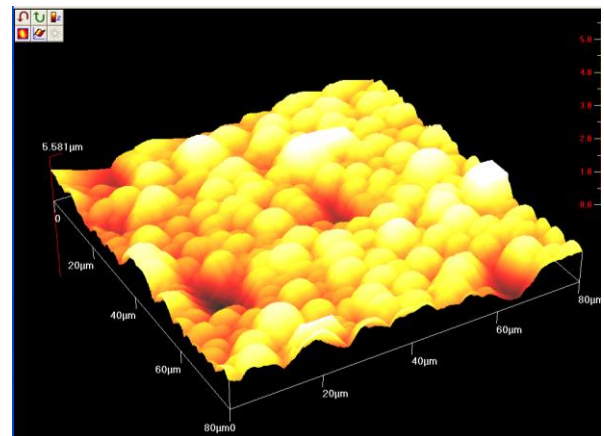
(b) i



(b) ii



(c) i



(c) ii

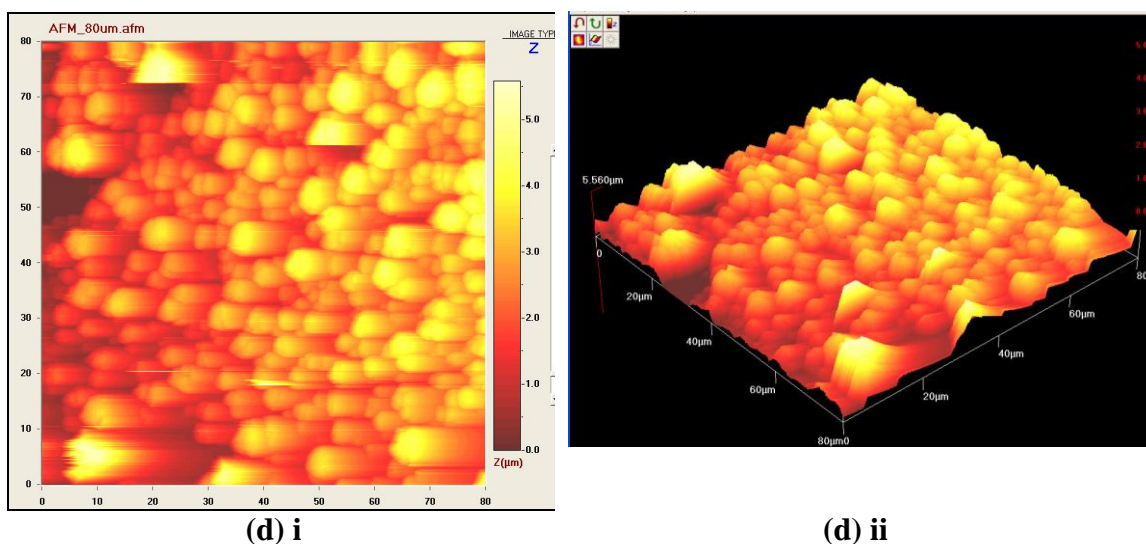


Figure 5.20:

2-D atomic force microscopy (AFM) image (i) and 3-D AFM topographical image (ii) of as-synthesized films: (a) $\text{Co}_{97}\text{-Pt}_3$ (surface area $80\text{ }\mu\text{m} \times 80\text{ }\mu\text{m}$), (b) $\text{Co}_{86}\text{-Pt}_{14}$ (surface area $40\text{ }\mu\text{m} \times 40\text{ }\mu\text{m}$), (c) $\text{Co}_{56}\text{-Pt}_{44}$ (surface area $80\text{ }\mu\text{m} \times 80\text{ }\mu\text{m}$) and (d) $\text{Co}_{43}\text{-Pt}_{57}$ (surface area $80\text{ }\mu\text{m} \times 80\text{ }\mu\text{m}$).

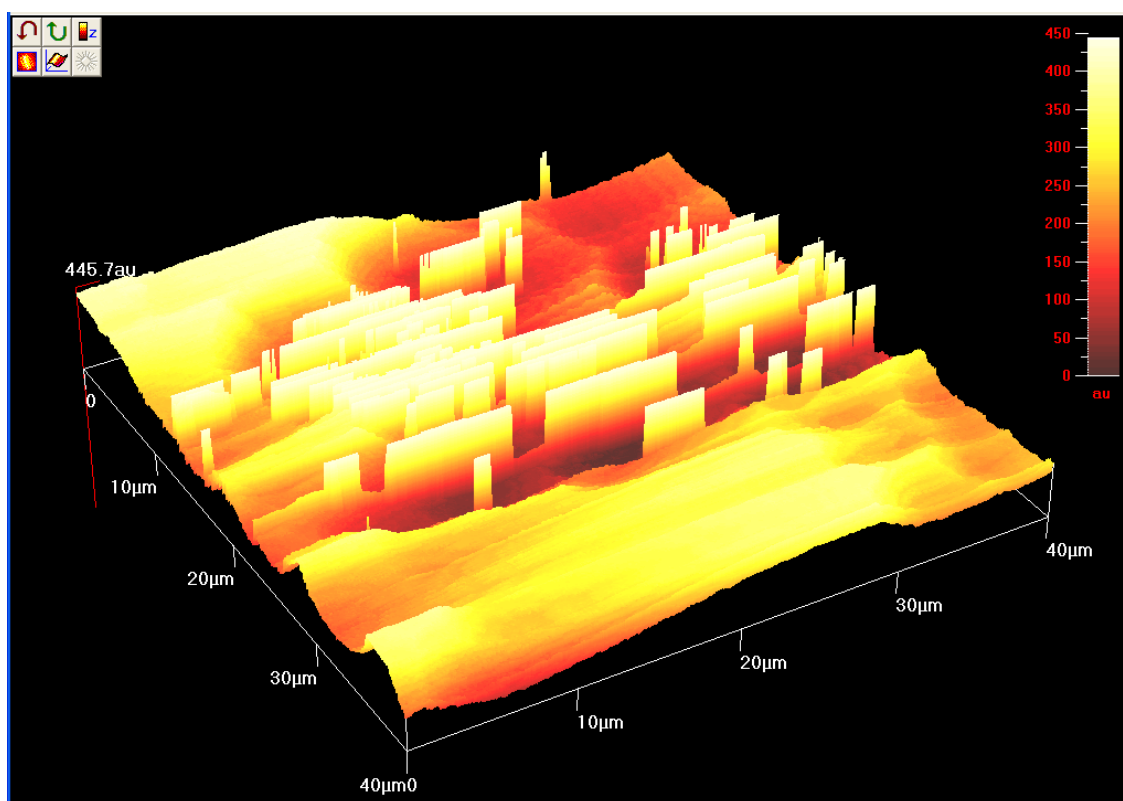


Figure 5.21:

3-D atomic force microscopy (AFM) topographic images of as-synthesized $\text{Co}_{86}\text{-Pt}_{14}$ film at surface area of $80\text{ }\mu\text{m} \times 80\text{ }\mu\text{m}$. The data is unusable as the granules shape was found be distorted and evidence of tearing of surface feature

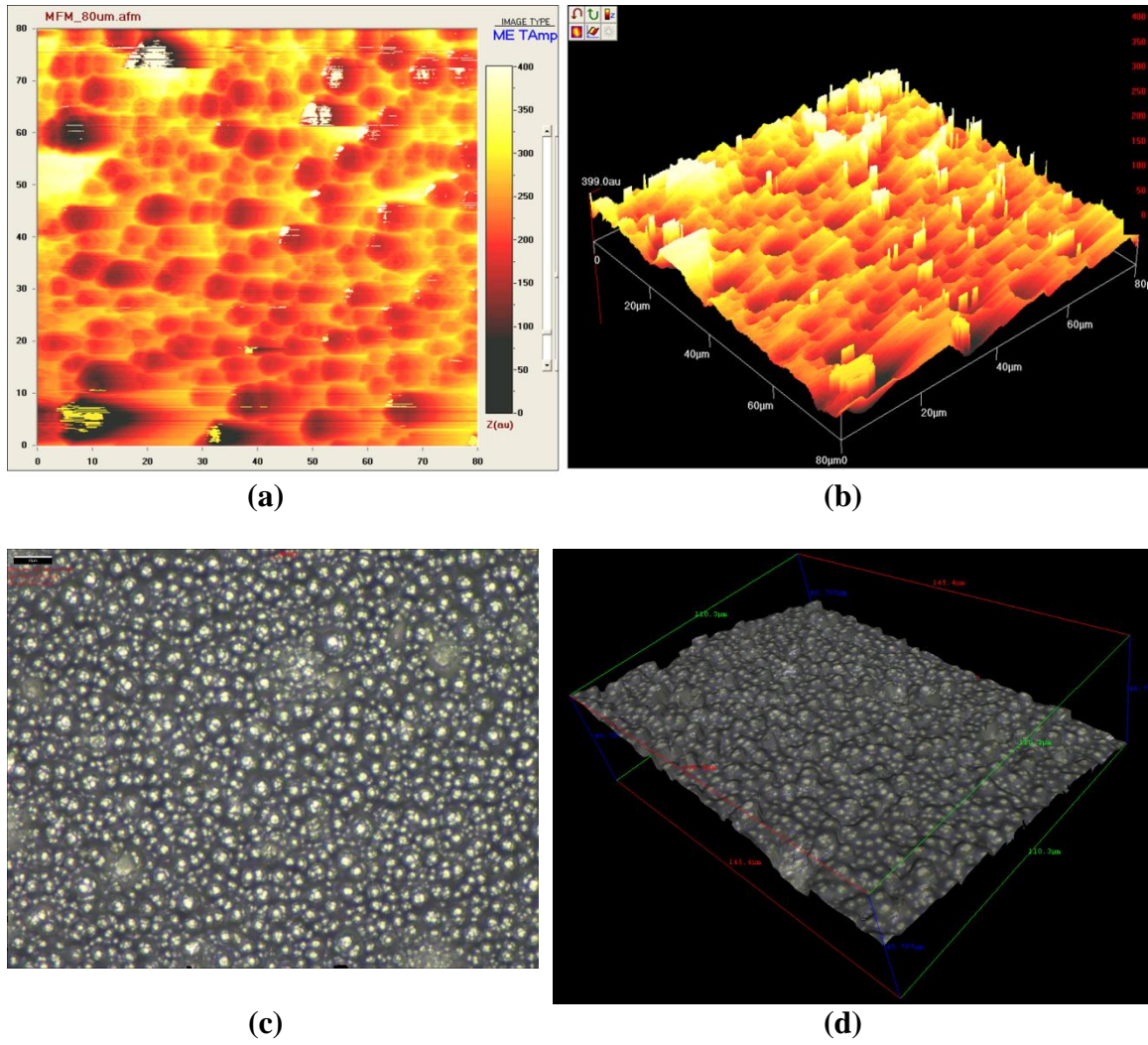
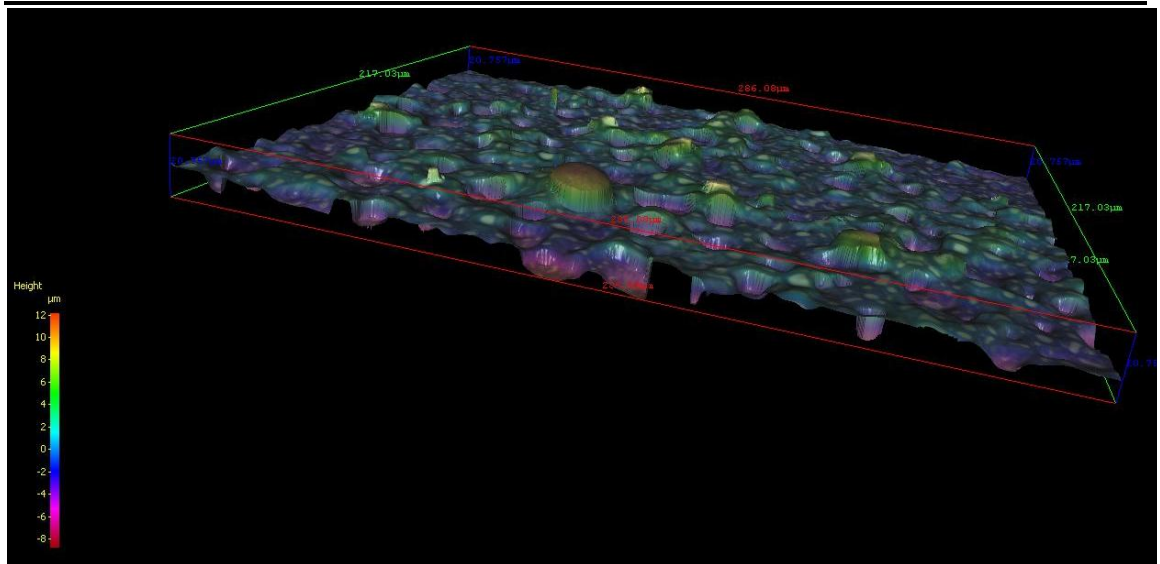
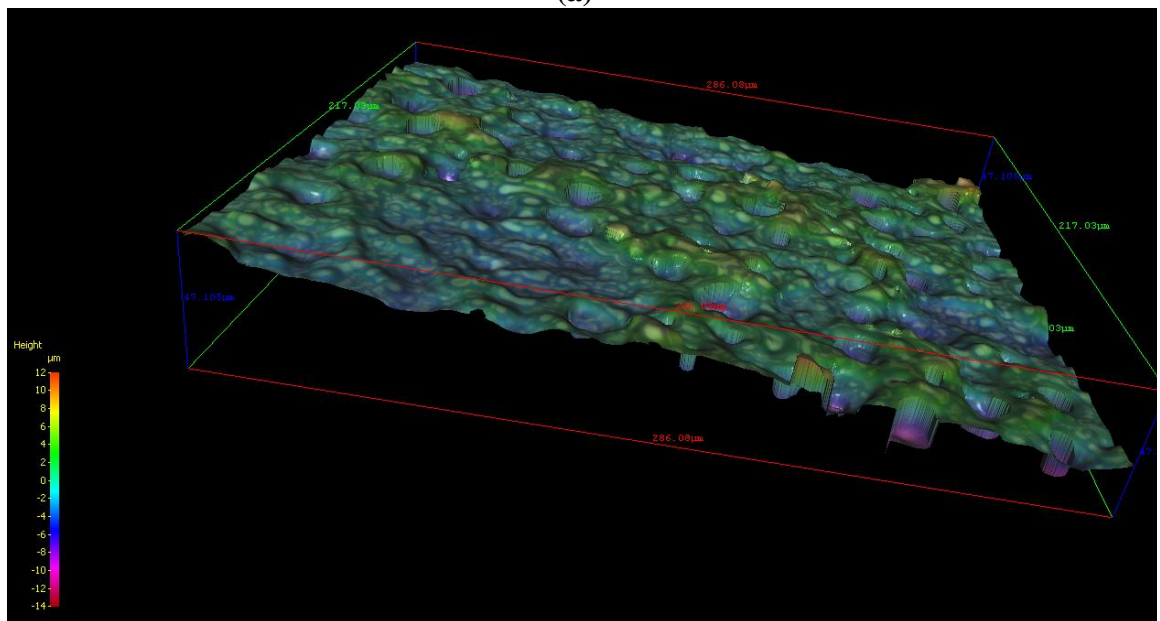


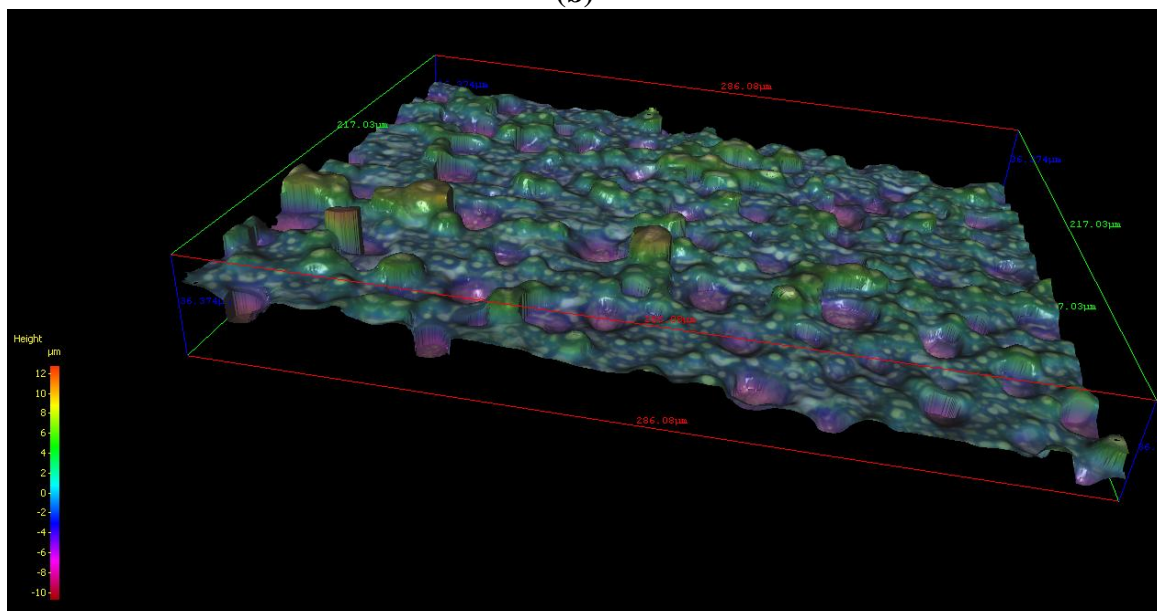
Figure 5.22:
2-D MFM, (b) 3-D MFM, (c) 2-D IFM and (d) 3-D IFM images of as-synthesized nanostructured $\text{Co}_{43}\text{-Pt}_{57}$ thin films. (Note: IFM magnification at 100x)



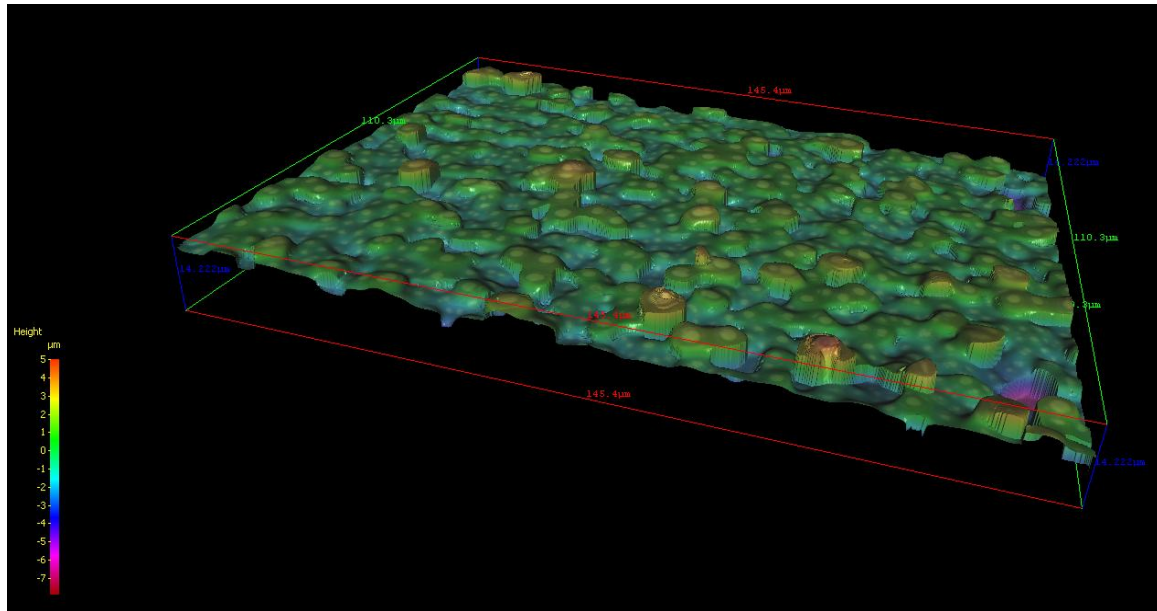
(a)



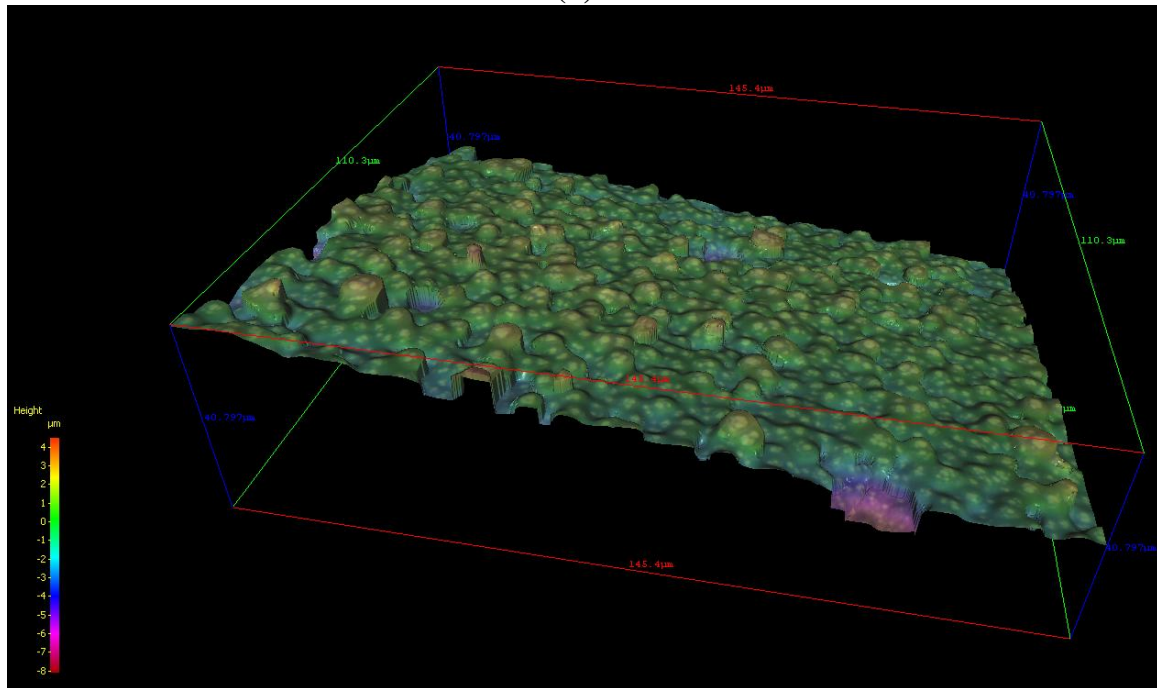
(b)



(c)

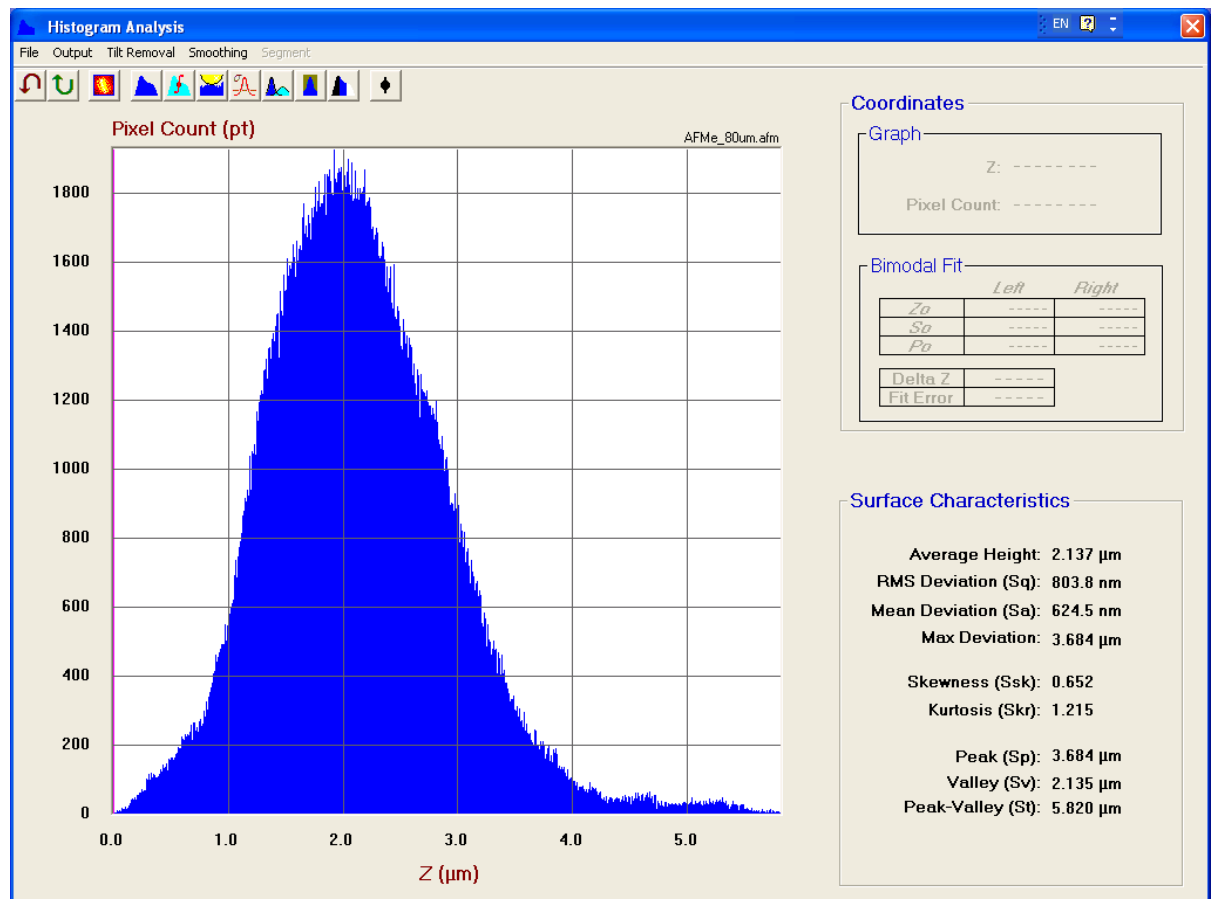


(d)

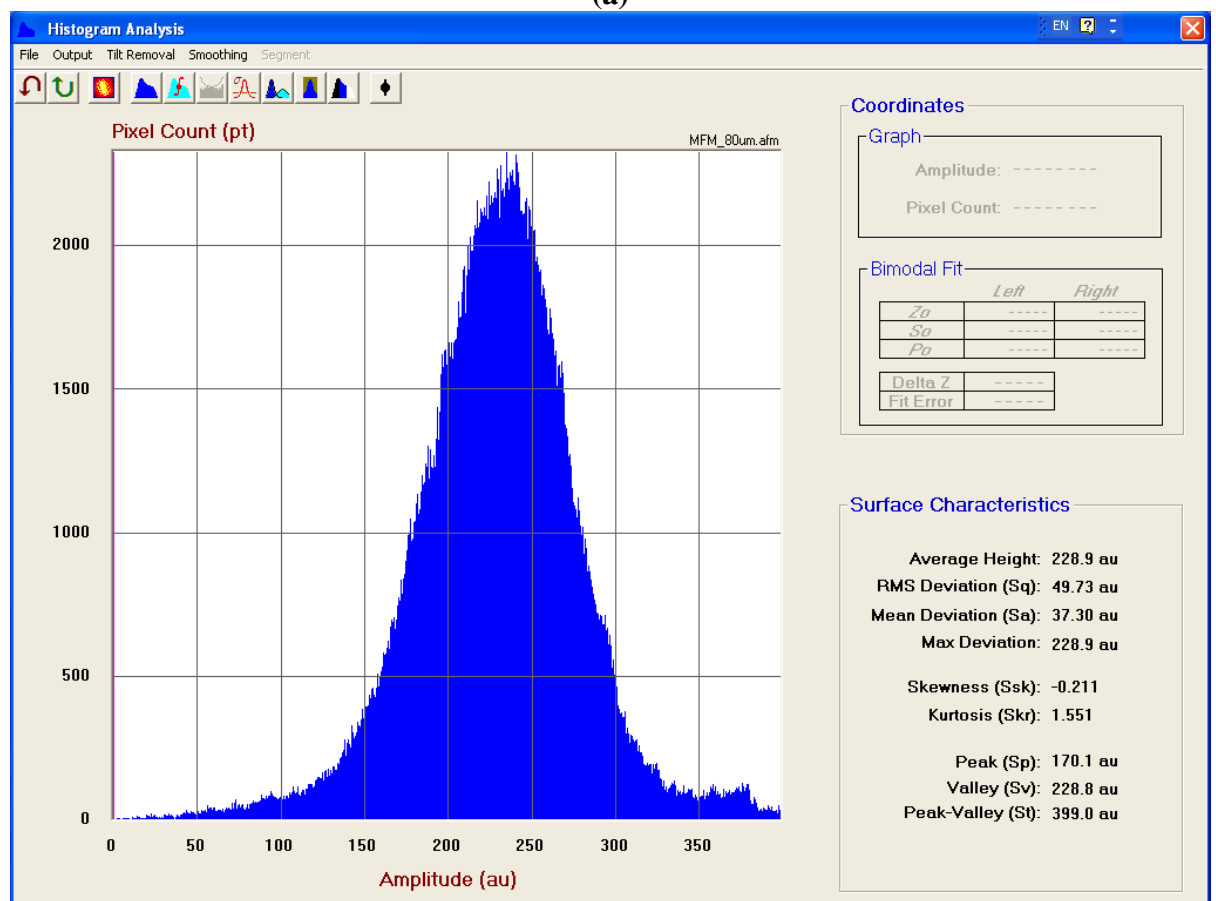


(e)

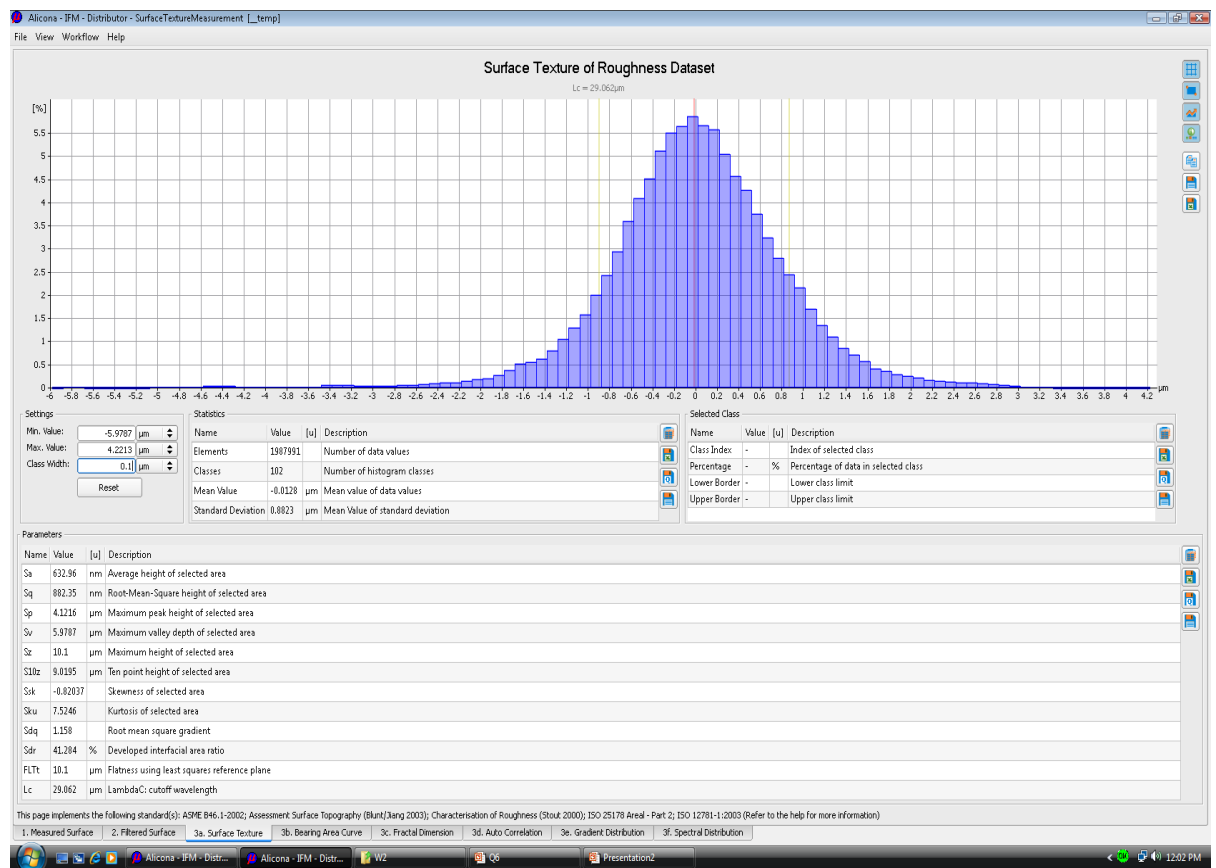
Figure 5.23:
3-D IFM images (in pseudo color) of as-synthesized nanocrystalline thin films: (a) $\text{Co}_{97}\text{-Pt}_3$, (b) $\text{Co}_{95}\text{-Pt}_5$, (c) $\text{Co}_{86}\text{-Pt}_{14}$, (d) $\text{Co}_{56}\text{-Pt}_{44}$ and (e) $\text{Co}_{43}\text{-Pt}_{57}$



(a)



(b)



(c)

Figure 5.24:
Histogram analysis of surface roughness obtained from (a) AFM, (b) MFM and (c) IFM
for as-synthesized nanostructured Co₄₃-Pt₅₇ thin films

5.2.6 Magnetic Properties

Figure 5.25 shows the typical parallel hysteresis curves of as-synthesized Co-Pt thin films. It was observed that the saturation magnetization (M_s) of Co-Pt films increases with increasing Co content in the deposits. It was seen that the obtained M_s values were smaller than those of sputtered films and bulk alloys with similar composition (Pattanaik, 2007). The smaller M_s value was possibly caused by the incorporation of oxygen containing non-magnetic phases in the growing films and the presence of void (Pattanaik, 2007). All the as-deposited films which were most likely consisted of disordered FCC and FCT structures are magnetically soft with coercivity (H_c) values of about 100 Oe (Wang, 2003). Co₅₆-Pt₄₄ film showed the highest H_c value

of 172.6 Oe, possibly due to near-equiatomic ratio of Co and P. This sample also exhibited a wider hysteresis loop.

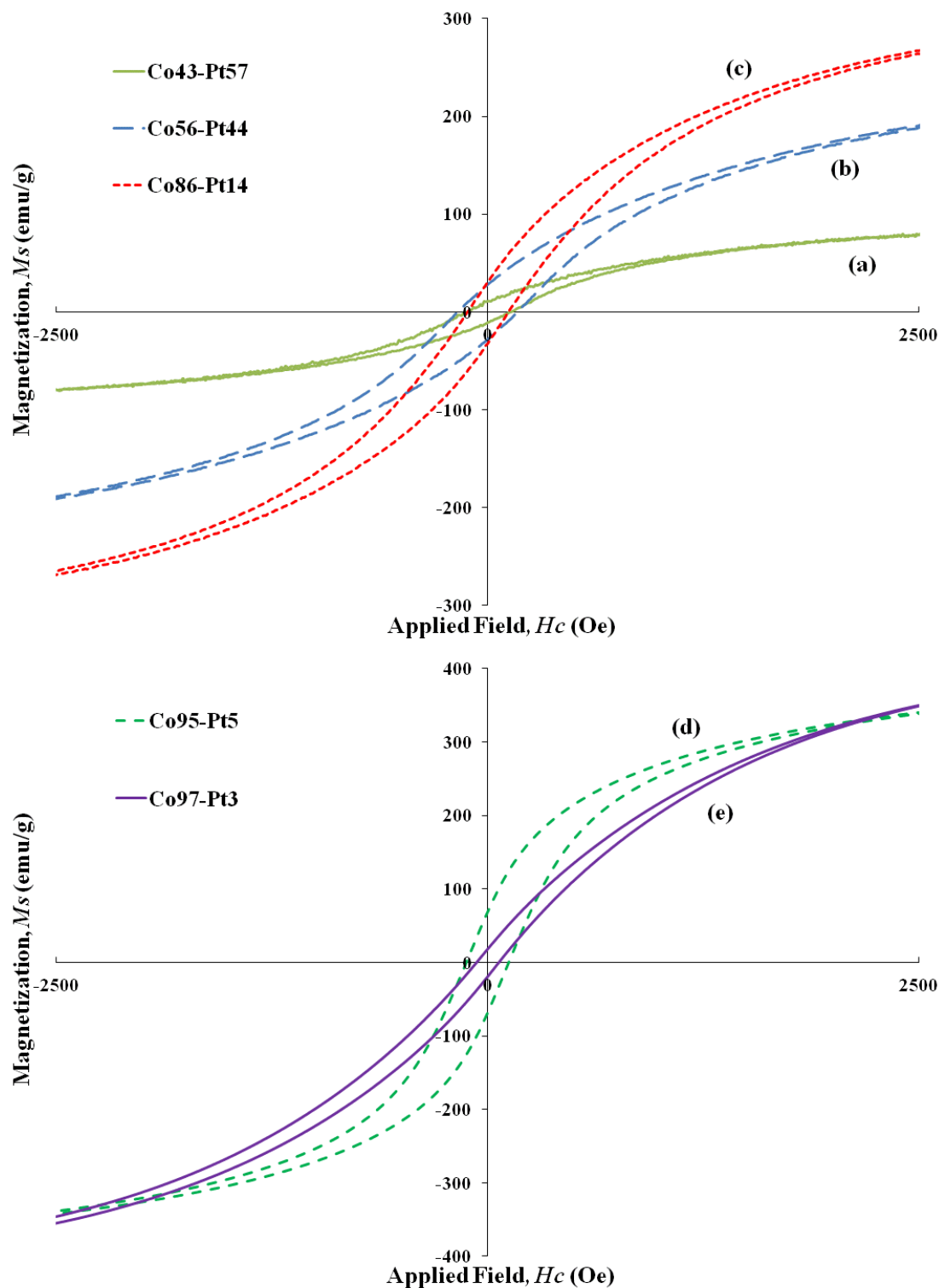


Figure 5.25:

Typical parallel hysteresis curves at room temperature of as-synthesized nanocrystalline thin films: (a) Co₉₇-Pt₃, (b) Co₉₅-Pt₅, (c) Co₈₆-Pt₁₄, (d) Co₅₆-Pt₄₄ and (e) Co₄₃-Pt₅₇. *Note: Hysteresis curves are shown from -2500Oe to + 2500Oe to emphasis the differences of Hc and Ms values of various samples.*

5.2.7 Summary

Cobalt-platinum nanocrystalline alloy thin films with various compositions were successfully electrodeposited on brass substrates. The EDS results revealed that tartrate-alkaline additives assisted the co-deposition of Co and Pt. The fabrication of Co–Pt thin films was controllable by selectively changing the plating bath compositions and deposition parameters. All the as-deposited Co-Pt thin films exhibited soft ferromagnetic characteristic. The compositions of Co-Pt nanostructured alloy films played an important role in their structural and magnetic properties.

5.3 Iron-Platinum and Cobalt-Iron-Platinum Films

5.3.1 Physical Appearance

Figure 5.26 shows physical appearance of as-synthesized nanocrystalline Fe-Pt and Co-Fe-Pt thin films. It is observed that all electrodeposits are grey in color.

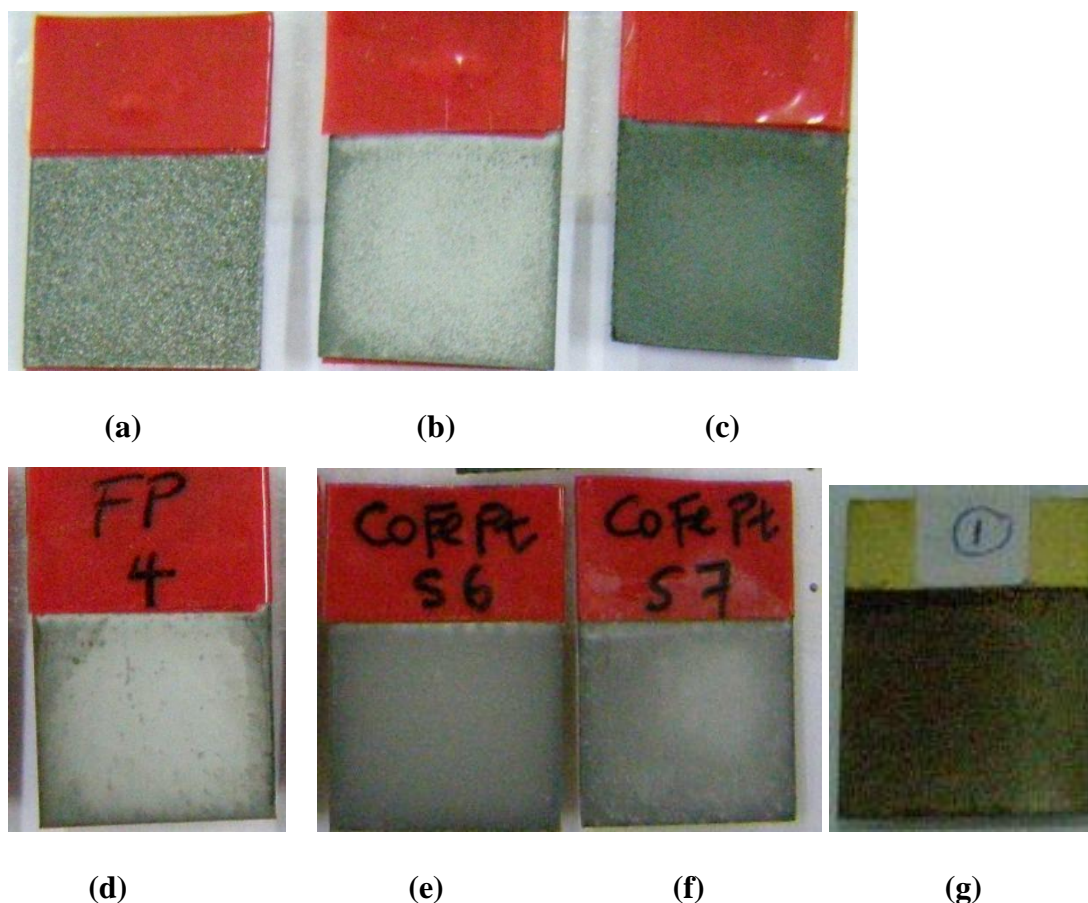


Figure 5.26:

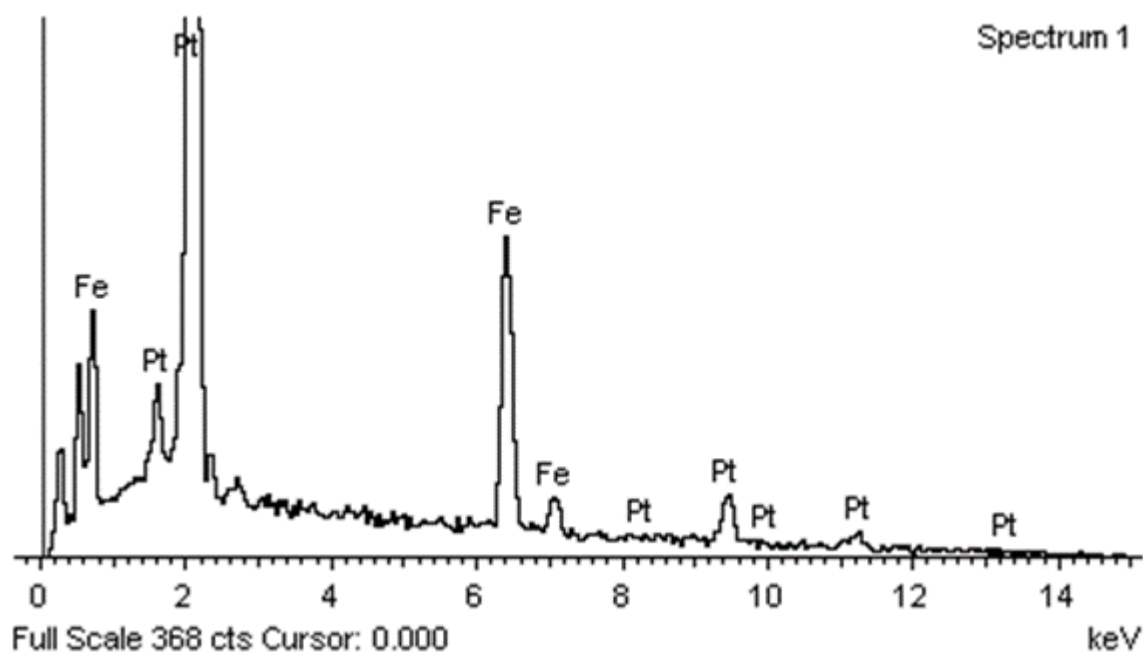
Physical appearance of as-synthesized nanocrystalline thin films: (a) $\text{Fe}_{54}\text{-Pt}_{46}$, (b) $\text{Co}_{15}\text{-Fe}_{18}\text{-Pt}_{67}$, (c) $\text{Co}_{17}\text{-Fe}_{11}\text{-Pt}_{72}$, (d) $\text{Fe}_{70}\text{-Pt}_{30}$, (e) $\text{Co}_{53}\text{-Fe}_8\text{-Pt}_{39}$, (f) $\text{Co}_{69}\text{-Fe}_5\text{-Pt}_{26}$ and (g) Pt_{100}

5.3.2 Chemical Composition

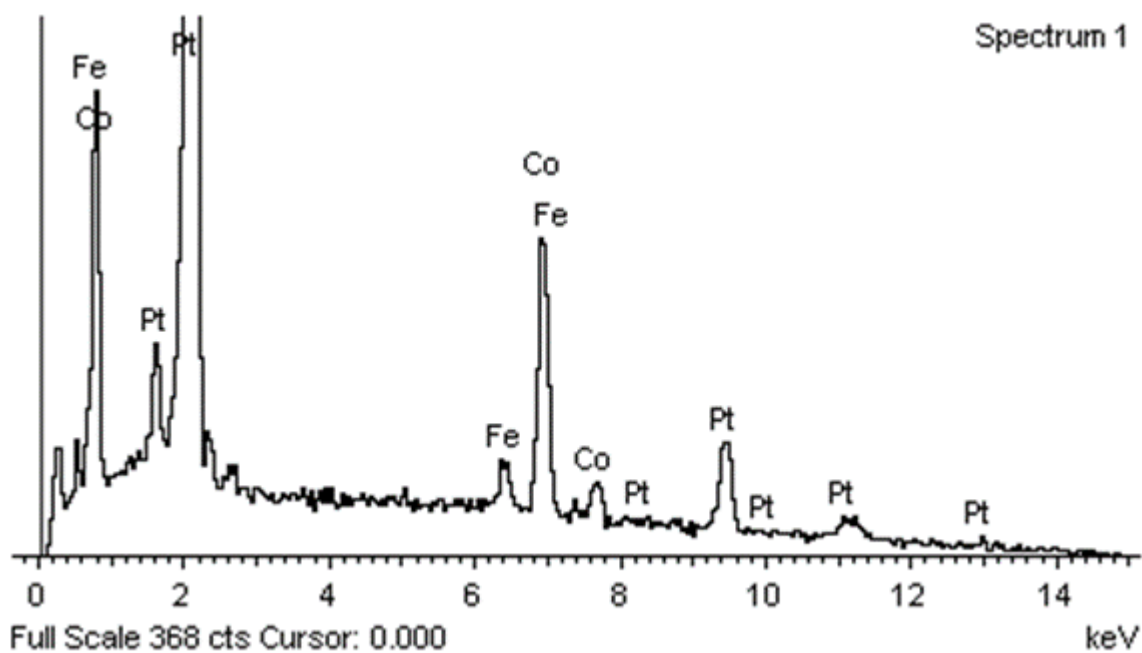
Figure 5.27 shows the energy dispersive X-ray spectroscopy (EDS) spectra of $\text{Fe}_{70}\text{-Pt}_{30}$, $\text{Co}_{53}\text{-Fe}_8\text{-Pt}_{39}$ and $\text{Co}_{69}\text{-Fe}_5\text{-Pt}_{26}$. The EDS spectra of $\text{Fe}_{70}\text{-Pt}_{30}$ contained only Co and Fe peaks. In comparison, it was clearly seen that the intensity of Co peaks was higher for $\text{Co}_{69}\text{-Fe}_5\text{-Pt}_{26}$ film compared to the $\text{Co}_{53}\text{-Fe}_8\text{-Pt}_{39}$ film. This corresponded to

higher Co content in the $\text{Co}_{69}\text{-Fe}_5\text{-Pt}_{26}$ film. The atomic percentages of Co, Fe and Pt were determined by EDS and shown in Table 5.9. The as-synthesized films were labeled according to their Co, Fe and Pt atomic percentage.

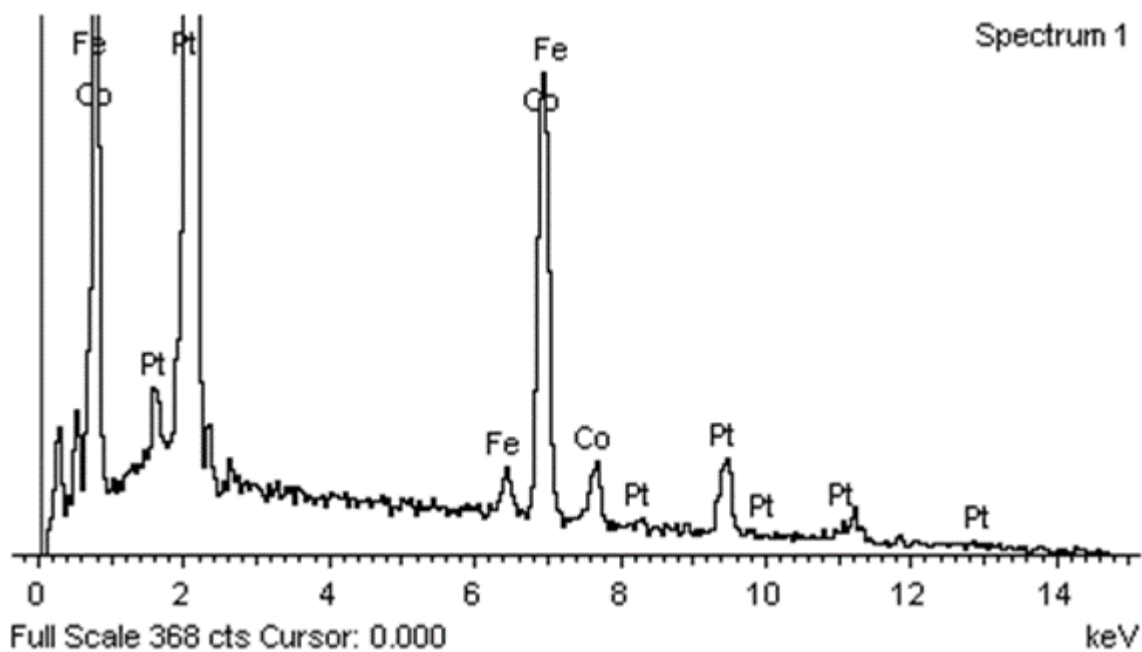
The standard reduction potentials of platinum, iron and cobalt are +0.73V, -0.440V and -0.277V, respectively with respect to standard hydrogen electrode (Skoog et al., 1996). The potential difference between iron and platinum or platinum and cobalt are relatively high, resulting in difficulty of the Fe and Pt or Co and Pt co-deposition. Moreover, Fe^{2+} ions are easily oxidized to Fe^{3+} , causing precipitation of $\text{Fe}(\text{OH})_3$ complexes (Shigeru et al., 2005). Previous study showed that Pt has higher standard reduction potentials compared to Fe and is more noble than the brass substrate. So, electrodeposition of Pt can take place even without applying current or electrical potential to the electroplating system (Teh and Yacob, 2009; Teh and Yacob, 2010a). Therefore, ammonium tartrate and ammonia solution were added to the electrolyte bath to form Fe and Co tartrate complexes to enhance the co-deposition with Pt complexes (Ge et al., 2007).



(a)



(b)



(c)

Figure 5.27:
Energy dispersive X-ray spectroscopy (EDS) spectra of (a) Fe₇₀-Pt₃₀, (b) Co₅₃-Fe₈-Pt₃₉
and (c) Co₆₉-Fe₅-Pt₂₆ films

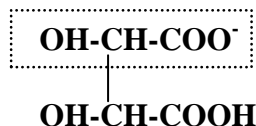


Figure 5.28:
Structure of complexing agent: tartrate

In general, the Pt atomic percentage decreased with increasing amount of complex forming additive in the electrolyte solution. It was seen that more deposition of Co and Fe compared to Pt as more Co and Fe tartrate complexes were formed. This fact was proven for samples of Fe₇₀-Pt₃₀, Co₅₃-Fe₈-Pt₃₉ and Co₆₉-Fe₅-Pt₂₆ which had lower atomic percentage of Pt even though higher amounts of Pt ions (0.03M H₂PtCl₆) were added to the electrolyte solution. The tartrate complexes ions could be attached to Co²⁺ and Fe²⁺ by coordination through the carboxyl group. Especially, the carboxyl group adjacent to hydroxyl groups (dotted lines in Figure 5.28) is easier to coordinate with the metal ions due to the electron donating effect (Weo et al., 2008). Therefore, Co and Fe can be obtained by electroreduction from the complexed or non-complexed ions. In the case of Co deposition, EDS analysis showed that Co was preferentially deposited compared to Fe during Co-Fe-Pt film electrodeposition even if only a small amount of cobalt was added into the electrolyte solution. This might be due to the fact that Fe is less noble than Co, which resulted in the formation of larger amount of Co tartrate complexes, though both Co²⁺ and Fe²⁺ ions were present in the electrolyte solution. The electrodeposition processes are shown in reactions 5.5, 5.6 and 5.7:



Where, L represents the tartrate complexes.

Elemental mapping was performed on thin films to examine the distributions of Co, Fe and Pt elements in the alloy films. The Co, Fe and Pt elements in the Fe₇₀-Pt₃₀, Co₅₃-Fe₈-Pt₃₉ and Co₆₉-Fe₅-Pt₂₆ thin films were uniformly distributed as shown in Figures 5.28, 5.29 and 5.30, respectively.

Table 5.7:
Molar ratio of electrolyte solutions and atomic percentages of Co, Fe and Pt determined by EDS

Bath	Concentration [M]				Composition			Thin film sample
	CoCl ₂	FeSO ₄	H ₂ PtCl ₆	(NH ₄) ₂ C ₄ H ₄ O ₆	Co at. %	Fe at. %	Pt at. %	
1	0	0.025	0.025	0.020	0	54	46	Fe ₅₄ -Pt ₄₆
2	0.005	0.020	0.025	0.020	15	18	67	Co ₁₅ -Fe ₁₈ -Pt ₆₇
3	0.010	0.015	0.025	0.020	17	11	72	Co ₁₇ -Fe ₁₁ -Pt ₇₂
4	0	0.020	0.030	0.030	0	70	30	Fe ₇₀ -Pt ₃₀
5	0.005	0.015	0.030	0.030	53	8	39	Co ₅₃ -Fe ₈ -Pt ₃₉
6	0.010	0.010	0.030	0.030	69	5	26	Co ₆₉ -Fe ₅ -Pt ₂₆
7	0	0.001	0.100	0	0	0	100	Pt ₁₀₀

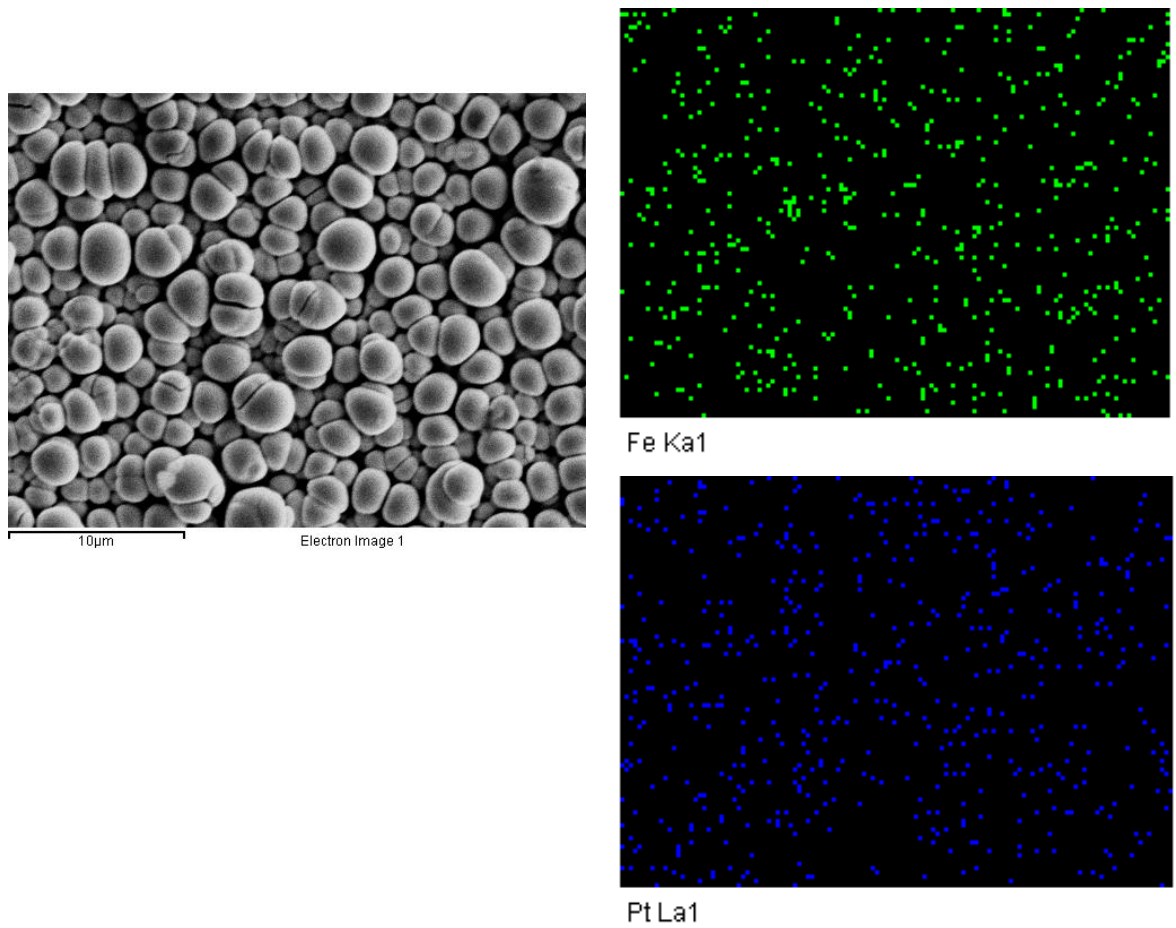


Figure 5.28:
Elemental mapping of as-synthesized $\text{Fe}_{70}\text{-Pt}_{30}$ nanocrystalline thin film

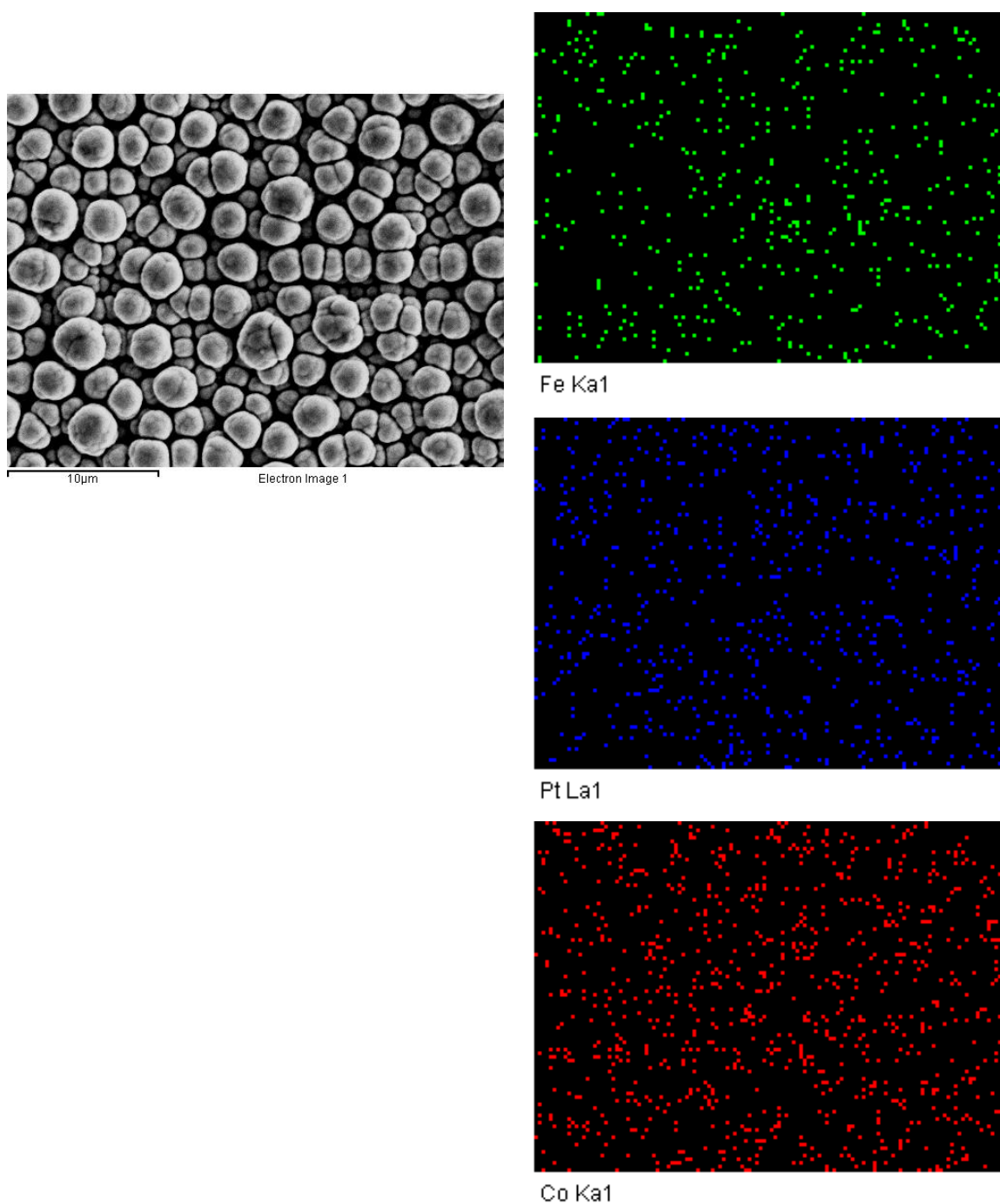


Figure 5.29:
Elemental mapping of as-synthesized $\text{Co}_{53}\text{-Fe}_8\text{-Pt}_{39}$ nanocrystalline thin film

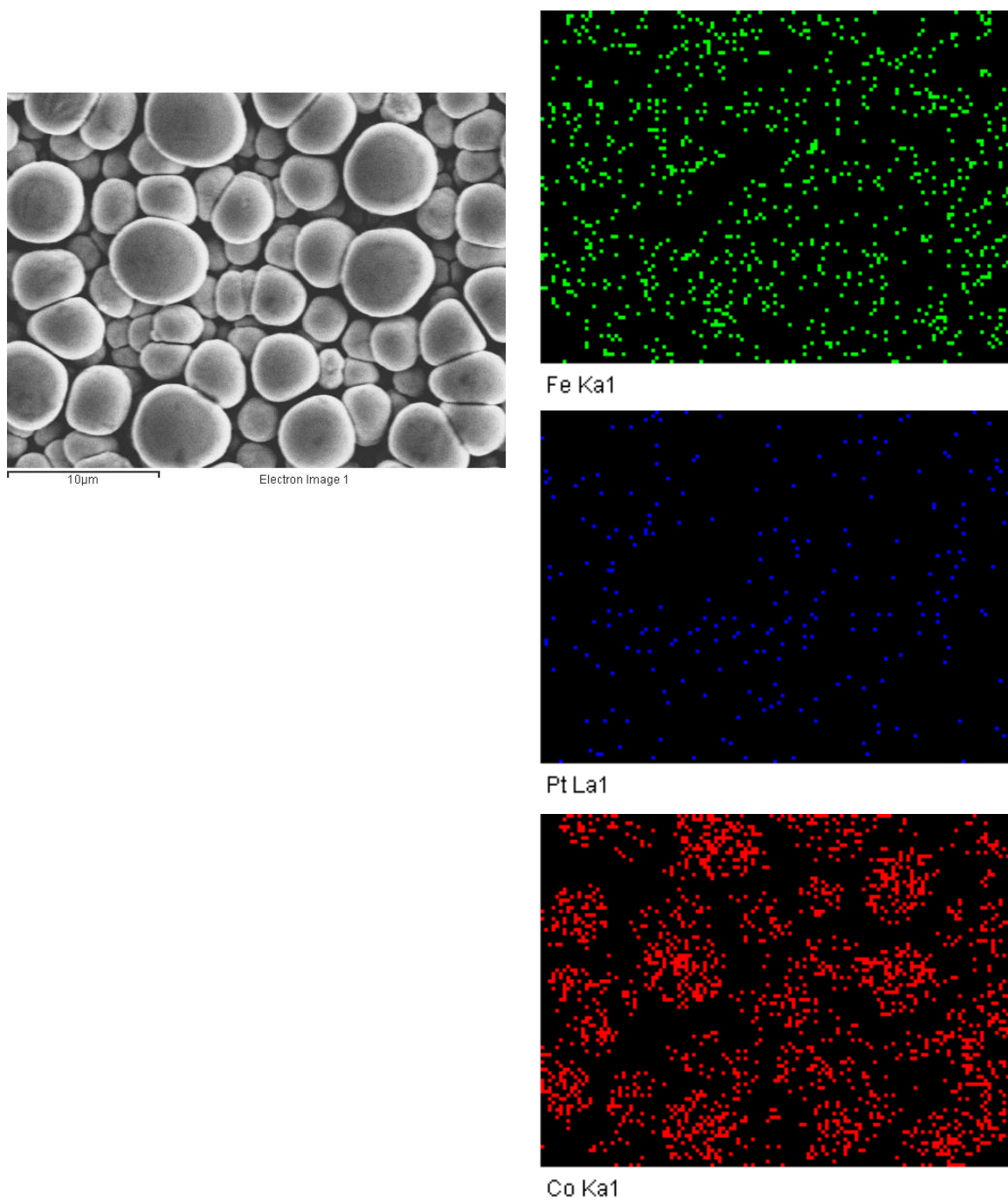


Figure 5.30:
Elemental mapping of as-synthesized $\text{Co}_{69}\text{-Fe}_5\text{-Pt}_{26}$ nanocrystalline thin film

5.3.3 X-ray Diffraction Analysis

The X-ray diffraction (XRD) patterns of all as-synthesized thin films are presented in Figure 5.31 and Figure 5.32. The XRD pattern indicated formation of Fe-Pt disordered face-centered cubic (FCC) phase (JCPDS 29-0717) with presence of (111), (200), (220) and (311) peaks approximately at $2\theta^\circ$ of 40.4, 46.7, 68.5 and 82.6. However, the lattice constant of the nanocrystalline films decreased with the presence of cobalt and all peaks were shifted to higher diffraction angles. This might be due to the fact that Co atom occupied the Fe site in Co-Fe-Pt alloy crystal ($r_{\text{Fe}}=0.126\text{nm}$, $r_{\text{Co}}=0.125\text{nm}$) (Wei, et al., 2008). Some shifted peaks might be attributed to the thermal stress as the films were deposited at temperature of 60°C and slight lattice mismatch was observed with brass substrates (Lai et al., 2004).

FePt exists in two crystallographic phases. The magnetically soft disordered phase, where the Fe and Pt atoms are distributed statistically in the fcc lattice, is stable at temperatures above 1300°C . Below that temperature, the compound changes into the ordered L_{10} structure, where Fe and Pt planes are stacked along $[100]$ directions (Weisheit, M et al., 2007). The crystal structure is compressed in the stacking direction (magnetic easy axis), which causes the high magnetic anisotropy. However, at room temperature the formation of the ordered phase is inhibited, necessitating high deposition or annealing temperatures. Figure 5.33 shows the schematic illustration of the unit cell of chemically disordered FCC Fe-Pt or FCC Co-Fe-Pt.

The full width at half maximum (FWHM) of the peak at $2\theta^\circ$ of about 40.4 was used to calculate the crystallite size of the films by using Debye Scherrer's equation (Hadi and Yaccob, 2007). After subtracting the instrumental peak broadening obtained by using standard LaB_6 powder, the $\text{Fe}_{54}\text{-Pt}_{46}$ film showed the broadest FWHM, indicating that the crystallite size is the smallest and calculated to be approximately 2.33

nm. The crystallite sizes for all the as-deposited films (except Fe₅₄-Pt₄₆ film) were larger than the superparamagnetic limit (3nm) of Fe-Pt (Koay and Yaccob, 2007), indicating the potential use of these nanostructured thin films for magnetic recording media. Table 5.10 shows the summary of crystallite structure, phases and sizes of as-synthesized Fe-Pt and Co-Fe-Pt nanostructured alloy thin films.

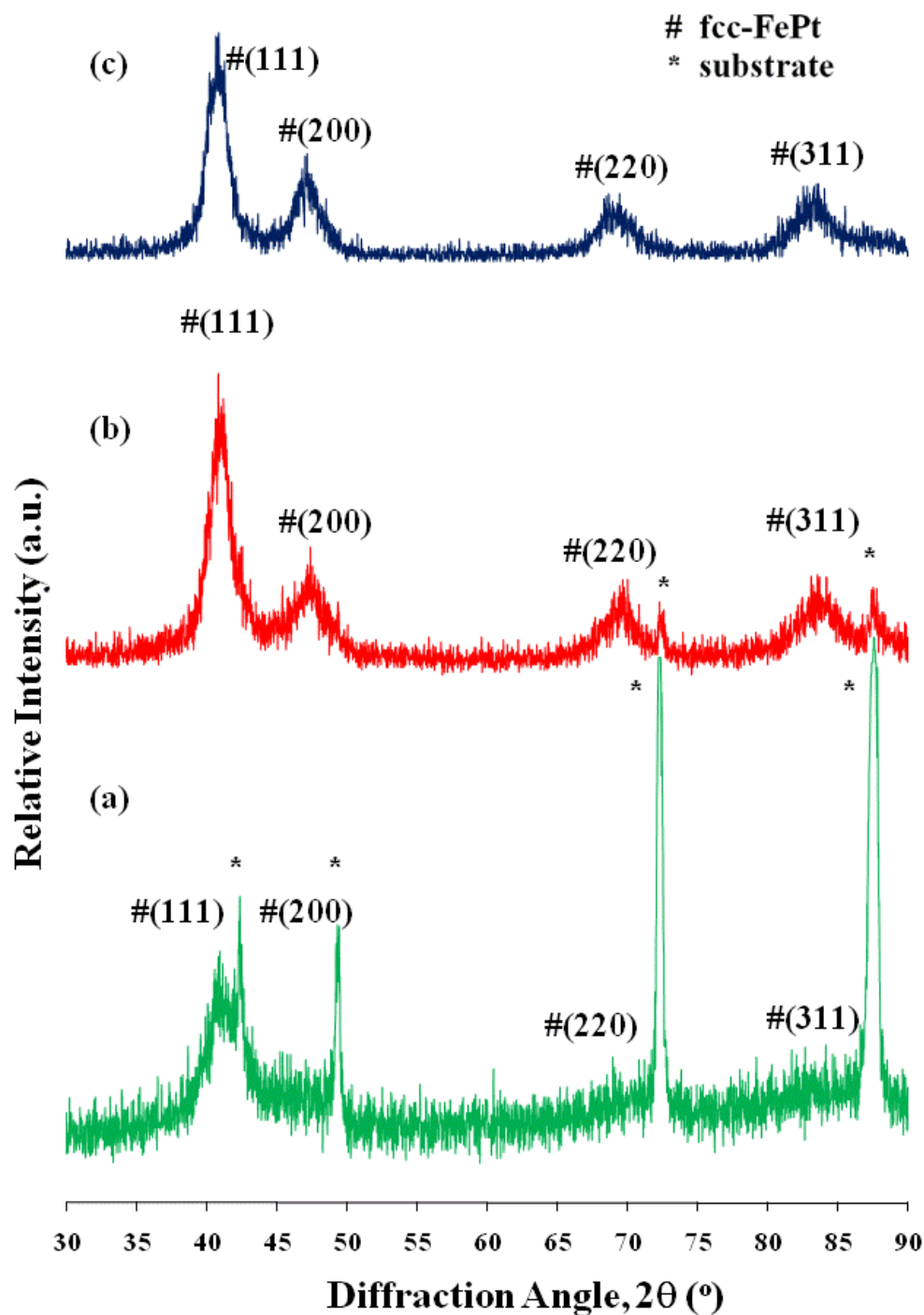


Figure 5.31:
X-ray diffraction (XRD) patterns of as-synthesized nanocrystalline thin films: (a) Fe₅₄-Pt₄₆, (b) Co₁₅-Fe₁₈-Pt₆₇ and (c) Co₁₇-Fe₁₁-Pt₇₂

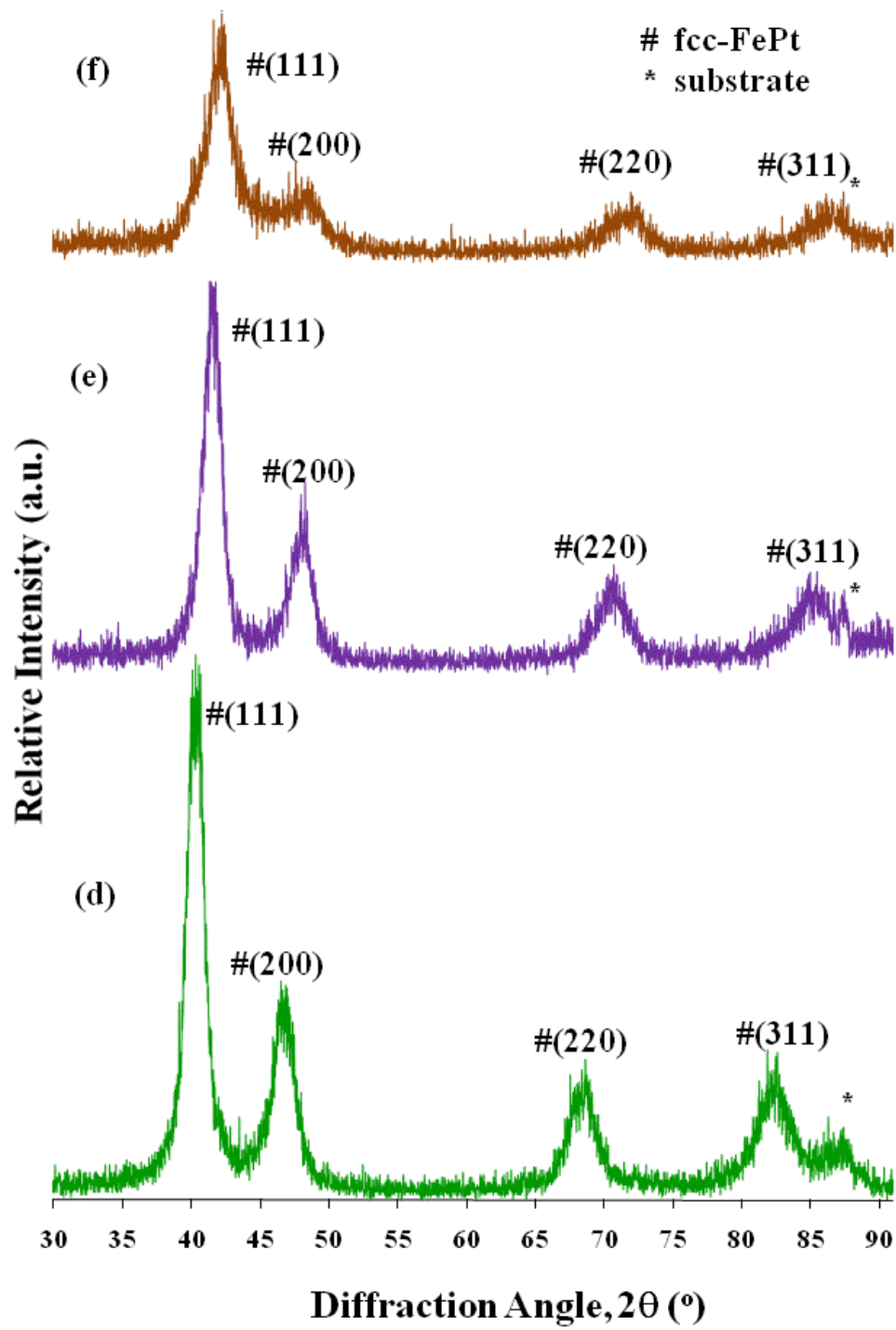


Figure 5.32:
X-ray diffraction (XRD) patterns of as-synthesized nanocrystalline thin films: (d) Fe₇₀-Pt₃₀, (e) Co₅₃-Fe₈-Pt₃₉ and (f) Co₆₉-Fe₅-Pt₂₆

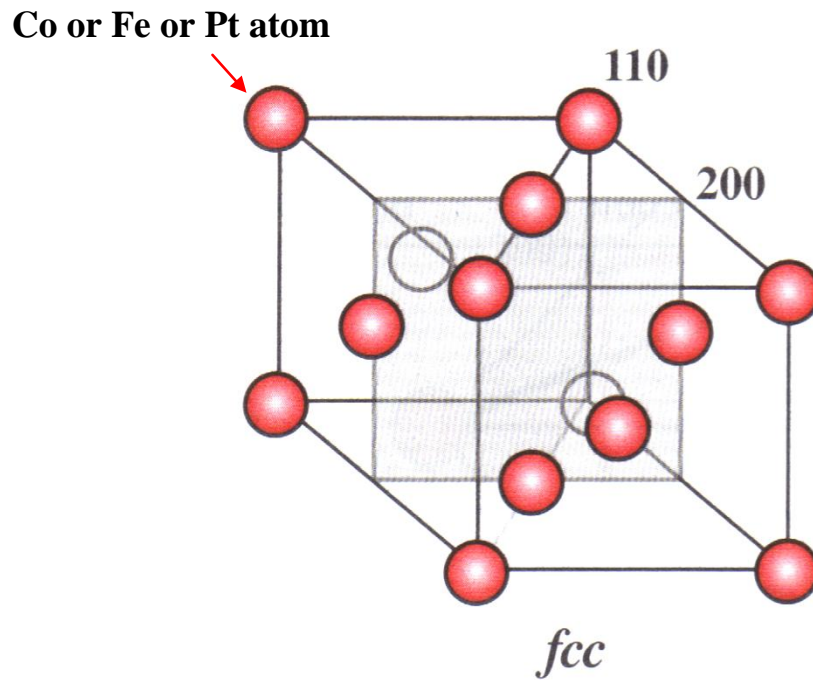


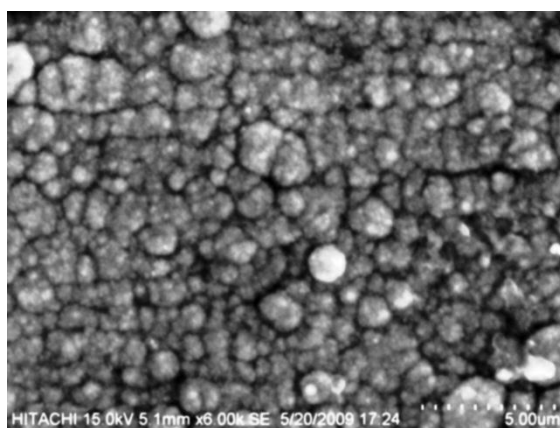
Figure 5.33:
Schematic illustration of the unit cell of disordered FCC Fe-Pt or FCC Co-Fe-Pt. The darker lattice points are to the front of the unit cells

Table 5.8:
Crystallite structure, phases and sizes of as-synthesized Fe-Pt and Co-Fe-Pt nanostructured alloy thin films

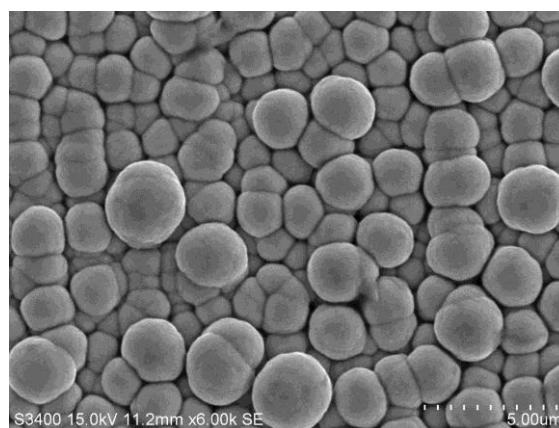
Sample	Crystal Structure	Phase	(hkl)	2θ (°)	FWHM (°) $\Delta 2\theta$	Crystallite size (nm)
Fe ₅₄ -Pt ₄₆	FCC	γ	(111)	40.43	3.792	2.33
Co ₁₅ -Fe ₁₈ -Pt ₆₇	FCC	γ	(111)	40.88	1.703	5.46
Co ₁₇ -Fe ₁₁ -Pt ₇₂	FCC	γ	(111)	40.70	1.611	5.79
Fe ₇₀ -Pt ₃₀	FCC	γ	(111)	40.30	1.442	6.54
Co ₅₃ -Fe ₈ -Pt ₃₉	FCC	γ	(111)	41.56	1.541	6.10
Co ₆₉ -Fe ₅ -Pt ₂₆	FCC	γ	(111)	42.10	2.307	3.94

5.3.4 Surface Morphology and Film Thickness

Scanning electron microscopy (SEM) images of Fe-Pt and Co-Fe-Pt alloy films are shown in Figure 5.34. It was seen that all the alloy films deposited with complex forming additive formed granular structures. The grains or crystallites were formed by independent nucleation and growth processes from the randomly oriented grains and spaced with respect to one another (Karmerski, 1980). The crystallite sizes estimated by XRD were much smaller than the size of granules (Table 5.11), indicating that these granules are polycrystalline (Teh, 2009). The granule size of as-deposited Fe₅₄-Pt₄₆ and Fe₇₀-Pt₃₀ films were smaller compared to Co-Fe-Pt thin films. As cobalt content was increased, some particles formed clusters with two or more granules as shown in the electrodeposited Co-Fe-Pt thin films. Similar observation was reported for Co-Fe-Pt films prepared by sputtering method (Lai et al., 2004). It was also seen that the granules of Co-Fe-Pt nanocrystalline alloy film do not coalesce to the adjacent granules, resulting in a more wavy or uneven surface.



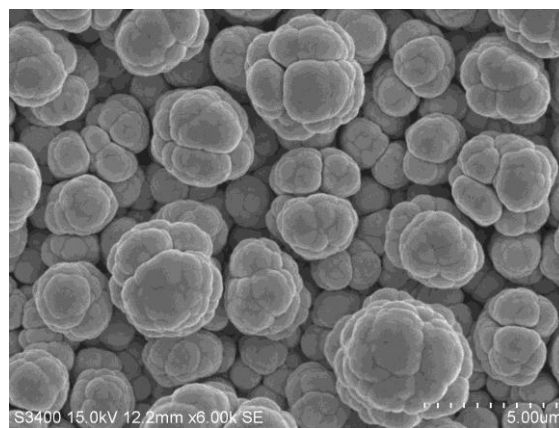
(a)



(d)



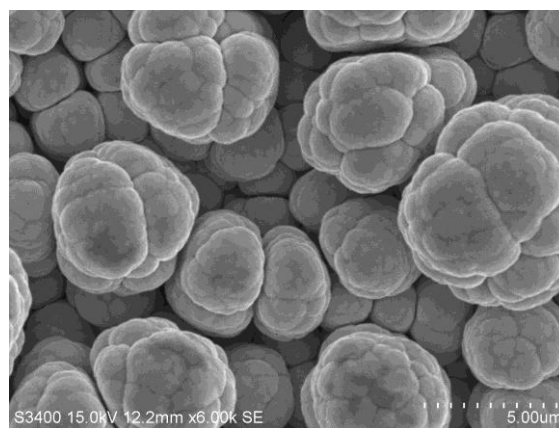
(b)



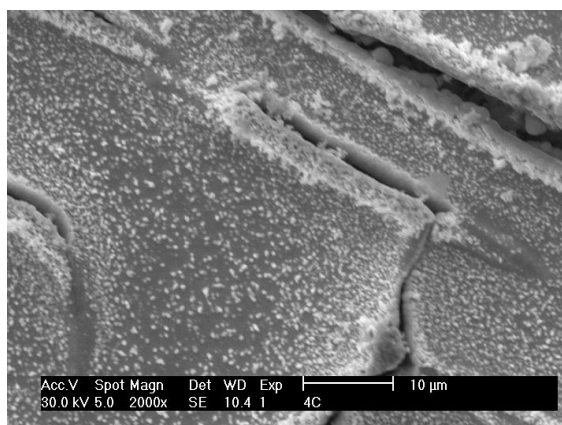
(e)



(c)



(f)



(g)

Figure 5.34:
Scanning electron microscopy (SEM) of as-prepared nanostructured alloy thin films: (a) $\text{Fe}_{54}\text{-Pt}_{46}$, (b) $\text{Co}_{15}\text{-Fe}_{18}\text{-Pt}_{67}$, (c) $\text{Co}_{17}\text{-Fe}_{11}\text{-Pt}_{72}$, (d) $\text{Fe}_{70}\text{-Pt}_{30}$, (e) $\text{Co}_{53}\text{-Fe}_8\text{-Pt}_{39}$, (f) $\text{Co}_{69}\text{-Fe}_5\text{-Pt}_{26}$ and (g) Pt_{100}

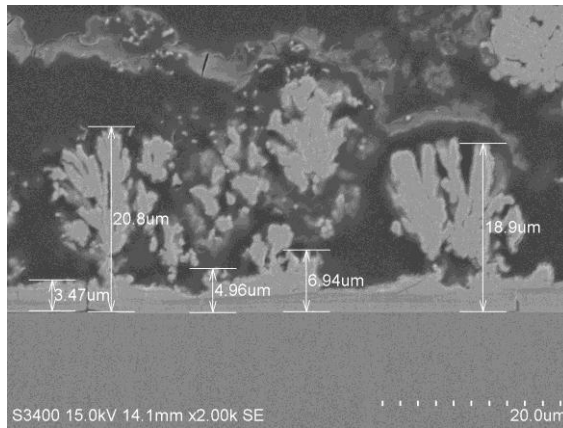
The films electrodeposited from complex salt solutions (Figure 5.34(a)-(f)) were of better quality than the film electrodeposited from simple salt electrolyte (Figure 5.34 (g)). The presence of insoluble tartrate complexes favored the formation of fresh nuclei and prevents their growth, leading to the formation of smoother and good quality of deposits (Teh et al., 2012). The Pt₁₀₀ film deposited without complex forming agent was not suitable for further characterization as it cracked and detached from the brass substrate.

Table 5.9:
Film thickness, granule size, saturation magnetization and coercivity values of Fe-Pt and Co-Fe-Pt thin films

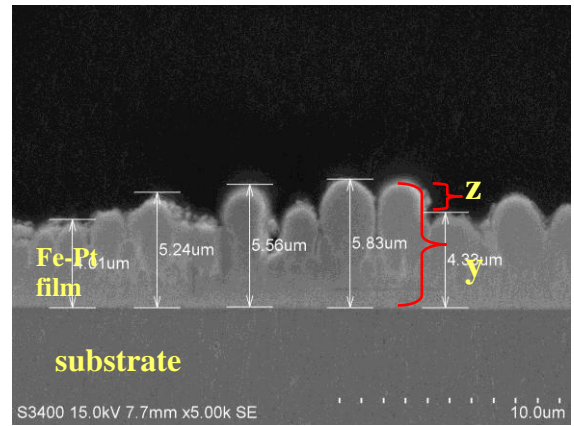
Sample	Film thickness [μm]	Granules Size [μm]	Saturation Magnetization, M_s [emu/g]	Coercivity, H_c [Oe]
Fe ₅₄ -Pt ₄₆	17.02	0.98	148.00	15.00
Co ₁₅ -Fe ₁₈ -Pt ₆₇	24.20	4.41	224.50	45.49
Co ₁₇ -Fe ₁₁ -Pt ₇₂	27.17	7.76	377.00	72.31
Fe ₇₀ -Pt ₃₀	5.10	1.43	61.78	53.51
Co ₅₃ -Fe ₈ -Pt ₃₉	5.29	2.16	82.60	110.00
Co ₆₉ -Fe ₅ -Pt ₂₆	13.65	3.00	213.86	111.00

Film thickness was measured by SEM on cross-sectioned area of the thin films. The average thickness was determined by measuring the distance from brass substrates to the maximum height of the granules. This procedure was repeated several times and average value was taken to represent the thickness value. Figure 5.35 shows that the granules are connected to adjacent granules and a wavy shape was formed. Grain growth was ceased when the surrounding grains or crystallites restricted further growth

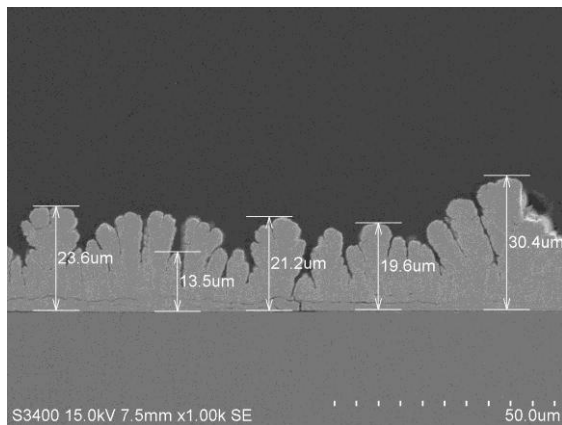
of the granules. Re-crystallization might be induced by annealing which might reduce the grain boundary surface area by diffusion (Karmerski, 1980). However, the effect of annealing towards the re-crystallization is not within the scope of this research. The average thickness of $\text{Co}_{69}\text{-Fe}_5\text{-Pt}_{26}$ film was $13.65\text{ }\mu\text{m}$ and it consisted of large granules compared to $\text{Fe}_{70}\text{-Pt}_{30}$ and $\text{Co}_{53}\text{-Fe}_8\text{-Pt}_{39}$ films.



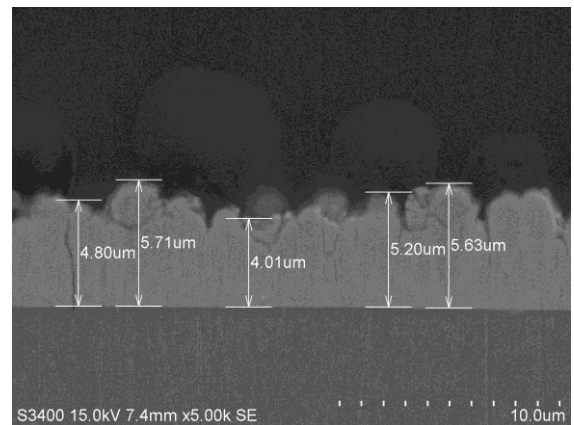
(a)



(d)



(b)



(e)

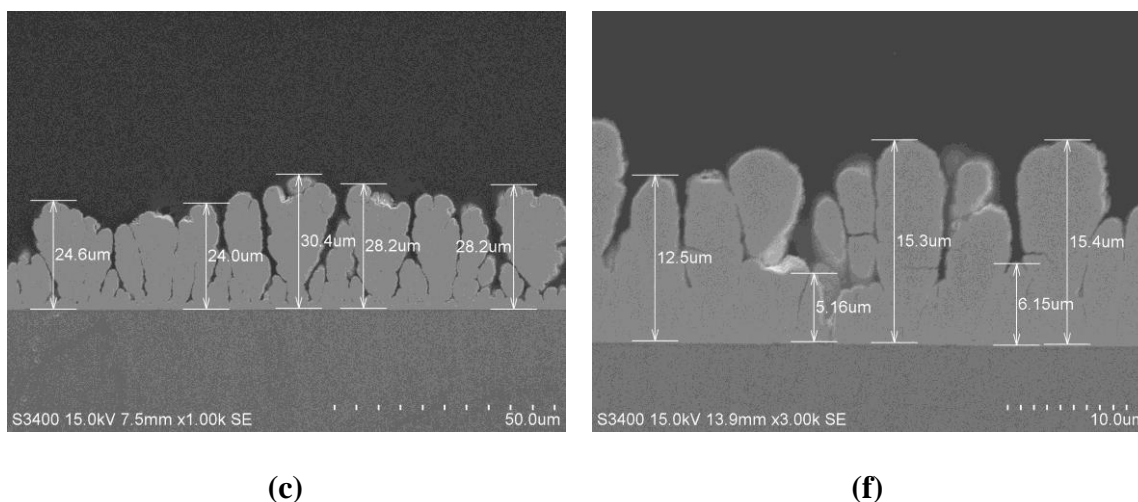


Figure 5.35:

Cross sectional scanning electron microscopy (SEM) of as-prepared alloy thin films: (a) $\text{Fe}_{54}\text{-Pt}_{46}$, (b) $\text{Co}_{15}\text{-Fe}_{18}\text{-Pt}_{67}$, (c) $\text{Co}_{17}\text{-Fe}_{11}\text{-Pt}_{72}$, (d) $\text{Fe}_{70}\text{-Pt}_{30}$, (e) $\text{Co}_{53}\text{-Fe}_8\text{-Pt}_{39}$ and (f) $\text{Co}_{69}\text{-Fe}_5\text{-Pt}_{26}$

5.3.5 Surface Roughness and Magnetic Force

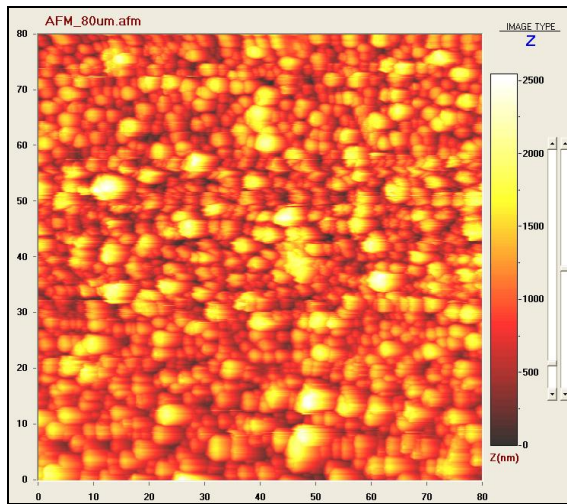
Figure 5.36 (i) and (ii) represents 2-D and 3-D atomic force microscopy (AFM) images of as-deposited $\text{Fe}_{70}\text{-Pt}_{30}$, $\text{Co}_{53}\text{-Fe}_8\text{-Pt}_{39}$ and $\text{Co}_{69}\text{-Fe}_5\text{-Pt}_{26}$ films, respectively. The working surface was $80\text{ }\mu\text{m} \times 80\text{ }\mu\text{m}$. The average height, maximum height and roughness (root mean square (RMS) variation) are summarized in the Table 5.12. In AFM contact mode, a tip at the end of a leaf spring or "cantilever" was touched lightly on the sample. The tip raster scanned the sample and vertical deflections of the cantilever indicating the local height were detected by a photo detector. Figure 5.35 (d) shows SEM cross sectional view of $\text{Fe}_{70}\text{-Pt}_{30}$ film, where y indicates the film thickness measured by SEM and z illustrates the average height measured by AFM. In general, the average height (AH) (Table 5.12) of the Fe-Pt thin films are much smaller compared to the average film thickness measured using SEM as presented in Table 5.11. This is because the average height of AFM was obtained by subtracting the maximum height with the minimum height of granules for a certain working surface. In addition, Fe-Pt

and Co-Fe-Pt thin films revealed granular morphology with increasing average heights and RMS variation as Co at. % was increased. These results were in agreement with the SEM results as shown in Figure 5.35 (d, e and f).

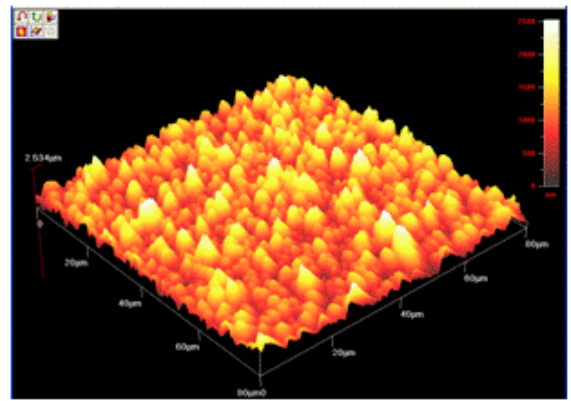
The MFM image of $\text{Co}_{69}\text{-Fe}_5\text{-Pt}_{26}$ film (Figure 5.37 (c)) was brighter than $\text{Fe}_{70}\text{-Pt}_{30}$ and $\text{Co}_{53}\text{-Fe}_8\text{-Pt}_{39}$ alloy film (Figure 5.37 (a) and (b)) indicating that the magnetic properties were stronger in the $\text{Co}_{69}\text{-Fe}_5\text{-Pt}_{26}$ alloy film. It was found that the magnetic force was correlated to the surface topography. This was proven by observation that the magnetic force (Table 5.12) increased with increasing surface roughness, granule size and clusters in the film. These results are in agreement with saturation magnetization and coercivity values as shown in Table 5.11. In addition, MFM and simultaneous AFM of all the films indicated a complex domain structure consisting of clusters with dimensions of several hundreds of nanometers, which seems to consist of interaction domains aligned along the boundaries of the polycrystalline aggregates (Jeong, 2001).

Table 5.10:
Surface roughness, average height, maximum height and magnetic force of Fe-Pt and Co-Fe-Pt thin films

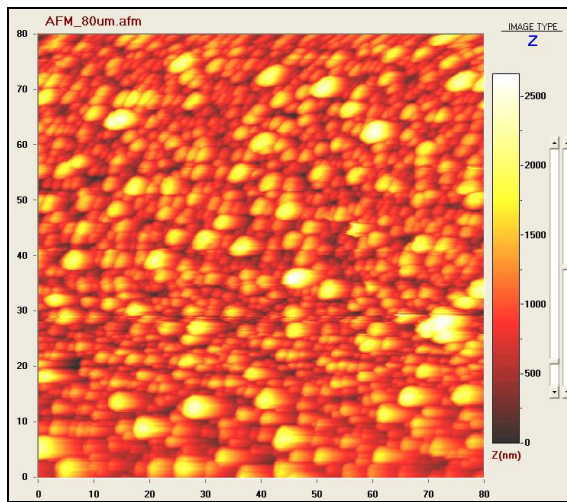
Sample	Surface roughness (nm)	Average height (μm)	Max height (μm)	Magnetic force (a.u.)
$\text{Fe}_{70}\text{-Pt}_{30}$	374.8	1.008	2.534	156.9
$\text{Co}_{53}\text{-Fe}_8\text{-Pt}_{39}$	383.7	1.008	2.651	167.8
$\text{Co}_{69}\text{-Fe}_5\text{-Pt}_{26}$	615.6	1.713	4.011	277.4



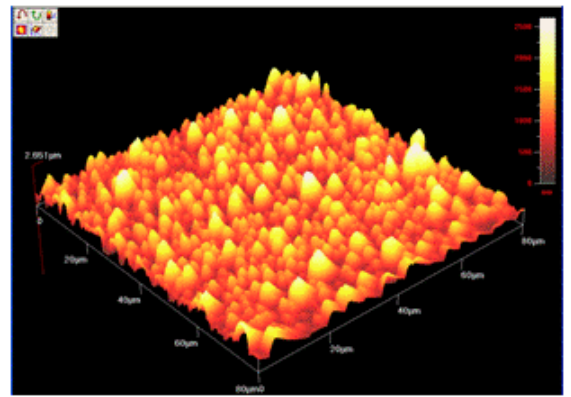
(a) i



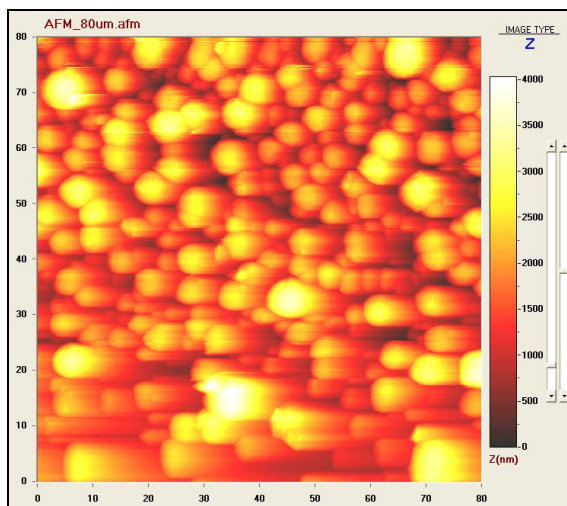
(a) ii



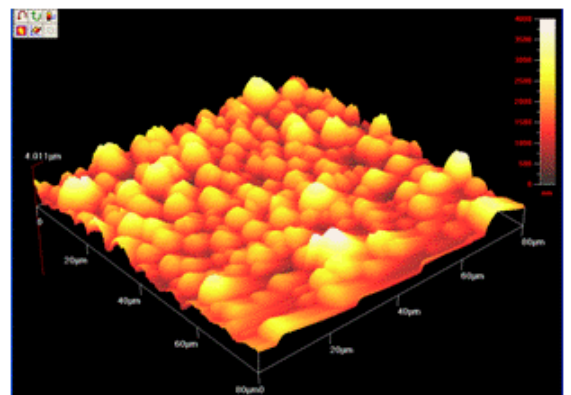
(b) i



(b) ii

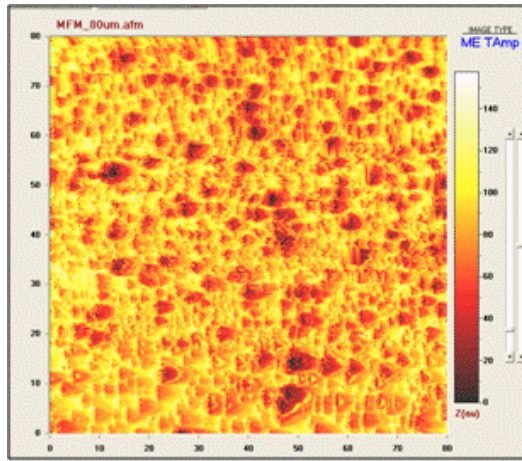


(c) i

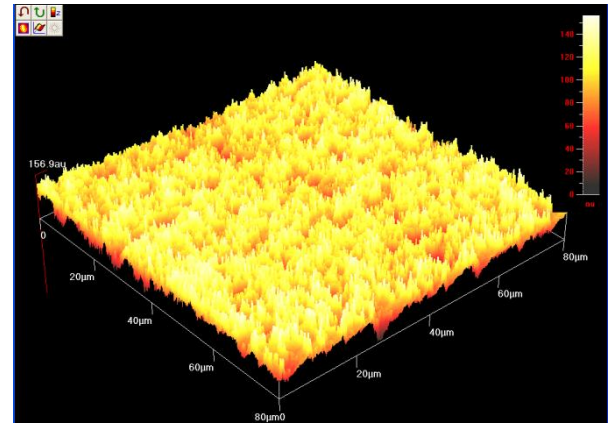


(c) ii

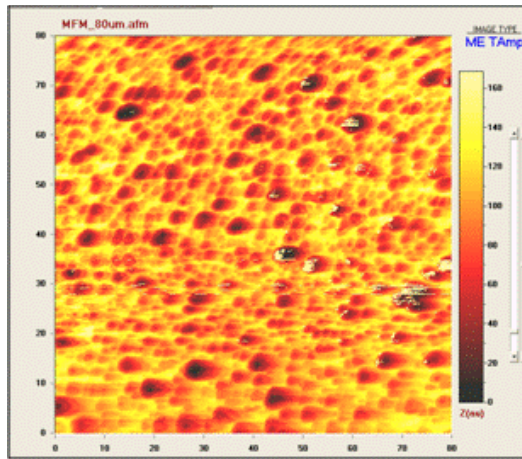
Figure 5.36:
2-D atomic force microscopy (AFM) images (i) and 3-D images (ii) of as-prepared thin films: (a) $\text{Fe}_{70}\text{-Pt}_{30}$, (b) $\text{Co}_{53}\text{-Fe}_8\text{-Pt}_{39}$ and (c) $\text{Co}_{69}\text{-Fe}_5\text{-Pt}_{26}$



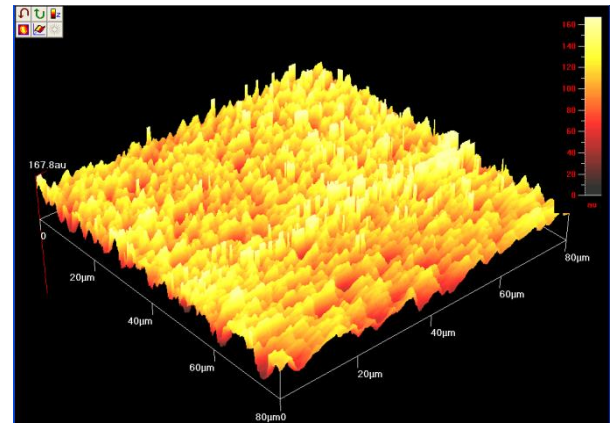
(a) i



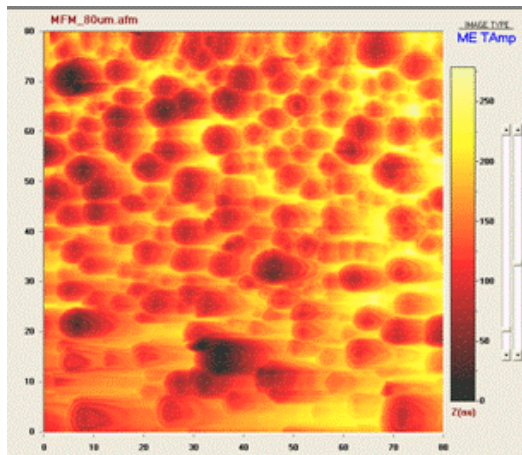
(a) ii



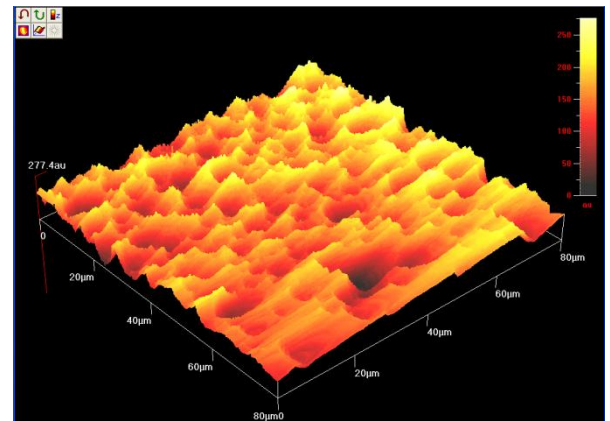
(b) i



(b) ii



(c) i



(c) ii

Figure 5.37:
2-D Magnetic force microscopy (MFM) images (i) and 3-D images (ii) of as-prepared thin films: (a) $\text{Fe}_{70}\text{-Pt}_{30}$, (b) $\text{Co}_{53}\text{-Fe}_8\text{-Pt}_{39}$ and (c) $\text{Co}_{69}\text{-Fe}_5\text{-Pt}_{26}$

5.3.6 Magnetic Properties

Figure 5.38 shows typical parallel hysteresis curves of as-synthesized Fe-Pt and Co-Fe-Pt thin films. It was observed that the saturation magnetization increased with the increase of Co content and granule size (Table 5.11). The coercivity of the as-synthesized samples was increased with increasing cobalt content, which was shown by a wider hysteresis loop. Fe₅₄-Pt₄₆ film showed the lowest coercivity value. This might be due to its smallest average crystallite size (2.33 nm) in the alloy film, which was at the margin of superparamagnetic limit. This film might be unstable and susceptible to thermal destabilization if it is used for magnetic recording and might result in the disappearance of memory information (Wang et al., 2004).

5.3.7 Summary

Electrolytic deposition techniques are envisaged as eligible alternatives for producing nanostructured magnetic Fe-Pt and Co-Fe-Pt alloy thin films with various compositions. EDS results revealed that tartrate-alkaline additives assisted the deposition of Fe and Co with Pt. Morphological studies revealed that the average sizes of spherical granules were ranging from 0.98 to 3.00 μm . Clusters were formed due to coalesce of two or more granules in the electrodeposited Co-Fe-Pt thin films as cobalt content was increased. SEM on cross-sectioned area of the thin films showed that the granules were connected to adjacent granules to form a wavy surface shape. The as-prepared thin films showed disordered FePt face centered cubic (FCC) structure. The average crystallite sizes of all the nanostructured thin films were above the superparamagnetic limit of Fe-Pt (except for Fe₅₄-Pt₄₆ film). AFM results showed the increment of average heights and surface roughness as the Co at. % was increased. Cobalt was found to enhance the saturation magnetization and coercivity values in the deposits.

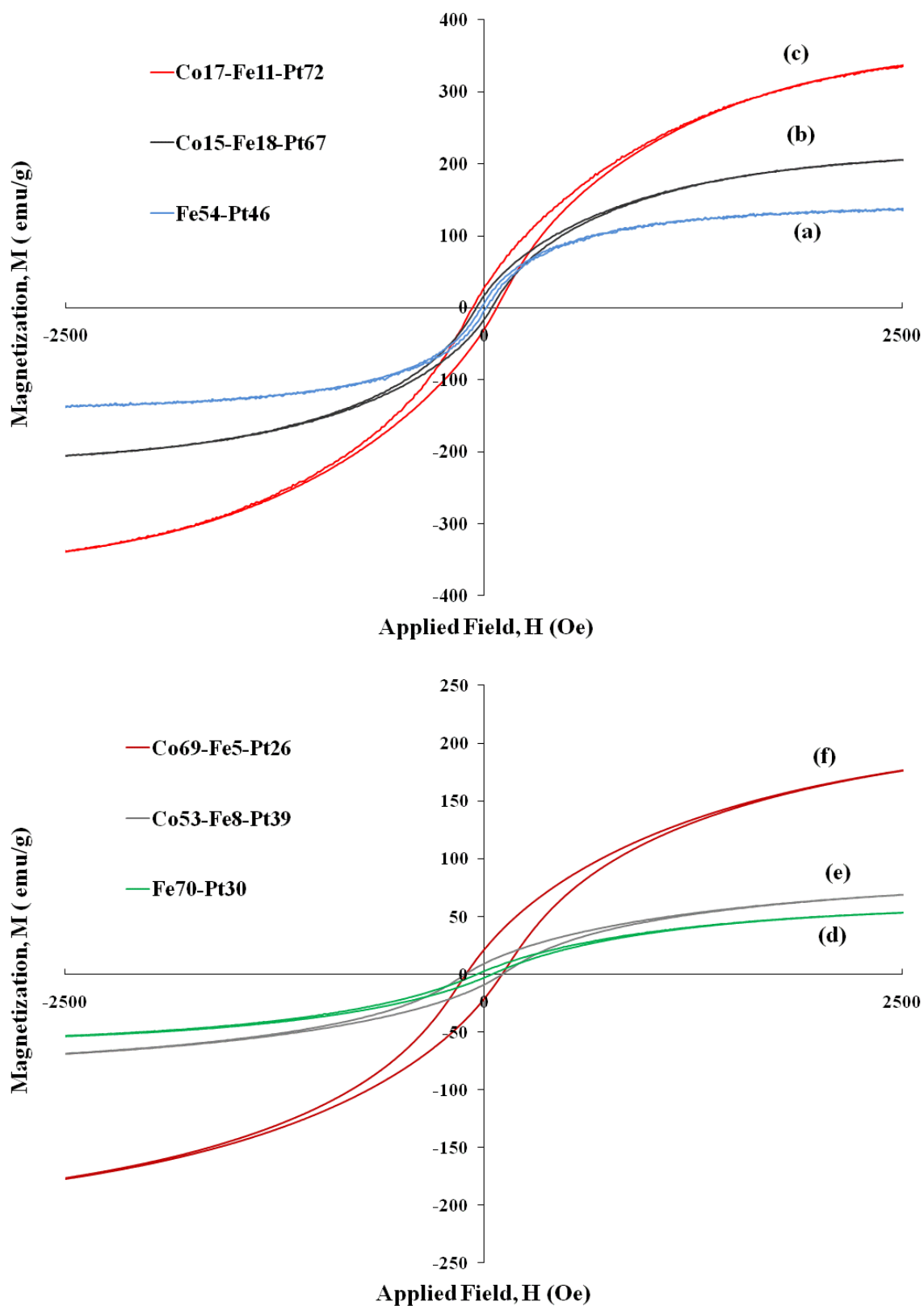


Figure 5.38:

Typical parallel hysteresis curves at room temperature of as-synthesised nanocrystalline thin films: (a) Fe₅₄-Pt₄₆, (b) Co₁₅-Fe₁₈-Pt₆₇, (c) Co₁₇-Fe₁₁-Pt₇₂, (d) Fe₇₀-Pt₃₀, (e) Co₅₃-Fe₈-Pt₃₉ and (f) Co₆₉-Fe₅-Pt₂₆. *Note: Hysteresis curves of samples are shown from -2500Oe to + 2500Oe to emphasis the differences of H_c and M_s values of various samples.*

CHAPTER 6: POTENTIAL APPLICATIONS, CONCLUSIONS AND RECOMMENDATIONS

6.1 Potential Applications

Completion of the present work has brought about several contributions to the development of electrodeposition technology. This work is the first in-depth study dealing with the synthesis of nanocrystalline soft magnetic materials by the electrodeposition processes. Operating parameter windows were found for the deposition of Co-Fe, Co-Pt, Fe-Pt and Co-Fe-Pt materials, which can be added to the growing list of nanocrystalline material for future applications. The nanoprocessed alloys discussed in the content of this research and those shown in Figure 1.2 represent technologically significant advancement in the materials available for soft magnetic applications. Table 6.1 shows potential applications of various thin film systems synthesized from this research and summarized from various literatures.

Recently, high magnetic anisotropy materials have received much attention to meet the demands of applications in the field of information technologies. For example, in magnetic recording, as the bit size is reduced to nano dimension, material with high magnetic-anisotropy energy (K_u) value is needed to stabilize spin state against thermal agitation. Other applications of such materials are permanent magnet or bias layer for spin electronic devices. This high magnetic anisotropy energy allows for thermally stable grain size down to 3 nm. Therefore, the CoPt, FePt and CoFePt ordered alloy may lead to the realization of a magnetic medium capable of recording densities beyond 1 Tb in^{-2} (Weller et al., 2000). In addition, due to the high Pt content, CoPt, FePt and CoFePt alloy exhibits a very good corrosive and wear resistance. Nevertheless, a disadvantage of these materials for practical applications is the relative high cost of Pt.

The breakthrough of this research is the development of novel electrodeposition synthesis method for Co-Fe-Pt films as there is no known literature on this Co-Fe-Pt system produced from electrodeposition process. The goal of this research was to develop synthesis method to produce nanocrystalline ferromagnets with specific grain size. This objective was basically achieved. This is evident that the crystallites sizes of Co-Pt, Fe-Pt and Co-Fe-Pt thin films were found in nano-scale and above the superparamagnetic limit. The results of Co-Pt, Fe-Pt and Co-Fe-Pt obtained from this research has shown potential applications in soft and hard magnetic layer in high resolution MFM tips, magneto-optical recording, perpendicular magnetic recording and most recently, hard magnetic components in MEMS, transformer, inductor cores, microwave devices, magnetic shielding, amplifiers, field sensors, etc. However, high temperature annealing treatment is needed to obtain ordered CoPt, FePt and CoFePt phase that can achieve hard magnetic properties. Therefore, a follow-up research is required to optimize annealing treatment before the field of the ideal hard magnet can be approached both in terms of saturation magnetization and coercivity. Furthermore, further research need to be done to reduce the temperatures of annealing treatment for a desired application.

Another nanoprocessed alloy which displays excellent potential for use in soft magnetic application is the Co-Fe system. Despite the higher price of Co, relative to Ni and Fe, gains in saturation induction in Co-Fe over the above that achievable with Fe alone may make certain applications cost-effective. The use of grain refining agent has improved the quality and physical appearance of Co-Fe film in this study. The CoFe results of this research are very promising and make these material attractive candidates for magnetic amplifiers, switching devices, relay armatures, magnetic transducers and some high quality telephone receivers soft underlayers in perpendicular media,

computer read/write heads, ferromagnetic electrodes in spin tunnel junctions or MRAM devices non-volatile magnetic memories.

It is now possible to fabricate nanocrystalline material in both bulk and thin film or layered structures to very accurate specifications. The ability to tailor application towards specific magnetic properties combined with other advantages of nanoprocessing will continue to reveal novel applications for future soft and hard magnetic materials.

Table 6.1:
Potential applications of various thin film systems synthesized from this research and summarized from literatures

System	Synthesis Method	H_c	M_s	Potential Applications	Reference
<u>CoFe</u>					
$Co_{100-x}Fe_x$ with $x = 0, 6, 11, 14$ and 18	Electro-deposition	14 -52 Oe	182- 1649 emu/g	magnetic amplifiers, switching devices, relay armatures, . magnetic transducers and some high quality telephone receivers soft underlayers in perpendicular media, computer read/write heads, ferromagnetic electrodes in spin tunnel junctions or MRAM devices, non-volatile magnetic memories, spintronics.	Teh and Yaacob (2011b)
CoFe	High target utilization sputtering technology (HiTus)	9 – 121 Oe	Nil	soft underlayers in perpendicular media, write elements in recording heads, ferromagnetic electrodes in spin tunnel junctions or MRAM devices	Vopsaroiu et al. (2005)

Co and Fe	e-beam evaporation	10-80 Oe; 30-180 Oe	~ 1200 emu/cm ³ ; ~ 1400 emu/cm ³	non-volatile magnetic memories, spintronics.	Islam et al. (2007)
Co ₃₄ -Fe ₆₆ and Co ₆₅ -F ₃₅	Electro-deposition	10 Oe	2.0 Tesla	write head core materials	Zhang and G. Ivey (2007)
Co-Fe	Electro-deposition	~ 29 Oe	~ 1597 emu/cm ³	computer read/write heads	Kockar et al. (2010)
Fe _{0.3} -Co _{0.7}	Electro-deposition	42.72 Oe	2974 emu/cm ³	radio frequency thin film inductors , computer read/write heads	Qiang et al. (2010)
Co ₄₀ -Fe ₆₀	Electro-deposition	2.5 - 6.5 Oe	2.45 Tesla	magnetic recording systems , microelectronic and biotechnological devices	Zong et al. (2008)
<u>CoPt</u>					
<i>Co_x-Pt_{100-x} with x = 43, 56, 86, 95 and 97</i>	<i>Electro-deposition</i>	<i>65 - 173 Oe</i>	<i>93-432 emu/g</i>	<i>transformer, inductor cores, microwave devices, magnetic shielding, amplifiers, field sensors, micro-electromechanical system (MEMS) devices, magnetic recording head, reading heads and data storage media</i>	<i>Teh et al. (2013)</i>
Co-Pt	Electro-deposition	510 - 1430Oe (par) and 600- 2550 Oe (perp)	Nil	perpendicular recording media	Franz et al. (2007)
Co ₃₁ -Pt ₆₉	Electro-deposition	100 Oe (as-made), 1k Oe (annealing)	Nil	magnetic recording systems	Wang et al. (2003)
Co ₄₈ -Pt ₅₂	Electro-deposition	652 kA m ⁻¹ (after annealing)	Nil	magnetic recording media	Wang et al. (2004)
Co ₄₃ -Pt ₅₇	Electro-deposition	15kA m ⁻¹ ; 881 kA m ⁻¹ (after annealing)	Nil	small motors and micromachines	Fujita et al. (2004)

<u>FePt</u>					
<i>Fe₅₄-Pt₄₆ and Fe₇₀-Pt₃₀</i>	<i>Electro-deposition</i>	<i>15 – 54 Oe</i>	<i>62-148 emu/g</i>	<i>magneto-optical recording, perpendicular magnetic recording and most recently, hard magnetic components in MEMS</i>	<i>Teh and Yaacob (2011a), Teh et al.(2013)</i>
FePt/FeCo/FePt	radio frequency (RF) magnetron sputtering	3.3k Oe (after annealing)	~750 emu/cm ³ (after annealing)	soft and hard magnetic layer in high resolution MFM tips	Rheem et al. (2005)
Fe _{100-x} Pt _x (x = 35–57)-	dc magnetron co-sputtering	1113 kA/m	0.594W b/ m ²	perpendicular magnetic recording media	Sun et al. (2011)
Fe ₅₂ Pt ₄₈	magnetron co-sputtering	6 kOe	Nil	magnetic recording media	Sun et al. (2005)
Fe ₄₉ Pt ₅₁	RF magnetron sputtering	9.66 kOe (after annealing)	856 emu/cm ³ (after annealing)	high-density recording media, permanent micromagnets, and magneto-optical materials	Chen et al. (2005)
<u>CoFePt</u>					
<i>Co-Fe-Pt</i>	<i>Electro-deposition</i>	<i>45 – 111 Oe</i>	<i>83-377 emu/g</i>	<i>magneto-optical recording, perpendicular magnetic recording and most recently, hard magnetic components in MEMS</i>	<i>Teh and Yaacob (2011a)</i>
(Fe Co) ₃ Pt	e-beam sputtering	~ 50 Oe	~1200 emu/cm ³	perpendicular magnetic media	Nahid et al. (2004)
(Fe _{1-x} Co _x) ₅₉ Pt ₄₁ (x = 0, 0.1, 0.2, 0.9)	UHV-based magnetron sputtering	434-9220 Oe (after annealing)	424-1196 emu/cm ³	high density magnetic recording	Lai et al. (2004)
Fe _{49-x} Co _x Pt ₅₁ (x = 1.3)	RF magnetron sputtering	6.31 kOe (after annealing)	1180 emu/cm ³ (after annealing)	high-density recording media, permanent micromagnets, and magneto-optical materials	Chen et al. (2005)

6.2 Conclusions

From the results presented in the previous chapters, it can be concluded that the production of nanocrystalline ferromagnetic films by electrodeposition for various applications is a viable proposition. In particular, throughout the course of this work, nanocrystalline Co-Fe, Co-Pt, Fe-Pt and Co-Fe-Pt alloy thin films were successfully synthesized. Plating baths and operating conditions for the synthesis of each of the mentioned systems were identified. Correlations between microstructure, crystallographic structure, morphology, surface roughness and magnetic properties are presented. Various nanoscale capable characterization methods are illustrated in this thesis and were applied in the characterization work in this research.

Nanostructured Co and Co-Fe alloy films with Fe content up to 18 at % were obtained from a sulfate salt based solution containing sodium saccharin as grain refining agent. The crystal structure is found to be dependent on the composition and is similar to the crystal structure reported in equilibrium phase diagram of Co-Fe. The saturation magnetization values are relatively high when a mixture of BCC and FCC phases were observed. The magnetic force is increased with the increase of surface roughness, granule size and clusters of the film. Co₁₀₀ and Co₉₄-Fe₆ films with MFM stripe domain structure shows lower magnetic force. In short, saturation magnetization values are affected by the change of the FCC to BCC ratio caused by the variation of the Co content.

Using a chloride-based solution containing ammonium tartrate as complex forming additive, Co-Pt alloys films was synthesized where the cobalt content was varied from 43 to 97 at. %. The difference between values of standard reduction potential for both Co and Pt is relatively high. Therefore, ammonium tartrate and ammonia solution were added to form Co tartrate complex to enhance the co-deposition with Pt complexes. The Co₄₃-Pt₅₇, Co₅₆-Pt₄₄ and Co₈₆-Pt₁₄ films were electrodeposited

with nanocrystalline microstructure with average crystallite sizes less than 10 nm. Both Co₉₅-Pt₅ and Co₉₇-Pt₃ films showed amorphous crystal structure. MFM characterization of Co₄₃-Pt₅₇ film showed granular domain structure and the magnetic force is correlated with the grain boundaries or surface topography. The saturation magnetization (M_s) values of as-synthesized nanostructured Co-Pt thin films increased with the increase of Co content.

To our knowledge, there is no publication on Co-Fe-Pt thin films prepared by electrochemical deposition method by using direct current because of the difficulty of the preparation of stable and effective electrolyte solution. This research is focused on the effects of the addition of various concentrations of Co towards the composition, crystallographic structure, microstructure and magnetic properties of the Fe-Pt alloy films. A mixture of chloride and sulfate salt solution containing ammonium tartrate as complex forming additive was used in the synthesis process. Cobalt was preferentially deposited compared to iron during Co-Fe-Pt film electrodeposition. XRD results showed the formation of disordered face centered cubic (FCC) Fe-Pt phase and all peaks were shifted to a slightly higher diffraction angles with increasing cobalt content. All the as-synthesized Fe-Pt and Co-Fe-Pt thin films possessed nanocrystalline microstructure and the average crystallite sizes varied from 2.33 nm to 6.54 nm. The saturation magnetization and coercivity increased with increasing cobalt content.

6.3 Recommendations for Future Research

Although the primary objective of the present work is to develop an electrodeposition process to produce nanostructured soft magnetic thin films, more research is required in order to further the understanding of these new nanocrystalline magnetic film that possesses unique structures and properties. Other metal deposition techniques such as pulse electrodeposition method and physical deposition (sputtering and evaporation) methods can be explored for future research work. The other method that might be used to synthesize alloy films with a wide range of composition is by using potentiostat or galvanostat and reference electrode. Typically, most of the researchers are using potentiostat or galvanostat to control the deposition voltage based on standard reduction potential of the element. In addition, Ag/AgCl or saturated calomel electrode (SCE) is used as reference electrode and all the electrode potentials in the research are referred to the potential of reference electrode.

Several studies have been performed on the influence of organic additives in the electrolyte bath. Some additives are known to enhance the morphological and physical properties of the electrodeposited metals. One of the suggestions for future research is to investigate in detail the effects of organic additives on the magnetic film, such as saccharin. Other type of grain refining agents, for instance, phthalimide might be used to improve the morphology and physical properties of magnetic film. In Chapter 5.2 and 5.3, it was shown that ammonium tartrate and ammonia solution was used as complex forming additive to promote the polarization of Co^{2+} , Fe^{2+} and Pt^{4+} and subsequently enhance the co-deposition of Co, Fe and Pt. It is recommended to use other type of complex forming additive such as ammonium citrate for future work.

The coercivity values obtained in the present research is relatively low. Some applications require higher coercivities. In general, annealing is required for phase transformation from soft magnetic face-centered cubic (fcc) phase, which exists in the

as-synthesized film, to hard magnetic $L1_0$ ordered face-centered tetragonal (fct) phase (Wang et al. 2004; Lim et al., 2004). Optimization of the annealing process by adjusting annealing duration and temperature is still necessary in future work. Although the present research investigated the magnetic force by MFM and the domain wall motion was generally discussed, future work should address these issues with more details and how the domain wall motion can be facilitated by controlling crystallographic texture, grain size distribution and magnetic properties should be focused. The domain structure of nanocrystalline materials is not well understood not only for materials produced by electrodeposition method, but also for materials produced by other methods.

A magnetic property is also recommended to be tested with external magnetic field applied at a defined higher temperature. Magnetic properties out of plane can be investigated in the future work. In addition, annealing in an external magnetic field, a practice commonly used in the manufacturing process of soft magnetic recording heads, could reduce the coercivity. However, such experiments must be carried out at a temperature below the onset of grain growth to preserve the nanostructure in the materials.

Based on literature, the oxygen content in deposits can be decreased by annealing in hydrogen atmosphere and magnetic properties of the materials are improved in comparison with the as-deposited and vacuum-annealed films. It is equally important to understand the reasons for the incorporation of oxygen and to find routes to avoid it. This requires more knowledge on the deposition mechanisms as well as the resulting composition and structure of the deposits.

In chapter 5.1, binary Co-Fe alloy deposits were successfully produced within a composition range of up to 18 at. % of Fe. The deposits with higher Fe content were easily oxidized and the results on these deposits are not included in this thesis.

Modification of the bath chemistry in the Co-Fe system is recommended to accommodate other alloys having higher Fe contents that are of scientific and engineering interests. Besides Co, Fe and Pt binary alloy system, it is recommended to develop other ferromagnetic materials such as Ni, Ni-Fe, Co-Ni, Co-Ni-Fe, etc by using electrodeposition technique. The effect of deposition parameters such as pH, plating bath temperature, duration and agitation on the composition of various nanocrystalline magnetic films and morphology should be studied in more details.

REFERENCES

- Abbaschian, R., Abbaschian, L., Reed-Hill, R.E. (2009). *Physical Metallurgy Principles*, 4th edn. United State of America: Cengage Learning. pp. 30.
- Abes, M., Venuat, J., Muller, D., Carvalho, A., Schmerber, G., Beaurepaire, E., Dinia, A. and Pierron-Bohnes, V. (2006). Structural properties of CoPt films patterned using ion irradiation. *Catalysis Today*. **113**. 245-250.
- Aktas, B., Tagirov, L. and Mikailov, F. (2003). *Nanostrucutred magnetic materials and their applications*. NATO Science Series. Netherlands: Kluwer Academic Publishers. pp. xxiii.
- Alper, M., Kockar, H., Sahin, T and Karaagac, O. (2010). Properties of Co-Fe films: dependence of cathode potentials. *IEEE Trans. Magn.* **46** (2). 390-393.
- Blitz, J. (1991). *Electrical and magnetic methods of nondestructive testing*. Adam Hilger. England: IOP publisher Ltd. pp. 20, 35-37.
- Bhushan, B. (2010) *Handbook of nanotechnology*, 3rd edn. Germany: Springer-Verlag Berlin Heidelberg. pp. 1.
- Bhushan, B., Fuchs, H. and Hosaka, S. (2004) *Applied scanning probe methods*. Germany: Springer-Verlag Berlin Heidelberg.
- Bob, B. H. (2009). *Two-dimensional X-Ray Diffraction*. United State of America: John Wiley & Sons, Ltd.
- Brandon, D.G. and Kaplan, W. D. (2008). *Microstructural characterization of materials* 2nd edn. England: John Wiley & Sons, Ltd. pp. 19-21, 30, 263, 405.
- Capek, I. (2006). Nanocomposite structures and dispersions: science and nanotechnology- fundamental principles and colloidal particles. Elsevier. pp 273.

Chen, S.K., Hsiao, S.N., Yuan, F.T. and Chang, W.C. (2005). Magnetic Property Enhancement of $\text{Fe}_{49-x}\text{Co}_x\text{Pt}_{51}$ ($x = 0.0, 0.7, 1.3, 2.2$) thin films. *J. Magn. Magn. Mater.* **41** (10). 3784-3786.

Cheung, C. (2001). *Synthesis and microstructural characterization of electrodeposited nanocrystalline soft magnets*. PHD Thesis. Department of Materials and Metallurgical Engineering, Queen's University, Kingston, Ontario, Canada. pp. 3,7, 11-12, 127.

Choy, K. L. (2002). *Innovative processing of films and nanocrystalline powders*. London: Imperial College Press. pp. 2, 27.

Correia, A. N., Oliveira, R.C.B. and Lima-Neto, P. (2006). Preparation and characterization of electrodeposited iron+cobalt thin films from a chloride bath. *J. Braz. Chem. Soc.* **17** (1). 90-97.

Corriu, R. and Trong Anh, N. (2009). *Molecular chemistry of sol-gel derived nanomaterials*. United Kingdom: John Wiley & Sons, Ltd. pp. 1,17.

Cullity, B.D. and Graham, C.D. (2009) *Introduction to magnetic materials*, 2nd edition. New Jersey, United State of America: John Willy & Sons. Inc. pp. 359-362.

Ding, Y.F., Chen, J.S. and Liu, E. (2005). Structural and magnetic properties of nanostructured FePt/MgO granular films. *Thin solid films.* **474**. 141-145.

Durney, L. J. (1996). *Electroplating Engineering handbook*, 4th edn. United Kingdom: Chapman & hall. pp. 60.

Eftekhari, A. (2008). *Nanostructured materials in electrochemistry*. Weinheim, Germany: WILEY-VCH Verlag GmbH & Co. KGaA. pp. vii, 291.

El-Sherik, A.M., Erb, U. (1995). Synthesis of bulk nanocrystalline nickel by pulsed electrodeposition, *J. mater. Sci.* **30**. 5743-5749.

Feynman, R. (1992). *There's plenty of room at the bottom*, transcript of the talk given by Richard Feynman on Dec 26, 1959 at the annual meeting American Physical Society. *J. Microelectromech. Systems*. **1**. 60-66.

Franz, S., Bestetti, M. and Cavallotti, P.L. (2007). Co-Pt thin films for magnetic recording by ECD from acidic electrolytes. *J. Magn. Magn. Mater.* **316**. e173-e176.

Fujita, N., Amasaki, S., Yumiba, H., Sasadaira, M., Wachi, H., Nakano, M. and Fukunaga, H. (2007). Preparation of Co-Pt thick film magnets by pulse electrodeposition. *J. Magn. Magn. Mater.* **310**. 2590-2592.

Ge, H.L., Wei, G.Y., Wu, Q., Zhou, Q.Y. and Wang, X.Y. (2007). Influence of bath composition on magnetic properties of electrodeposited Co-Pt-W thin films. *J. of Iron and Steel Research*. **14** (4). 65-68.

Geoffrey, A.O. and Andre, C. A. (2006). *Nanochemistry, a chemical approach to nanomaterials*. London: The Royal Society of Chemistry. pp. 2.

Goldstein, J.I., Newbury, D.E., Echlin, P., Joy, D.C., Fiori, C. and Lifshin, E. (1981). *Scanning electron microscopy and X-ray microanalysis*. New York: Prentice Hall Press. pp. 205-207.

Hammond, P. (1978). *Electromagnetism for engineers: an introductory course*, 2nd edn. United Kingdom: Pergamon Press, Oxford. pp. 152.

Heimendahl, M.V. (1980). *Electron microscopy of materials: An introduction*. University of Erlangen-Nurnberg West Germany: Academic Press. pp. 20-21.

Hodes, G. (2001). *Electrochemistry of nanomaterials*. Weinheim. Germany: WILEY-VCH Verlag GmbH & Co. KGaA. pp. V.

Holloway, P.H. and Vaidyanathan, P.N. (2010). *Characterization of metals and alloys*. United State of America: Momentum Press. pp. 144-145, 253.

Iniewski, K. (2011). *Nanoelectronics: nanowires, molecular electronics and nanodevices*. United State of America: Mc Graw Hill. pp. V.

Islam, J., Yamamoto, Y., Shikoh, E., Fujiwara, A. and Hori, H. (2008). A comparative study of Co and Fe thin films deposited on GaAs(001) substrate, *J. Magn. Magn. Mater.* **320**. 571-574.

Jack W.D. (1993) *Electrodeposition: The material science of deposits and substrates*, New Jersey, United State of America: Noyes publications.

Jeong, G.H., Lee, C.H., Jang, J.H., Park, N.J. and Suh, S.J. (2008). The microstructure and magnetic properties of electrodeposited Co-Pt thin films on Ru buffer layer, *J. Magn. Magn. Mater.* **320**. 2985-2987.

Jeong, S., Hsu, Y.N., Laughlin, D.E. and Henry, M.E. (2001). Atomic ordering and coercivity mechanism in FePt and CoPt Polycrystalline Thin Films. *IEEE Trans. Magn.* **37** (4). 1299-1301.

Judy, J.W. and Myung, N. (2001). *Magnetic materials for MEMS*. University of California, Los Angeles, United State of America.

Kazmerski, L.L. (1980). *Polycrystalline and amorphous thin films and devices*. United State of America: Academic Press, Inc. pp.2-5

Kelsall, R.W., Hamley, I.W. and Mark, G. (2005). *Nanoscale science and technology*. United Kingdom: Wiley Inter Science. pp. 71.

Koay, M.H. and Yaacob, I.I. (2007). Preparation of Iron-Platinum nanoparticles in water/triton/cyclohexane microemulsions. *J. Mater. Processing Tech.* **191**. 48-50.

Kockar, H., Alper, M., Sahin, T. and Karaagac, Oznur. (2010). Role of electrolyte pH on structural and magnetic properties of Co-Fe films, *J. Magn. Magn. Mater.* **322**. 1095-1097.

Kovacs, A., Sato, K. and Hirotsu, Y. (2007). Improvement of structural and magnetic properties of L1₀-FePd Nanocrystals by Co addition. *IEEE Trans. Magn.* **43** (6). 3097-3099.

Lacheisserie, E.D.T. and M. Schlenker, D.G. (2003). *Magnetism fundamentals*. United State of America: Kluwer Academic Publishers. pp.186, 268.

Lai, Y.C., Chang, Y.H. and Chen, Y.K. (2004). The magnetic properties of Fe-Co-Pt alloys films. *Thin Solid Films*. **469-470**. 290-294.

Lai, Y.C., Chang, Y.H., Chen, Y.C., Lin, H.J. and Chen, G.J. (2007). The influence of alloying Fe₅₉Pt₄₁ thin films with Co on their magnetic and microstructural properties. *J. Mater. Sci.* **42**. 6887-6894.

Lallemand, F., Ricq, L., Bercot, P and Pagetti, J. (2002). Effects of the structure of organic additives in the electrochemical preparation and characterization of CoFe film. *Electrochimica Acta*. **47**. 4149-4156.

Lee, Y. S. (2008). *Self-assembly and nanotechnology: a force balance approach*. United State of America: John Wiley & Sons, Inc. pp. 249.

Li, S. J., Jagdish, S., Li, H., Ipsita, A. and Banerjee, I. (2011). *Biosensor nanomaterials*. Weinheim, Germany: WILEY-VCH Verlag GmbH & Co. KGaA. pp. 39.

Lim, B.C., Chen, J.S. and Wang, J.P. (2004). Thickness dependence of structural and magnetic properties of FePt films. *J. Magn. Magn. Mater.* **271**.159-164.

Liu, X., Evans, P. and Zangari, G. (2000) Electrodeposited Co-Fe and Co-Fe-Ni alloy films for magnetic recording write heads. *IEEE Trans. Magn.* **36 (5)**. 3479-3481.

Lorrain, P., R. Corson, D. and Lorrain, F.(1988). *Electromagnetic fields and waves*. United State of America: W.H. Freeman and company. pp. 374-375.

Manhabosco, T.M. and Muller, I.L. (2008). Influence of saccharin on morphology and properties of cobalt thin films electrodeposited over n-Si (100). *Surface & Coating Technology*. **202**. 3585-3590.

Martin, J.A. (1999). *Magnetic properties of nanocrystalline transition metals*. PHD Thesis, Department of Materials and Metallurgical Engineering, Queen's University, Kingston, Ontario, Canada. pp. 39, 132-134, 177-180, 184.

Nahid, M.A.I. and Suzuki, T. (2004). Magnetic and magneto-optical properties of FeCo₃Pt alloy thin films. *J. Magn. Magn. Mater.* **282**. 260-263

Nahid, M.A.I. and Suzuki, T. (2005). Magnetic properties and structure of Fe_xCo_{100-x})₃Pt alloy thin films. *J. Magn. Magn. Mater.* **286**. 315-319.

Nalwa, N.S. (2000), *Nanostructured materials and nanotechnology*. United States of America: Academic Press. pp. 1, 101.

Nalwa, N.S. (2002), *Magnetic nanostructures*. United States of America: American Scientific Publishers. pp. 95, 112.

Owens, F. J. and Poole, C.P. (2008). *The physics and chemistry of nanosolids*. United States of America: John Wiley & Sons, Inc. pp. 63, 396-397.

Parthasaradhy, N.V. (1989). *Practical electroplating handbook*. New Jersey, United States of America: Prentice Hall Inc. pp. 28.

Pattanaik, G., Kirkwood, D. M., Xu, X. and Zangari, G. (2007). Electrodeposition of hard magnetic films and microstructures. *Electrochimica Acta*. **52**. 2755-2764.

Qiang, C.W., Xu J.C., Xiao, S.T., Jiao, Y.J., Zhang, Z.Q., Liu, Y. and Tian, Z.Z. (2010). The influence of pH and batch composition on the properties of Fe-Co alloy films electrodeposition. *Applied surface science*. **257**. 1371-1376.

Rao, C.N.R., Muller, A. and Cheetham, A.K. (2004). *The chemistry of nanomaterials. Vol 1*. Germany: Wiley-VCH Verlag GmbH & Co. pp.1.

Rheem, Y., Saito, H. and Shunji, I. (2005). Fabrication of FePt/FeCo/FePt exchange-spring trilayer with very thin FeCo layer for high resolution MFM Tips. *IEEE Trans. Magn.* **41** (10). 3793-3795

Samardzija, Z., Rozman, K. Z. and Kobe, S. (2009). Determination of the composition of Co-Pt thin films with quantitative electron-probe microanalysis. *Mater. Characterization*. **60**. 1241-1247.

Seki, T., Shima, T., Takanashi, K., Takanashi, Y., Matsubara, E. and Hono, K. (2004). Optimum compositions for the low-temperature fabrication of highly ordered FePt (001) and FePt (110). *IEEE Trans. Magn.* **40** (4). 2522-2524

Shigeru, I, Miki, U and Tohru, D. (2005). Electrodeposited of FePt magnetic material and embedding into anodic alumina-nanoholes, *IEEE Trans. Magn.* **41** (10). 3349-3351.

Shindo, D. and Oikawa, T. (2002). *Analytical electron microscopy for materials science*. Japan: Springer-Verlag. pp. 86.

Sun, A.C., Chen, S.C., Kuo, P.C., Chou, C.Y., Fang, Y.H., Hsu, J.H., Huang, H.L. and Chang, H.W. (2005). Reduction of grain size and ordering temperature in L10 FePt thin films. *IEEE Trans. Magn.* **41**(10). 3773-3774.

Sun, T.H., Chen, S.C., Su, W.H., Shen, C.L., Kuo, P.C. and Chen J.R. (2011). Magnetic properties and microstructures of single-layered Fe_{100-x}Pt_x films deposited onto heated substrates. *Thin Solid Films*. Article in press.

Suryanaraya, C. and Norton, M. G. (1998). *X-ray diffraction: a practical approach*. New York: Plenum Press. pp. 21-22.

Suzuki, T., Notarys, H. and Dobberty, D.C. (1992). Coercivity mechanism and microstructure of (Co/Pt) multilayers. *IEEE Trans. Magn.* **28** (6). 2754-2759.

Tang, Z. and Sheng, P. (2003). *Nano science and technology: novel structures and phenomena*. London and New York: Taylor & Francis Inc. pp. 25-26, 28, 39.

Teh, C.L. (2003). *Synthesis of barium ferrite fine powder via modified high-energy ball milling and heat treatment*. Master of Engineering Science. Thesis. Institutes of Postgraduate Studies and Research, University of Malaya. pp. 64.

Teh, S.H. and Yaacob, I.I. (2009). Synthesis and characterization of electrodeposited iron-platinum nanostructured thin films. *Mater. Research Innovations*. **13** (3). 199-202.

Teh, S.H. and Yaacob, I.I. (2010). The effect of cobalt addition on structural and magnetic properties of electrodeposited iron-platinum nanocrystalline thin films. *Mater. Sci. Forum.* **654-656**. 1736-1739.

Teh, S.H. and Yaacob, I.I. (2011a). Synthesis and characterization of Fe-Pt and Co-Fe-Pt nanocrystalline magnetic thin films electrodeposited from a tartrate-alkaline electrolyte solution. *Mater. Research Innovations.* **15 (3)**. 196-201.

Teh, S.H. and Yaacob, I.I. (2011b). Synthesis and characterization of Co-Fe nanocrystalline magnetic films electrodeposited from electrolyte solution containing sodium saccharin. *IEEE Trans. Magn.* **47 (10)**. 4398-4401.

Teh, S.H., Yaacob, I.I. and Johan, M. R. (2013). Preparation and characterization of Fe-Pt nanostructured magnetic films electrodeposited from tartrate-stablized sulfate baths. *Int. J. Electrochem. Sci.*, 8. Accepted for publication.

Thomas, S. and Stephen, R. (2010) *Rubber Nanocomposites: Preparation, Properties and Applications*. Singapore: John Wiley & Sons, Ltd. pp. 262.

Vollath, D. (2008). *Nanomaterials: an introduction to synthesis, properties and applications*. Weinheim, Germany: WILEY-VCH Verlag GmbH & Co. KGaA. pp. 1-3, 109-110.

Vopsaroiu, M., Thwaites, M.J., Fernandez, G.V., Lepadatu, S., O'Grady, K. (2005). Grain size effects in metallic thin films prepared using a new sputtering technology. *Journal of optoelectronics and advanced materials.* **7(5)**. 2713-2720.

Wang, F., Doi, S., Hosoiri, K. and Watanabe, T. (2004). Microstructure of electrodeposited Fe-Pt binary alloy films. *Mater. Sci. Eng.* **A 375-377**. 1289-1293.

Wang, F., Hosoiri, K., Doi, S., Okamoto, N., Kuzushima, T., Totsuka, T. and Watanabe, T. (2004b). Nanostructured L₁₀ Co-Pt thin films by an electrodeposition process. *Electrochem. Comm.* **6**. 1149-1152.

Wang, A., Li, T., Zhou, Y., Jiang, H. and Zheng, W. (2003). Coupled Co-Pt nanoparticles in C matrix. *Mater. Sci. Eng.* **B103**. 118-121, 2003.

Wee, Andrew T. A. (1997). *Synthesis and characterization of magnetic thin films*. Master thesis, National University of Singapore. pp.16.

Wei, D.H., Yu, C.C., Fong, S.C., Yuan, F.T., Chang, H.W., You, K.L., Liou, Y., Chin, T.S. and Yao, Y.D. (2007). Grain refining and decoupling in FePt/SiO₂ nanogranular films for magnetic recording. *IEEE Trans. Magn.* **43** (6).

Wei, D.H., You, K.L., Yao, Y.D., Chiang, D.P., Liou, Y., Chin, T.S. and Yu, C.C. (2007b). Grain size refining and microstructure of FePt/MgO nanogranular thin films. *J. Magn. Magn. Mater.* **310**. e753-e755.

Wei, G., Ge, H.L., Huang, L.H., Wu, Q., Wang, Q.Q. and Huang, L.M. (2008). Influence of complexing agent on the electrodeposited Co-Pt-W magnetic thin films *Appl. Surface Sci.* **254**. 3425-3430.

Weisheit, M. Lai, Schultz, L. and Fähler, S. (2007). Temperature dependence of FePt thin film growth on MgO (100). *Thin Solid Films.* **515**. 3952.

Wilde, G. (2009). *Nanostructured materials*. Netherlands: Elsevier Ltd. pp. 2-4, 30.

Williams, D.B. and Barry, C.C. (2009). *Transmission Electron Microscopy: A textbook for Materials Science*, 2nd edn. United State of America: Springer Science + Business Media. pp. 55-57.

Zana, I., Zangari, G. and Shamsuzzoha, M. (2004). Enhancing the perpendicular magnetic anisotropy of Co-Pt (P) films by epitaxial electrodeposition onto Cu (111) substrates. *J. Magn. Magn. Mater.* **292**. 266-280.

Zhang, Y. and Douglas, G. I. (2007). Characterization of Co-Fe and Co-Fe-Ni soft magnetic films electrodeposited from citrate-stabilized sulfate baths. *Mater. Sci. Eng.* **B140**. 15-22.

Zong, B.Y., Han, G.C., Qiu, J.J., Guo, Z.B., Wang, Li, Yeo, W.K. and Liu, Bo. (2008). Ultrashort and High Magnetic Moment CoFe Films Directly Electrodeposited from a B-Reducer Contained Solution. *Research letters in physical chemistry*. doi:10.1155/2008/342976.

Zhou, X.S., Liu, Q. and Ivey, D.G. (2008). *Phase analysis of cobalt-iron films electrodeposited from ammonium citrate stabilized electrolytes*. 2nd IEEE International Nanoelectronics Conference (INEC 2008).

Zuzek Kozman, K., Krause, A., Leistner, K., Fahler, S., Schultz, L. and Schlorb, H. (2007). Electrodeposition and hard magnetic properties of Co-Pt films in comparison to Fe-Pt films. *J. Magn. Magn. Mater.* **314**. 116-121.

Internet reference, a. <http://www.materialsviews.com/novel-gold-nanoparticle-based-assay-for-understanding-alzheimers-disease/>

Internet reference, b. http://www.corrosionclinic.com/corrosion_courses/

Internet reference, c. <http://en.wikipedia.org/wiki/Cobalt>

Internet reference, d. <http://en.wikipedia.org/wiki/Iron>

Internet reference, e. <http://en.wikipedia.org/wiki/Platinum>

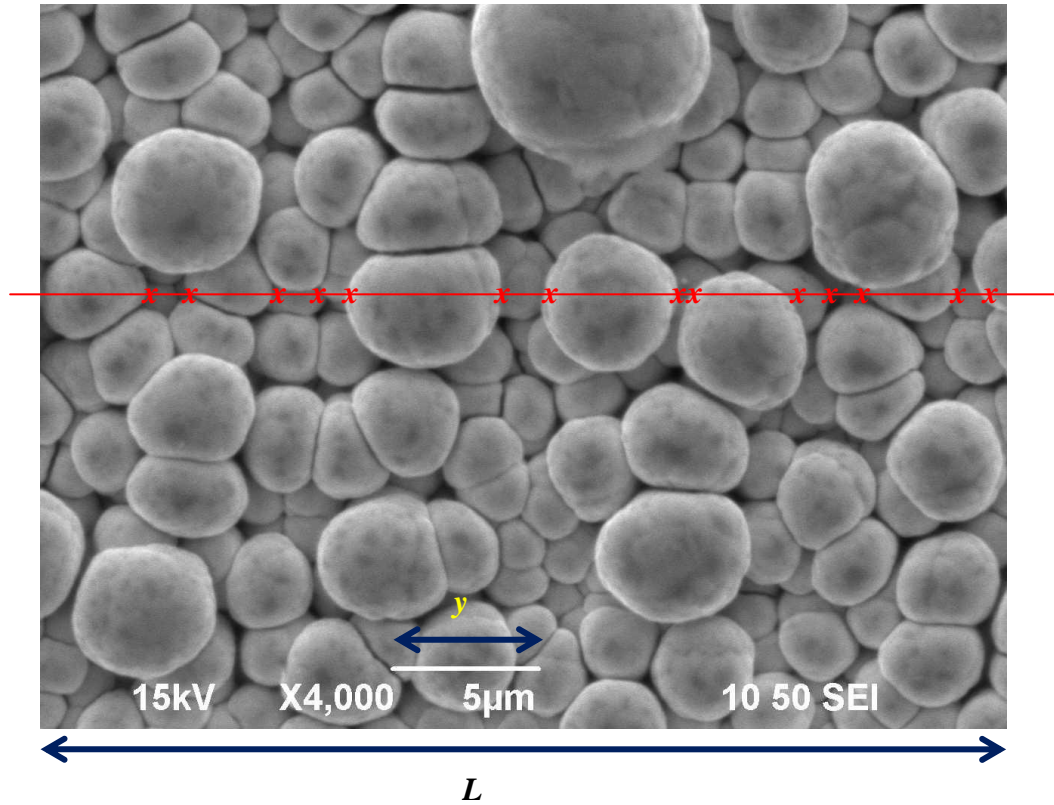
APPENDICES

A. Granule size measurement of Co₄₃-Pt₅₇ alloy thin film by linear intercept method by using SEM micrograph

Magnification = (Length of magnification line, y) / Magnification scale on SEM Micrograph

N_L = (Number of intercept x Magnification) / Length of line, L

Average granule size = $D_L = N_L^{-1} = 1 / N_L$



For example, D_{LI}

Magnification = $0.032 / 0.000005 = 6400$, where $y = 0.032\text{m}$

N_{LI} = (Number of intercept/ length of the line, L) x Magnification

= $(14 / 0.205) \times 6400 = 437073 \text{ m}^{-1}$, where $L = 0.205\text{m}$

$N_{LI}^{-1} = (1 / 437073) \times 1000000$

= **2.2 μm**

Therefore, the average granule size calculated from line 1 is 2.2 μm

Note: The procedure was repeated for 10 lines, and average granule size was obtained from the average of all the data

B. The SEM micrograph, EDS spectrum, atomic and weight percentage of elements of Co₄₃-Pt₅₇ alloy film.

Spectrum Label: Spectrum 1

Livetime 60.0 s

Acquisition geometry (degrees):

Tilt = 0.0

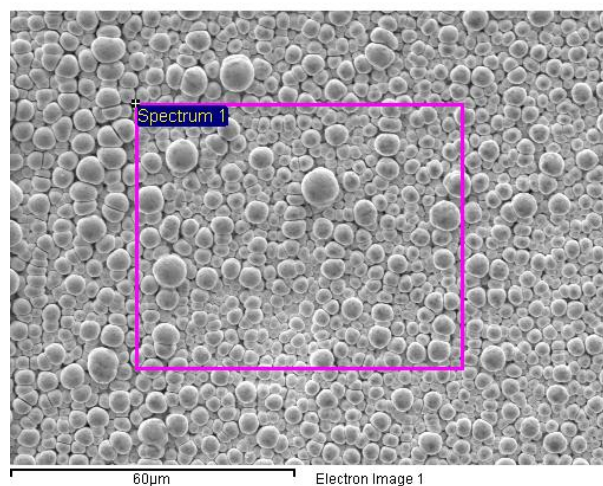
Azimuth = 0.0

Elevation = 35.0

Accelerating voltage = 15.00 kV

Total spectrum counts = 80092

Sample data :	Energy (eV)	Resn. (eV)	Area
Strobe :	2.5	45.60	596845
Optimization data : Cobalt K series			
	Energy (eV)	Resn. (eV)	Area
Strobe :	.0	46.24	291948
Optimization element :	6925.9	140.88	24696



Spectrum processing :

Peaks possibly omitted : 0.270, 6.250 keV

Processing option : All elements analyzed (Normalised)

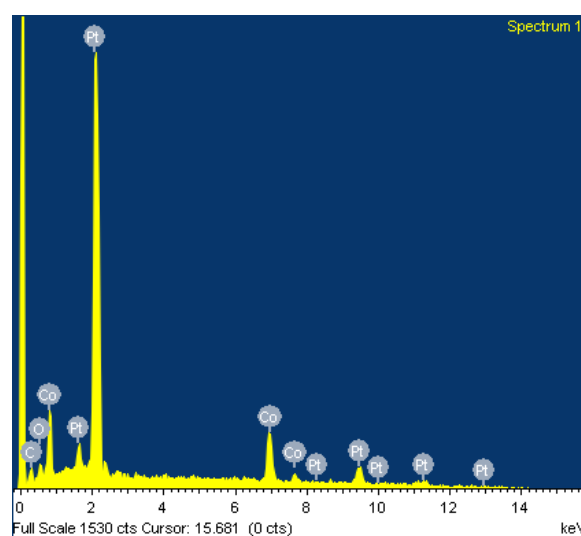
Number of iterations = 2

Standard :

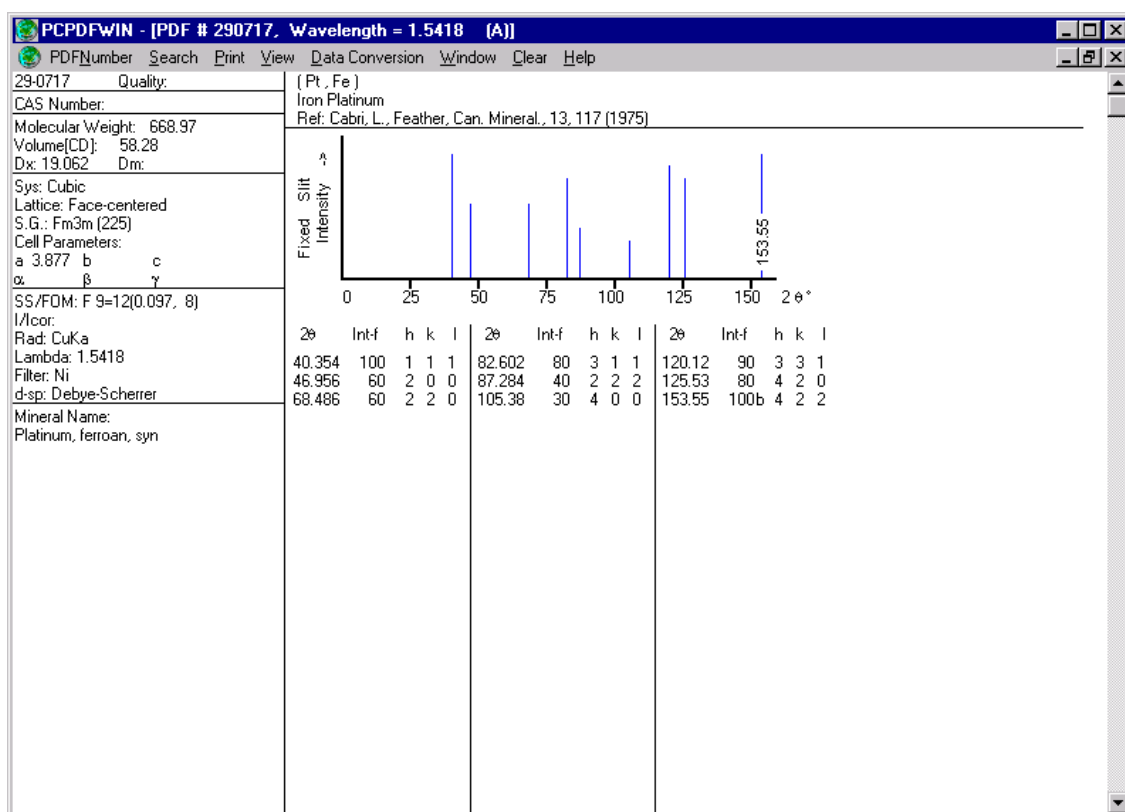
Co Co 1-Jun-1999 12:00 AM

Pt Pt 1-Jun-1999 12:00 AM

Element	Weight%	Atomic%
Co K	20.33	45.80
Pt M	79.67	54.20
Totals	100.00	



C. Example of XRD reference peaks: Fe-Pt face-centered cubic (FCC) phase from JCPDS 29-0717.



D. The XRD peak data and experiment parameter of Co₄₃-Pt₅₇ alloy film obtained using X'Pert Graphics & Identify software.

X'Pert Graphics & Identify mss
(searched) peak list: Q3 2 2/15/09 14:17

Original scan: Q3 Date: 2/3/09 10:25
Description of scan:

Used wavelength: K-Alpha1

K-Alpha1 wavelength (Å): 1.54056
K-Alpha2 wavelength (Å): 1.54439
K-Alpha2/K-Alpha1 intensity ratio : 0.50000
K-Alpha wavelength (Å): 1.54056
K-Beta wavelength (Å): 1.39222

Peak search parameter set: As Measured Intensities
Set created: 1/29/01 11:25
Peak positions defined by: Minimum of 2nd derivative
Minimum peak tip width (°2Theta): 0.00
Minimum peak tip width (°2Theta): 1.00
Peak base width (°2Theta): 2.00
Minimum significance: 0.60

d-spacing (Å)	Relative Intensity (%)	Angle (°2Theta)	Peak Height (counts/s)	Background Width (counts/s)	Tip (°2Theta)	Significance
3.23673	4.03	27.53478	9.66	12.22	0.14000	0.61
2.20429	87.51	40.90682	209.74	53.04	0.48000	1.68
2.17420	100.00	41.49898	239.67	52.40	0.48000	2.35
1.57547	3.55	58.53954	8.51	7.13	0.24000	0.94
1.09746	2.54	89.15537	6.09	20.87	0.14000	0.87

E. Full width at half maximum (FWHM) value of Co₄₃-Pt₅₇ alloy film obtained using Philips Electronics's ProFitTM software.

Experiment: D:\SERENE\Q3.PRF

13-jan-2012 14:16

Philips AnalyticalX-Ray

Peak Fit parameters

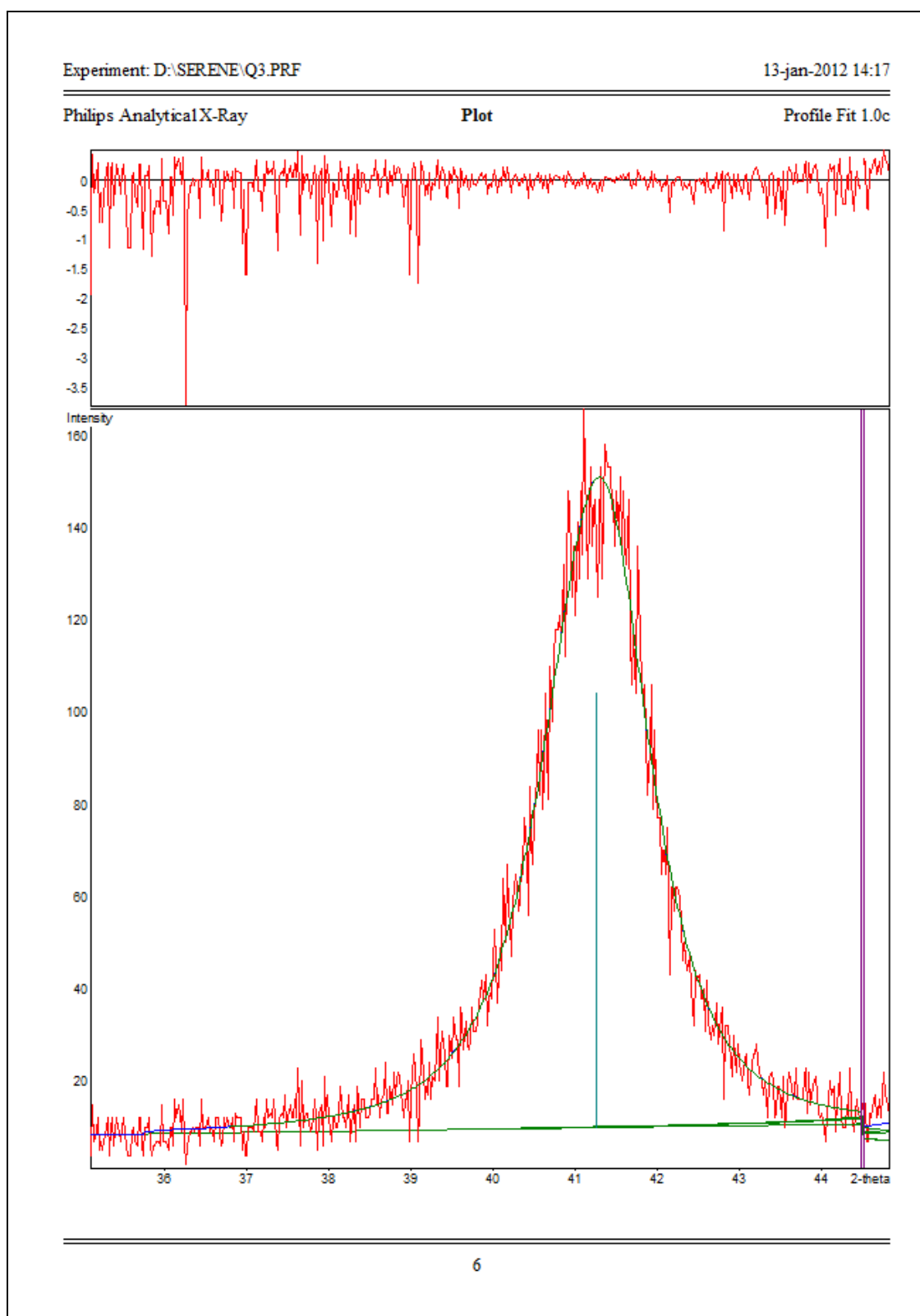
Profile Fit 1.0c

Num	Group	K	&	2θ	Intensity	FWHM	Asymm	μ & ε	a2/a1	Inter.	Breadth	Ratio			
1	1	1		41.2648	Y	94	Y	1.4884	Y	5.00	1.60	0.50	8991.10	1.907	0.780
2	2	1		47.0613	Y	7	Y	2.4584	Y	5.00	1.60	0.50	1060.45	3.150	0.780
3	2	1		47.8833	Y	26	Y	1.7333	Y	5.00	1.60	0.50	2873.52	2.221	0.780
4	2	8	Y	48.4900	Y	11	Y	0.5800	Y	5.00	1.60	0.50	0.00	0.000	0.000
5	2	1	Y	49.2318	Y	1	Y	1.7333	Y	5.00	1.60	0.50	89.86	2.221	0.780
6	3	1		69.6188	Y	0	Y	2.5006	Y	5.00	1.60	0.50	22.39	3.204	0.780
7	3	1	Y	70.0595	Y	18	Y	2.5006	Y	5.00	1.60	0.50	2915.96	3.204	0.780
8	3	1		71.0525	Y	5	Y	0.1403	Y	5.00	1.60	0.50	41.42	0.180	0.780
9	4	1		83.8026	Y	10	Y	2.3193	Y	5.00	1.60	0.50	1506.07	2.972	0.780
10	4	1		84.7382	Y	6	Y	0.1431	Y	5.00	1.60	0.50	54.96	0.183	0.780
11	4	1		85.3212	Y	9	Y	1.8488	Y	5.00	1.60	0.50	1029.46	2.369	0.780

Num	Total area	Overlap	Bg Res
1	13194.77	0.00	9.97
2	1407.57	0.68	6.56
3	4143.56	0.16	6.28
4	0.00	0.00	0.00
5	85.57	0.90	5.82
6	21.14	0.99	4.52
7	4201.93	0.01	4.52
8	57.13	0.70	4.54
9	2125.45	0.18	8.24
10	77.26	0.68	8.71
11	1442.20	0.27	9.02

F. The deconvoluted XRD peak of Co₄₃Pt₅₇ alloy film obtained using Philips

Electronics's ProFitTM software.



G. Crystallite size determination of nanostructured Co₄₃-Pt₅₇ alloy thin film

(Debye Scherrer' equation)

$$\text{Crystallite size, } D = \frac{0.9\lambda}{FWHM \cos\theta}$$

Where λ = wavelength of the X-ray and θ = angles of diffraction

Calculation of crystallite size was determined from the most pronounced XRD peak.

$$\lambda = 1.541, 2\theta = 41.2648, \theta = 20.6324, \pi = 3.142$$

$$FWHM \text{ of sample at } 2\theta^\circ = 1.4884$$

$$FWHM \text{ of LaB}_6 \text{ at } 2\theta^\circ \text{ (equipment peak broadening effect)} = 0.1492$$

$$\text{Actual FWHM} = (1.4884 - 0.1492) / 180 * \pi = 0.0234 \text{ radian}$$

$$D = \frac{0.9\lambda}{FWHM \cos\theta}$$

$$D = (0.9 \times 1.541) / (0.0234) \times (\cos 20.6324 / 180 * \pi)$$

$$= 1.3869 / (0.0234 \times 0.9358)$$

$$= 63.4 \text{ \AA}$$

$$= \mathbf{6.34 \text{ nm}}$$

Therefore, the average crystallite size calculated from 2θ of 41.26° is 6.34 nm

LIST OF PUBLICATIONS

1. Teh, S.H. and Yaacob, I.I. (2010). The effect of cobalt addition on structural and magnetic properties of electrodeposited iron-platinum nanocrystalline thin films. *Materials Science Forum*. Vol. 654-656. 1736-1739.
2. Teh, S.H. and Yaacob, I.I. (2011). Synthesis and characterization of Fe-Pt and Co-Fe-Pt nanocrystalline magnetic thin films electrodeposited from a tartrate-alkaline electrolyte solution. *Mater. Research Innovations*, Vol. 15. No. 3. 196-201. (*ISI Journal, Q4, Impact factor 0.409 for year 2011*)
3. Teh, S.H. and Yaacob, I.I. (2011). Synthesis and characterization of Co-Fe nanocrystalline magnetic films electrodeposited from electrolyte solution containing sodium saccharin. *IEEE Transactions on Magnetics*. Vol. 47. No 10. 4398-4401. (*ISI Journal, Q2, Impact factor 1.363 for year 2011*)
4. Teh, S.H., Yaacob, I.I. and Johan, M. R. (2013). Preparation and Characterization of Fe-Pt Nanostructured Magnetic Films Electrodeposited from Tartrate-stabilized Sulfate Baths. *Int. J. Electrochem. Sci.*, 8. Accepted for publication. (*ISI Journal, Q2, Impact factor 3.729 for year 2011*)
5. Teh, S.H., Yaacob, I.I. and Johan, M. R. (2013). Synthesis and characterization of electrodeposited nanostructured Co-Pt magnetic films. *Mater. Research Innovations*. Submitted for review.
6. Teh, S.H. and Yaacob, I.I. (2011). Synthesis and characterization of Co-Fe nanocrystalline magnetic films electrodeposited from electrolyte solution containing sodium saccharin. Extended digest (HB-10) in IEEE International Magnetics Conference. (INTERMAG 2011).
7. Teh, S.H. and Yaacob, I.I. (2011). Synthesis and characterization of Co-Fe nanocrystalline magnetic films electrodeposited from electrolyte solution containing sodium saccharin. Presented in IEEE International Magnetics Conference April 25-29, 2011 in Taipei, Taiwan (INTERMAG 2011).
8. Teh, S.H., Yaacob, I.I. and Johan, M. R. (2012). "Synthesis and characterization of electrodeposited nanostructured Co-Pt magnetic films", extended digest (ES-07) in IEEE International Magnetics Conference. (INTERMAG 2012).
9. Teh, S.H., Yaacob, I.I. and Johan, M. R. (2012). Synthesis and characterization of electrodeposited nanostructured Co-Pt magnetic films. Presented in IEEE International Magnetics Conference May 8-12, 2012 in Vancouver, Canada (INTERMAG 2012).